Fachbereich C - Mathematik und
Naturwissenschaften

Bergische Universität Wuppertal

Dissertation

zur Erlangung des Doktorgrades
(Dr. rer. nat.)

Search for Ultra-High Energy Photons with the Surface Detector of the Pierre Auger Observatory

---

Der Fachgruppe Physik vorgelegt von

Nicole Krohm

März 2017

**BERGISCHE
UNIVERSITÄT
WUPPERTAL**

Referent:
Prof. Dr. K. - H. Kampert
Korreferent:
Dr. J. A. Bellido-Caceres

Contents

List of Figures

List of Tables

Nomenclature

5T5 T5 trigger with 5 active surrounding stations, page 35

6T5 T5 trigger with 6 active surrounding stations, page 35

AGN Active Galactic Nucleus or Active Galactic Nuclei, page 11

Auger Short for the Pierre Auger Observatory or the Pierre Auger Collaboration, page 6

c.d.f. Cumulative Distribution Function, page 84

C.L. Confidence Level, page 22

CC Charged Current, page 22

CDAS Central Data Acquisition System, page 35

Cen A Centaurus A, page 11

CIC Constant Intensity Cut, page 43

CMB Cosmic Microwave Background, page 7

CR Cosmic Rays, page 1

DLE Direct Light Effect(s), page 72

DSA Diffusive Shock Acceleration, page 13

EM ElectroMagnetic, page 25

FADC Flash Analog-to-Digital Converter, page 35

FY Fluorescence Yield, page 8

GMF Galactic Magnetic Field, page 17

GRB Gamma-Ray Burst(s), page 14

GZK Greisen-Zatsepin-Kuz'min, page 2

HG High-Gain, page 38

IGMF InterGalactic Magnetic Fields, page 17

IRB InfraRed Background, page 19

ISM InterStellar Medium, page 13

LDF Lateral Distribution Function, page 29

LG Low-Gain, page 38

LHC Large-Hadron-Collider, page 32

MF Magnetic Field, page 17

NC Neutral Current, page 22

NKG Nishimura-Kamata-Greisen, page 29

p.d.f. Probability Density Function, page 57

PCA Principal Component Analysis, page 105

SD Surface Detector, page 2

SHDM Super-Heavy Dark Matter, page 16

SNR SuperNova Remnant(s), page 14

T1 Trigger level 1, page 35

T2 Trigger level 2, page 35

T3 Trigger level 3, page 35

T4 Trigger level 4, page 35

T5 Trigger level 5, page 35

TD Topological Defects, page 16

TOT Time-Over-Threshold trigger, page 35

UHECR Ultra-High Energy Cosmic Rays, page 1

VCV Véron-Cetty Véron, page 11

VEM Vertical Equivalent Muons, page 35

Selbstständigkeitserklärung

Hiermit versichere ich, dass ich diese Arbeit selbstständig verfasst und keine anderen als die angegebenen Hilfsmittel und Quellen benutzt sowie alle wörtlich oder inhaltlich übernommenen Stellen als solche gekennzeichnet habe. Die Dissertation hat weder in der gegenwärtigen noch in einer anderen Fassung schon einem anderen Fachbereich einer wissenschaftlichen Hochschule vorgelegen.

.....
Ort, Datum

.....
Nicole Krohm

CHAPTER 1

Introduction

Nuclei of extremely high energies are persistently bombarding the Earth. The so-called *ultra-high energy cosmic rays* (UHECR) were discovered about 100 years ago and they are found to cover a wide range of more than ten orders of magnitude in energy. While for cosmic rays (CR) with lower energies many fundamental questions have been answered, for energies above 10^{17} eV it is not clear:

$\mathcal{W}$hat is the origin of UHECR? Where is the transition from Galactic to Extragalactic sources?

$\mathcal{H}$ow are they accelerated? Is there a maximum energy?

$\mathcal{H}$ow do UHECR propagate to Earth?

$\mathcal{W}$hat is their mass composition?

In this energy regime, the low CR flux is observed indirectly at ground by the air showers that are produced when a CR primary passes the Earth's atmosphere. This challenges the analysis of the mass composition, energy and direction. The world's largest UHECR experiment for energies above 10^{17} eV is the Pierre Auger Observatory in Argentina, sampling air showers during their passage through the atmosphere and at when they reach the ground. After more than ten years of operation it has accumulated a large amount of air shower measurements to tackle the open questions. The more information that is combined, such as studies of the energy spectrum, arrival direction and mass composition of CR, the more concrete our picture becomes. Studies of charged primaries are complemented by searches for neutral primaries. Although not observed yet, there might be a small fraction of primary photons of less than a few percent from the CR acceleration, propagation or from exotic CR sources. Thus, a discovery of UHE photons would open a completely new window. Together with gamma rays, neutrinos, neutrons and the charged primaries, UHE photons would contribute to a multimessenger observation of cosmic rays. Neutral particles propagate on straight lines, pointing back to the location of their production, which eventually might be an astrophysical source of cosmic rays, if close enough. UHE photons and neutrinos are expected to be created in resonant pion photoproductions of UHECR with photon backgrounds during their propagation. Alternatively, several exotic top-down[1] models predict a significant photon fraction from decays of extremely heavy particles.

[1] Non-acceleration models

These models were introduced to explain the energy spectrum published by the AGASA collaboration in 1998 which does not show a suppression at highest energies. Some top-down models predict a dominance of UHE photons above $\sim 10^{20}$ eV and were already disfavoured by upper limits on the UHE photon flux and fraction. Today, on the contrary, a flux suppression of the spectrum above 5×10^{19} eV has been observed by several air shower experiments. The origin of this suppression is still under discussion. An observation of UHE photons would help to solve the question about the origin of UHECR. UHE photons have not yet been observed above a few hundreds TeV. Upper limits on the photon flux and fraction have been placed by different experiments, such as for the surface detector (2008) and the hybrid detector (2016) of the Pierre Auger Observatory. Some of the top-down models have been disfavoured by these limits. Searches for neutral primaries also help to understand the processes at CR sources and during the propagation. Simulations of the UHECR propagation rely on assumptions about e.g. the spectrum at the source, the observed spectrum, on the source distribution, backgrounds (intergalactic magnetic fields and photons) and the mass composition. Upper limits on UHE photon flux and fraction constrain the parameter range of possible astrophysical scenarios used in the simulation.
The main goal of this work is an update and improvement of the upper limits on UHE photons with the surface detector (SD) of the Pierre Auger Observatory. The SD becomes fully efficient for triggering photon-induced showers above 10 EeV. Air showers from primary hadrons and photons differ in their longitudinal development in the atmosphere as well as in their lateral distribution of the electromagnetic and muonic shower component at ground. As the SD does not measure these parameters directly in the standard data reconstruction, correlated SD observables are being investigated in order to establish a photon-hadron separation in the energy range above 10 EeV. Two parameters are combined in a multivariate analysis to optimize the separation power and to make use of the large SD aperture: Δ_{Leeds} (signal risetime) and $\log_{10}(R_{\mathrm{NKG},1000})$ (shape of the lateral density function). Those parameters allow for a powerful compromise of high selection efficiency, which is found when optimizing the data selection towards large statistics preserving a sufficient reconstruction quality, and good photon-hadron seperation. An update of existing photon energy calibrations is presented and the separation parameters are studied carefully. Throughout the search of rare particles, a proper understanding of the electronics and possible faults or rare physical events is needed as they can create photon-like events. Electronics issues are discussed, such as direct light effects or PMT afterpulses. The main result of this work is a significant improvement of the last published limits, entering the region of photon-optimistic GZK-predictions. The upper limit (95% C.L.) on the diffusive, integral photon flux above 10 EeV for zenith angles between 30° and 60° is $1.9 \cdot 10^{-3}$ km^{-2} sr^{-1} yr^{-1}, corresponding to a maximum photon fraction of 0.72%. For 20 EeV (40 EeV) it is $0.99 \cdot 10^{-3}$ km^{-2} sr^{-1} yr^{-1} ($0.49 \cdot 10^{-3}$ km^{-2} sr^{-1} yr^{-1}), corresponding to a maximum photon fraction of 1.6% (6.17%). A differential upper limit has also been placed for the first time in the range of $10 - 30$ EeV, with a maximum photon flux of 2.59 km^{-2} sr^{-1} yr^{-1} and a maximum photon fraction of $\sim 2.73\%$. In this region it is most likely to observe a photon. Photon candidate events are being discussed.

Thesis structure

Chapter 2 introduces the physics of cosmic rays and in particular photons created by cosmic rays. The detection of extensive air showers at the Pierre Auger Observatory is described in Chap. 3. This chapter contains as well technical checks performed for this analysis. A brief introduction of the detection of photons with the surface detector of the Pierre Auger Observatory can be found in Chap. 4. This chapter provides a collection of different technical studies needed to establish a search for UHE photons: a photon energy scale, separation parameters, an understanding of possible detector effects and the formalism to derive an upper limit. Dataset and simulations are described in Chap. 5. The study of SD observables as photon-hadron separation parameters are discussed and compared in Chap. 6. The combination of the most powerful parameters in a multivariate analysis and an update of the upper limits on the flux and fraction of UHE photons are presented in Chap. 7. Conclusions and a brief outlook can be found in Chap. 8.

CHAPTER 2

Cosmic Rays

During the last decades the field of (astro-)particle physics has developed a lot. We start with a brief overview over the current status of cosmic ray physics, with focus on the energy range above a few EeV. In the first sections, the CR energy spectrum, mass composition and directional distribution are introduced, connecting observations and possible interpretations. Section 2.4 outlines the field of possible astrophysical CR sources and acceleration scenarios as well as exotic non-acceleration scenarios. Section 2.5 focusses on the propagation of cosmic rays in magnetic fields, while the remaining interactions are discussed thereafter in connection with the creation of UHE photons. Section 2.6 introduces UHE photons as one possible UHECR component. A last paragraph is dedicated to multimessenger observations of cosmic rays.

2.1 Energy Spectrum

Today we know that the energy spectrum of cosmic rays covers a range from a few hundreds MeV up to to beyond 10^{20} eV. In first order approximation, the differential CR flux follows a power law over a wide energy range,

$$J = \frac{dN}{dE} \propto E^{-\gamma},$$

with $\gamma \approx 2.7$ the spectral index at the observer. During their propagation, primary UHECR interact with surrounding fields. The apparent structures in the observed energy spectrum are closely related to CR composition, the maximum source energy, a galactic or extragalactic source origin and CR propagation. An all-particle spectrum is shown in Fig. 2.1. Above 100 EeV there are only a few particles per km^2 and century.

Knee

The steepening of the spectrum around 4×10^{15} eV is called knee [9]. The spectral index changes from 2.7 to 3.1 [10]. Actually, there is more sub-structure in this energy region. An increase of the mean mass above the knee region was first found by *Khristiansen et al.* in 1994 [11] and was more recently reported by KASCADE [10] and other experiments. The study of the spectrum of

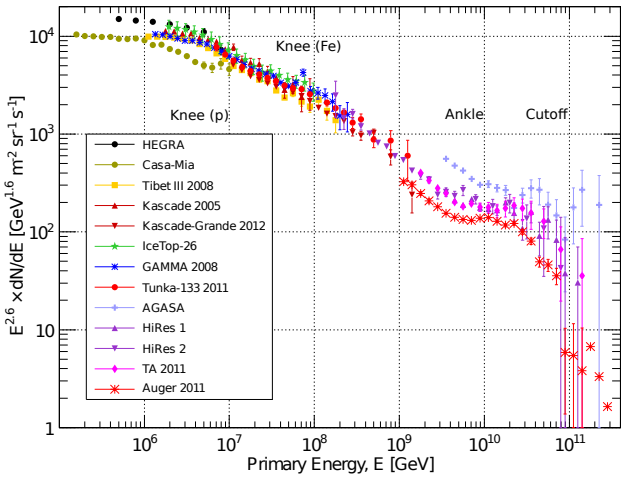

Figure 2.1: The CR energy spectrum as compiled from different air shower experiments above 100 TeV, with flux multiplied by $E^{2.6}$. Adapted from [1], references therein.

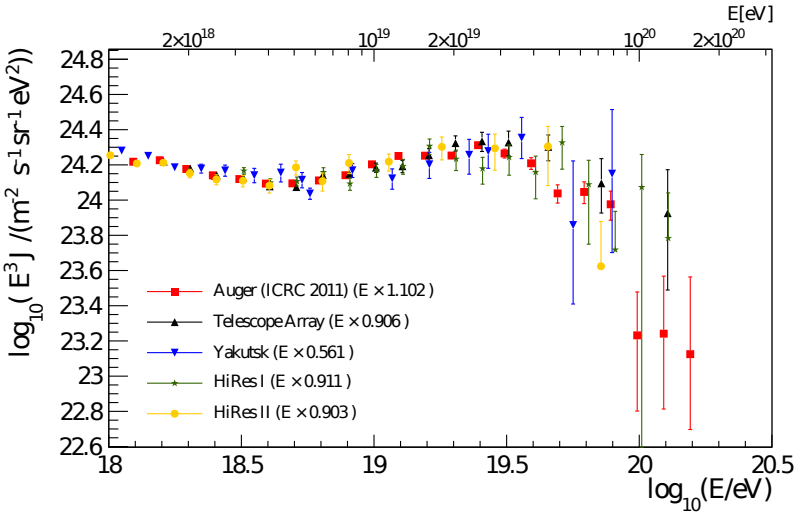

Figure 2.2: Ankle and high energy suppression: Compilation of UHECR energy spectra, published by Auger (combined Hybrid/SD) [2], Telescope Array SD [3, 4], Yakutsk SD [5, 6], HiRes I and HiRes II [7]. The flux is multiplied by E^3. An energy-rescaling has been applied, as shown in the figure. The reference spectrum is the average of those from Auger and TA. From [8].

heavy mass groups brought a remarkable result in 2011. KASCADE-Grande observed a knee-like structure at $10^{16.9}$ eV, referred to as **Fe-knee**, with a statistical significance of 3.5σ [12]. In the all-particle spectrum the range between $10^{16.3}$ eV and 10^{18} eV can be described by a single power law [12], which is expected if the sources emit similar spectra. These observations could be interpreted towards a rigidity-dependent maximum energy of galactic CR sources. The knee-position for different masses is expected to scale with the charge Z of the primary particle [13], starting with the knee of light mass groups (indexed **p-knee**) at $(3-5)\times10^{15}$ eV. Another possible mechanism is a rigidity-dependent leakage of CR from the Galaxy, which could also occur on top of other effects. In both cases the Fe-knee would mark the end of the galactic CR spectrum.

Ankle

The ankle is located at about 4×10^{18} eV [14] where the all particle spectrum becomes more flat (see Fig. 2.2). An early observation by the Fly's Eye experiment was discussed in 1993 [14]. KASCADE-Grande reported an ankle in the spectrum of light mass groups at $10^{17.1}$ eV in 2013 [15], with a statistical significance of 5.8σ. An important question is at which energy the galactic-extragalactic transition takes place. One possible interpretation of the spectrum is that the transition region is located around the ankle of the all particle spectrum. This would be the case for a rigidity-dependent maximum source energy or leakage from the Galaxy or both. The increase of the mean mass above the knee supports this interpretation [16]. The ankle is then due to an overlap of the galactic and extragalactic CR spectrum. Another model by *Berezinsky et al.* [17, 18] predicts a dip at 2.3×10^{18} eV due to pair production of UHE protons with the cosmic microwave background (CMB). To make this mechanism work efficiently, a proton-dominated composition is needed above the ankle. In this scenario the transition is expected already at the Fe-knee. The ankle could also be interpreted as the onset of a different galactic source population. Current studies of the mass composition from the Pierre Auger Collaboration challenge a pure composition and disfavour the dip-model [19, 20].

Highest energies and flux suppression

Another interesting region is the high energy end of the spectrum. Almost 50 years after the prediction of a flux suppression due to resonant pion-photoproduction of UHE nuclei with photon backgrounds (described later), a flux suppression above an energy $E_{\mathrm{th}} = (4-6)\times10^{19}$ eV has been observed by HiRes [21, 22], the Pierre Auger Observatory [23] (with $> 6\sigma$) and Telescope Array [24]. The origin for this structure is still unclear. One possible explanation is the GZK-process where UHE nucleons interact with the CMB in a resonant pion-photoproduction, predicted by *Greisen, Zatsepin and Kuz'min* in 1966 [25, 26]. This process is described in Sec. 2.6.1. Another reason could be the limited energy of CR sources. An additional channel to answer the question about the existence of the GZK effect are UHE photons and neutrinos. The first beyond-GZK event with an energy of 10^{20} eV has been observed already in 1962 with the Volcano Ranch experiment [27]. Their origin and mass composition of beyond-GZK events is still under discussion (for a detailed review see e.g. [28]). In the presence of the GZK effect, the maximum distance of observable sources, called 'GZK horizon', is less than 100 Mpc for proton or iron with energies above the GZK threshold of about 70 EeV [29]. For light nuclei the GZK horizon is an order of magnitude closer. At the end of the 90's, AGASA published a spectrum that continues

at highest energies [30, 31], fueling discussions about non-acceleration scenarios of CR. Today most of these scenarios are ruled out by stringent upper limits on the UHE photon flux and fraction, cf. Sec. 4.4.4.
The ankle and the high energy suppression of the spectrum have been measured by various air shower experiments (see Fig. 2.2). After re-normalizing the spectra within the systematic uncertainties[1][2] of the energy scale to the average spectrum of Auger and TA, there is a fair agreement. The effect of the fluorescence yield (FY) model and optical efficiency on the energy scale is discussed in [32], indicating that in a simple analytical model the energy scale of Auger would be increased by 9% (3%) if the FY model of the TA (HiRes) was used instead. Further discussion about the spectrum can be found e.g. in [16, 33, 34].

2.2 Mass Composition

One, or probably the most important key information for solving the fundamental questions about CR, is the mass composition. This becomes clear in the interpretation of structures in the CR spectrum and in anisotropy studies. While below 100 TeV the mass of CR particles can be measured directly, air shower experiments are so far used for an analysis of the average mass composition at highest energies, with progress towards event-by-event analyses. This involves air shower physics (for details see Chap. 3) and in particular simulations of different primaries. In air shower simulations there is a large variance between the hadronic interaction models at highest energies above 10^{17} eV. This region is not accessible with collider experiments and depends strongly on extrapolations. This poses a restriction to the experimental mass composition studies. Studies of the average mass composition are based on air shower observables that allow to derive energy and mass, such as the longitudinal shower profile in case of fluorescence detectors or the lateral distribution of the electromagnetic and muonic shower component at ground for an array of ground detectors. Here we focus on the longitudinal shower profile.
Showers of different primaries differ in their average depth[3] of the first interaction and in their shower development. The depth of the first interaction, X_1, cannot be observed directly, as the observation level is below the depth of the shower maximum for a reliable energy measurement. The depth of the shower maximum, X_{max}, can be used to study the mass composition: At fixed energy, showers of heavy primaries with mass A reach their maximum earlier in the atmosphere,

$$\langle X_{\mathrm{max}} \rangle^{\mathrm{A}} \approx \langle X_{\mathrm{max}} \rangle^{\mathrm{p}} - D_{\mathrm{p}} \langle \ln A \rangle \,, \tag{2.1}$$

with $D_{\mathrm{p}} = \mathrm{d} \langle X_{\mathrm{max}} \rangle^{\mathrm{p}} / \mathrm{d} \ln E$ the elongation rate of proton primaries (cf. Eq. 3.2). This relation is based on the *Heitler model* [44], extended for nuclear primaries [45, 46]. It assumes that a nucleus with energy E is composed of A nuclei, each carrying an energy $E' = E/A$.
Measurements of X_{max} from different air shower experiments are shown in Fig. 2.3(a). The average mass composition at a certain energy is reflected in $\langle X_{\mathrm{max}} \rangle$. A change towards a heavier CR composition can be observed in a decrease of the elongation rate compared to the proton case as $D = D_{\mathrm{p}} \cdot (1 - \mathrm{d} \langle \ln A \rangle / \mathrm{d} \ln E)$. Above the p-knee a decrease of D is observed, indicating a

[1] Source of systematic uncertainties in energy measurements are the photometric calibration, fluorescence yield, atmosphere, reconstruction and invisible energy. For comparison and discussion see [8].
[2] Systematic uncertainties of the energy scale are on average 20% for the experiments shown in the plot. The shift of the re-normalized spectrum of Auger and TA is about ±10%.
[3] The *slant depth* describes the length in equidistant amounts of traversed matter density in $\mathrm{g/cm^2}$.

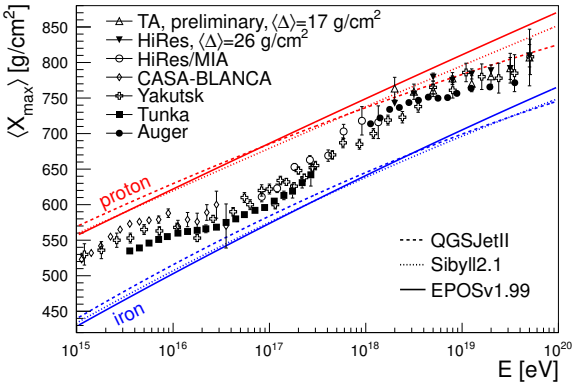

(a) $\langle X_{\max} \rangle$ from different air shower experiments [19, 35–42]. HiRes and TA data have been corrected for detector effects. Air shower simulations of proton and iron with different hadronic interaction models are indicated by solid, dashed and dotted lines. From [43] and references therein

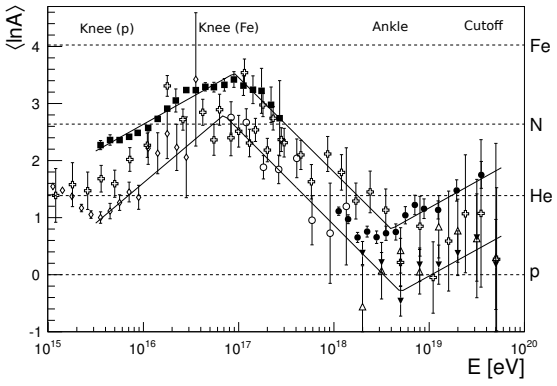

(b) $\langle \ln A \rangle$ derived from $X_{\max}$ measurements (experiments as in Fig. 2.3(a)), for the QGSJetII interaction model. Lines indicate lower and upper boundaries of data within experimental systematics. From [43] and references therein.

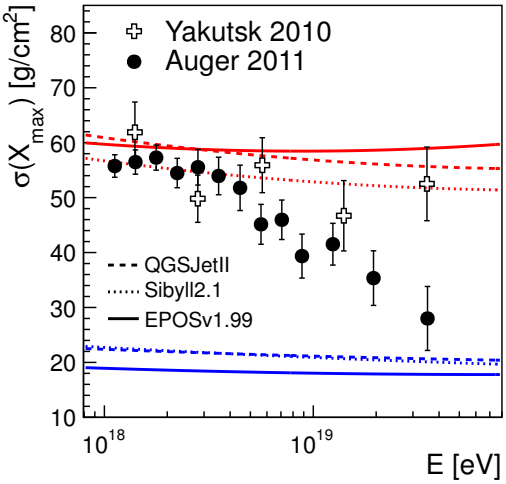

(c) $\sigma(X_{\max})$ measured with Auger and Yakutsk [19, 37], compared to air shower simulations. From [43] and references therein.

Figure 2.3: Measurements of the average depth of the shower maximum $\langle X_{\max} \rangle$, its spread $\sigma = \sigma(X_{\max})$ and the average logarithmic mass $\langle \ln A \rangle$. From [43]

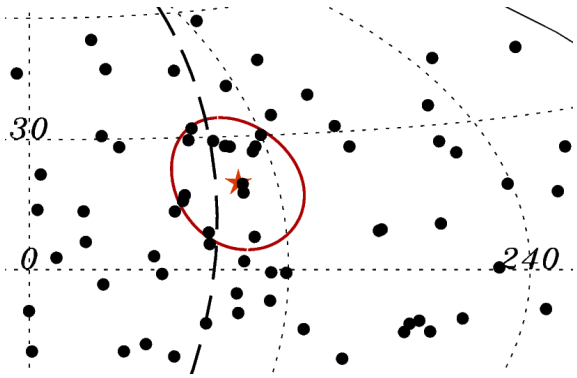

Figure 2.4: The arrival directions of the events with $E \geq 58$ EeV (black dots) within a region of 15° around the direction of Cen A (red star), indicated by a red circle. The map is shown in galactic coordinates. From [48]

change to a heavier composition as expected from rigidity. The elongation rate between Fe-knee and ankle indicates a transition to a lighter composition. In and above the ankle region the QGSJetII model predicts the lowest values of $\langle X_{\max} \rangle$ and elongation rate for proton primaries, which is not far from most of the measured data. Above 10^{18} eV the average depth $\langle X_{\max} \rangle$ differs by more than the systematics between the experiments. The difference between the Auger and TA results was addressed in [47]. The variance between the hadronic interaction models is very large (~ 40 g/cm^2 difference between QGSJetII and Epos1.99 at 10 EeV).
Not only the mean value but also the spread of the $X_{\max}$ distribution depends on the mass composition. In the simplified picture of the superposition model, the spread of the shower maximum for a nucleus with mass A, $\sigma_A(X_{\max})$, is expected to be smaller than for primary proton. Measurements of $\sigma(X_{\max})$ above 10^{18} eV are shown in Fig. 2.3(c), confirming the findings of the $\langle X_{\max} \rangle$ measurements. Another observable that can be derived from $X_{\max}$ measurements is the mean logarithmic mass, $\langle \ln A \rangle$ (cf. Eq. 3.3). Different experimental results are shown in Fig. 2.3(b). Structures are visible at the same energy positions as in Figs. 2.3(a) and 2.3(c).
Recent results of the Pierre Auger Collaboration challenge a light composition above the ankle and thus the dip-model [20].

2.3 Arrival Directions

An obvious study is the search for a clustering in the arrival directions of cosmic rays. Anisotropies are reduced during their propagation in galactic and extragalactic magnetic fields, depending on the mass composition and energy (cf. Eqs. 2.3 and 2.5). This has to be taken into account in anisotropy studies.
A large scale anisotropy at energies from ~ 100 GeV up to a few PeV was reported by several experiments [49–53]. The structure up to 100 TeV is found to be rather constant and is dominated by a dipole moment and a smaller quadrupole moment. Above 100 TeV there is a significant small scale contribution from higher harmonics. The anisotropies found are an important tool to understand the galactic CR propagation [54]. No significant large scale anisotropy was observed for energies from 4 EeV to 8 EeV with the Pierre Auger Observatory [54, 55]. Above 8 EeV, a significant dipole moment was reported in [54] with no excess in higher multipoles.

Upper limits on the dipole and quadrupole moment challenge "an origin from stationary galactic sources densely distributed in the galactic disk and emitting predominantly light particles in all directions" [56].
If the GZK effect is apparent for UHECR, a small scale anisotropy for energies beyond 55 EeV would be expected. The CR flux at these energies is significantly reduced and the source distance is restricted to about 100 Mpc, depending on the mass of the primary (see Sec. 2.6.1). A correlation of the arrival directions of UHECR with nearby AGN (closer than 75 Mpc) from the Véron-Cetty Véron (VCV) catalogue, within an angular window $\psi = 3.1°$, was reported by the Pierre Auger Collaboration in 2008 [57]. The correlating fraction has decreased to $28.1^{+3.8}_{-3.6}\%$ since then (with 21% for the isotropic expectation) [48]. As the magnetic deflection scales with the inverse of the energy (cf. Eq. 2.3), an alignment in groups of arrival directions (multiplets) would be expected for proton primaries. A search for multiplets in Auger data does not show a strong evidence [58]. For a discussion of the source density based on Auger data see [59].
A very interesting source candidate within the GZK horizon is Cen A. With a distance of 3.8 Mpc it is the closest AGN. A scan of events within 15° centered at the direction of Cen A and for energies $E > 58$ EeV (cf. Fig. 2.4) has lead to a probability of 1.4% for isotropy [48]. An excess in the direction of Cen A is seen also in cross-correlation searches against different catalogues. On the other hand, it has been shown that there are "no significant excesses around the Galactic Center, the Galactic Plane, or the Super-Galactic Plane" [48], challenging a galactic origin of UHECR with energies of $40 - 80$ EeV.

2.4 Acceleration, Astrophysical Sources and Exotics

A fundamental question, which is still not solved for highest energies, is *how* and *where* cosmic rays gain their energies. CR with energies up to at least the knee region are most probably of galactic origin. This is supported by measurements of large scale anisotropies. The maximum energy for a proton that can be confined in the Galaxy (with $B \approx 0.3$ μG, $L < 1$ kpc and $\beta = 1$) is $E_{\mathrm{max,Gal}} < 0.3$ EeV, according to Eq. 2.2. Thus, even if galactic accelerators could exceed EeV energies, most of these particles would escape the Galaxy. Given the Larmor radius of the Galaxy, the maximum energy of galactic accelerators, the structures in the CR energy spectrum and the lack of correlation with galactic sources, it is likely that the highest energy CR are of extragalactic origin.
There exist two different approaches that explain the CR energy by either acceleration in astrophysical sources (**bottom-up**) or by decays of extremely massive relic particles (**top-down**). They are outlined in the following.

2.4.1 Acceleration mechanisms (bottom-up)

Cosmic rays are accelerated in regions of high energy carried in macroscopic motion or magnetic fields that is transferred to single particles. There are two different types of acceleration processes. One is the (single) acceleration in an electrostatic field, which can be found for example in pulsars or in the magnetosphere around the supermassive black hole of an AGN. In this case a power law spectrum does not follow naturally. A different process is the stochastic acceleration in moving, magnetized regions. The most prominent mechanism for the latter process is

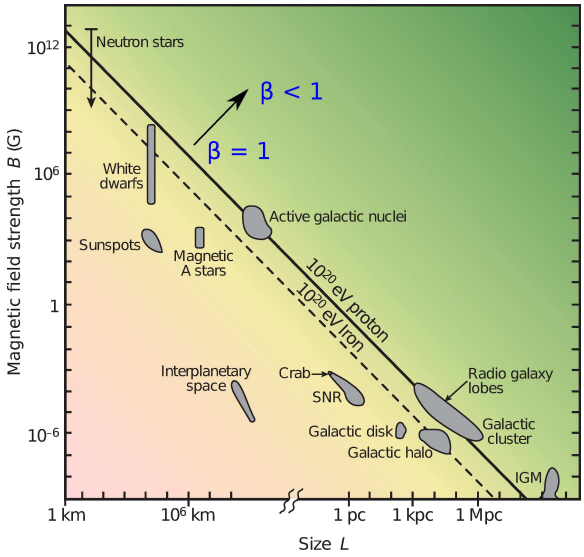

Figure 2.5: Hillas plot (adapted from [60]): The maximum energy of a charged particle that can be confined in a region of size L, with a magnetic field B, is $E_{\max} = 1\ \text{EeV} \times Z \times \beta \times B[\ \mu\text{G}] \times L[\ \text{kpc}]$ (cf. Eq. 2.2). For a certain particle type it depends on the velocity of the particle, $\beta = v/c$. Setting $\beta = 1$, the source properties for confining proton and iron nuclei of 10^{20} eV with are indicated by the diagonal lines. Possible sources must be in the upper right region above the line.

Fermi acceleration. The basic idea is that a test particle[4] gains energy in n successive head-on encounters with moving regions of magnetic fields (e.g in a shock wave), with E_0 the initial energy, $\Delta E = \xi E$ the energy gain per collision and P_{esc} the probability that the particle leaves the acceleration cycle. The number of particles follows a power law in E,

$$N(E) = N_0 \cdot \left(\frac{E}{E_0}\right)^{\frac{\ln(1-P_{\text{esc}})}{\ln(1+\xi)}} \approx N_0 \cdot \left(\frac{E}{E_0}\right)^{-\alpha}$$

with spectral index $\alpha \approx \frac{P_{\text{esc}}}{\xi}$ (for P_{esc} and ξ both small).

Fermi acceleration (second order)

Fermi suggested the following stochastic mechanism in 1949 [61]. Cosmic rays collide with a magnetized cloud that randomly moves with speed $u = \beta c$ under an angle θ_{in} with energy E_{in} and momentum p_{in}. The cloud acts as a magnetic mirror and scatters the particle elastically. The particle leaves the cloud with an angle θ_{out}, energy E_{out} and momentum p_{out}. Here we assume a heavy cloud that moves slowly. The final energy in the laboratory system is

$$E_{\text{out}} \approx \gamma^2 E'_{\text{in}}(1 - \beta\cos\theta_{\text{in}})\ (1 + \beta\cos\theta'_{\text{out}})$$

[4] In the test particle approximation it is assumed that during the acceleration the CR particle does not interact with the plasma of the shock.

with γ the Lorentz factor and assuming $E'_{\rm in} = E'_{\rm out}$ for elastic scattering, $\langle \cos\theta'_{\rm out} \rangle = 0$ for isotropic directions in the cloud system and $\langle \cos\theta_{\rm in} \rangle \propto \beta$. Therefore the average energy gain is

$$\left\langle \frac{\Delta E}{E_{\rm in}} \right\rangle \propto \beta^2.$$

The mechanism is called second order Fermi acceleration.

Fermi acceleration (first order)

A more efficient and faster mechanism was developed later in the 1970's (e.g. see [62]) where CR are accelerated in shocks, for example in supernovae. The shock propagates with velocity u in the laboratory system. In the system of the shock front, the gas in the upstream region is receding with speed $1/4\ u$ and in the downstream region inceding with u. In multiple crossings of the shock region during the successive scattering of CR in magnetized regions in the plasma the particle "sees" the region approaching with speed $3/4\ u$. Therefore the process is faster and more efficient than the second order Fermi acceleration and the average particle direction before and after the scattering does not depend on β. It can be shown [63] that

$$\left\langle \frac{\Delta E}{E_{\rm in}} \right\rangle \propto \beta.$$

The spectral index depends on the compression ratio of the shock. For strong shocks it is $\alpha \approx 2$ [64]. This mechanism and the maximum energy can be extended when accounting for the interactions between the flux of accelerated particles and the magnetic field in the context of magneto-hydrodynamics. Resonant and non-resonant instabilities are shown to be able to amplify the CR acceleration under certain conditions [64]. The first order Fermi acceleration mechanism is also referred to as **diffusive shock acceleration** (DSA).

Astrophysical sources

Shock acceleration can be found in different astrophysical objects. It occurs for example in the region of stellar explosions, in the region of gravitational accretion of matter or in their relativistic jets of black holes where accelerated particles traverse interstellar medium (ISM). High energies can be achieved for a large turbulent magnetic field component. Possible CR sources are visualized in the so-called Hillas plot in Fig. 2.5. The maximum energy of a particle to be confined in a region, such as its source region, can be estimated by the Hillas criterion [65]. It requires the Larmor radius to be smaller than the size of the acceleration region,

$$E < 1\ \text{EeV} \times Z \times \beta \times B[\ \mu\text{G}] \times L[\ \text{kpc}], \tag{2.2}$$

where B and L are the magnetic field and size of the acceleration region and Z and $\beta = v/c$ the charge and velocity of the particle.
The total luminosity of CR in the Galaxy is

$$L_{\rm CR} = \frac{4\pi}{c} \int\int {\rm d}E{\rm d}V\ t_{\rm cr}(E)^{-1} \times E \times j(E) \approx 10^{41}\ {\rm erg\,sec}^{-1},$$

(cf. [66]) with $j(E)$ the CR spectrum and $t_{\rm cr}(E)$ the mean residence time of CR in the Galaxy that can be inferred from the ratio of secondary to primary nuclei. This corresponds to an

energy density of

$$u_{\mathrm{CR}} = \frac{4\pi}{c} \int \mathrm{d}E \; E \times j(E) \approx 1 \text{ eV cm}^{-3}.$$

(cf. [66]). A possible CR source must allow for the acceleration of a certain particle type to maximum energies as observed. The CR flux must be large enough to replenish diffusive galactic propagation losses and to explain a substantial fraction of the observed cosmic rays. A possible class of sources must be able to explain the observed power-law spectrum and the features in different energy ranges.

- **Supernova remnants** (SNR): Already in 1934, supernovae were discussed as CR accelerators by *Baade & Zwicky* [67]. From measurements of the arrival directions of GeV γ-rays, SNR have been identified as possible galactic CR sources (see Sec. 2.7). SNR cover a large range of spatial extensions, age and differ in their interactions with a dense medium [68]. They are a widely discussed possible source for CR up to PeV energies (or even higher). While the energy density for about 3 SN per century is sufficient to produce the CR flux (without accounting for plasma instabilities) the acceleration time needed to reach these energies might be longer than the age of the SNR at which the shock has slowed down too much. The most variable parameter towards the maximum energy is the magnetic field B and its turbulent component, which depends on magneto-hydrodynamical processes in the plasma. It has been shown that resonant and non-resonant instabilities can amplify the CR acceleration under certain conditions [64]. The highest chance to achieve PeV energies is for young SNR before the Sedov phase[5], for very dense media and high masses. SNR are the most intuitive source candidate for galactic CR in and probably above the knee region due to their maximum energy, energy density and source spectral index.

- **Gamma-Ray Bursts** (GRB): The major fraction of GRBs, in particular long-duration[6] GRBs, is found to coincide with supernovae [69]. In the so-called collapsar model [70] it is suggested that rotating, heavy stars form a black hole during the collapse of the iron-core with highly variable jets and relativistic flows. It is said that "while only a small fraction of supernovae make GRBs, [...] collapsars will always make supernovae similar to SN 1998bw" [70]. CR acceleration can occur in multiple shocks of the GRB explosion [34] or in its jets [71]. The GRB rate of about 0.3 Gpc^{-3} yr^{-1} could be enough to produce the CR density needed for the Galatic CR flux [34]. Also the lack of a significant correlation of UHECR arrival directions with stationary point sources could be explained by GRBs.

- **Pulsars**: The rotation of the strong surface magnetic fields of highly rotating neutron star, called pulsar, induces an electric field that creates highly relativistic outflows. The maximum energy increases with the rotation frequency, radius and the magnetic field of the pulsar [34, 72]. Therefore young pulsars are of particular interest. Even with a fraction of some percents of all pulsars matching the conditions for highest energies might be enough to account for UHECR energies [34].

- **Clusters of Galaxies**: Cosmic rays can be accelerated in gravitational accretion shocks of dark matter. The spatial extension of the Local Group is a few Mpc and magnetic fields outside the cluster center can reach a few μG [34] on both sides of the shock. Within the

[5] Sedov phase: Phase in which the SN shell is swept off.
[6] Long-duration: longer than a few seconds.

background magnetic field radiation losses can be significant and restrict the maximum energy. Based on cosmological hydrodynamic simulations it is suggested that protons can be accelerated up to 6×10^{19} eV with a flux at 10 EeV, consistent with the observed CR flux [73].

- **Active Galactic Nucleus** (AGN): Cosmic rays can be accelerated in different regions of an active galaxy. The region closest to the center is the **magnetosphere** around the supermassive black hole where CR can undergo electrostatic acceleration. In principle the magnetic fields could be sufficient to accelerate particles to highes energies, but radiative losses are large in the dense medium of the accretion disk [34]. Some AGN have two **relativistic jets** where CR can be accelerated as well, mostly by diffusive acceleration or shear acceleration (due to a velocity gradient) [71]. The maximum energy is restricted by adiabatic losses and interactions with the jet. If an active galaxy has long jets (> 100 kpc), their termination can be observed as **radio lobes**. At so-called hot spots, occuring in the region where the jet collides with ISM and creates large magnetic fields, CR can be accelerated to highest energies by first order Fermi acceleration [74]. In this case energy losses are lower compared to the acceleration in jets while the maximum energy is compatible [34]. Thus **radio galaxies**, in particular blazars or FR II galaxies, are particularly interesting UHECR source candidates. Two radio galaxies that lie in the detectable volume for the UHE photon search with the Pierre Auger Observatory (within 4.5 Mpc, corresponding to the mean free path of an EeV photon) are Cen A and M87. Within the results of [20], which challenge a light composition, Cen A is of particular interest as it is the closest radio galaxy and might suffer least deflections for some directions. An excess of events in this direction has been reported by the Pierre Auger Collaboration in [48].

2.4.2 Non-acceleration mechanisms (top-down)

As an alternative to astrophysical sources that accelerate cosmic rays up to highest energies, several exotic non-acceleration models were introduced. Their original motivation is to explain the CR energy spectrum reported by the AGASA Collaboration [30, 31] that does not show a suppression at highest energies. In top-down models UHECR are created by decays or annihilation of primordial relic particles (X-particles) relatively close to the Earth with masses $m_X \geq 10^{21}$ eV. In the following paragraphs the models are briefly described. It should be pointed out that all models require an additional low-energy component of cosmic rays in addition to the decay products of the resonances or relic particles to fit the measured CR spectrum [75]. In this work the predictions by *G. Gelmini et al.* [75] (SHDM model also from [76]) are compared with the derived upper limits, for the case of the AGASA spectrum as the models were introduced to explain this spectrum. The predictions of the integral photon flux in [75] for the case of the HiRes spectrum are about 1.5 orders of magnitude lower than for AGASA but still already challenged or ruled out by the upper limits. The current experimental status, including the upper limits derived in this work, is shown in Figs. 4.14(a) and 4.14(b).

Z-Burst

In the Z-Burst model [77] UHE neutrinos annihilate with relic background neutrinos in a Z-resonance,

$$\nu + \nu_{\text{relic}} \rightarrow Z \rightarrow f\bar{f}.$$

This process requires a neutrino energy[7] of $E_\nu = m_Z^2/2m_\nu = 4 \cdot 10^{21}$ eV $\times$ (eV$/m_\nu$), which in turn poses a limit to the maximum energy of the spectrum of decay secondaries. The resonance decays into fermion-antifermion pairs, such as hadrons, neutrinos, quarks or charged leptons, at different branching ratios. In consequent decays photons and neutrinos are produced. The Z-Burst model is restricted by measurements of the GeV gamma-ray [75, 78] and neutrino flux [75].

Topological Defects (TD)

In the TD model (review in [66]), topological defects produce GUT-scale mass particles. The mass of these particles directly restricts the maximum possible energy for the UHECR produced in decays of these particles. Decay channels are quarks and leptons. After hadronization of the quarks, hadrons and leptons decay into photons, leptons and nucleons. The ratio can be of the order of several photons per nucleon, depending on the decay model. In [75], the mass is assumed to be $m_X = 2 \times 10^{22}$ eV.

Super-Heavy Dark Matter (SHDM)

In this model, metastable superheavy particles, produced in the early Universe during inflation, are assumed to compose part of the cold dark matter and in particular of the dark halo of our Galaxy. These long-lived[8] particles have a mass of $\gtrsim 10^{21}$ eV. Possible candidates are e.g. thermal production by gravitinos or magnetic monopoles connected by strings [79], cryptons [76, 80] or Wimpzillas [81]. They can decay [79, 80, 82] or annihilate [81] into UHECR. The resulting spectrum is mainly determined by the QCD fragmentation function.
Signatures of this model are a dominant photon fraction above the ankle region and a small anisotropy in the direction of the galactic halo or clumps of dark matter. Depending on the threshold energy for a dominant SHDM contribution to the cosmic ray flux and the contribution of UHECR above this threshold, this model is restricted or supported by measurements of the arrival directions of gamma-rays by SUGAR [83, 84]. For energies $E > 4 \times 10^{19}$ eV annihilation and decay of SHDM are rejected, for $E > 6 \times 10^{19}$ eV the decay model is supported. The feasibility of a search for SHDM decay signal from the galactic halo with the Pierre Auger Observatory is discussed in [85].

Today top-down models are restricted by upper limits on the UHE photon fraction as well as gamma-ray measurements in the GeV range, within certain model assumptions. In particular the Z-Burst model does not allow for much variation in the parameters due to restrictions by the measured flux of GeV gamma-rays and neutrinos. Still, there is a significant dependence of the level of limitation on the CR spectrum used for normalization. As a complementary information, the increasing mean mass at highest energies observed with the Pierre Auger Observatory (see Sec. 2.2) challenges top-down models.

[7] Assuming that $E_{\nu_{\text{relic}}} \simeq m_\nu$ and $E_\nu \simeq p_\nu$.
[8] Long-lived means here $\tau \geq t_0$, with t_0 the age of the Universe.

2.5 Propagation

In surrounding backgrounds, such as magnetic fields (MF), radiation or matter, cosmic ray nucleons and nuclei undergo different interactions that attenuate the primary flux with respect to the injected energy spectrum. In this section we focus on the diffusive CR propagation and magnetic fields. A summary of other propagation processes with focus on UHE photons can be found in Section 2.6.1.

2.5.1 Galactic

Cosmic rays propagate in the galactic disk and in the galactic halo. In a simple model, the so-called *leaky box model* [86], the Galaxy is approximated as a propagation volume in which injected CR nuclei from a source spectrum $\Phi(E)$ can propagate diffusively. They interact with surrounding cosmic backgrounds (MF, radiation fields and ISM) within an interaction length, $\lambda_{\rm int}$, and leave the volume within a loss length, $\lambda_{\rm esc,Gal}$. Regarding the propagation of CR with energies above $10^{18.5}$ eV, the most relevant backround is the galactic magnetic field (GMF). The angular deflection ψ of a cosmic ray primary with charge Z and energy E after travelling a distance L in a regular magnetic field of strength B is

$$\psi_{\rm reg} \leq 2.7^\circ \times Z \times \frac{60\ {\rm EeV}}{E} \times \int_0^L \frac{{\rm d}X}{1\ {\rm kpc}} \times \frac{B}{3\ \mu{\rm G}} \tag{2.3}$$

$$= 0.9^\circ \times Z \times \frac{60\ {\rm EeV}}{E} \times \int_0^L \frac{{\rm d}X}{1\ {\rm Mpc}} \times \frac{B}{10^{-9}\ {\rm G}}. \tag{2.4}$$

In a turbulent magnetic field with coherence length $L_{\rm c}$ it is

$$\psi \leq 0.1^\circ \times Z \times \frac{60\ {\rm EeV}}{E} \times \frac{B_{\rm rms}}{1\ \mu{\rm G}} \times \sqrt{\frac{L_{\rm c}}{100\ {\rm pc}}} \times \sqrt{\frac{L}{1\ {\rm kpc}}} \tag{2.5}$$

$$= 4^\circ \times Z \times \frac{60\ {\rm EeV}}{E} \times \frac{B_{\rm rms}}{10^{-9}\ {\rm G}} \times \sqrt{\frac{L_{\rm c}}{1\ {\rm Mpc}}} \times \sqrt{\frac{L}{100\ {\rm Mpc}}} \tag{2.6}$$

(cf. [57]). Assuming a large-scale GMF with a regular component of $B \approx 1\ \mu$G, the angular deflection after travelling a distance of 1 kpc is a few degrees for a 60 EeV proton (cf. Eq. 2.3). With a turbulent GMF component of 1 μG and a coherence length of the order of 100 pc [87], the deflection for the same travelling distance is less than a degree (cf. Eq. 2.5) and plays a subdominant role compared to the regular component. For heavier primaries, the deflection scales with the charge Z in both cases. A detailed knowledge of the different magnetic field components is needed to study possible patterns in the CR arrival directions. For a recent study of the GMF see [88].

2.5.2 Extragalactic

Our knowledge about the intergalactic[9] magnetic fields (IGMF) is very restricted. The IGMF is expected to be a few μG in the center of Galaxy clusters [89] and $10^{-16} - 10^{-9}$ G in the filamentary structures [34]. The coherence length is also very uncertain to several orders of

[9] Extragalactic or intergalactic is used synonymously here.

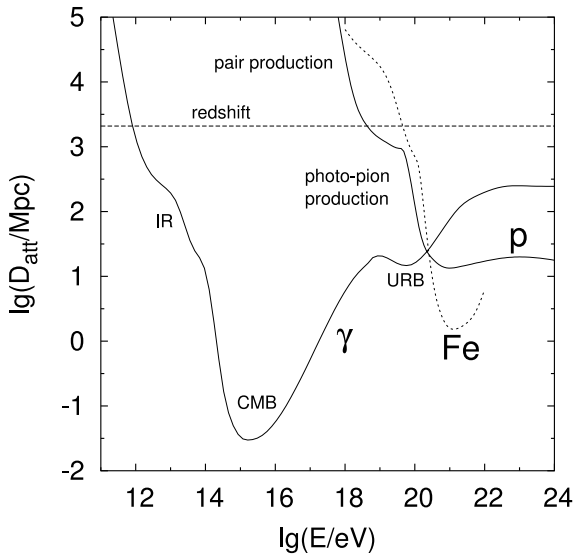

Figure 2.6: Energy loss length for different primaries. Shown are lines for photon, proton and iron. A continous energy loss is given by the expansion of the universe (redshift). With increasing energy, photons interact with different background fields, e.g. the infrared (IR) background, cosmic microwave background (CMB) and the universal radio background (URB). The most probable source of energy loss for proton or iron with energies below some EeV is the redshift. Above, pair production and pion-photoproduction processes of proton with the CMB become dominant. Iron interacts in similar processes and can be treated as a collection of A free nucleons, each with an energy E/A. From [92].

magnitude, in particular in the filaments [90]. Thus the parameter space for a parametrical desciption of IGMF in numerical simulations is large as well and there exist different models [90, 91].
If one assumes a field strength of 10^{-12} G and a coherence length of 1 Mpc [34], the angular deflection for a 60 EeV proton after traveling a distance of 100 Mpc is less than a degree (cf. Eq. 2.5). But this result is clearly subject to large uncertainties.

2.6 Cosmic-Ray Photons

Cosmic Rays interact with background photon fields during their propagation. Here we focus on the creation of UHE photons during the propagation of UHECR in astrophysical scenarios (acceleration), but the same mechanisms hold also for hadrons from top-down scenarios.

2.6.1 Production and propagation of UHE photons

One possible explanation for the observed high-energy cutoff in the CR energy spectrum is the **GZK-process** where UHE nucleons interact with the cosmic microwave background (CMB) in a resonant pion-photoproduction [25, 26], in the simplest case the production of a single pion

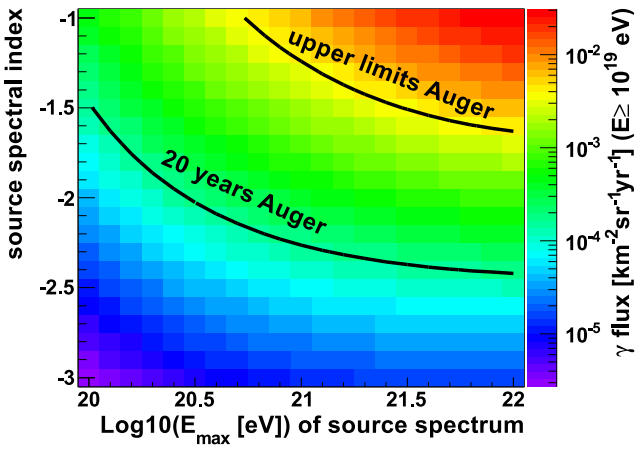

Figure 2.7: Integrated photon fluxes for $E \geq 10^{19}$ eV expected from proton sources in the high-photon scenario (see text), in dependence of the source spectrum parameters (slope α and maximum energy $E_{\max}$). The upper limits shown are from [93]. From [94].

(here for the case of a primary proton):

$$\begin{aligned} p + \gamma_{\mathrm{CMB}} \rightarrow \Delta^+(1232) &\rightarrow p + \pi^0 \\ p + \gamma_{\mathrm{CMB}} \rightarrow \Delta^+(1232) &\rightarrow n + \pi^+. \end{aligned} \tag{2.7}$$

The minimum proton energy needed for the first process is

$$\begin{aligned} E_{\mathrm{p}}^{\mathrm{th}} &= m_\pi \cdot \frac{(m_{\mathrm{p}} + m_\pi/2)}{E_\gamma \cdot (1 + \cos(\alpha))} \\ &\approx 6.9 \cdot 10^{19}\ \mathrm{eV} \times \left(\frac{E_\gamma}{10^{-3}\ \mathrm{eV}} \right)^{-1} \text{(for a head-on collision, } \alpha = 0), \end{aligned} \tag{2.8}$$

with $E_{\mathrm{p}} \simeq p_{\mathrm{p}}$ the proton energy and with m_{p}, m_π the proton and pion mass, E_γ the energy of a CMB photon and α the collision angle. Protons of lower energies mostly interact with the CMB in a production of e^+e^--pairs. Depending on the proton energy, also higher resonances can be created. The pions carry $\sim 20\%$ of the primary energy [95].
During their propagation, UHE nuclei can interact in the same resonant processes as described above, where the nucleus can be treated as a collection of A free nucleons of energy E/A in a simplified superposition model. Nuclei can disintegrate into nucleons [96–98] by the giant dipole resonance (photon energies below $30 - 50$ MeV in the nucleus rest frame), by quasideuteron emission ($50 - 150$ MeV) or baryonic resonances (above 150 MeV) [98]. This way the flux of photons produced by nuclei is lower than for nucleons of the same primary energy. Photo-disintegration happens mainly in the CMB and the infrared background (IRB) and can already happen near the source, depending on the intensity of the IRB. A third interaction channel is nuclear decay. The average energy loss for iron drops rapidly with energy, in particular above 10^{19} EeV (see Fig. 2.6). Note that above 10^{20} eV the energy loss length for iron is smaller than for proton, reaching a minimum of only a few Mpc at 10^{21} eV.

In consequent interactions the pions produced decay into photons and leptons:

$$\begin{aligned} \pi^0 &\rightarrow \gamma + \gamma \\ \pi^0 &\rightarrow \gamma + e^+ + e^- \\ \pi^+ &\rightarrow \mu^+ + \nu_\mu. \end{aligned} \tag{2.9}$$

The muons decay after 2.2μs in their rest system:

$$\mu^+ \rightarrow e^+ + \bar{\nu}_\mu + \nu_e. \tag{2.10}$$

The electromagnetic component initiates a cascade of pair production processes, inverse Compton scattering in cosmological backgrounds and synchroton radiation in IGMF (for reviews see [66, 99]). UHE photons carry about 10% of the proton energy. Depending on their energy, they interact with the different components of the cosmological background (CMB, infrared, optical and radio[10]) by pair production processes. At PeV energies the energy loss length is less than 1 Mpc, which makes it difficult to probe CR sources by searching for PeV photons. For UHE photons, the radio background is the most important background with respect to pair production processes [66]. Within an energy loss length of a few Mpc (see Fig. 2.6), depending on the primary CR, an EeV photon cascades down to energies of hundreds GeV where the Universe becomes transparent. This restricts observations of UHE photons to the local Universe. If they exist, EeV photons are expected to be produced either during interactions of UHECR with background photon fields or in decays of heavy relic particles. As discussed in Sec. 2.4.1, two radio galaxies lie within the detectable volume for EeV photons with the Pierre Auger Observatory: Cen A and M87.

GZK photon predictions

The photon flux and fraction depend mainly on the UHECR spectrum at the source, which is characterized by a slope parameter α and maximum energy[11] E_{max}, the mass composition, the source distribution and the cosmological background (in particular magnetic fields and the radio background). As a demonstrative example, a comparatively large photon flux could be found for low photon backgrounds, a source spectrum with high maximum energy and small slope and small magnetic fields. The possible parameter range is restricted by limits on the photon flux, as shown in Fig. 2.7, and by measurements the UHECR spectrum.
In [100] the prediction of *Gelmini et al.* [75] is used for the case of fitting the spectrum on Earth to HiRes data [22] and with the assumptions for a photon-optimistic[12] scenario (injecting pure proton, **pI**). In 2011 the predictions were updated to the Auger energy spectrum [101] by *B. Sarkar et al.* [94]. The propagation of nuclei in this paper has been done with the CRPropa code [102, 103]. A high-photon (pure proton) and a low-photon scenario (pure iron) are used to define the band for GZK photon predictions for the different primaries (**pII/FeII**). A third set of predictions is suggested by *D. Hooper et al.* [104], indexed as **pIII/FeIII**, which has been fitted to the Auger energy spectrum [23]. The predictions are in the range of the predictions by

[10] The estimation of the radio background is very uncertain and imposes an uncertainty of the energy loss length [66].
[11] Where $E^{\mathrm{p}}_{\mathrm{max}} = E_{\mathrm{max}}/Z$ scaled to the proton case.
[12] The largest photon flux is expected for an injection of pure proton. In the propagated spectrum on Earth protons and photons are taken into account.

B. Sarkar.
A compilation of different predictions on the integral GZK photon flux and fraction can be found in Fig. 4.14(a) and . Details about the scenarios are summarized in Tab. E.3 in the appendix. There is an apparent range in the predicted photon flux from the GZK effect during CR propagation. For primary iron the flux is at least an order of magnitude lower than for primary proton. With increasing spectral index, α, the flux decreases. In general the predictions from different analyses and thus different reference CR spectra etc. are compatible if the source spectrum is the same. The same holds for the photon fraction. Throughout this work we will show the predictions pII and FeII as they have been obtained with the Auger energy spectrum.

2.7 Multimessenger Observations

UHE photons are one of several messengers of primary cosmic rays. During the acceleration and propagation of charged cosmic rays and the subsequent propagation of decay products of secondary pions a large bandwidth of photons, neutrons, neutrinos and $e^{\pm}$ is created. The combination of searches for the full bandwidth of footprints of cosmic rays on their way from the source to the observer is a powerful tool to understand the processes at their sources.

2.7.1 Electrons, positrons

In addition to the acceleration of electrons at astrophysical sources, electrons and positrons are created during CR propagation in interactions of mostly galactic CR with the interstellar matter. High statistics measurements of the e^+/e^- fraction were first published by PAMELA [105] and confirmed by Fermi-LAT [106] and AMS-02 [107]. Measurements of AMS-02 in the range of $0.5 - 350$ GeV are consistent with a secondary origin of the positrons [108]. It does not require an additional primary component from astrophysical sources (e.g. pulsars or dark matter). Within the assumption of a secondary source the CR propagation time is constrained by $t_{\rm esc}(10\ {\rm GeV}) \geq 30{\rm Myr}$ and $t_{\rm esc}(20\ {\rm GeV}) \leq {\rm Myr}$. PAMELA data are well described by only plain diffusion or low reacceleration models, without any need for a charge-asymmetric extra component [108]. An increase of the positron fraction up to 250 GeV is confirmed by all three experiments.

2.7.2 Neutrons

Neutrons are produced by UHE protons in resonances along with the main process of pion productions. The decay length of neutrons is 9.2 kpc $\times E[$ EeV], with E the neutron energy. Within the decay length, the energy flux of EeV neutrons from primary protons should exceed 1 eV/(cm^2 s) [109], as derived from the TeV photon flux of galactic sources. The Pierre Auger Observatory reported an absence of a neutron signal and published upper limits on the neutron flux, which challenges stationary galactic EeV proton sources with low densities and large CR fluxes [109, 110].

2.7.3 Gamma rays

Gamma rays are produced in hadronic processes (production and decay of π^0) and leptonic processes (bremsstrahlung, synchroton radiation, inverse Compton). For energies of up to 100 GeV,

gamma rays are observed with space-based experiments (e.g. EGRET, Fermi LAT). A fraction of the directions of GeV gamma rays coincide with the positions of astrophysical objects, such as SNR [68], pulsars, galaxies and different types of AGN [111, 112]. They help to understand the acceleration processes in the region they are produced. In 2013, the Fermi LAT collaboration reported the detection of a pion decay signature in the spectral energy distributions of two SNR [113], which is very likely from interactions of relativistic protons with dense gas. In the same year they established the first Fermi LAT SNR catalogue [68] based on gamma ray measurements in the range of $1 - 100$ GeV. Within a set of 19 identified and 25 possible SNR, different classes have been probed. A possible correlation between the radio and GeV signal is suggested. At higher energies, gamma rays are detected indirectly at ground with Cherenkov telescopes (MAGIC, VERITAS, H.E.S.S.). The highest energy photons ever detected have energies of some hundreds TeV [99, 111]. The fluxes of gamma rays and TeV-PeV neutrinos are correlated to the ratio of charged to neutral pions [114]. Both can reach the Earth from cosmological distances, enlarging the detectable volume compared to UHE photons.

2.7.4 Neutrinos

UHE neutrinos are direct indicators of hadronic processes. Neutrinos with TeV-PeV energies could be produced in AGN [114]. Cosmogenic[13] neutrinos are expected to carry $\sim 5\%$ of the proton energy, which corresponds to the range above a few EeV [115]. If detected, neutrinos allow for an insight into the region where they were created. For energies above some PeV, neutrinos are observed in large detector volumes, such as the atmosphere, the Earth or a volume of ice or water. The IceCube neutrino detector at the South Pole observes neutrinos indirectly by Cherenkov light from charged leptons created in a charged current (CC) weak interaction. In 2013, IceCube reported an observation of 28 neutrino events between 30 and 1200 TeV at a 4σ significance [116], updated in [117] and confirmed in [118]. They are found to be inconsistent with background expectations from atmospheric neutrinos or muons. So far no point source or clustering in time has been identified [119]. Upper limits on the diffusive $(\nu_\mu + \bar{\nu}_\mu)$-flux at at 90% confidence level (C.L.) are approaching the region of astrophysical flux predictions [120]. Neutrinos of all flavours can as well be observed indirectly by air showers they induce in the atmosphere by CC or NC (neutral current) interactions in different mechanisms [121–124].

2.7.5 UHE photons

The current status of the search for a diffusive flux of UHE photons has already been discussed. Integral upper limits on the photon flux and fraction are approaching the GZK region for primary proton with flat injection spectra. They also restrict the allowed parameter range for astrophysical source scenarios. A search for point sources of EeV photons with Auger hybrid data has been published in [125, 126], with no significant excess. This result challenges stationary galactic EeV proton sources, complementing similar results the neutron search and the lack of large scale anisotropy in the ankle region. An observation of UHE photons might probe the GZK effect of protons or similar processes for heavy nuclei and help to understand the CR production and acceleration of sources in the local universe. UHE photon searches pose further restrictions on Lorentz invariance violation. Photon-induced cascades could probe QCD and

[13] The term *cosmogenic* refers to the neutrino production by the decay of $\pi^\pm$ from the GZK-process.

QED at highest energies by preshowers in the geomagnetic field (see Sec. 3.2.1) and by photonuclear interactions. Finally, an observation of a few photons could reduce the uncertainty of the photonuclear cross-section.

CHAPTER 3

Ground-Based Detection of UHECR

In the 1930s, the existence of extensive air showers of secondary CR particles was unveiled by Bothe, Rossi, Schmeiser, Clay, Kohlhörster and Auger [127–132]. When hitting the Earth's atmosphere, UHE cosmic rays start a cascade of nuclear and electromagnetic interactions that develops to an extensive air shower of millions of secondary particles. Above 100 TeV the low CR flux requires indirect measurements of air showers at ground. These experiments sample the shower front at different locations spread over extensive areas at ground. The Earth's atmosphere is used as part of the detector, compatible to a large calorimeter. Air showers are characterized by their longitudinal development, measured on the base of fluorescence and Cherenkov light produced in the atmosphere, and by lateral particle densities at ground. The interpretation of observational results requires precise knowledge about the atmosphere, nuclear (in particular proton-air) and photo-nuclear cross-sections and the geomagnetic field. Section 3.1 gives an introduction into the physics and characteristics of air showers. Photon-induced air showers are discussed separately in Sec. 3.2. In a further section, basic information about air shower simulations can be found. Section 3.4 introduces the air shower detection at the Pierre Auger Observatory, with focus on the surface detector.

3.1 Extensive Air Showers

A simplified sketch of cascade processes in a proton air shower is shown in Fig. 3.1(a). The first interaction of a primary CR nucleon or nucleus in the Earth's atmosphere happens on average after traversing a depth $\lambda_{A-\mathrm{air}}$, according to the interaction length for inelastic nucleus-air collisions. The leading nucleon propagates close to the shower axis. Productions of neutral and charged pions and kaons drive two main cascade processes: a pionic and an electromagnetic (EM) cascade. The shower consists of four components:

- **Electromagnetic**

  Pure EM from the electromagnetic cascade (bremsstrahlung, pair production)

  EM from μ - contributions from pion cascade

  EM from hadr. jets

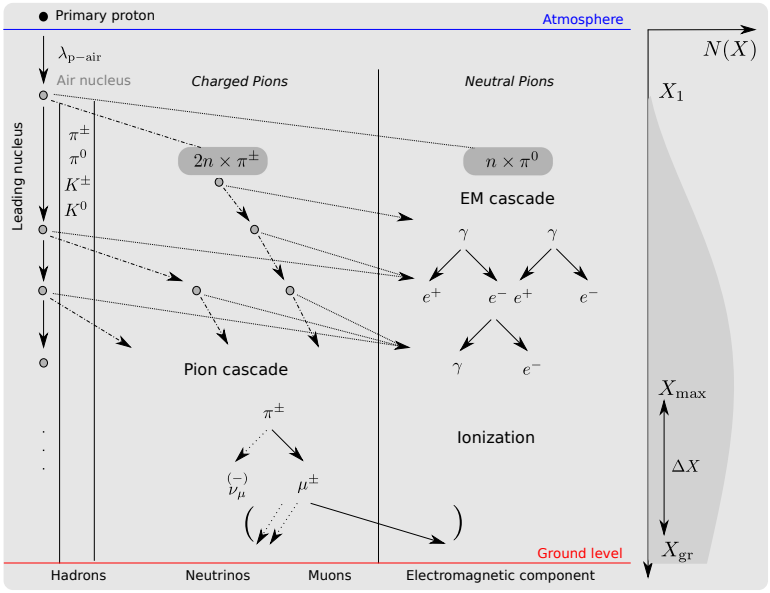

(a) A simplified sketch of cascade processes in extensive air showers and shower compenents at ground level. Characteristic properties of the logitudinal shower development, as shown on the right, are the depth of first interaction (X_1) and of the shower maximum (X_{max}).

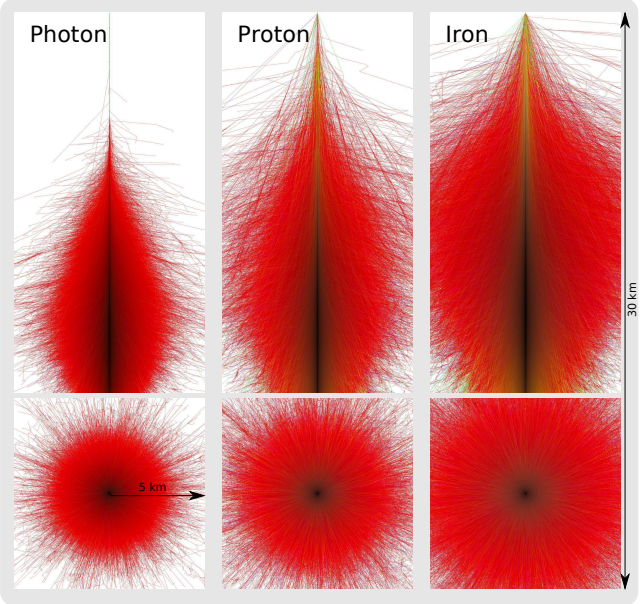

(b) Vertical showers of photon, proton and iron primaries with an energy of 1 PeV. The height of the first interaction is fixed to 30 km. Shown are the longitudinal development (top panels) and lateral distribution at ground (bottom panels). Red lines correspond to electromagnetic particles, green to the muon component and blue indicates hadrons. Modified from [133].

Figure 3.1: Extensive air showers: Longitudinal shower development and underlying cascade processes.

- **Muons**
- **Hadrons** (nucleons, $\pi^{\pm,0}$, $K^{\pm,0}$)
- **Neutrinos**

In case of EM primaries, the first interaction initiates an electromagnetic cascade and, except for a small fraction of photonuclear interactions and consequently a small muon fraction, the main component are EM particles.

3.1.1 Electromagnetic cascade

Neutral pions undergo an electroweak decay almost immediately ($\pi^0 \rightarrow \gamma + \gamma$), feeding the electromagnetic cascade. It is based on two processes, pair production and bremsstrahlung. The number of shower particles is maximal at a depth $X_{\max}$ where ionization processes become dominant. The longitudinal development of the EM cascade can approximately be described by a simple toy model, the *Heitler model* [44]. It is based on the assumption that two particles are created per interaction. The shower maximum of the electromagnetic cascade is at

$$\langle X_{\max} \rangle^{\mathrm{EM}} = X_0 \ln \left(\frac{E}{\varepsilon_{\mathrm{c}}^{\mathrm{EM}}} \right), \tag{3.1}$$

where $X_0 \approx 36.62$ g/cm^2 is the radiation length in air, E the primary energy and $\varepsilon_{\mathrm{c}}^{\mathrm{EM}} \approx 84$ MeV the critical energy. Below the critical energy, ionization processes are dominant.

3.1.2 Hadronic showers

The Heitler model has been generalized for hadronic showers by *Matthews* in [46]. Here we follow the introduction presended in [43]. About 2/3 of the primary energy go in productions of charged pions. In a pionic cascade, which is driven by charged pions, each step transfers 1/3 of the energy to the electromagnetic cascade. In each hadronic interaction N_{ch} charged pions are created. After n_{d} interactions we have

$$N = (N_{\mathrm{ch}})^{n_{\mathrm{d}}} = \left(\frac{E}{\varepsilon_{\mathrm{d}}^{\pi}} \right)^{\beta}$$

charged pions[1]. Therefore the number of secondaries is proportional to the primary energy. At this stage, the energy per $\pi^{\pm}$ is $\varepsilon_{\mathrm{d}}^{\pi} \approx 10$ GeV [46] and the pions decouple from the shower by decays into muons and neutrinos. The energy of the electromagnetic component is

$$E_{\mathrm{cal}} = E \cdot \left(1 - \left(\frac{2}{3} \right)^{n_{\mathrm{d}}} \right)$$

with $n_{\mathrm{d}} \approx 6$ (e.g. [43, 136]). Thus the electromagnetic energy is a good measure of the primary energy.
If N hadrons are produced in the first interaction with elasticity κ_{ela}, the *depth of the shower maximum* for a primary proton is [43]

$$\langle X_{\max} \rangle^{\mathrm{p}} \approx \lambda_{\mathrm{p}} + X_0 \ln \left(\frac{\kappa_{\mathrm{ela}} E}{2 \varepsilon_{\mathrm{c}}^{\mathrm{EM}}} \right),$$

[1] Here we assume that $\beta = \ln N_{\mathrm{ch}} / \ln (3/2 N_{\mathrm{ch}}) \approx 0.85$ for $N_{\mathrm{ch}} = 11$, for an energy-independent multiplicity [134, 135]

where the factor 1/2 accounts for decay in two photons and λ_p is the interaction length of the proton. The *elongation rate* D quantifies the change of the average shower maximum per logartithm in energy, $D = \mathrm{d}\langle X_\mathrm{max}\rangle / \mathrm{dln}\, E$. In a semi-superposition model, with energy E/A per nucleon, we find for nuclei with mass A that

$$\langle X_\mathrm{max}\rangle^\mathrm{A} \approx c + D_\mathrm{p} \ln(E/A) = \langle X_\mathrm{max}\rangle^\mathrm{p} - D_\mathrm{p} \cdot \ln A, \tag{3.2}$$

where the elongation rate of primary proton, $D_\mathrm{p} = \mathrm{d}\langle X_\mathrm{max}\rangle^\mathrm{p} / \mathrm{d}\ln E$, is approximately constant in the logarithmic energy. This holds for a modest energy dependence of the inelastic cross-section [137] and the multiplicity following a power law in E. D_p and c depend on the properties of the first interaction and on the multiplicity. For mixed compositions of nuclei of mass A_i at fixed energy E, with fractions f_i, the mean logarithmic mass is

$$\langle \ln A\rangle = \frac{\langle X_\mathrm{max}\rangle^\mathrm{p} - \langle X_\mathrm{max}\rangle}{D_\mathrm{p}}, \tag{3.3}$$

where $\langle X_\mathrm{max}\rangle = \sum_i f_i \langle X_\mathrm{max}\rangle_i$ and $\langle \ln A\rangle = \sum_i f_i \ln A_i$. There is an apparent linear relation between $\langle X_\mathrm{max}\rangle$ and $\langle \ln A\rangle$. The study of the shower maximum can be carried out to the fluctuations $\sigma(X_\mathrm{max})$ (see e.g. [43]), but here we refrain from further introduction. Experimental results of analyses of the shower maximum are shown in Figs. 2.3(a) to 2.3(c).
Actually, for composition studies, X_1 would be the intuitive shower property to look at, but with ground detectors it is not directly observable. If we had a monochromatic proton beam initiating an air shower, the depth of the first interaction X_1 would be distributed exponentially. X_max follows the X_1 distribution folded with the energy spectrum, mass composition as physical contributions and with the detector resolution. One popular function to parametrize the number of particles as function of slant depth X, the *longitudinal profile*, is the Gaisser-Hillas function [138]:

$$\begin{aligned} N(X) &= N_\mathrm{max} \left(\frac{X - X_0}{X_\mathrm{max} - X_0}\right)^{(X_\mathrm{max}-X_0)/\Lambda} \exp\left(\frac{X_\mathrm{max} - X}{\Lambda}\right) \\ &= N_\mathrm{max} (1+\varepsilon)^\xi \exp(-\varepsilon\,\xi), \end{aligned} \tag{3.4}$$

with $\varepsilon = (X - X_\mathrm{max})/(X_\mathrm{max} - X_0)$ and $\xi = (X_\mathrm{max} - X_0)/\Lambda$. N_max is the maximum shower size and Λ and X_0 are shape parameters (X_0 lies in the region of the depth of the first interaction but has mostly negative values).

3.1.3 Lateral distribution of charged particles

Electromagnetic component

The shower components propagate to the ground in a curved shower front, mainly EM particles and fewer muons. Their spatial distribution and the arrival times at ground are different because of different interaction processes in the longitudinal shower development. The shower development reaches its full development at the shower maximum (labeled as 'max'). The number of muons in a proton shower, $N^\mathrm{p}_{\mu,\mathrm{max}}$, follows the number of charged pions (cf. Eq. 3.2). Around and after the shower maximum the total energy is distributed between electrons and muons,

$$E = N_{e,\mathrm{max}}\, \varepsilon_\mathrm{c}^\mathrm{EM} + N_{\mu,\mathrm{max}}\, \varepsilon_c^\pi \approx N_{e,\mathrm{max}}\, \varepsilon_\mathrm{c}^\mathrm{EM}. \tag{3.5}$$

For UHE showers and for $\varepsilon_c^{\mathrm{EM}} = 84$ MeV and $\varepsilon_c^{\pi} = 10$ GeV, the number of electrons can be approximated by the electromagnetic cascade only, independent of the primary nucleus. $N_{e,\max}$ depends mainly on the primary energy and thus allows for an energy measurement.
Surface detector arrays have to be located deeper than the shower maximum, at the observation level $X_{\mathrm{gr}} = x_{\mathrm{gr}}/\cos(\theta)$ (where x_{gr} is the vertical depth of the ground level). As $X_{\max}$ depends on the primary mass, the detector site is chosen according to the lightest primaries and the energies of interest to assure that the showers have reached their maximum before the observation level. For combined detector systems this choice is a compromise of all systems. The development stage of a shower at depth X is quantified by the shower age[2],

$$s(X; X_{\max}) = \frac{3}{1 + 2X_{\max}/X} \in [0, 3]\,, \tag{3.6}$$

where $s = 1$ corresponds to the position of the shower maximum. A related quantity is

$$\Delta X = X - X_{\max} = t \cdot X_0. \tag{3.7}$$

The shower age s, the stage t and the depth ΔX after the shower maximum are closely related. The latter we need for the concept of the reconstruction of the photon energy based on shower universality.
It has been found that the (pure) EM component develops **universally** in the atmosphere [142–148]. For an observation level below the shower maximum, the best universality is obtained in $t = \Delta X/X_0$ (in [147, 149]). The lateral distribution of $e^{\pm}$ for different electron energies ε is universal in t. At large distances from the shower axis, the lateral $e^{\pm}$ distribution differs for hadronic primaries and primary photons. This comes mainly from the decay of charged pions [147].
The **lateral distribution function** (LDF) of electromagnetic particles as function of the shower age (for $0.5 < s < 1.5$) has been derived by *Nishimura & Kamata* in 1958 [150] and was adapted by *Greisen* [151] to what we call an **NKG-type function**:

$$\rho_{\mathrm{NKG}}(r, s, N_e) = \frac{N_e}{r_{\mathrm{M}}^2} \times \frac{\Gamma(4.5 - s)}{2\pi\,\Gamma(s)\,\Gamma(4.5 - 2s)} \times \left(\frac{r}{r_{\mathrm{M}}}\right)^{s-2} \left(1 + \frac{r}{r_{\mathrm{M}}}\right)^{-(4.5-s)}, \tag{3.8}$$

with r_{M} the Moliére radius and r the perpendicular distance to the shower axis. The electron number arriving at the detector with depth X_{gr} can be obtained from the maximum component, $N_{e,\max}$, at the shower maximum that is attenuated when propagating a depth $\Delta X_{\mathrm{gr}} = X_{\mathrm{gr}} - X_{\max}$ thereafter (cf. Eq. 3.4).

Combined

The single shower components (muon and EM) develop universally in the shower age [146, 152]. The LDF of all EM particles and muons at ground is primary-dependent. For showers of heavier primaries, $X_{\max}$ and N_μ increase. As muons can propagate further away from the shower axis, the LDF is flatter for heavy than for light primaries of the same energy. The main contribution at distances close to the shower core comes from the pure EM cascade processes and the energy is almost contained in the EM component. For a fixed primary type, the shower size and the distance-dependence of the LDF vary with $X_{\max}$ and thus with energy. The shape of the LDF

[2] The concept of the shower age was already developed in 1937 [139–141] studying the cascade equations.

apparently contains information about the mass composition and energy. There exists a huge variety of functions to describe the combined LDF of all components. One possible choice, which is used here, is again an NKG-type function (cf. Eq. 3.18).

Muon component

According to the superposition model, the muon number for nuclei of mass A is:

$$N^A_{\mu,\max} = N^{\mathrm{p}}_{\mu,\max}\, A^{1-\beta} \tag{3.9}$$

(cf. [43]). The muon number can be used as a mass-sensitive parameter.

3.2 Photon-Induced Air Showers

Photon-induced air showers are formed by an almost purely electromagnetic cascade, as described in Sec. 3.1.1. They can be detected with the same detectors as hadronic showers, but they have some specific features which will be discussed in the following paragraphs.

3.2.1 Preshower effect

Photons with energies above $10^{19.5}$ eV can convert into an $e^{\pm}$ pair in the geomagnetic field [153]. The energy is usually split symmetrically. The pair looses energy by synchroton radiation, which can create another $e^{\pm}$ pair in case of sufficient energies. Instead of a single photon, several lower energetic electromagnetic particles, called *preshower*, arrive at Earth, each of which carrying a fraction of the initial photon energy. Most of the primary photon energy is carried by preshower photons. In the Earth's atmosphere they will initiate an electromagnetic air shower. The rate of pair production is expressed by a dimensionless parameter [154]

$$\chi = \frac{E_\gamma}{m_e c^2}\frac{B_\perp}{B_{\mathrm{cr}}}, \tag{3.10}$$

where E_γ is the photon energy, $B_\perp$ the component of the magnetic field perpendicular to the direction of the propagation and $B_{\mathrm{cr}} = m_e^2 c^2/(e\hbar) \approx 4 \times 10^9$ T the natural quantum mechanical measure of the magnetic field. This way the probability for a photon to create a preshower depends on the actual trajectory and thus on the arrival direction on Earth. The attenuation length is given by [155]

$$L = \frac{2\lambda_{\mathrm{C}}}{\alpha}\frac{B_\perp}{B_{\mathrm{cr}} T(\chi)}, \tag{3.11}$$

with λ_{C} the Compton wavelength of the electron and α the fine structure constant. Assuming the weakest geomagnetic field intensity in 2010, which is 0.23 G (cf. [156]), we expect a clear attenuation above 10^{19} eV [155]. This effect has been implemented in the PRESHOWER code [157] that can be used along with CORSIKA [158] and CONEX [159] or as standalone. The preshower effect reduces the difference in the shower maximum of photon- and hadron-induced showers for energies above $10^{19.5}$ eV and thus changes the elongation rate.

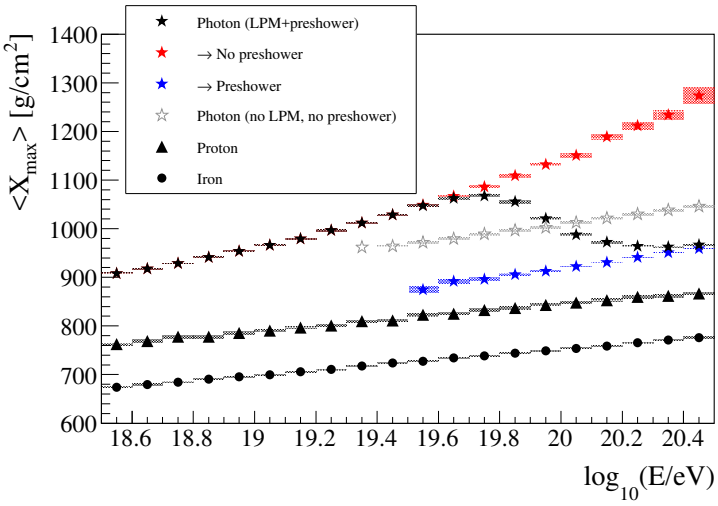

Figure 3.2: The elongation rate for proton, iron and photon showers (with $x_{\mathrm{gr}}/\cos(\theta) - X_{\max} > -50$ g/cm^2 for $x_{\mathrm{gr}} = 880$ g/cm^2 the observation level of Auger), simulated with CONEX (dataset is described in App. B) with $\theta < 60°$. Preshowered photons are shown with blue, non-preshowered photons with red and the full sample with black stars. A simulation without LPM effect and without preshowering, for energies above $10^{19.4}$ eV, is indicated as hollow stars. A data point at $10^{19.4}$ eV ($\langle X_{\max}\rangle = 899 \pm 45$ g/cm^2) with only two events.

3.2.2 Landau-Pomeranchuk-Migdal effect

In the bremsstrahlung process of high-energy electrons only a small longitudinal momentum is transferred to the nucleus. According to the uncertainty principle, this corresponds to a certain distance over which this transfer takes place. If the trajectory of an electron is changed within this interaction distance through multiple scattering, bremsstrahlung is suppressed. In a similar way also pair production is suppressed for photons. The so-called LPM effect [160, 161] reduces the Bethe-Heitler cross-sections for pair production and bremsstrahlung [162]. The energy threshold for the case of bremsstrahlung depends on the medium [163]:

$$E_{\mathrm{LPM}} = \frac{m^2 c^3 \alpha}{4\pi\hbar} \times X_0 \propto 7.7 \text{ TeV/ cm} \times X_0, \tag{3.12}$$

with $X_0 \approx 37$ g/cm^2 the radiation length in air. At a height of 300 m and 5 EeV at 20 km the energy threshold is approximately 10^{17} eV (cf. [164]). The LPM effect delays the longitudinal development of the electromagnetic cascade. This effect increases on average the difference in the shower maximum of photon- and hadron-induced showers, but also the spread of the shower maximum for photon showers.

3.2.3 Shower properties

The basic difference between photon-induced and hadronic showers lies in $X_{\max}$ and N_μ. A photon shower develops on average deeper in the atmosphere and reaches its shower maximum later than a hadronic shower of the same energy. The elongation rate has been compiled in a study based on CONEX simulations of different primary particles (for the dataset see App. B)

is shown in Fig. 3.2. The competing effects of the LPM and preshower effect are clearly visible. While the shower maximum of a 20 EeV proton shower is well above ground, even for a vertical geometry, the maximum of a photon shower of the same energy can be below ground (in particular for higher energies). The average observation level of the Pierre Auger Observatory is at $X_{\mathrm{gr}} = 880\ \mathrm{g/cm^2}/\cos(\theta)$. This poses a geometrical restriction on the search of UHE photons when requiring a shower maximum above ground (discussed in Sec. 5.2). The electromagnetic cascade develops almost universally in the shower age. Due to the very small muon component from photonuclear interactions, the lateral distribution is more compact than for hadronic showers. Geometry and muon content are also reflected in the arrival time distribution of the shower particles, resulting in a smaller mean value for hadronic showers.

3.3 Air Shower Simulations

For the interpretation of experimental results of air shower experiments, such as composition studies, air shower simulations of different primaries are inevitable. Simulations are based on our current knowledge of electromagnetic, hadronic and photonuclear cross-sections, and in particular their extrapolations to highest energies. Shower particles and their interactions are tracked throughout their development in the atmosphere. In this section we review the different interactions and the Monte-Carlo simulation of air showers in CORSIKA.

3.3.1 Electromagnetic interactions

Electromagnetic interactions are comparatively well-understood. A popular model is the EGS4 model [165].

3.3.2 Hadronic interactions

The nominal center-of-mass energy at the Large-Hadron-Collider (LHC) is $\sqrt{s} = 14$ TeV, while for 10 EeV air showers $\sqrt{s} \approx 57$ TeV. Thus hadronic interactions cannot be studied in the full energy range needed for the simulation of air showers. An extrapolation of the inelastic proton-proton cross-section $\sigma_{\mathrm{p-p}}$ measurements to highest energies and to the proton-air cross-section $\sigma_{\mathrm{p-air}}$ is made, which is the largest source of uncertainties for mass composition studies. Different hadronic interaction models for air shower physics are: SIBYLL [166, 167], QGSJETII.03 [168–170], QGSJETII.04 [171], EPOS1.99 [172, 173], EPOS-LHC. The muon signal in the QGSJET model is underestimated by about 40% for 10 EeV proton showers [174, 175]. The EPOS1.99 model has been tuned to LHC data at 7 TeV. For detailed comparisons to hadronic interaction models from collider physics, discussion of the uncertainties within air shower models and to a measurement of $\sigma_{\mathrm{p-p}}$ from the Pierre Auger Observatory, the reader is referred to [137, 176, 177]. The measurement of $\sigma_{\mathrm{p-p}}$ provides a powerful lever arm to check the extrapolations of the models. The current large variation between the models for air shower simulations due to uncertainties in the extrapolations pose a severe restriction on composition studies and on background studies for the UHE photon search.

3.3.3 Photonuclear interactions

The cross-section for photonuclear interactions is expected to be 10 mb at 10 EeV [92], compared to a Bethe-Heitler cross-section for pair-production of 0.5 b [178]. The photonuclear cross-section

is reduced by a factor of 50, which for photon air shower simulations reduces the dependence of the longitudinal shower development on the hadronic interaction model. Still, the muon component and $X_{\max}$ of the shower cascade depend on the extrapolation of the photonuclear cross-section to highest energies (e.g. the *PDG 2004* extrapolation [179, 180] as a reference value and *Donnachie & Landshoff 2001* [181] as the extreme case). For further discussion see [178]). For the photon search this means that an uncertainty in the extrapolations translates to an uncertainty in the photon-hadron separation. Thus it is important to know the extreme cases, in particular the maximum possible cross-section, as this would reduce the discrimination. An increase of the PDG extrapolation by more than 80% is disfavoured [92, 178]. As a last step, the photonuclear cross-section has to be converted into a photon-air cross-section which involves nuclear interactions (Glauber theory [182]). Assuming a slightly modified cross-section with respect to the PDG extrapolation, the uncertainties have been estimated to be as moderate as 10 g/cm^2 in $X_{\max}$ and 15% in N_μ [178]. The uncertainties in $X_{\max}$ for converted photons are expected to be smaller than for unconverted photons, whereas the effect of preshowering on N_μ is comparatively small.

3.3.4 Corsika

A popular software package for Monte-Carlo simulation of air showers is CORSIKA [158]. It allows for an easy selection of the primary particle type and properties, interaction models, atmospheric model, the location and height of the observation level etc. CORSIKA returns the particle types, numbers and energies at certain atmospheric depths and calculates basic observables, such as the shower maximum. It should be mentioned that this extrapolation only works if the shower maximum is above observation level because the simulation stops there. In order to reduce computation time, showers can be *thinned* [183, 184]. The thinning level ε_{th} defines the energy of all secondary particles, $\sum_j E_{\text{j}} = \varepsilon_{\text{th}} E_0$, below which particles are represented by one particle carrying an according weight w. Thus shower fluctuations are increased with $\varepsilon_{\text{th}} > 0$. It has been found that $\varepsilon_{\text{th}} = 10^{-6}$ is sufficient for hadronic showers to avoid a bias of basic Auger surface detector observables [185].

3.4 The Pierre Auger Observatory

The Pierre Auger Observatory [189] is located in the Argentinean Pampa Amarilla with an average altitude of 1400 m above sea level. It covers an area of about 3000 km^2 to sample the footprint of highly energetic air showers at ground. A map of the detector is shown in Fig. 3.3(a). The Surface Detector (SD) array consists of 1660 water Cherenkov detectors that are arranged on a triangular grid with a spacing of 1.5 km [190]. The atmosphere above the detector field is overlooked by fluorescence telescopes from five sites at the borders of the observatory. The fluorescence detector (FD) measures the longitudinal shower development by fluorescence and Cherenkov light produced in the atmosphere. Here we will not introduce this detector further but refer the reader to [191]. FD measurements are restricted to clear moonless nights, resulting in duty cycle of 13% for the FD [191] compared to approx. 100% for the SD [187]. A subclass of events which is detected by the SD and FD is called Hybrid, or Golden-Hybrid in case of an additional independent SD reconstruction. Golden-Hybrid events can be used for a simulation-independent energy calibration of the SD based on the calorimetric energy measured by the FD. The current uncertainty on the SD energy scale is 18% at 3 EeV [192]. Several additional

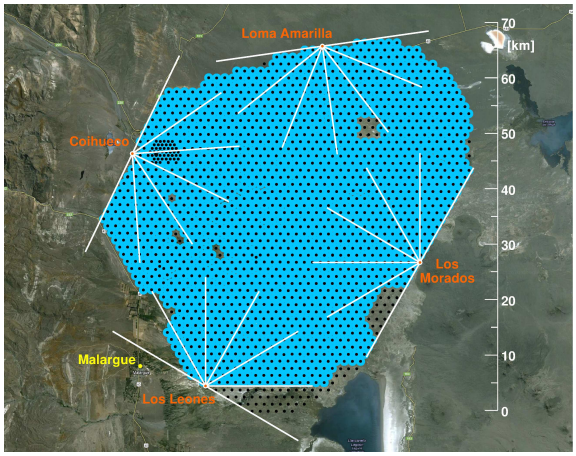

(a) Map of the Pierre Auger Observatory. Each dot corresponds to one surface detector station. The field-of-view of the fluorescence telescopes is indicated as lines. Modified from [186].

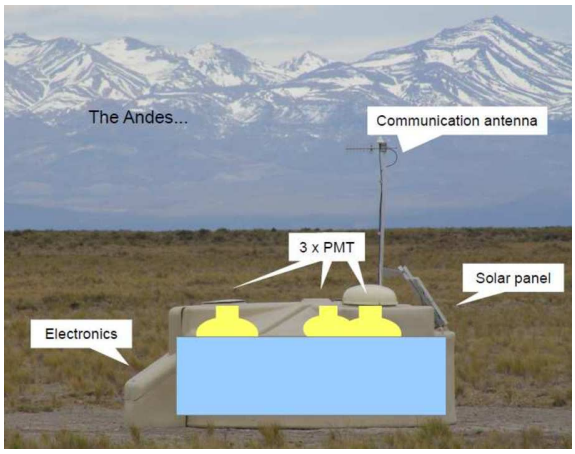

(b) Sketch of a surface detector station. Three PMTs are mounted at the top of the water tank. The high-voltage is supplied by a solar panel and battery. Each detector station has a communication and GPS antenna.

Figure 3.3: The Pierre Auger Observatory

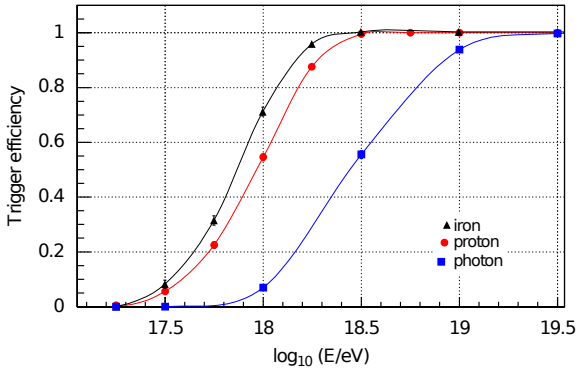

(a) Trigger efficiency for air showers as a function of the simulated (true) energy, integrated for showers with $\theta < 60°$. Shown are proton, iron and photon primaries. From [187].

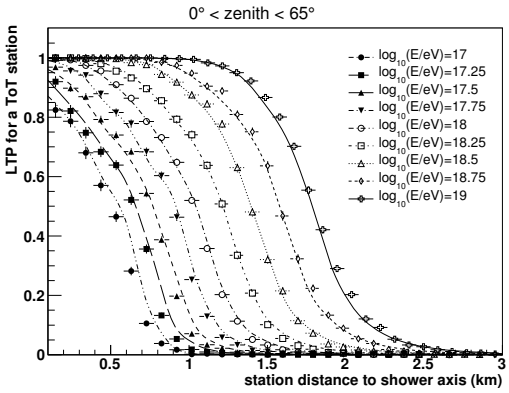

(b) Lateral trigger probability (LTP) for a ToT station as a function of the station distance, shown for proton-induced showers of different energies. A parametrized function is superimposed as a line. The plot contains zenith angles $0° - 65°$. From [188].

Figure 3.4: SD trigger probability for different primary energies.

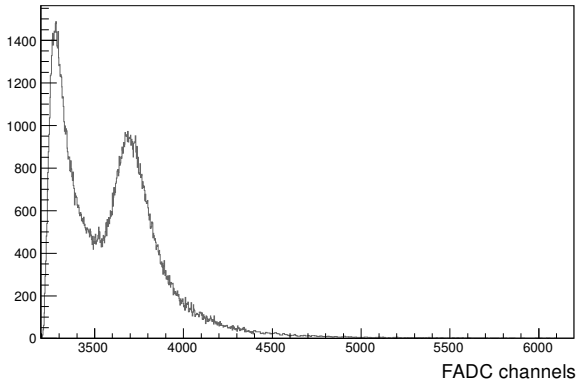

Figure 3.5: Charge histogram (Event 200800501005, station 111, sum of all PMTs)

detectors systems or sub-arrays, such as radio antennae, muon detectors or additional SD tanks with smaller spacing, have been added to the Observatory, making it a super-Hybrid detector. The first surface detector was deployed in 2002, stable data have been taken since January 2004 and the construction of the whole detector array was finished in June 2008 [193]. Thus there are currently more than 10 years of SD data for analysis.

3.4.1 The surface detector

A description of the surface detector can be found in [190]. The SD array is built of 1660 water Cherenkov detectors. Each self-contained detector station (see Fig. 3.3(b)) is a round, opaque tank of 1.2 m height and 3.6 m diameter, filled with purified water. The relativistic electrons and photons arrive with a mean energy of around 10 MeV and muons of around 1 GeV. High energy charged particles produce a short[3] Cherenkov light pulse in the water. The surface detectors are sensitive to both, signals from muons and EM particles. The walls of the tanks are covered with a Tyvek® liner to diffuse the Cherenkov light for a stable signal measurement. Three 9" PMTs are directed downwards into the water and their signals are digitized by 10-bit flash analog-to-digital converters (FADCs) each 25 ns. Each PMT is read out from a *low-gain* (anode) and *high-gain* (dynode, amplified by a factor 32) to increase the dynamic range, which translates to a radial range of the measurement from some hundred meters up to ~ 3 km [194]. Data are transferred wireless to a central data acquisition system (CDAS) using a proprietary protocol. Each tank is equipped with a solar panel and battery to allow for an autonomous operation. Timing and positions are available from a GPS antenna. A shower front hits several tanks, depending on the shower geometry and energy, and produces a lateral distribution of measured signals between several tanks. The time structure of the signals contains physical information about the shower. The SD can be understood as a calorimeter with only one layer.

Signal calibration

The ADC counts are converted to units of the signal that would be deposited in a tank by *vertical equivalent muons* (VEM). The distribution of incident angles of background muons is dominated by vertical muons, leaving a peak ($Q_{\mathrm{VEM}}^{\mathrm{peak}}$) in the distribution of the integrated ADC

[3]The light pulses, including multiple reflections, have a duration of about 100 ns.

charge and a peak ($I^{\text{peak}}_{\text{VEM}}$) in the histogram of the photocurrent [195]. Actually, the shape of the charge histogram is folded with a distribution of muons from different paths in the tank, affecting the peak value.
A local VEM calibration has been set up [195]: The **end-to-end gains** and high voltage of each single PMT are adjusted to match the charge peak of a reference tank. An automatic **online calibration** of the VEM value is performed continuously using background muons. The convergence algoritm starts with a first estimate of $I^{\text{peak}}_{\text{VEM}} = 50$ch (ADC channels). Within a target rate of 100 Hz for 3-fold coincidences above $1.75\, I^{\text{peak}}_{\text{VEM}}$ (first level trigger, **T1**), the rate above a trigger level of $2.5 I^{\text{peak}}_{\text{VEM}}$ is recorded. In a convergence algorithm the value of $I^{\text{peak}}_{\text{VEM}}$ is then tuned to obtain a rate 70 Hz above $2.5 I^{\text{peak}}_{\text{VEM}}$. In addition to $I^{\text{peak}}_{\text{VEM}}$, the charge value $Q^{\text{peak}}_{\text{VEM}}$ is also estimated based on the charge distribution of pulses within 10% of the peak photocurrent $I^{\text{peak}}_{\text{VEM}}$. The charge histogram for single PMTs, their sum and the pulse shape are saved for an **offline calibration** of the signal based on the peak[4] of the charge histograms (see Fig. 3.5). The VEM calibration has an accuracy of $\sim 6\%$ [194]. The physical conditions of each station and the PMT quality are monitored continuously in intervals of several minutes: Temperature, pressure, voltages, currents, battery status, water level, dynode-to-anode ratio (D/A), the VEM peak, etc. [196]. This assures a stable signal measurement and allows to control the detector operation. The VEM signal is defined as

$$S = (N_{\text{ADC}} - B)/c \tag{3.13}$$

with N_{ADC} the number of ADC counts, B the baseline of the channel and c the conversion factor from ADC counts to VEM charge.

Trigger and aperture

Out of the datastream of first level triggers, which is recorded for calibration, physical showers are selected in a sequence of trigger levels. Possibly interesting stations that could be part of an air shower must have either a peak value of at least 3.2 VEM (**T2**) or multiple[5] bins above a threshold of 0.2 VEM (**ToT**). An air shower requires also clusters of coincident signals in different stations (**T3**). The **T4** trigger selects an event as a shower candidate based on certain patterns of T3 stations. Finally, the **T5** trigger checks for 6 active stations surrounding the station with the highest signal to assure a good detection and reconstruction accuracy [197]. The trigger efficiency of an air shower event is almost 100% for air showers with zenith angle below 60° and energies above 3 EeV for the most conservative case of primary proton (cf. Fig. 3.4(a)). Due to the more compact electromagnetic showers, photons reach full efficiency at about 10 EeV. The probability to trigger a single station reaches 100% above 10 VEM. For details on the trigger probability see [187]. The lateral dependence for a fixed primary changes with energy and inclination angle.
The exposure A of the surface detector for a period Δt can be calculated geometrically from the number of elementary cells (see Fig. 3.6(a)) with a 6T5 trigger and for events with full trigger efficiency ($E > 3$ EeV and $\theta < 60°$). Each elementary cell contributes $a_{\text{cell}} \approx 4.59$ km^2 sr to the exposure [187]:

$$A = N_{\text{cells}} \cdot a_{\text{cell}} \cdot \Delta t. \tag{3.14}$$

[4] Actually the second peak, as the first peak is created by trigger effects (see [195]).
[5] At least 13 bins within 3 μs.

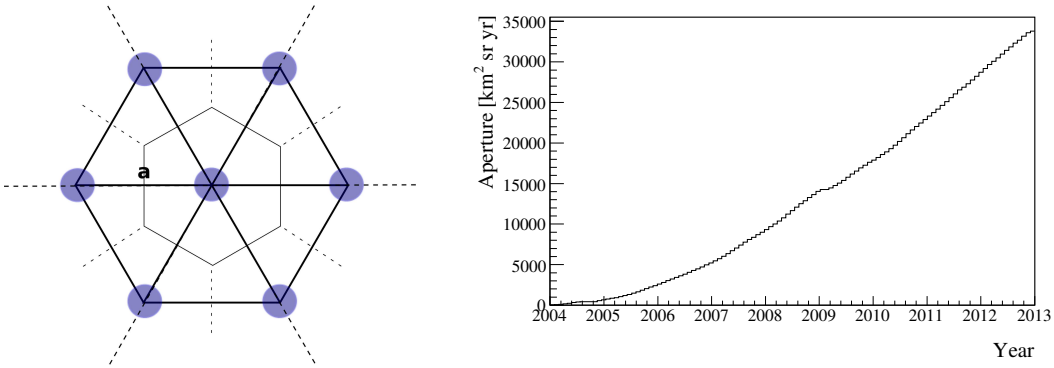

(a) A single elementary cell within a hexagon of 7 tanks in the surface detector array. The distance between two detector stations is $a = 1.5$ km. The detector aperture is calculated based on the number of operating elementary cells in a time interval.

(b) Development of the 6T5 aperture as a function of the time (for $\theta = 0° - 60°$).

Figure 3.6: Aperture of the surface detector.

The exposure for a smaller zenith angle range can be obtained by a geometrical correction factor:

$$A_{\mathrm{corr}} = A \frac{\cos(2\,\theta_{\mathrm{min}}) - \cos(2\,\theta_{\mathrm{max}})}{1 - \cos(2\,\theta_{\mathrm{max}})}, \tag{3.15}$$

which corresponds to a factor 2/3 for a zenith angle range of 30°-60°. As the calculation of the aperture is based on the number of active hexagons in the array, which is calculated from the T2 files [198], it has to be assured that the observed data and the T2 files are synchronized. It was found that $\sim 3\%$ of the 6T5 triggers in data are not contained in the T2 files [199, 200]. These fake events are rejected in this analysis. The accuracy of the aperture is found to be better than 1%.

3.4.2 Data reconstruction

The reconstruction of physical quantities, such as the shower geometry or energy from data (or simulations) of different detectors, is done with $\overline{\mathrm{Off}}\underline{\mathrm{line}}$ [201], a software framework that is developed by the collaboration. The functionalities are organized in modules and can be customized easily on the base of XML cards. For a detailed description of the SD reconstruction the reader is referred to [202]. An example SD reconstruction chain can be found in App. D. In the following, a few modules relevant for this analysis are described briefly. The version used for this thesis is revision 23943, which is the reference version for physics results prepared at the ICRC conference 2013 [192].

Module: SdPMTQualityChecker

A flawless performance of the PMTs is necessary in particular for searches of very rare particles. Hardware failures are not simulated and can produce artificial photon-like signals in parameters based on the VEM trace. The PMT quality is monitored continuously. A documentation of the

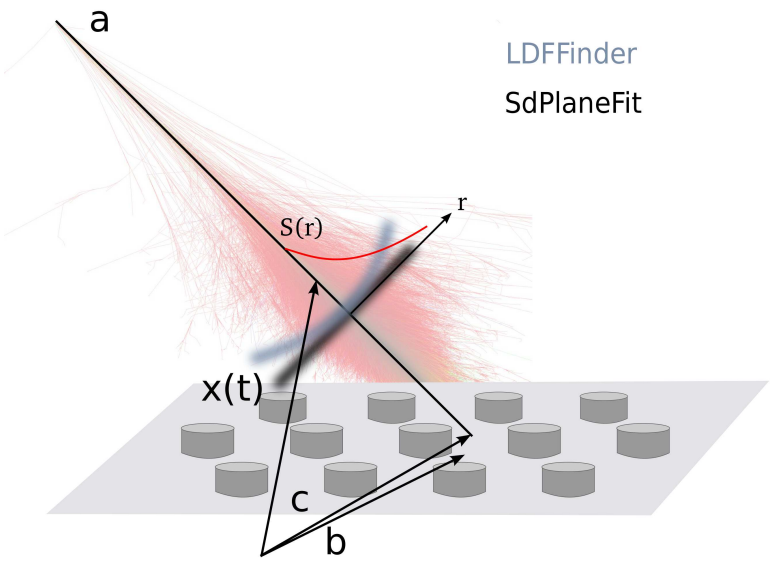

Figure 3.7: Reconstruction of the shower geometry with the surface detector: The geometry is described by the shower core **c** (first estimated by the barycenter **b**), the shower axis **a** and the curvature of the shower front. (Shower image in the background from [133].)

information available in the CDAS can be found in [196]. The monitoring information is used to reject single defective PMTs that show anomalies or instabilities in the VEM peak value, the dynode or anode baseline or in the mean or the RMS of the dynode-to-anode ratio. In addition, this module assures a correct treatment for events of a period with communication problems [196, 203], referred to as *Comm's crisis*. It assures that only PMTs of stations are used which have been alive at the time of the event (and the following 120 seconds). Occasionally it happens that a station is not alive according to the T2Life information while still recording data. As the exposure is calculated on the base of the T2Life information, the additional data taken must be rejected for T5 events.

Module: SdCalibrator

The calibration of the SD signal has been described earlier in this section. The main task of this module is the conversion of the FADC trace of the PMTs to a signal trace. This is done in three steps. The baseline is computed together with the start- and stopt-time of the signal for one shower. Signals are identified as time bins with at least 3 FADC counts above baseline. These bins are then merged and finally related PMT and station quantities are calculated and set. This module rejects stations without trigger, with random trigger, without local station calibration data or without GPS data. Actually, a modified version of the SdCalibrator has been used [204, 205] for this work which is needed for a proper calculation of the signal stoptime and thus the station risetime (see Sec. 6.3) and signal. The modifications are (with the affected channel[6] given in brackets)

1. Use the trace of the respective gain channel for the search of signal pieces in the trace.

[6] HG: High-gain, LG: Low-gain

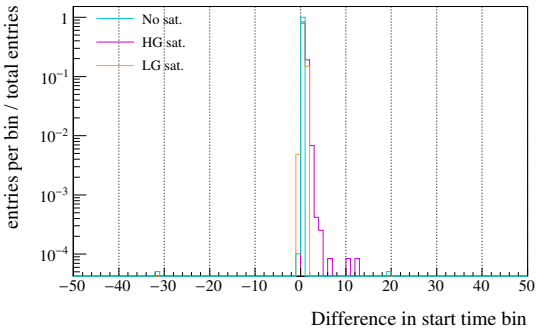

(a) Starttime bin (difference in multiples of 25 ns)

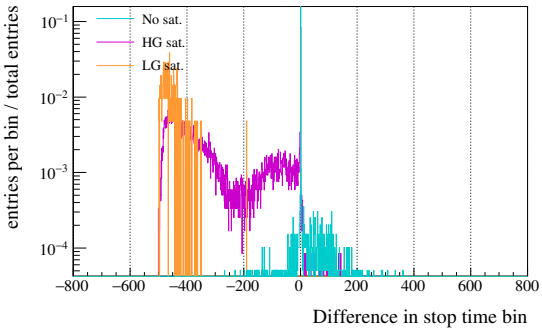

(b) Stoptime bin (difference in multiples of 25 ns)

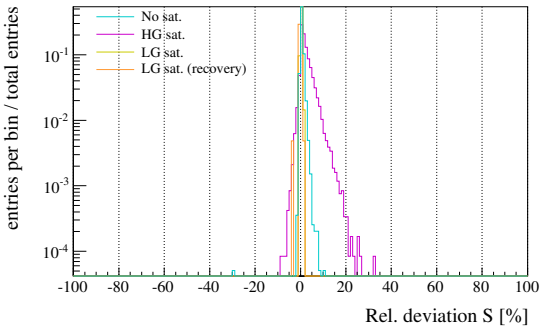

(c) Signal S

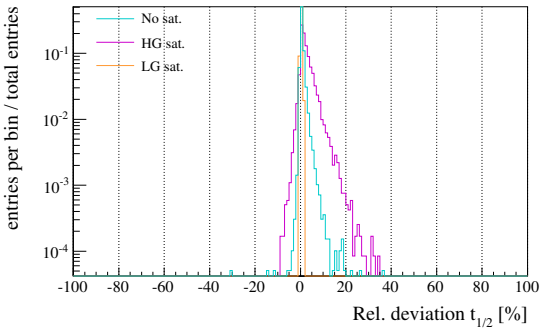

(d) Risetime $t_{1/2}$

Figure 3.8: Relative difference of reconstructed quantities with and without applying **all modifications** to the SdCalibrator, applied on **observed data**. Mean and standard deviation can be found in Tab. E.2. Cyan: Selected non-saturated stations of events with no saturated station, magenta: selected HG-saturated stations of events with at least one HG-saturated station, orange: LG-saturated stations of events with at least one HG-saturated station.

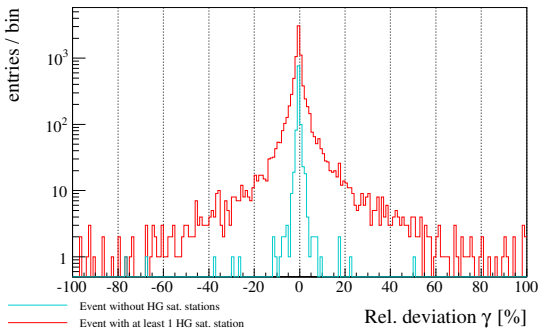

(a) LDF shape parameter γ

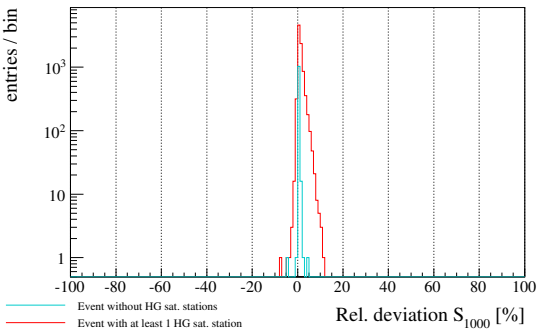

(b) S_{1000}

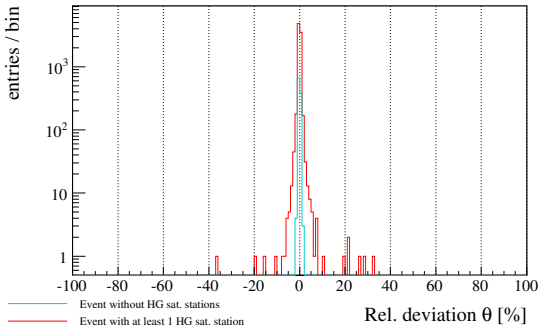

(c) Zenith angle θ

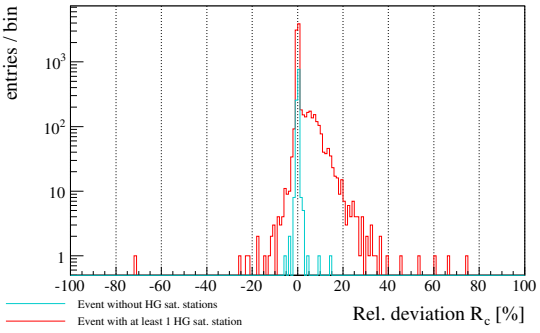

(d) Radius of curvature R_c

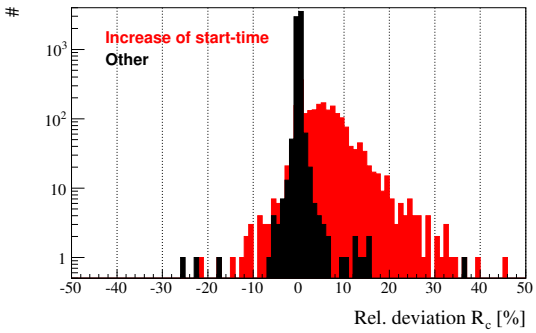

(e) Radius of curvature R_c: The structure in the distribution in Fig. 3.9(d) can be explained by at least one HG-saturated station having an increased start-time due to the modifications of the SdCalibrator.

Figure 3.9: Relative difference of reconstructed quantities with and without applying **all modifications** to the SdCalibrator, applied on **observed data**. Mean and standard deviation can be found in Tab. E.2. Cyan: Selected non-saturated stations of events with no saturated station, magenta: selected HG-saturated stations of events with at least one HG-saturated station, orange: LG-saturated stations of events with at least one HG-saturated station.

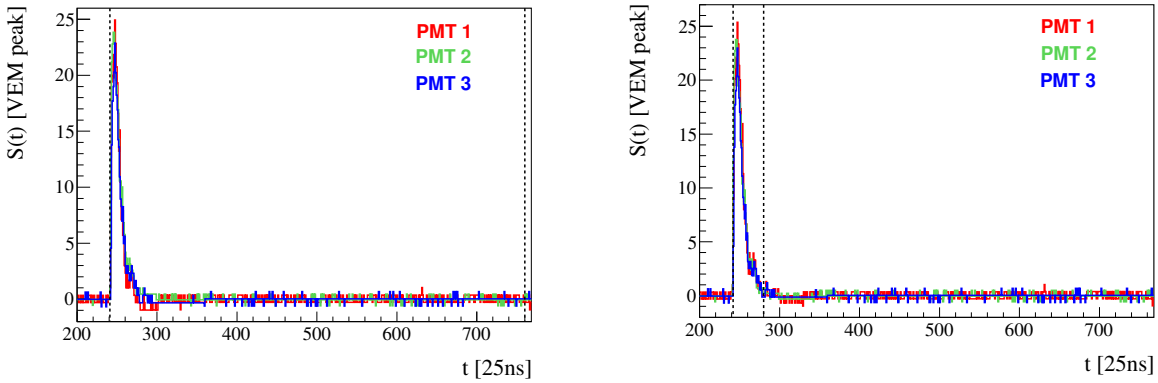

(a) Standard SdCalibrator (the dashed lines indicate start- and stoptime).

(b) Modified SdCalibrator (the dashed lines indicate start- and stoptime).

Figure 3.10: Event 4403320, station 1312: Correction of the stoptime and the baseline.

The standard would be using the high-gain channel always. [LG]

2. Backward search for flat pieces that are used to determine the baseline. The standard is the forward direction which can be problematic in case of long tails in the signal which are mistaken as a flat piece. The baseline is overestimated then. [LG+HG]

3. In the search for flat pieces in the low gain trace, reduce the maximum allowed absolute difference in the FADC counts of each bin compared to the first bin within a flat piece by one count with respect to the high gain trace. [LG]

The effect of these modifications has been checked on data from year 2008 (bad periods and lightning rejected), with 6T5 trigger, $E > 3$ EeV, $\theta < 60°$, a reconstructed curvature and a station signal of at least 10 VEM. The total effect is a smaller, improved stoptime (see Fig. 3.8(b) and the example in Figs. 3.10(a) and 3.10(b)) and an improved baseline, which are reflected in the station signal and risetime (see Figs. 3.8(c) and 3.8(d)). The changes to the time trace affect the LDF fit, and in particular the shape parameter γ (see Fig. 3.9(a)). For high-gain-saturated stations with an increased start-time the radius of curvature increases systematically by about 5% (see Figs. 3.9(d) and 3.9(e)). A consecutive study of each single modification has been performed. For a summary of the results see Tab. E.2 in the appendix. The reconstruction and all included parametrizations have been optimized for the standard SdCalibrator. Thus the effect on S_{1000} has been checked as this affects the energy scale. It has a systematic offset of $\sim 1\%$ with a standard deviation of 1%. The application of the modifications in the reconstruction of MC photon showers is discussed in Chap. 4.

Module: SdEventSelector

This module selects *candidate stations*[7] and twin stations[8]. In case of a so-called *bottom-up* selection, as used in this thesis, the shower geometry is estimated from the triangle that maximizes the sum of signals (seed). The geometry is used to check for the time compatibility of each additional station and to reject outliers from the candidate stations as *accidental*. Isolated stations, stations without reconstructed data and stations which show a typical trace as occurring in case of a lightning are also rejected from the candidates. Events can be selected according to their trigger level (T4, T5) or rejected in case of lightning or if they fall in a bad data-taking period, based on an xml card.

Module: SdPlaneFit

The reconstruction of the shower geometry is done in several steps. The geometry consists of the showe core (x, y) and the direction of the shower axis (θ, φ). The shape of the lateral distribution is parametrized by two parameters (β, γ). Depending on the number of stations, the radius of the shower front curvature R_c is either fitted or evaluated from a parametrization. These fits are not independent. A sketch of the shower geometry is shown in Fig. 3.7. The first guess for the location and arrival time of the shower core are taken from the barycenter $\mathbf{b}$ of the candidate stations,

$$\mathbf{b} = \mathbf{x}_0 + \frac{\sum_{i=1}^{N} \mathbf{x}_i \cdot \sqrt{S_i}}{\sum_{i=1}^{N} \sqrt{S_i}}. \tag{3.16}$$

with $\mathbf{x}_i$ and S_i the position and signal of the station. The barytime, t_b, is calculated analogously. The showerfront moves with the speed of light along the shower axis with direction $\hat{a}$,

$$\mathbf{x}(t) - \mathbf{b} = -c\,(t - t_b)\,\hat{a}.$$

A first estimate for the shower direction, assuming a planar shower front, is obtained by minimizing

$$\chi^2 = \frac{1}{\sigma_t^2} \sum_{i=1}^{N} (t_i - t(\mathbf{x}_i))^2$$

with the time variance given by

$$\begin{aligned} \sigma_t^2 &= a_2 \cdot \left(\frac{2\,T_{50}}{n}\right)^2 \cdot \frac{n-1}{n+1} + b_2 \\ a_2 &= 0.67612 + \cos(\theta) \cdot (0.16106 - 0.47641 \cdot \cos(\theta)) \\ b_2 &= 128\mathrm{ns}^2 + \cos(\theta) \cdot (-184 + 413 \cdot \cos(\theta))\,\mathrm{ns}^2. \end{aligned} \tag{3.17}$$

Here T_{50} is the time in [ns] corresponding to a cumulative signal of 50% and $n = s/(\cos(\theta) + (2 \cdot 1.2 \cdot \sin(\theta)/(1.8 \cdot \pi))$ is the effective number of particles producing the signal. In Offline this model is tagged as `eCDASv4r8`.

[7] Candidate stations are stations that have measured a coincident signal with time delay according to the shower geometry.

[8] Twin stations refer to those stations which have a partner a few meters next to it for a measurement of the signal uncertainty.

Module: LDFFinder

The LDF is parameterized by a modified NKG-type function [206]:

$$S(r) = S_{1000} \cdot \left(\frac{r}{r_{\text{opt}}}\right)^{\beta} \cdot \left(\frac{r + 700\ \text{m}}{r_{\text{opt}} + 700\ \text{m}}\right)^{\beta+\gamma}, \tag{3.18}$$

with β and γ shape parameters. Note that β and γ are by default not free in the fit but fixed to a parametrization in S_{1000} and θ obtained from data. The parametrization can be found in Eq. D.5 in the appendix. The use of an average LDF allows to reduce the number of free parameters to the energy estimator S_{1000} and the shower core and thus allows for a fit at low station multiplicities. At a reference distance of $r_{\text{opt}} = 1000$ m, the fluctuations of the expected signal due to a lack of knowledge of the LDF shape is minimal (<5%) [207] and depends mainly on the detector geometry. The uncertainty of signal S_i of a station i is [208, 209]

$$\sigma_{S_i} = (0.34 + 0.64 \cdot \sec\theta) \cdot \sqrt{S_{\text{exp},i}}. \tag{3.19}$$

The fit method is a maximum likelihood fit that accounts for stations with small and large signals, saturated and silent[9] stations. The probabilities are multiplied to a single likelihood. The minimum number of stations needed for an LDF fit with fixed shape is 3 stations. As a next step the **curvature** is taken into account. A full fit of the radius of curvature (R_{c}), the shower front start time (t_0) and the shower core requires at least 5 stations and is done by minimizing

$$\chi^2 = \sum_{i=1}^{N} \frac{\left[c\,(t_i - t_0) - |R_{\text{c}}\,\hat{\mathbf{a}} - \mathbf{x}_i|\right]^2}{c^2\,\sigma_t^2}, \tag{3.20}$$

with σ_t the time uncertainty (cf. Eq. 3.17). Finally, S_{1000} and the shower core are fitted again with the new estimate of the axis.
The **energy** is obtained based on S_{1000} [210]. The calibration relies on the constant intensity cut method (CIC) which assumes that all CR arrive at Earth isotropically without a preferred direction. S_{1000} shows a dependence on the shower geometry wich can be corrected to a signal at a zenith angle of 38°, which is the median of the zenith angle distribution up to 60° [192]:

$$S^{38} = S_{1000} \cdot \left(1 + 0.987 \cdot c(\theta) - 1.682 \cdot c(\theta)^2 - 1.299 \cdot c(\theta)^3\right)^{-1} \tag{3.21}$$

with $c(\theta) = \cos^2(\theta) - \cos^2(38°)$. The energy is obtained with a simple conversion,

$$E_{\text{SD}} = A \cdot \left(S^{38}\right)^{B}, \tag{3.22}$$

with $A_{\text{cal}} = 0.190$ and $B_{\text{cal}} = 1.025$ from a study of hybrid events [192, 211].

3.4.3 Surface detector simulation

The simulation of the time-dependent SD response in Offline starts from the single secondary particles of a CORSIKA shower at observation level. The simulation part is simply added to the

[9] Silent means non-triggering here.

module sequence before the reconstruction. In CORSIKA the shower is thinned [158]: A particle is only followed until the total energy of its secondary particles falls below

$$E_{\mathrm{th}} = \epsilon_{\mathrm{th}} E_0. \tag{3.23}$$

Below this energy only one random particle is followed, carrying a weight

$$w = \frac{\epsilon_{\mathrm{th}} E_0}{E_j}, \tag{3.24}$$

with E_j the energy of the representative particle and $\varepsilon_{\mathrm{th}}$ the thinning level. An *unthinning* (or *resampling*) procedure is being applied to get from the thinned shower an estimate of the distribution of secondary particles [212]. In order to assure a suffcient sample size of particles arriving at the detector and to reduce the introduced Poissonian fluctuations, the sampling area for a station is not the true detector size A_{det} but an area A_{samp} around the location at core distance r within $\pm 10\% \cdot r$. The effective number of particles is then $w \cdot A_{\mathrm{det}}/A_{\mathrm{samp}}$. The arrival time of each particle is smeared to avoid muon-like peaks and the positions are distributed uniformly over the sampling area. Then the detector response is simulated using GEANT4 [213]. The module sequence used here can be found in App. C. The SD detector simulation has been verified by a comparison to measurements of atmospheric muons entering an SD tank under certain zenith angles, realized by additional muon hodoscopes [214].

CHAPTER 4

UHE Photon Detection

This chapter contains the most important parts that are needed to set upper limits on the flux of UHE photons with the surface detector of the Pierre Auger Observatory. We present technical studies needed for the photon detection with the SD of Auger the $\overline{\text{Off}}\underline{\text{line}}$: a modification of the event reconstruction procedure for an improvement of the signal risetime, which is used as one separation parameter for the photon search, and an update of the energy calibration procedure to obtain an energy scale for (non-preshowered) photons. A short motivation is presented next about the differences of photon- and hadron-induced showers in the SD. The fourth section outlines the current experimental status of the upper limits on the UHE photon flux and fraction and briefly sketches the Frequentist construction of upper limits.

4.1 SdCalibrator

The SdCalibrator has been modified to improve the stop-time calculation of the time trace, in particular for stations with at least one high-gain-saturated PMT, as described in Sec. 3.4.2. This was suggested in [215] for risetime studies. Here we summarize the effect on simulated photon showers (see Figs. 4.1(a) to 4.2(b) and Figs. 3.8(b) to 3.9(b)).

- The usage of the respective gain for the signal search affects photons and data differently. The shape of the distributions is similar (except for the stop-time distribution, which might be related to actual differences in the observed LDF shape and length and the muon fraction) but photon showers are affected stronger. In principle this modification should be safe to be used and differences are expected to be of physical nature.

- The change of the tolerance in the search for flat pieces affects the start-time of high-gain-saturated stations for photon primaries but not for data. For the remaining observables the effect is almost compatible.

- The effect of the backwards scan of the trace for flat pieces on the start- and stop-time of high-gain-saturated stations is stronger for photon primaries than for data. This difference is reflected in the station risetime and signal. This might be related to a difference in the signal fluctuations for the different primaries.

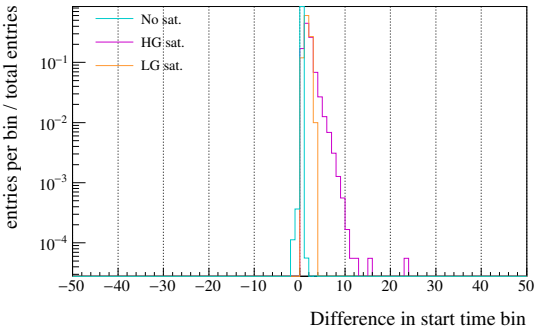

(a) Starttime bin (in multiples of 25 ns)

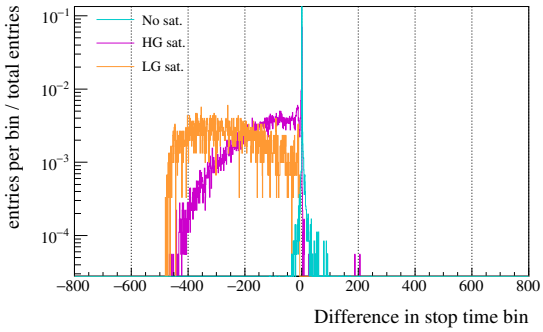

(b) Stoptime bin (in multiples of 25 ns)

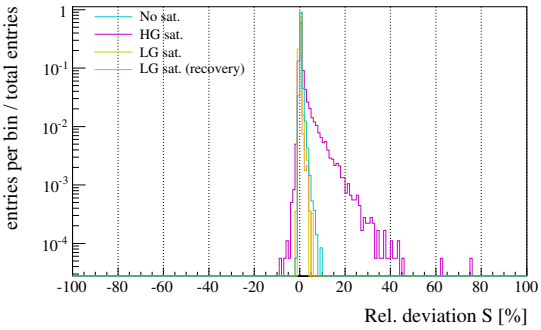

(c) Signal S

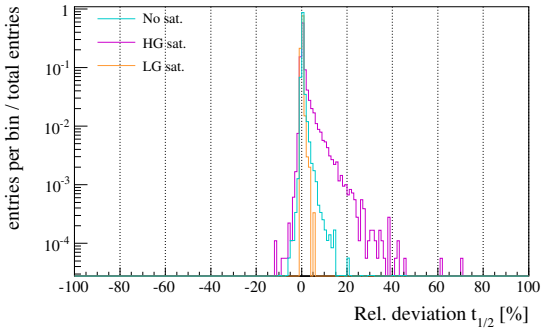

(d) Risetime $t_{1/2}$

Figure 4.1: Relative difference of reconstructed quantities with and without applying **all modifications** to the SdCalibrator, applied on **MC photon**s. Mean and standard deviation can be found in Tab. E.2. Cyan: Selected non-saturated stations of events with no saturated station, magenta: selected HG-saturated stations of events with at least one HG-saturated station, orange: LG-saturated stations of events with at least one HG-saturated station.

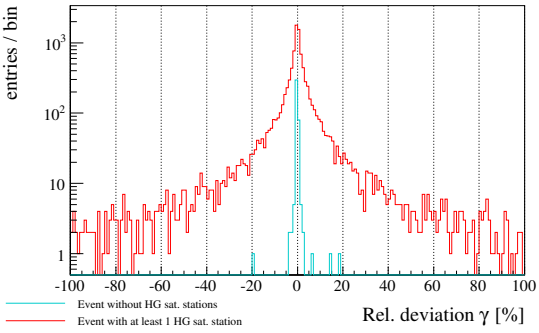

(a) LDF shape parameter γ

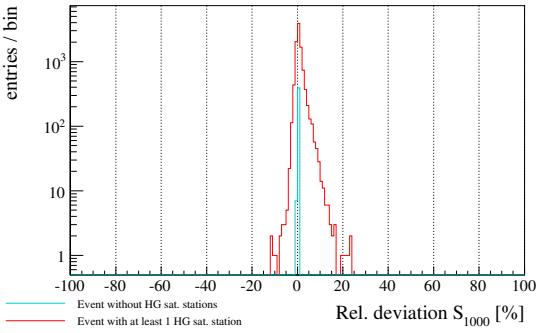

(b) S_{1000}

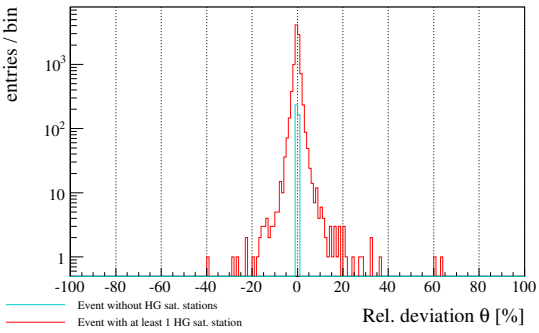

(c) Zenith angle θ

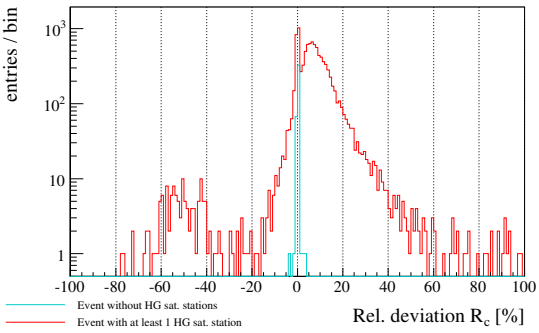

(d) Radius of curvature R_c

Figure 4.2: Relative difference of reconstructed quantities with and without applying **all modifications** to the SdCalibrator, applied on **MC photon**s. Mean and standard deviation can be found in Tab. E.2. Cyan: Selected non-saturated stations of events with no saturated station, magenta: selected HG-saturated stations of events with at least one HG-saturated station, orange: LG-saturated stations of events with at least one HG-saturated station.

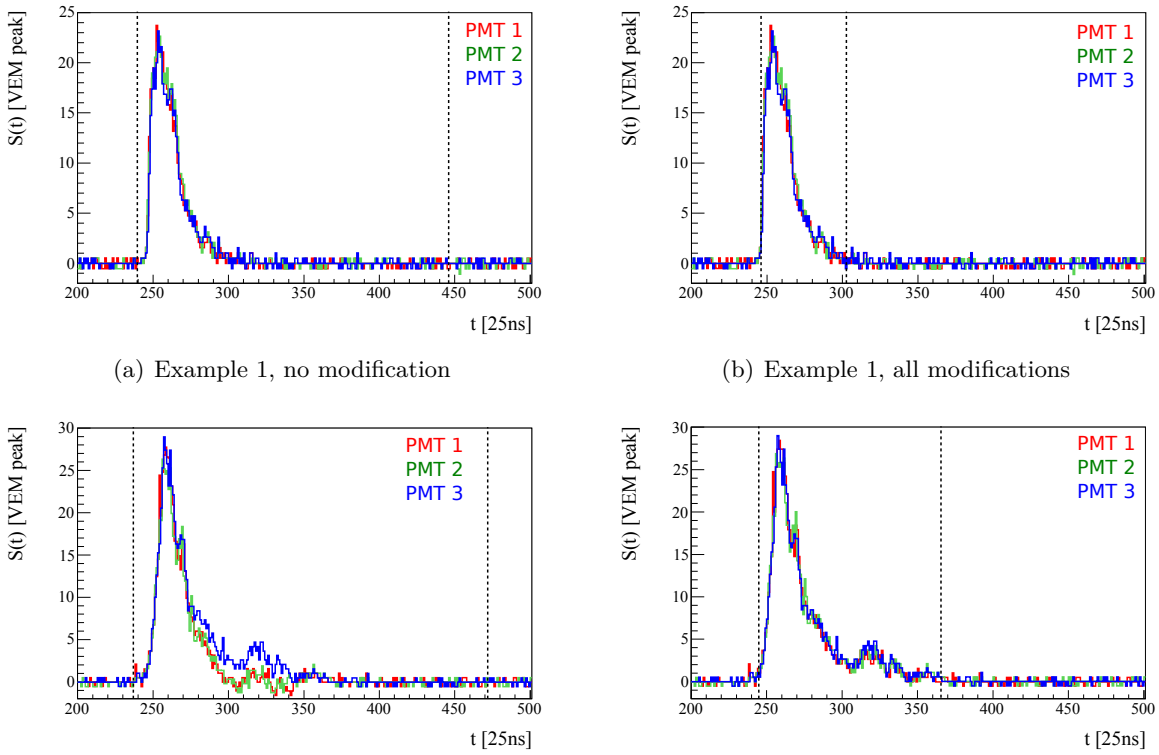

(a) Example 1, no modification

(b) Example 1, all modifications

(c) Example 2, no modification

(d) Example 2, all modifications

Figure 4.3: Effect of the SD calibrator modifications on start- and stoptime, indicated as dashed lines, for a HG-saturated station (MC photons).

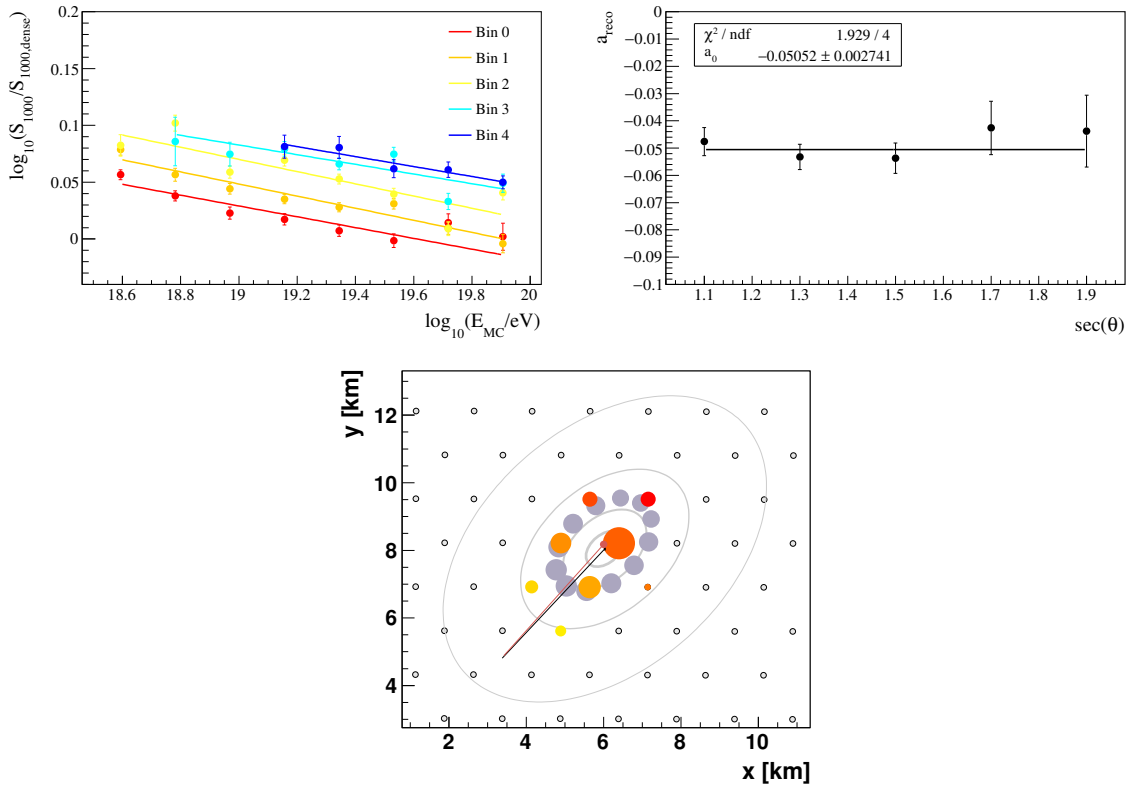

Figure 4.4: Reconstruction bias of S_{1000} in the LDF fit applied on simulated photons, studied on the base of dense stations inserted at 1000 m from the core. Top: Sketch of an SD event on the detector array. The ring of grey dots indicates the dense stations inserted at 1000 m. The black line shows the shower direction, yellow to red colors indicate the time delay and the size of the dots shows the SD signal. Bottom: Inserting 12 dense stations to each event (grey dots), here a simulated photon shower with $E = 18$ EeV and $\theta = 50°$. Top left: Energy dependence of $\log_{10}(S_{1000}/S_{1000,\mathrm{dense}})$, fitted with a function $f(E) = b_{\mathrm{reco}} + a_{\mathrm{reco}} \cdot (\log_{10}(E_{\mathrm{MC}}/\ \mathrm{eV}) - 18)$. The color scale indicates equidistant bins in $\sec(\theta)$. The bias is positive and decreases with energy. Top right: Zenith angle dependence of α. The fit is compatible with a constant.

In the example shown in Figs. 4.3(a) to 4.3(b) it is clearly visible that the stoptime is improved by the modifications. Another example shown in Figs. 4.3(c) to 4.3(d) shows an improvement of the start-time and baseline. The reduction of the flat piece tolerance (modification 3) affects the start-time of MC photons stronger than for data. The increase of the start-time is reasonable, but a detailed check (in particular of the flat piece tolerance) is an important topic for future studies. For now we conclude that the modifications can be applied for the SD photon search, being aware that the radius of curvature has to be used carefully. The risetime is improved significantly.

The reconstruction and all contained parametrizations are optimized to describe the data. Since the data is dominated by hadronic showers, this fixed LDF shape is not expected to describe photon-induced showers. Consequently S_{1000}, the shower axis and the core position are biased. The shift of the reconstructed zenith angle from the MC truth for simulated photons is shown

in Fig. E.10 in the appendix. It is centered at zero and with a standard deviation of about 1.2°. There is no apparent systematic shift. For the reconstruction of S_{1000} an overestimation is expected qualitatively because of two reasons: the LDF of an EM shower is compact, with a large fraction of the triggered stations within 1000 m from the core in the detector simulation, and the slope used for the LDF fit is underestimated. A quantitative check of the bias in the reconstructed S_{1000} has been performed using additional (dense) stations at 1000 m from the core, as shown in the top left plot in Fig. 4.4. The average observed signal at the dense stations is compared to the reconstructed LDF at the same distance. For this comparison we require that all 12 tanks have been triggered. The energy dependence of $\log_{10}(S_{1000}/S_{1000,\mathrm{dense}})$ has been fitted with a function

$$f(E) = b_{\mathrm{reco}} + a_{\mathrm{reco}} \cdot \log_{10}(E_{\mathrm{MC}}/\ \mathrm{EeV}) \tag{4.1}$$

as a first order approximation, with E_{MC} the true energy. It is shown the top left plot in Fig. 4.4. The bias is positive, showing an expected overestimation of S_{1000}, and decreases with energy and for vertical showers. With respect to the photon energy scale, we are particularly interested in the energy-dependent term a_{reco}. The top right plot in Fig. 4.4 shows that a_{reco} is constant in the zenith angle with $a_0 = -0.5$.

4.2 Photon Energy Scale

Other than for hadronic primaries, photon showers develop later in the atmosphere and under certain conditions (high energies and vertical showers) the shower maximum can be below ground level. In this case the shower is not fully developed and S_{1000} is underestimated. The CIC method cannot easily be applied here as the shower age has to be accounted for in the energy calibration. The calibration is based on the universality[1] of the longitudinal shower development of the pure EM cascade, which is the main component of a photon-induced air shower. The shower size (S_{1000}) for a given energy follows a universal profile in the shower age and thus in $\Delta X_{\mathrm{gr}} = X_{\mathrm{gr}} - X_{\mathrm{max}}$ (X_{gr} is the observation level), with a shape similar to a Gaisser-Hillas function and a shift due to lateral diffusion. The universal profile can be used to estimate the primary energy of a photon-induced airshower based on S_{1000}, the zenith angle θ and the elongation rate (parametrized for non-preshowered photons). This method has been discussed in [216] by *Billoir et al.* but it is there based on the true S_{1000}(MC) that is taken from the SD simulation. Due to the lack of muons in hadronic interaction models (see Sec. 3.3), S_{1000}(MC) is underestimated and the reconstructed energy overestimated when applied on the reconstructed S_{1000}. It has been updated by *Ros et al.* [217] using the reconstructed S_{1000} for a zenith range $30° - 60°$. Here the parametrizations are updated for the reconstruction used in this work and further improved.
Details about the set of photon simulations used here can be found in Chap. 5. For the following parametrizations non-preshowered photons have been used with a reconstructed LDF, a 6T5 trigger, with $\log_{10}(E_{\mathrm{MC}}/\ \mathrm{eV})$ in the range $18.5 - 20.5$ for the elongation rate or $19.0 - 20.5$ for the universal profile, with $X_{\mathrm{max}} > 500$ g/cm^2 (due to problems in the simulations, cf. Fig. 5.1), with $\Delta X_{\mathrm{gr}} > -50$ g/cm^2 and θ in a range of 0° to 60°. If nothing else is mentioned, each simulated event is based on a unique CORSIKA simulation instead of reusing a single event in multiple detector simulations. The simulated spectrum is E^{-1}.

[1] We assume here that the universality holds approximately also for the sum of the shower components (EM,μ).

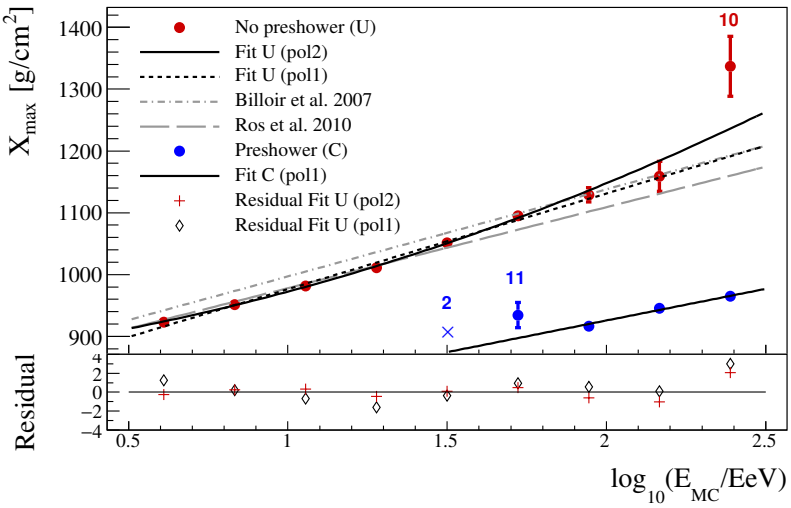

Figure 4.5: The elongation rate of simulated photons. Data of non-preshowered (preshowered) photons are shown with red (blue) markers. The shift between both classes is clearly visible. The parametrizations of non-preshowered photons (U) with a linear and a quadratic fit (black lines) are compared to the results from [216] and [217] (gray lines, both linear). The quality of the linear (quadratic) fit, shown by the dashed (full) black line, is $\chi^2/\mathrm{NDF} = 15.1/7$ (6.5/6). A linear fit for preshowered photons (C) is shown as well, with a fit quality of $\chi^2/\mathrm{NDF} = 6.1/2$. A data point of photons (C) has been removed at $10^{19.5}$ eV ($\langle X_{\mathrm{max}} \rangle = 903 \pm 44$ g/cm^2) with a statistics of 2 events. The number of events has been added explicitely for less than 15 events.

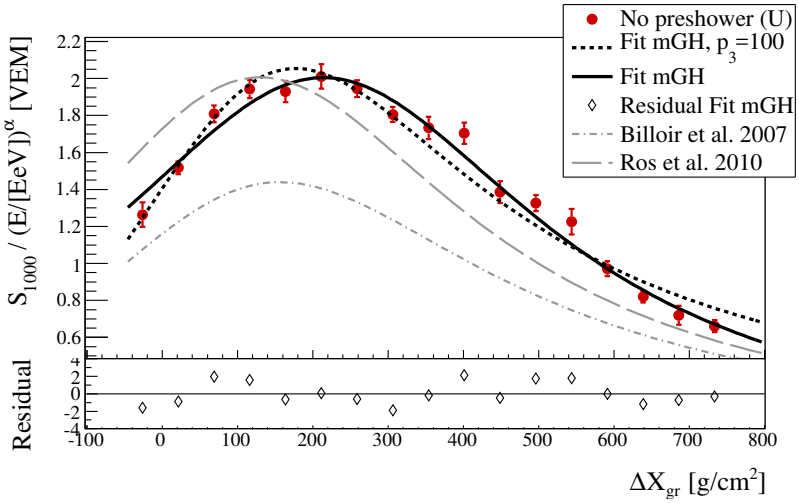

Figure 4.6: The universal profile for simulated, non-preshowered photons ($\alpha = 1$). Fits with a linear an quadratic function are compared to the results from [216, 217]. Black lines show the result of fitting the same functional to data of this work. The dashed line is for $p_3 = 100$ g/cm^2 fixed, the full line for 4 free parameters.

The **elongation rate** for this simulated dataset is shown in Fig. 4.5. A linear fit, as suggested in [216] and as expected from Eq. 3.1, gives the following parametrization for non-preshowered photons:

$$X_{\max} = q_0 + q_1 \cdot \log_{10}(E/\text{ EeV}) \tag{4.2}$$

with E the primary energy and $q_0 = 822 \pm 6$ g/cm^2, $q_1 = 155 \pm 5$ g/cm^2 (χ^2/NDF = 15.1/7). The parametrization can be improved by adding a quadratic term to account for the energy-dependent slope:

$$X_{\max} = q_0 + q_1 \cdot \log_{10}(E/\text{ EeV}) + q_2 \cdot \log^2_{10}(E/\text{ EeV}) \tag{4.3}$$

with $q_0 = 871 \pm 18$ g/cm^2, $q_1 = 64 \pm 31$ g/cm^2 and $q_2 = 37 \pm 12$ g/cm^2. The fit quality is improved to χ^2/NDF ≈ 1. The quadratic form might be explained by the LPM effect. The last data point contains 10 events and three of them have an $X_{\max}$ of more than 1500 g/cm^2, which is most probably due to the LPM effect. The comparatively high value of the first data point for photons (C) might be explained by the following: The average zenith angle for preshowered photons increases for low energies close to the threshold (more than five degrees difference between $10^{19.5}$ eV and 10^{20} eV). This corresponds to a larger value of $X_{\max}$ as the path of the photon in the upper, less dense amosphere is longer.
Note that we require $\Delta X_{\text{gr}} > -50$ g/cm^2 which introduces a bias in the elongation rate (see also Fig. 5.1). This cannot be avoided as the CORSIKA shower is simulated to the obervation level and the calculation of $X_{\max}$ for deeper showers becomes unreliable. The efficiency of this selection is shown in Fig. 7.1. With decent statistics this might be a topic for future studies to fit the $X_{\max}$ distribution in bins of energy (which is still not trivial due to the LPM effect). Thus, the average $X_{\max}$ is overestimated in particular at high energies. As expected, the elongation rate for preshowered photons is lower, as shown in Fig. 4.5.
For the **universal profile** we start with the same functional form as suggested in [216],

$$\frac{S_{1000}}{E/\text{ EeV}} = p_0 \times \frac{1 + \frac{\Delta X_{\text{gr}} - p_3}{p_1}}{1 + \left(\frac{\Delta X_{\text{gr}} - p_3}{p_2}\right)^2}, \tag{4.4}$$

with a shape close to a Gaisser-Hillas function (abbreviated **mGH** in the following), as shown in Fig. 4.6. The parametrization from *Billoir et al.* is below the data shown here as expected from the difference in the S_{1000} used. The parametrization from *Ros et al.* does not describe our data sufficiently either. In a first fit we set $p_3 = 100$ g/cm^2 (dashed black line), with $p_0 = 1.92 \pm 2 \cdot 0.02$ VEM/ EeV, $p_1 = 540 \pm 39$ g/cm^2 and $p_2 = 299 \pm 8$ g/cm^2 (fit quality χ^2/NDF = 55.6/14). Leaving p_3 free improves the fit (χ^2/NDF = 27.1/13, full red line) and gives a shift $p_3 \approx 200$ g/cm^2, but p_1 becomes unstable.
Before further studying the functional form, an energy dependence of the distribution, clearly visible in Fig. 4.7(c), breaks the universality and must be accounted for. Note that deviations from the universal profile are expected because the reconstruction of the LDF is not optimal for photons. The universality can partly be recovered by introducing a **correction factor** α so that

$$\log_{10}(S_{1000}/\text{ VEM}) \quad = \quad \alpha \cdot \log_{10}(E/\text{ EeV}) + \beta. \tag{4.5}$$

β contains the actual profile and α quantifies the energy dependence of S_{1000}. First we fit the energy dependence in 6 equidistant bins of ΔX_{gr} (see Fig. 4.7(a)). Figure 4.7(b) shows the

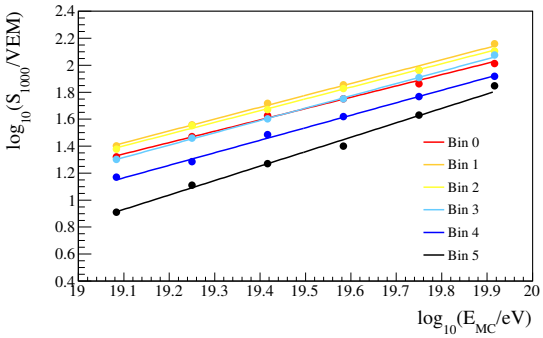

(a) Linear fit of the energy dependence of S_{1000} in 6 equidistant bins of ΔX_{gr}, for ΔX_{gr} between -50 g/cm^2 and 900 g/cm^2.

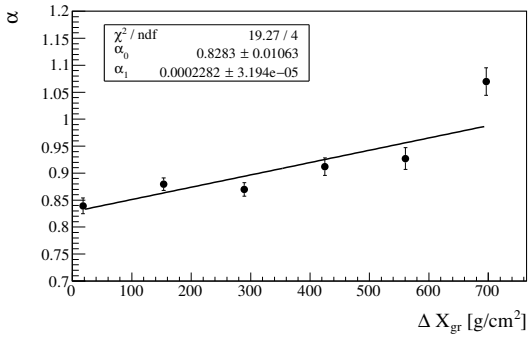

(b) Correction factor α.

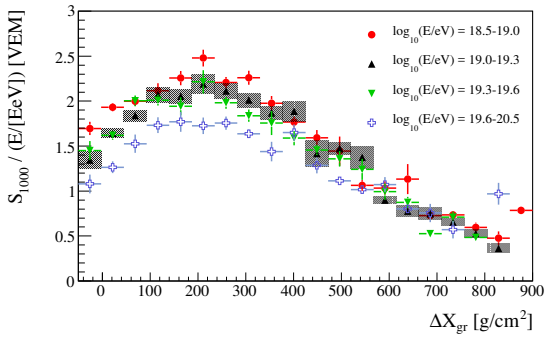

(c) Energy dependence before correction.

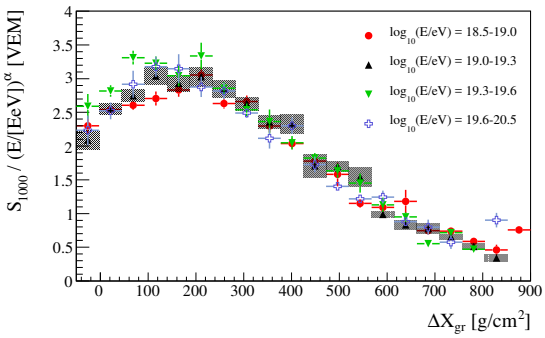

(d) Energy dependence after correction.

Figure 4.7: Partial recovery of the universal profile (for simulated, non-preshowered photons) by adding a correction factor α in S_{1000}/E^{α}. The correction factor has been optimized on the energy range of 10^{19} eV to 10^{20} eV.

consequent parametrization of α in ΔX_{gr},

$$\alpha = \alpha_0 + \alpha_1 \cdot \Delta X_{\mathrm{gr}}, \tag{4.6}$$

with $\alpha_0 = 0.83$ and $\alpha_1 = 2.3 \cdot 10^{-4}(\text{ g/cm}^2)^{-1}$. Here each shower has been simulated in the detector five times to increase the statistics. If we compare this result to the energy dependence expected from the reconstruction bias of S_{1000}, a part of the energy-dependence of the profile can be explained by the reconstruction bias of the LDF fit. Assuming a universality of $S_{1000,\mathrm{dense}}/E$, with $S_{1000,\mathrm{dense}}$ an estimator of the true S_{1000} from dense stations, we find for the reconstructed (biased) S_{1000} that $S_{1000}/(E/\text{ EeV})^{1-a_{\mathrm{reco}}} = b_{\mathrm{reco}} \cdot f(\Delta X_{\mathrm{gr}})$. Here $f(\Delta X_{\mathrm{gr}})$ is the universal profile and a_{reco} and b_{reco} from Eq. 4.1. The corrected universal profile is shown in bins of the true energy in Fig. 4.7(d). The energy dependence is almost removed. The last step is now the study of the functional form of the universal profile. Motivated by [218, 219], we suggest to fit

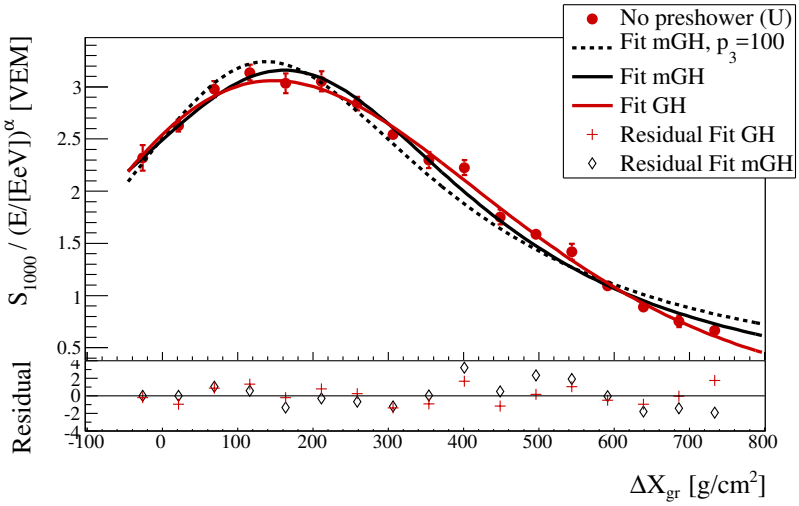

Figure 4.8: The corrected universal profile for simulated, non-preshowered photons. Different functional forms are compared, as described in the text.

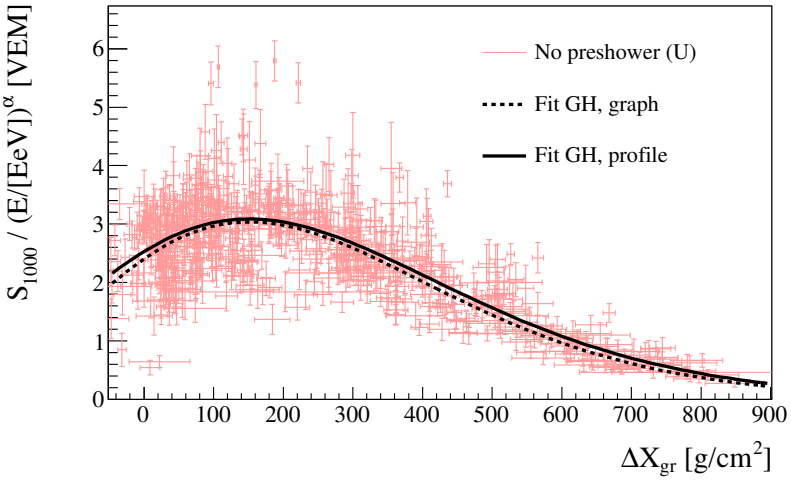

Figure 4.9: The corrected universal profile for simulated, non-preshowered photons in the energy range $10^{19} - 10^{19.5}$ eV. Shown is a comparison of a fit of the binned profile (mean value and its error) to a fit to single values within their uncertainties (for details see text). The functional form is a Gaisser-Hillas shape. Different functional forms are compared, as described in the text.

the EM component with a Gaisser-Hillas-shaped profile (abbreviated **GH** in the following):

$$\frac{S_{1000}}{(E/\text{ EeV})^{\alpha}} = S_{\max} \times \left(\frac{\Delta X_{\rm gr} - \Delta X_{0,\rm gr}}{X_{\max} - X_0}\right)^{\frac{\Delta X_{\max} - \Delta X_0}{\Lambda}} \cdot \mathrm{e}^{(\Delta X_{\max,\rm gr} - \Delta X_{\rm gr})/\Lambda} \tag{4.7}$$

$$= p_0 \times \left(1 + \frac{\Delta X_{\rm gr} - p_2}{p_1}\right)^{p_1/\Lambda} \cdot \mathrm{e}^{-(\Delta X_{\rm gr} - p_2)/\Lambda}, \tag{4.8}$$

with an attenuation length[2] $\Lambda \approx 100$ g/cm^2 after the shower maximum [218], $\Delta X_{\rm gr} = X - X_{\rm gr}$, $\Delta X_{\max,\rm gr} = X_{\max} - X_{\rm gr}$ and $\Delta X_{0,gr} = X_0 - X_{\rm gr}$. A simplified rewriting gives $p_0 = S_{\max}$, $p_2 = \Delta X_{\max,\rm gr}$ and $p_1 = X_{\max} - X_0$. The fit with the GH function improves the fit quality ($\chi^2/\text{NDF} \approx 1$, reduced by a factor 2) and the parameters in GH are more stable. Thus we decide to use the GH form. In order to reduce the spread due to the LPM effect and the need for a proper reweighting of the spectrum, we restrict the dataset to an energy bin of 10^{19} - $10^{19.5}$ eV. The final parametrization is obtained using single measured values with uncertainty estimates (see Fig. 4.9 and Tab. 4.1). The uncertainties are

$$\Delta(\Delta X_{\rm gr}) = x_{\rm gr} \cdot \tan(\theta) \cdot \Delta\theta, \tag{4.9}$$

$$\Delta(S_{1000}/(E/\text{ EeV})^{\alpha}) = \sqrt{\frac{\Delta S_{1000}}{(E/\text{ EeV})^{\alpha}}^2 + \left(\frac{S_{1000}}{(E/\text{ EeV})^{\alpha}} \cdot \ln(E/\text{ EeV}) \cdot \Delta\alpha\right)^2}, \tag{4.10}$$

$$\Delta\alpha = \sqrt{1.13 \cdot 10^{-4} + 1.02 \cdot 10^{-9} + 2 \cdot -2.77 \cdot 10^{-7}} \tag{4.11}$$

with $\Delta\theta$, ΔS_{1000} the reconstruction uncertainties of the zenith angle and S_{1000} and $\Delta\alpha$ the uncertainty of the parametrization of α. All parametrizations for the photon energy scale are summarized in Tab. 4.1.

The **energy calibration** is based on an interative procedure [216]:

- Start with a first assumption of $E = 2 \times E_{\rm hadr,rec}$, where $E_{\rm hadr,rec}$ is the reconstructed hadronic energy scale
- Get $X_{\max}$ from the parametrized elongation rate of non-preshowered photons
- Get a new estimate of the energy from the parametrized universal profile based on S_{1000}, θ and $X_{\max}$

It converges on average after $\sim$ 8 iterations (cf. Fig. 4.11, left plot). The selection required for this energy calibration is a reconstructed S_{1000}, $\Delta X_{\rm gr} > -50$ g/cm^2 above ground and a conversion of the calibration procedure ($\epsilon = E_i - E_{i-1} < 10^{-5}$). A final comparison of the stability of the obtained calibration and of former work can be found in Fig. 4.10(a). It clearly shows the effect of consequently using the reconstructed S_{1000}. The effect of the correction is significant in particular at low energies. The new photon energy calibration is stable up to about $10^{19.8}$ eV with a resolution of $\sim 35\%$. The remaining energy dependence at high energies (with a systematic shift $< 20\%$ below 10^{20} eV) comes from the cut on the $X_{\max}$ distribution by selecting showers above the ground level. This was checked by selecting showers with both the reconstructed and the true $X_{\max}$ above ground (see Fig. 9.1(a) in the appendix) for which the energy dependence is removed. Another source of outliers with a significant overestimation

[2]The assumption $\Lambda \approx 100$ g/cm^2 holds approximately also in [219] (it is slightly larger than the average for all energies and between 100 m and 2500 m).

Table 4.1: Photon energy calibration

Function	*Ref.*	*Parameter*	*Value*
Elongation rate	Eq. 4.3	q_0	(871 ± 18) g/cm^2
		q_1	(64 ± 31) g/cm^2
		q_2	(37 ± 12) g/cm^2
Universal profile	Eq. 4.6	α_0	0.83 ± 0.01
		α_1	$(2.3 \pm 0.3) \cdot 10^{-4}(g/cm^2)^{-1}$
	Eq. 4.7	p_0	3.04 ± 0.01 VEM
		p_1	592 ± 13 g/cm^2
		p_2	152 ± 2 g/cm^2

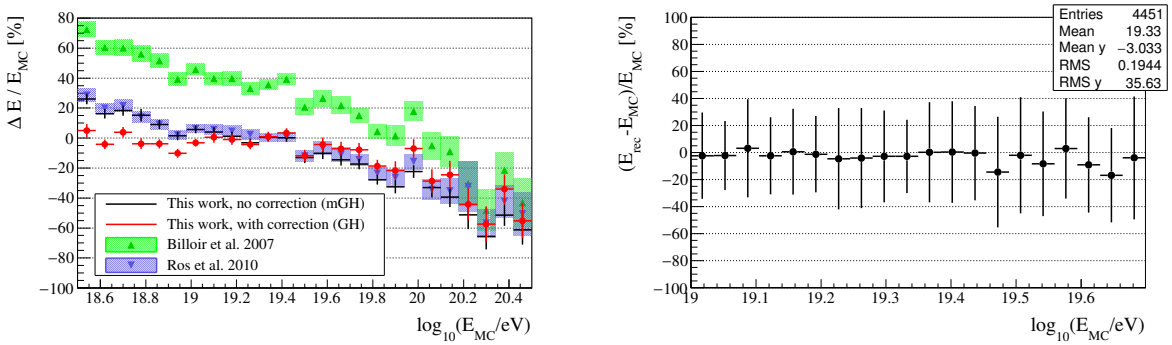

(a) $\Delta X_{\mathrm{gr}} > -50$ g/cm^2 (reconstructed X_{max}), showing mean and error of the mean

(b) $\Delta X_{\mathrm{gr}} > -50$ g/cm^2 (reconstructed X_{max}), showing mean and standard deviation (approx. 35%).

Figure 4.10: Relative error of the reconstructed photon energy with respect to the MC truth, as function of the true energy. Different energy scales are compared. Showers have been simulated in the detector five times.

of the reconstructed energy due to an exceptionally deep shower maxima is the LPM effect. Energies can be overestimated by up to a factor 2 or even more. This bias cannot be resolved with the described calibration method which bases on an average X_{max}. The energy spectrum for non-preshowered photons is shown in Fig. 4.11 on the right, visualizing the migration of events due to the energy reconstruction. For the integral number of events above 10^{19} eV ($10^{19.5}$ eV), the fraction of events migrating below/above threshold in the reconstructed photon energy is 11%/2% (12%/11%), without accounting for reweighting of the photon spectrum. This migration is accounted for in the efficiency calculation. The photon energy calibration has been improved significantly by the introduced correction.
The calibration is tuned on non-preshowered photons. This is obvious from the elongation rate. The relative error of this energy scale to the true MC value, when applied on preshowered photons, can be found in Fig. 9.1(b) in the appendix. It amounts to approximately -20%. The relative error of the hadronic scale to the MC value, when applied on non-preshowered photons, is approximately -60% or a half decade (same figure).

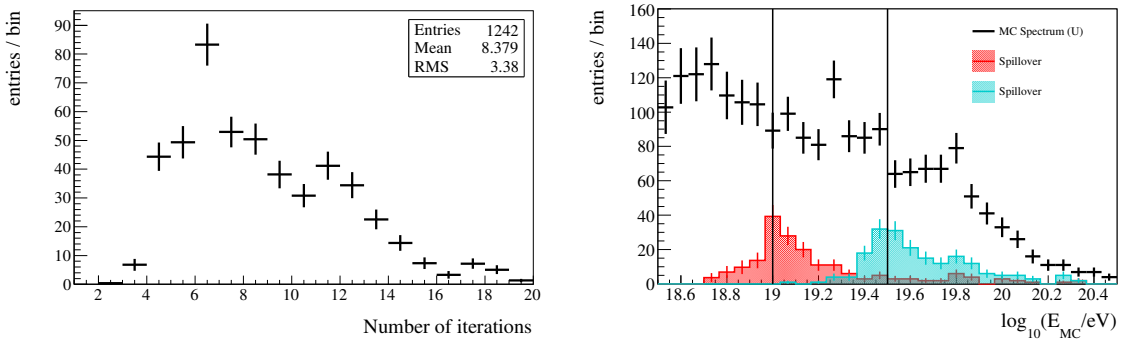

Figure 4.11: Photon energy calibration. Left: Shown is the number of iterations until a convergence is reached. Right: The migration of events (spillover) due to the energy reconstruction is shown on top of the spectrum of non-converted MC photons. The events left of the threshold have a higher reconstructed energy, events right of it have a lower reconstructed energy.

4.3 Separation Parameters

For the photon search it is neccessary to establish a photon-hadron separation based on different SD observables. Compared to an average hadron-induced shower, a photon-induced shower of the same energy reaches its shower maximum $X_{\max}$ deeper in the atmosphere, which is reflected in a smaller curvature radius of the shower front. The shower cascade produces less muons, which is reflected in a smaller shower size at ground, in a steeper LDF and in their arrival time distribution (cf. Fig. 4.12). These parameters contain information about the time and space domain of the air shower. Chapter 6 introduces the separation parameters used in this work.

4.4 Upper Limits on UHE Photons

The goal of this analysis is to set upper limits on the integral photon flux and fraction.
First it is necessary to estimate the number of photon candidates at confidence level. The statistical framework is a Frequentist construction of a confidence interval. Let $\hat{\theta}(x_1, x_2 \ldots, x_n)$ be the estimator of an unknown parameter θ. The estimator $\hat{\theta}$ (and the observed value $\hat{\theta}_{\text{obs}}$) is based on a sample of n observations of a random variable x and is distributed according to the probability density function (p.d.f.) $f(\hat{\theta}; \theta)$. We assume that, while θ is not known, we know how its estimator is distributed and that the p.d.f. contains the true value. Let us focus on the upper limit of a central and of a one-sided confidence interval. The construction and interpretation is different in different approaches. Frequentist constructions are the classical *Neyman construction* [220] and the *Feldman-Cousins approach* that extends the former by an ordering principle. Steps that are left out here can be found in App. A.

4.4.1 Frequentist approach (Neyman construction)

The central confidence interval $[a, b]$ is the region that would include the true value θ in a fraction $1 - \alpha$ of the repeated experiments measuring $\hat{\theta}$. Assuming that for the estimator this region is limited by $u_{\alpha/2}(\theta)$ and $v_{\alpha/2}(\theta)$ (an example has been compiled in Fig. 4.13(a)), the probability

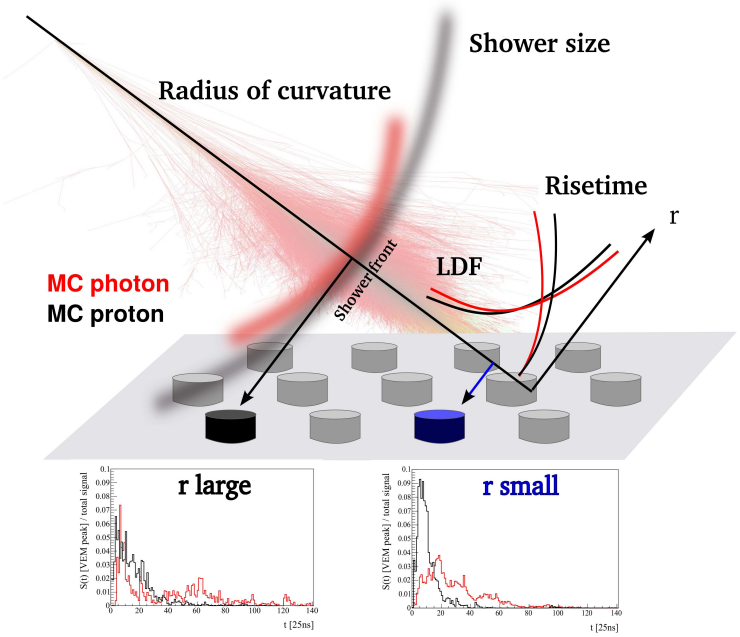

Figure 4.12: Some footprints in the surface detector that differ for photon- and hadron-induced air showers. (Shower image in the background from [133].)

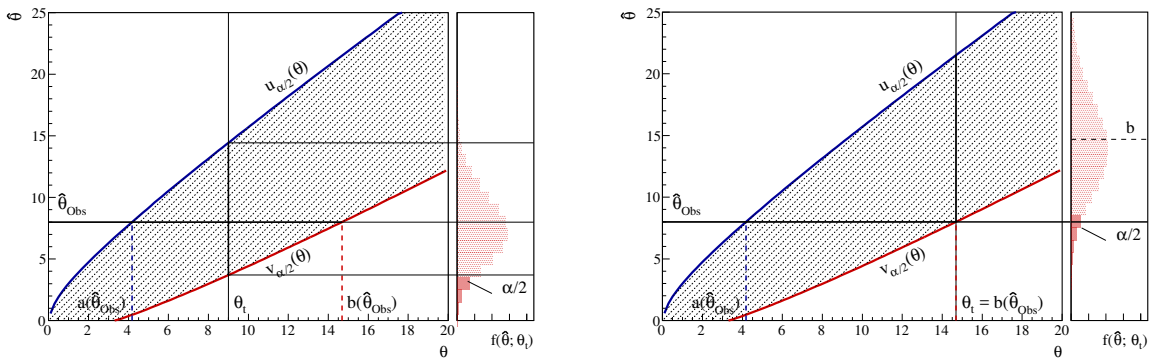

(a) $\theta_\mathrm{t} \neq b(\hat{\theta}_\mathrm{Obs})$ arbitrary

(b) $\theta_\mathrm{t} = b(\hat{\theta}_\mathrm{Obs})$

Figure 4.13: Example of a central confidence belt (shaded region) which is limited by $u_{\alpha/2}(\theta)$, $v_{\alpha/2}(\theta)$, with focus on the upper limit. The rotated plots indicate the p.d.f $f(\hat{\theta};\theta_\mathrm{t})$, here for the case of a Poissonian distribution. The horizontal line indicates a fixed value $\hat{\theta}_\mathrm{Obs}$. (a) The belt of the central interval is constructed for each θ according to the p.d.f. and confidence level. (b) The relation of the quantities becomes clear when choosing $\theta_\mathrm{t} = b(\hat{\theta}_\mathrm{Obs})$.

for $\hat{\theta}$ to be outside the confidence interval at the corresponding side is

$$1 - \alpha/2 = P(\hat{\theta} \geq v_{\alpha/2}(\theta)) = \int_{v_{\alpha/2}(\theta)}^{+\infty} f(\hat{\theta}; \theta) \mathrm{d}\hat{\theta} = 1 - F(v_{\alpha/2}(\theta); \theta), \tag{4.12}$$

where F is the cumulative distribution of f. With $v_{\alpha/2}(\theta)$ monotonically increasing, the upper limit as function of the estimator $\hat{\theta}$ is given by the inverse function

$$b(\hat{\theta}) \equiv v^{-1}_{\alpha/2}(\theta). \tag{4.13}$$

This means that the inequalities $\hat{\theta} \leq v_{\alpha/2}(\theta)$ and $b(\hat{\theta}) \geq \theta$ are equivalent and that

$$P(a(\hat{\theta}) \leq \theta \leq b(\hat{\theta})) = P(u_{\alpha/2}(\theta) \geq \hat{\theta}) + P(v_{\alpha/2}(\theta) \leq \hat{\theta}) = 1 - \alpha, \tag{4.14}$$

which is the *confidence level* (C.L.) or *coverage probability*. The Frequentist confidence interval or upper limit does **not** make a statement about the true value θ but about the probability that the true value is covered in a series of experiments. The upper limit can be understood as a hypothetical value of θ that is constructed, according to a given p.d.f., so that a fraction $1 - \alpha/2$ of observed events is larger (smaller) than $\hat{\theta}_{\mathrm{Obs}}$. Under the hypothesis $\theta = b$, as shown in Fig. 4.13(b), we find $v_{\alpha/2}(b) = \hat{\theta}_{\mathrm{Obs}}$ and

$$\alpha/2 = \int_{\hat{\theta}_{\mathrm{Obs}}}^{+\infty} f(\hat{\theta}; b) \mathrm{d}\hat{\theta} = F(\hat{\theta}_{\mathrm{Obs}}; b). \tag{4.15}$$

In the case of the photon search we have an unknown Poisson-distributed (integer and positive) parameter with mean ν, estimated by $n = \hat{\nu}$. We want to find the upper limit b so that

$$\begin{aligned} \alpha/2 &= P(n \leq b) \\ &= \sum_{n=0}^{n-1} \frac{b^n}{n!} e^{-b} \\ &= 1 - F_{\chi^2}\,(2b,\ 2(n+1)), \end{aligned} \tag{4.16}$$

where F_{χ^2} is the cumulative χ^2-distribution for $2(n+1)$ degrees of freedom. The upper limit is

$$b = \frac{1}{2} F^{-1}_{\chi^2}\,(1 - \alpha/2,\ 2(n+1)), \tag{4.17}$$

with F_{χ^2} the quantile of the χ^2-distribution. Let ν be composed of a signal with mean ν_{sig} and a (known) background with mean ν_{bkg}, both independent Poissonian distributions. With $\nu = \nu_{\mathrm{sig}} + \nu_{\mathrm{bkg}}$ and $\nu^{\mathrm{up}}_{\mathrm{sig}}$ the upper limit on the signal, Eq. 4.16 becomes

$$\begin{aligned} \alpha/2 &= P(n \leq \nu^{\mathrm{up}}_{\mathrm{sig}} + \nu_{\mathrm{bkg}}) \\ &= \sum_{n=0}^{n} \frac{(\nu^{\mathrm{up}}_{\mathrm{sig}} + \nu_{\mathrm{bkg}})^n}{n!} e^{-(\nu^{\mathrm{up}}_{\mathrm{sig}} + \nu_{\mathrm{bkg}})}. \end{aligned} \tag{4.18}$$

Comparing Eqs. 4.16 and 4.18 finally gives

$$b \;=\; \nu_{\mathrm{sig}}^{\mathrm{up}} + \nu_{\mathrm{bkg}}. \tag{4.19}$$

Dealing with integer values, the confidence belt is actually not defined for all values of θ. This is taken into account by the inequations $a(\hat{\theta}) \leq \theta \leq b(\hat{\theta})$ instead of requiring equality. Thus the confidence slightly overcovers[3]. This degree of conservativeness is given by the mathematical problem and cannot be removed. It is obvious that a one-sided upper or lower limit can be obtained the way as described above, but then the confidence level is $1 - \alpha/2$.

4.4.2 Frequentist approach (Feldman-Cousins)

The classical Neyman construction has two problems that are related to the coverage:

- If data are used to decide whether to state a one- or a two-sided confidence region, the jump at the point of switching between the different types causes a coverage that is smaller than the confidence level (*undercoverage*).
- In the case of boundaries (such as $\theta > 0$) there exist unphysical and maybe empty regions of n that one might want to treat differently. An over-conservative treatment (and thus an *overcoverage*) makes the method less powerful.

If the decision is taken beforehand and the results are shown consistently whatever the observed result is (in particular for zero background), the classical Neyman construction is sufficient. But as soon as any posterior decisions are made, the result gets biased. The Neyman construction has been extended in the work of *Feldman & Cousins* [221] to solve these problems. It is based on a ranking according to the likelihood ratio

$$R = f(n; \nu_{\mathrm{sig}}) / f(n; \nu_{\mathrm{sig}}^{\mathrm{best}}) \tag{4.20}$$

with $\nu_{\mathrm{sig}}^{\mathrm{best}} = \max(0, n - \nu_{\mathrm{bkg}})$ the most likely, physically allowed fit result of the signal for an observed n and

$$f(n; \nu_{\mathrm{sig}}) = \frac{(\nu_{\mathrm{sig}} + \nu_{\mathrm{bkg}})^n}{n!} e^{-(\nu_{\mathrm{sig}} + \nu_{\mathrm{bkg}})}. \tag{4.21}$$

The construction of the confidence interval is done in four steps. For fixed background and given n the best fit signal is obtained. For fixed signal the likelihood ratios are added in a scan over n until the confidence level is reached. The second step is then repeated for different signals. Finally the procedure can be repeated for different assumptions on the background. The obtained confidence interval smoothly combines one- and two-sided regions. For large n it is approximately central (as in the Neyman construction). For this work the Feldman-Cousins approach will be used.

4.4.3 Upper limits on the photon flux and fraction

The upper limit on the integral **photon flux** at 95% C.L. is calculated as

$$\Phi_\gamma^{95}(E_\gamma > E_0) = \frac{1}{\varepsilon} \cdot \frac{N_\gamma^{95}(E_\gamma > E_0)}{A'_{\mathrm{corr}}} \tag{4.22}$$

[3] If $P(\theta > b(\hat{\theta})) > \alpha/2$, then the confidence interval *overcovers*.

Table 4.2: Experimental results for UHE photon searches

Experiment	*Det. technique*	*C-Variable(s)*	*Operation*	*Refs.*
Haverah Park	SD (water Cherenkov)	E-spectrum	1974-1987	[223] (flux limits after private comm. related to [232])
AGASA	SD (scint. + μ-det.)	μ-density	1990-2003	[222, 224, 233]
Yakutsk	SD (scint. + μ-det.)	μ-density	since 1973	[224–226]
Pierre Auger Obs.	SD (water Cherenkov)	risetime, curvature	since 2004	[93]
	Hybrid (SD + fluor.)	$X_{\max}$, LDF		[100, 229]
Telescope Array	SD (scint.)	curvature	since 2007	[227, 228]

with N_γ^{95} the number of photon candidates at 95% C.L., E_γ the reconstructed photon energy, $A'_{\rm corr} = 0.98 A_{\rm corr}$ the exposure A corrected for the zenith angle range (cf. Eq. 3.15) and for a burn sample of 2% of all data and ε is the photon selection and reconstruction efficiency, above an energy threshold E_0. The upper limit on the integral **photon fraction** at 95% C.L. is calculated as

$$\begin{aligned} F_\gamma^{95}(E_\gamma > E_0) &= \frac{N_\gamma^{95}(E_\gamma > E_0)}{N_\gamma(E_\gamma > E_0) + N_{\rm non-\gamma}(E_{\rm hadr} > E_0) \cdot \frac{A'_{\rm corr} \cdot \varepsilon}{A}} \\ &\approx \frac{N_\gamma^{95}(E_\gamma > E_0)}{N_{\rm all}(E_{\rm hadr} > E_0) \cdot \frac{A'_{\rm corr} \cdot \varepsilon}{A}} \end{aligned} \tag{4.23}$$

with N_γ the number of photon candidates found in the analysis, $N_{\rm non-\gamma}$ number of non-photon events, $N_{\rm all}$ the total number of events and $E_{\rm hadr}$ the reconstructed hadronic energy.

4.4.4 Current upper limits on the diffusive photon flux and fraction

Upper limits on the diffusive photon flux and fraction have been placed by different EAS experiments (see Tab. 4.2). AGASA, Yakutsk and Telescope Array have operated or are operating scintillation counters. Telescope Array uses the curvature of the shower front as the composition-sensitive variable (C-variable). AGASA and Yakutsk combine scintillators and muon detectors, using the muon density as the C-variable. They have also published a combined limit in [224], given very similar detectors and a compatible energy calibration. Haverah Park and the Pierre Auger Observatory use water Cherenkov detectors. Haverah Park tries to match the spectrum varying the γ/p-fraction. The Pierre Auger Observatory has published photon limits for the SD alone and for the Hybrid measurement (SD+FD). The C-variables for the SD alone are the risetime and the radius of curvature of the shower front. For the Hybrid analysis the most stringent parameter is the depth of the shower maximum, $X_{\max}$, and in addition a parameter related to the shape of the lateral distribution is used. The SD energy estimator of the primary particle for scintillators and water Cherenkov detector is a particle density obtained at a distance that minimizes fluctuations due to a lack of knowledge of the LDF shape. Depending on the experiment, the energy is calibrated either with simulations or with a complementary detector. The limits are compiled in Figs. 4.14(a) and 4.14(b) and compared to the predictions discussed in Secs. 2.6.1 and 2.4.2. It should be mentioned that the limits from Haverah Park [223] and

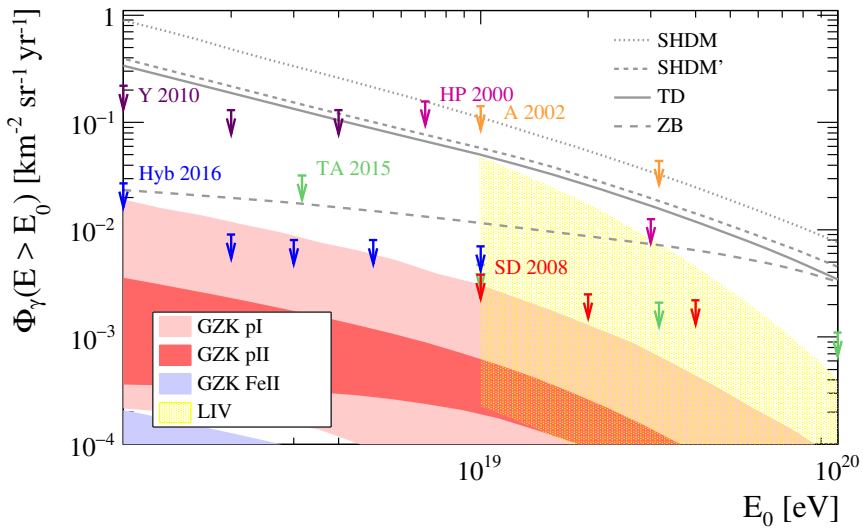

(a) Integral photon flux, Φ_γ

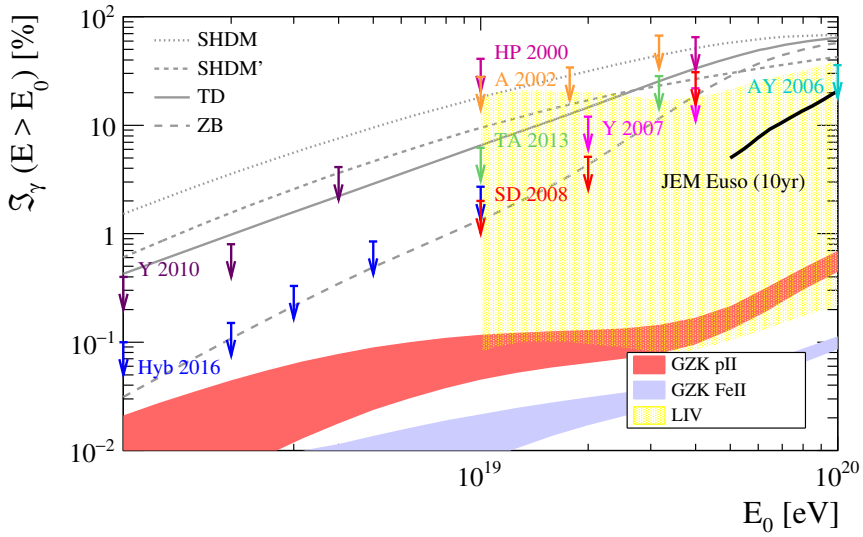

(b) Integral photon fraction, $\Im_\gamma$

Figure 4.14: Upper limits (95% C.L.) on the integral, diffusive photon flux and fraction derived from UHECR experiments: AGASA (A) [222], Haverah Park [223], AGASA-Yakutsk (AY) [224], Yakutsk (Y) [225, 226], Telescope Array (TA) [227, 228] and the Pierre Auger Observatory (SD, Hyb) [93, 229]. Shown is also the sensitivity for JEM-Euso [230] for 10 years operation in the Nadir mode. Assumed is an E^{-2}-spectrum for photons. A list of the experiments and data shown can be found in Tab. 4.2. In addition to top-down models (TD, Z-Burst and SHDM from [75], SHDM' from [76]) and GZK photons in astrophysical scenarios (cf. Sec. 2.6.1) [75, 94], predictions for Lorentz invariance violation (LIV) [231] are shown.

AGASA [222, 233] are only mentioned for completeness but are not shown as the energy scale is not fully compatible in this case.
As discussed earlier in Sec. 2.4.2, most top-down models are significantly restricted by Auger SD and Hybrid upper limits. The predicted integral fraction of GZK photons from proton accelerated in astrophysical scenarios is below 0.1% in most of the energy range (for the case of *Sarkar et al.* [94]). For heavier compositions it is lower. Limits are approaching the GZK region for primary proton with flat injection spectra.

CHAPTER 5

Dataset and MC Simulations

This chapter introduces the datasets of experimental data and photon Monte-Carlo simulations.

5.1 Experimental Data

The set of experimental data from the surface detector contains the period from January 1st, 2004 until May 14th, 2013. The CDAS version is v1r0, which already contains the PMT monitoring information needed to reject faulty PMTs. It has been reconstructed with Offline v2r9p3 (revision 23943, corresponding to the version used for the ICRC 2013 [192]). The module sequence of the SdReconstruction can be found in App. D. If nothing else is specified, we use the modified version of the SdCalibrator as described in Sec. 3.4.1.

5.1.1 Burn sample

For purposes of optimizing and comparing parameters for the photon search and for defining the principal component axis in the multivariate analysis we use a burn sample of 2% of all data. Events have been chosen randomly out of all good events above 3 EeV with a T4 and 6T5 trigger, with $\theta < 60^\circ$ and a reconstructed LDF, with a probability of 2%.

5.2 Photon Simulations

5.2.1 Air shower

Details about air shower simulations and the software CORSIKA can be found in Sec. 3.3. The photon signal for this analysis has been simulated with CORSIKA 6.970, amounting to 4000 simulated showers. An E^{-1} spectrum has been simulated for energies from $10^{18.5}$ eV to $10^{20.5}$ eV (other spectral indices are realized by a proper reweighting of each event). The solid angle distribution follows the assumption of a flat detector, with zenith angles from 0° to 65°. For low energy interactions the UrQMD 1.3.1 model has been used [234, 235]. High energy interactions have been treated with the QGSJetII.03 model [169, 170]. Electromagnetic interactions are treated with the EGS4 model [165]. Photonuclear interactions are simulated according to the PDG extrapolation *Cudell et al.* [236]. In order to reduce computing time, showers have been

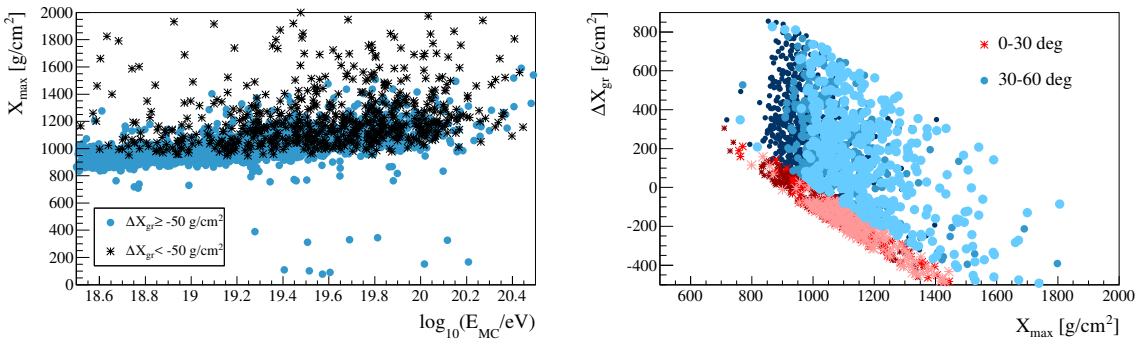

Figure 5.1: $X_{\max}$ distributions. Left: Energy dependence of $X_{\max}$ for simulated photon showers without geomagnetic preshower, comparing showers with $X_{\max}$ below and above the observation level. Right: Correlation of ΔX_{gr} and $X_{\max}$. A cut on ΔX_{gr} is not trivial in $X_{\max}$ and thus also the effect on the elongation rate.

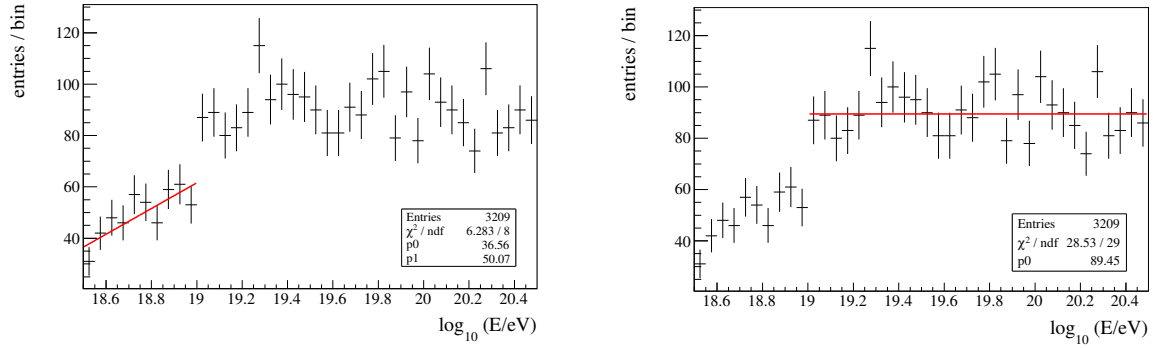

(a) Left part (linear fit)

(b) Right part (constant)

Figure 5.2: Event weighting factor to recover an E^{-1} spectrum.

thinned (see Sec. 3.3.4) with a thinning level of 10^{-6} optimal for photons. The preshowering in the geomagnetic field is accounted for with the option PRESHOWER. For this purpose, a modified version of CORSIKA has been used with the IGRF-11 model [237] updated to the year 2010 [238]. The simulated CORSIKA showers used in this thesis have been provided by C. Bleve, as well as technical support.
It has already been reported in [239] that there are two problems in CORSIKA 6.970 which are also apparent in this work. First, in some photon showers all energy is deposited in the first interaction due to a bug in the software (backwards-flying particles that are wrongly interpreted as energy deposit). This creates very small values of X_{max}, which can be mostly fixed by discarding events with $X_{\mathrm{max}} < 500$ g/cm^2 (see Fig. 5.1). As the simulation stops at the observation level, which is on average 880 g/cm^2 for the Pierre Auger Observatory, a cut on X_{max} above ground has to be introduced. This cut affects only photon-induced showers as they develop very deep in the atmosphere, in particular if they do not convert in the geomagnetic field and for the LPM effect. This cut on the X_{max} distribution introduces a bias in $\langle X_{\mathrm{max}} \rangle$, in particular above $10^{19.5}$ eV and for vertical shower geometries (see Fig. 5.1), that cannot be avoided. The preshower information was read from the lst-files of the CORSIKA output as this information is not processed to Offline.
Another issue is that a very small fraction of CORSIKA showers does not finish the simulation. This does not impose a bias. The few files missing in the energy bin $10^{18.5} - 10^{19}$ eV (true MC energy) were corrected by a weighting factor w_{add} to recover the simulated spectrum with slope $\alpha_{\mathrm{sim}} = -1$. It is shown in Figs. 5.2(a) and 5.2(b). The simulated spectrum is then weighted to a spectrum of slope α with a factor $w = (E/10^{19.})^{\alpha - \alpha_{\mathrm{sim}}}$. A common assumption is $\alpha = -2$.

5.2.2 Detector simulation

Each CORSIKA shower is simulated in the surface detector and reconstructed with the Offline application SdSimulationReconstruction. The corresponding module sequence can be found in App. C. Each physical shower has been resampled five times to enlarge statistics for efficiency calculations (otherwise each shower is only simulated once in the detector as long as nothing else is mentioned). The atmosphere used is the Malargue seasonal atmosphere.

5.3 Proton Simulations

The protons for parameters studies of this analysis have been simulated with CORSIKA 6.970, amounting to 4000 simulated showers. Interaction models, thinning level, energy range, spectral index and solid angle distribution are the same as for photon simulations. Each event is weighted to the Auger energy spectrum [240]. Note that these proton showers were simulated and reconstructed in the detector with an older software version, Offline v2r7p8, and without modifications of the SdCalibrator. Whenever necessary, differences in the reconstruction are pointed out.

CHAPTER 6

Study of Separation Parameters

In this chapter different observables are studied to establish event parameters for a photon-hadron separation. In order to avoid any reference to hadronic simulations in quantitative studies of the photon-hadron separation, we use a burn sample of data instead (see Sec. 5.1.1) together with the simulated MC photons. From current upper limits we can conclude that the integral photon fraction is below 2% above 10 EeV. Whenever proton simulations are shown they are only used for demonstration.

6.1 Technical Study: Noisy PMTs

In general, the SD monitoring is at a very sophisticated level and is done carefully to assure the quality of the signal measurement and reconstruction (in particular the energy). Other than analyses based on large statistics (e.g. the energy spectrum), the search of very rare classes of events based on the form of the signal trace and not only the integral is very sensitive to the proper functionality of the PMTs. Hardware malfunctions are not being simulated and may pose a background to the searched signal that should not be rejected looking only for some events. The best way is to identify malfunctioning PMTs in the monitoring and reject them from physical analyses. Some PMTs show noisy traces for different reasons. This issue was addressed in collaboration with the SD acceptance task and in particular with I. L'Henry-Yvon, P. L. Ghia, P. Billoir and Y. Guardincerri. In the following we will give an overview over the pathologies. Note that most of them can create an exeptionally large signal risetime and falltime. A list of PMTs that have been removed in this analysis can be found in Tab. 6.1.

Afterpulse

Some PMTs produce significant afterpulses, as shown in Fig. 6.1(a). The station risetime might be overestimated by a factor of more than two. The time periods of this behaviour correlate with an exponential drop in the VEM peak value. The noise has an almost constant offset of ~ 2500 ns after the signal start time. This malfunction can be identified in the monitoring.

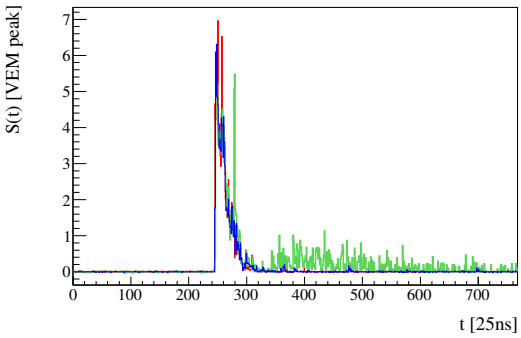

(a) Afterpulse (Event 1091764, station 573): Risetime 25 ns / 70 ns / 28 ns (PMT 1/2/3).

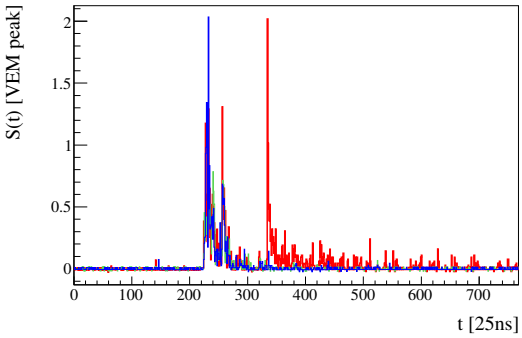

(b) Late event (Event 6394688, station 722): Risetime 220 ns / 35ns / 23 ns (PMT 1/2/3).

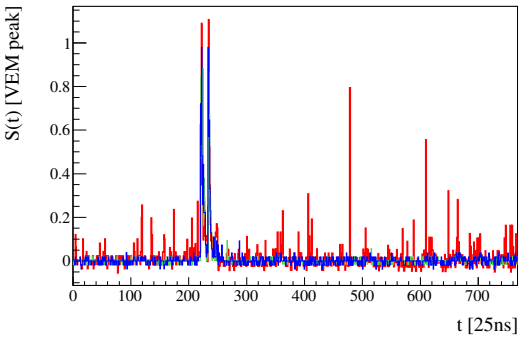

(c) Noisy baseline (Event 4587327, station 576): The physical signal is too low for a senseful risetime.

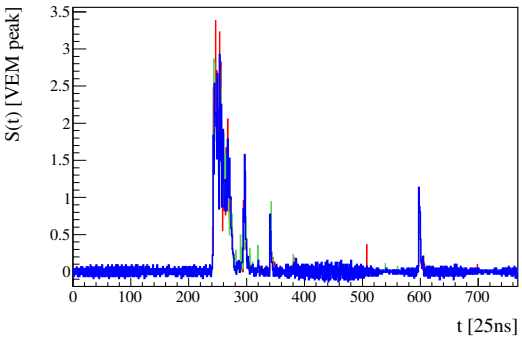

(d) Oscillating baseline (Event 13873446, station 880): Risetime 30 ns / 38 ns / 38 ns (PMT 1/2/3).

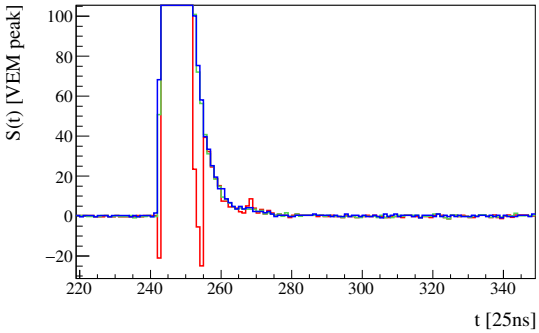

(e) Negative signal spike (Event 4654487, station 157).

Figure 6.1: Examples traces of PMT malfunctions and their risetime, with PMTs 1/2/3 shown in red/green/blue.

Table 6.1: List of PMTs to be excluded [241]

Station_PMT	*YYMMDD start*	*YYMMDD end*	*Problem*
573_2	41130	60610	Afterpulse
764_3	40101	90203	Afterpulse
1156_3	40101	81106	Afterpulse
1187_2	40101	90240	Afterpulse
1286_1	40101	81008	Afterpulse
1288_3	40101	90206	Afterpulse
1387_3	100331	x	Afterpulse
1440_2	40101	100602	Afterpulse
376_2	40101	x	Decay time
405_1	71006	90316	Decay time
602_2	90314	100721	Decay time
762_1	100304	x	Decay time
922_3	40101	111003	Decay time
151_3	100504	x	Other

Late event

The pathology shown in Fig. 6.1(b) occurs randomly and might be physical. After the main pulse of the event, a second pulse followed by noise is measured by only one PMT. It was suggested by the SD acceptance task that these might be delta rays produced by an electron close at a PMT. For the photon search, the rejection will be done only in case that a photon candidate shows this specific behaviour. The pathology is unlikely to be a single muon as the other PMTs do not detect any light.

Noisy / oscillating baseline

Some PMTs have a high level of noise that is independent of the signal start time. Two types of noise have been identified: Noise with no specific pattern and oscillating baselines (see Figs. 6.1(c) and 6.1(d)). Most of these PMTs are already masked by the PMT quality cuts (see Sec. 3.4.2), but some remain outside the cut region.

Other

The SD acceptance task identified further malfunctions related to only small afterpulses or to problems with the decay time (very long time scales in the signal trace).

6.2 Technical Study: Direct Light Correction

The surface detectors are designed to diffuse the Cherenkov light of incoming particles on the Tyvek® surface, that it arrives at the 3 PMTs in equal amounts. This is usually the case for almost vertical showers. Under certain geometrical conditions, the light can hit a PMT after a few reflections or even without being reflected. Direct light causes a geometry-dependent asymmetry of the PMT signal balance, where a signal excess in one PMT is measured earlier

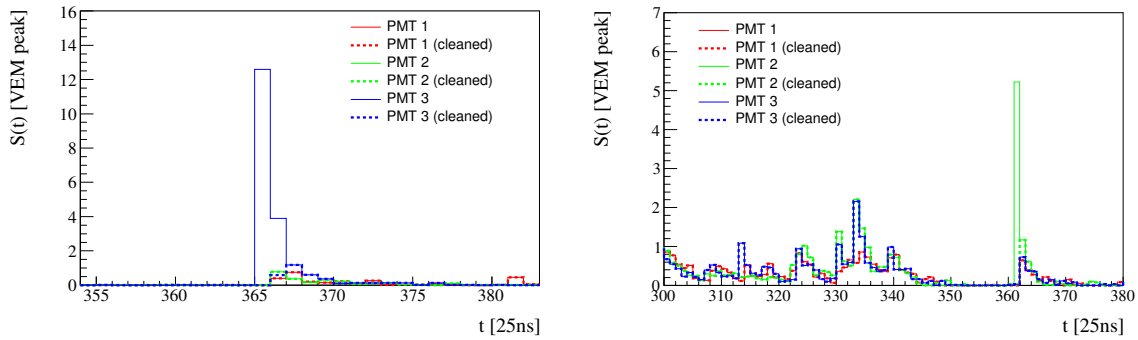

Figure 6.2: Correction of a large signal in a single PMT. The signal trace before the DLE correction is indicated as thin lines, the DLE-corrected signal is indicated as bold lines. Left: Example event from Data, right: Example event from MC photon

than the well-diffused light. A significant signal bias can be found in particular above 47° (which is 90° minus the Cherenkov angle in water). In addition, direct light as well as direct hits of the PMTs by single particles can cause signal excesses in single (or very few) time bins of only one PMT. Depending on the strength and the delay of the excess to the start time, these effects can lead to a significant underestimation of the risetime and thus contribute to an artificial background for the photon search.
Direct light effects (DLE) and a correction algorithm have already been studied in the past. Direct light is said to be the dominant reason for the signal asymmetry between the PMTs of a station [242]. The signal balance, which is the signal of one PMT compared to the average signal all PMTs of a station, shows a zenith-dependent azimuthal asymmetry. Shifting the PMTs according to their relative positions $\phi_{0,i}$, the asymmetry has been parametrized in [243] and [244]. A correction algorithm has already been developed in 2007 by *Wileman et al.* [245] and implemented in $\overline{\text{Off}}\underline{\text{line}}$ (module `DLECorrectionGG`). The idea is to search and correct for the effects of average direct light as well as single spikes by comparing the PMT traces of a station. The old method is being revisited and improved. The particular aim in this thesis is to correct huge excesses in a way that it can be applied to photons and hadronic primaries without introducing strong biases.
In the following we use SD data of the year 2008, reconstructed with $\overline{\text{Off}}\underline{\text{line}}$ v2r9p3 (modified SdCalibrator, as discussed in Sec. 3.4.2). This reconstruction includes PMT quality cuts based on monitoring information. Events are selected with T4 trigger, a minimum energy above 3 EeV, a reconstructed axis, at least tree stations, and within a zenith range as specified in this section ($\theta < 60°$ for the individual correction). Bad periods and lightning events are excluded. Stations are required to have a minimum signal of 3 VEM (10 VEM for setting up the individual correction). The required number of good PMTs and cuts on the PMT or station saturation are given whenever needed. To assure that PMTs work normally, we reject noisy PMTs. For the parametrization of the signal asymmetry and for the average DLE correction we also reject stations with known PMT miscablings or rotations [246]. An example of the correction of a large signal in only one PMT is shown in Fig. 6.2.

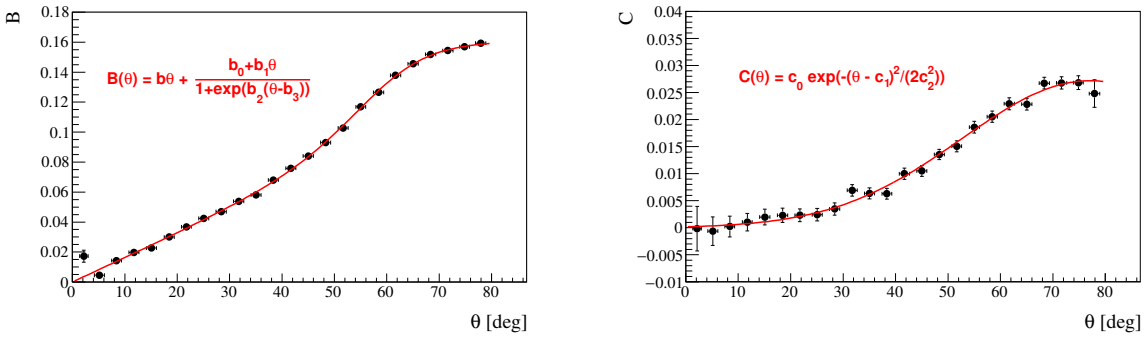

(a) Linear term, B (χ^2/NDF = 15.8/19)

(b) Quadratic term, C (χ^2/NDF = 11.1/21)

Figure 6.3: Parametrization of the zenith angle dependence of the asymmetry parameters B, C of the signal balance $S_i/\bar{S}$. The fit is applied on data of the year 2008, with stations with 3 non-saturated good PMTs. The linear term (B) is fit first and kept fixed in a second fit for the quadratic term (C).

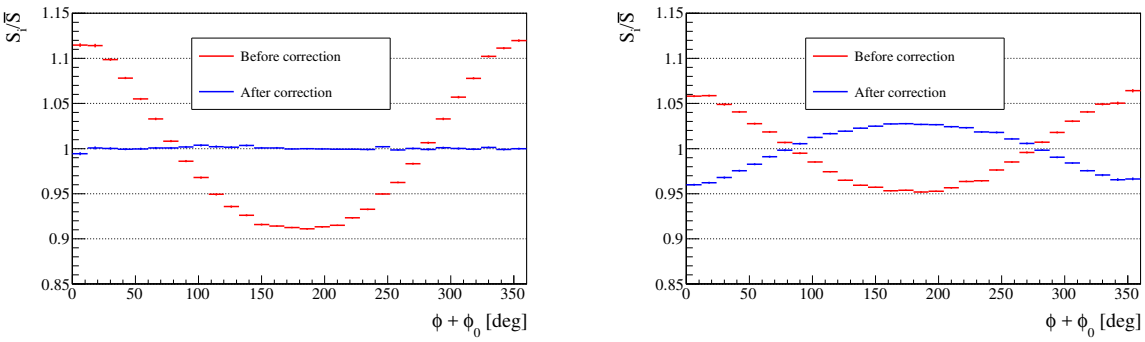

(a) Azimuthal asymmetry of the signal balance before (red) and after correction (blue), applied on data of the year 2008.

(b) Azimuthal asymmetry of the signal balance before (red) and after correction (blue), applied on simulated photons.

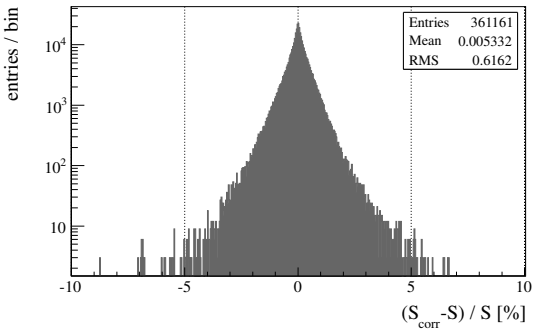

(c) Relative difference of the signal before and after correction (labeled as *corr*), applied on data of the year 2008. A log-scale has been chosen to visualize differences.

Figure 6.4: Application of the average asymmetry correction (non-saturated stations with 3 good PMTs).

6.2.1 Average correction

The signal balance, $S_i/\bar{S}$, is the fraction of the signal measured in one PMT compared to the average signal in all PMTs. A value of 1 is expected if all light is well diffused. DLE cause an asymmetry of the signal balance in the azimuth angle ϕ_i. The asymmetry increases for inclined showers. The azimuthal dependence can be parametrized by the sum of two cosine terms,

$$f_i = S_i/\bar{S} - 1 = b(\theta) \cdot \cos(\phi + \phi_{0,i}) + c(\theta) \cdot (2\cos^2(\phi + \phi_{0,i}) - 1), \tag{6.1}$$

which is equivalent to the function used in [244]. The azimuthal positions $\phi_{0,i}$ of PMT i are:

$$\begin{aligned} \phi_{0,1} &= 30^\circ \\ \phi_{0,2} &= 270^\circ \\ \phi_{0,3} &= 150^\circ \end{aligned}$$

Accounting for the $\phi_{0,i}$, a combined sample can be obtained. The fit of the signal balance as function of the azimuth angle, for events with $\theta = 0 - 80^\circ$ and stations with 3 non-saturated PMTs, is shown in Fig. E.11. The fit of the zenith angle dependence of $B(\theta)$ and $C(\theta)$ is shown in Figs. 6.3(a) and 6.3(b)) with

$$B(\theta) = b \cdot \theta + \frac{b_0 + b_1 \cdot \theta}{1 + e^{b_2 \cdot (\theta - b_3)}}, \tag{6.2}$$

$$C(\theta) = c_0 \cdot \exp\left(-\frac{(\theta - c_1)^2}{2c_2^2}\right). \tag{6.3}$$

A first fit treats only the linear dependence which is kept fixed in a second fit of the quadratic term. The result is

$$\begin{aligned} b &= 0.00163 \pm 0.00004 \\ b_0 &= 0.159 \pm 0.002 \\ b_1 &= -0.00161 \pm 0.00003 \\ b_2 &= -0.15 \pm 0.01 \\ b_3 &= 58.4 \pm 0.8 \\ c_0 &= 0.027 \pm 0.001 \\ c_1 &= 77 \pm 2 \\ c_2 &= 24 \pm 1. \end{aligned} \tag{6.4}$$

This parametrization is done with the total PMT signals S_i integrated over the trace. From Eq. 6.1 it follows that the corrected signal, S_i^{corr}, is:

$$S_i^{\mathrm{corr}} = \frac{S_i}{1 + f_i}. \tag{6.5}$$

Although this parametrization is done with the total PMT signals S_i integrated over the trace, this parametrization can be used for an average correction of the signal asymmetry in each time

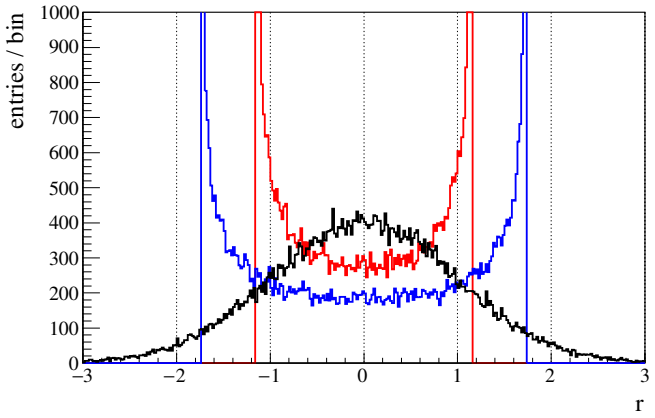

Figure 6.5: Definition of an uncertainty-weighted residual, based on a toy Monte-Carlo. The red distribution shows $r = (S_2 - (S_1 + S_2 + S_3)/3)/\sigma_S$, the blue distribution shows $r = (S_2 - (S_1 + S_3)/2)/\sigma_S$ and the black distribution shows the new definition, $r = (S_2 - (S_1 + S_3)/2)/\Delta$. The standard deviation σ_S is estimated from three signal measurements S_i. Δ is the uncertainty of the deviation of S_2 from the mean value $(S_1 + S_3)/2$.

bin as

$$\begin{aligned} S_i^{\text{corr}} &= \int S_i^{\text{corr}}(t)\mathrm{d}t \\ &= \frac{1}{1+f_i}\int S_i(t)\mathrm{d}t \\ &= \frac{1}{1+f_i}\,S_i. \end{aligned} \tag{6.6}$$

The successful correction of the asymmetry for a sample of non-saturated stations from data is shown in Fig. 6.4(c). The effect on the signal is illustrated in Fig. 6.4(a) and shown to be below ±10%, with a mean around zero and a spread of less than 1%. In addition, the asymmetry for high-gain-saturated stations has been checked (see Figs. 9.9(a) and 9.9(b) in the appendix). The correction obtained from non-saturated stations is applicable here as well. Note that it needs at least an estimate of the geometry. In the photon[1] search, the average correction of direct light is not being applied. As shown in Fig. 6.4(b), the amount of direct light is expected to be lower for photon-induced showers because of the lower muon component and thus the correction obtained from data would over-correct the signal of photons. In addition, the correction does **not** affect the risetime. Thus we decide to **not** apply it for the photon search.

6.2.2 Individual correction

The bin-by-bin identification of single instances of direct light effects (DLE) is the actual aim of this section. In the DLECorrectionGG module in Offline the identification is based on the

[1] We found that the position of the minimum signal balance in the SD simulation is rotated by 60° with respect to the situation found in data - and fixed it in Offline revision 25307. For older revisions this has to be accounted for when applying the average DLE correction on simulations.

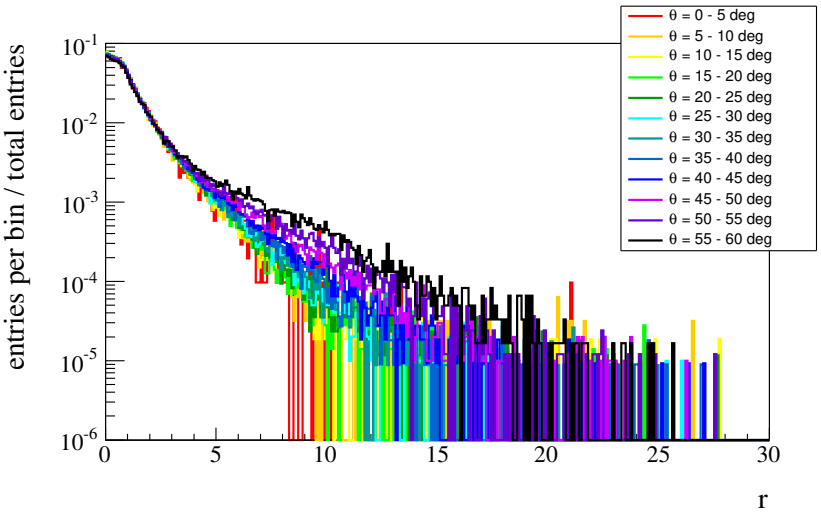

(a) Distribution of the residual, r, positive side

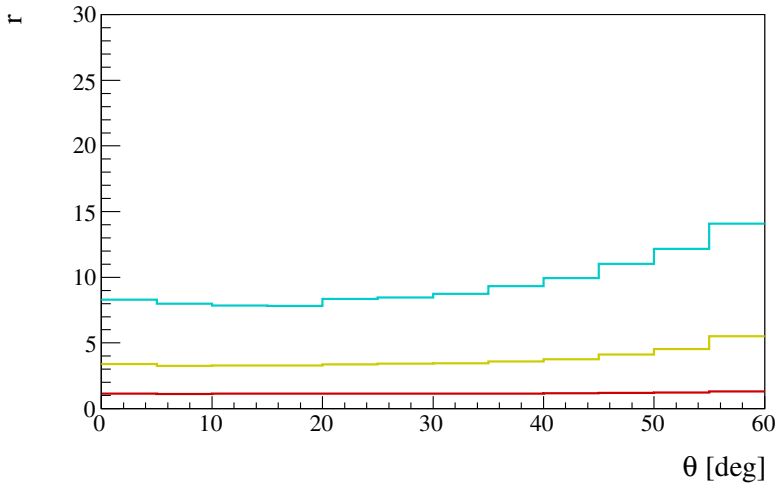

(b) Zenith angle dependence of the confidence levels according to 68% (red), 95% (yellow) and 99.7% (cyan) probability.

Figure 6.6: Fixing the threshold value of r to identify signal outliers in one PMT, for stations with 3 good and non-saturated PMTs.

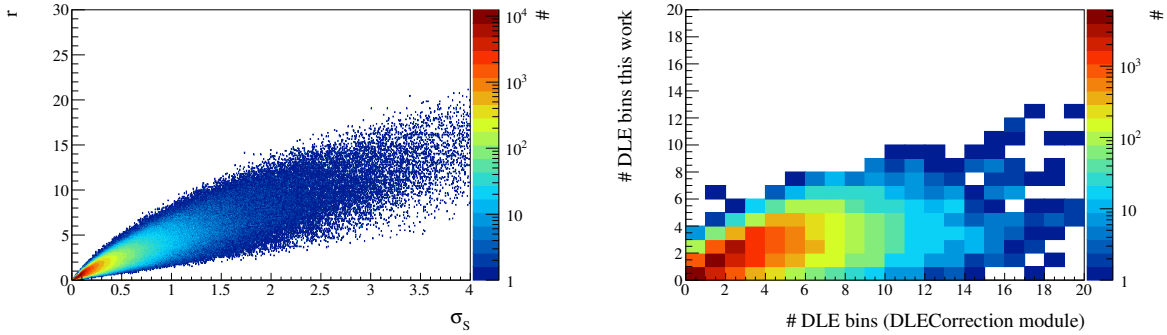

(a) Filter values: Residual, r, versus the standard deviation of the signal, $\sigma(t)$

(b) Number of identified bins per station

Figure 6.7: Comparison of both algorithms, DLECorrectionGG and the update in this work.

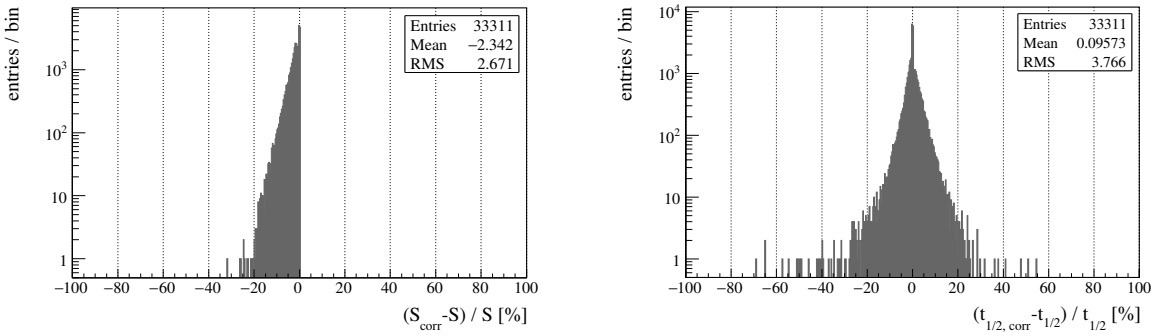

(a) Station signal, S

(b) Station risetime, $t_{1/2}$

Figure 6.8: Effect of the correction of single DLE instances on station signal and risetime, for stations with 3 good and non-saturated PMTs.

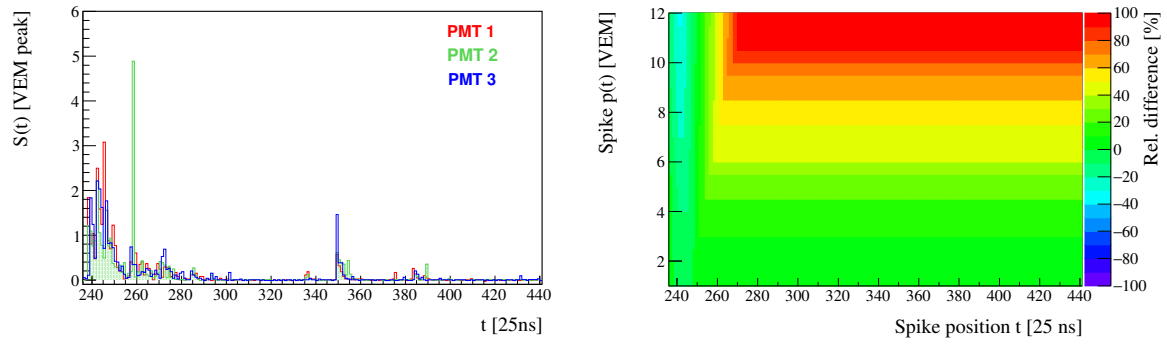

Figure 6.9: Mock study of the station risetime, $t_{1/2}$, for event 8944584, station 457, PMT 2. Left: Inserting a fake signal in PMT 2. Right: Effect on the station risetime.

standard deviation of the signal in a time bin,

$$\sigma_S(t) = \sqrt{\frac{1}{N}\sum_{i=1}^{N}(S_i(t) - \bar{S}(t))}, \tag{6.7}$$

with $N \leq 3$ the number of PMTs per station and $S_i(t)$ the signal. The identification is based on time bins where $\sigma_S(t) \geq 1$ VEM. If a time bin is identified, the maximum signal is replaced by the mean of the remaining PMTs. The correction is done for stations with ≥ 2 non-saturated PMTs. In this case the threshold value is an absolute signal that does not account for uncertainties of the PMT signal. The PMT signal in a time bin is defined as

$$S_i(t) = \frac{N_{\mathrm{FADC}} - B}{p}, \tag{6.8}$$

with N_{FADC} the FADC counts, B the baseline counts, p the peak value. The signal uncertainty cannot be estimated easily but depends on a number of quantities. We approximate the uncertainty by statistical fluctuations,

$$\Delta_i(t) = \sqrt{\left(\frac{\sqrt{N_{\mathrm{FADC}}}}{p}\right)^2 + \left(\frac{\Delta B}{p}\right)^2 + \left(\frac{S_i(t)}{p}\cdot\Delta p\right)^2}, \tag{6.9}$$

where ΔB, Δp the corresponding uncertainties. The new algoritm checks for the compatibility of the measured signals within statistical fluctuations by defining an (uncertainty-weighted) residual

$$r_{\mathrm{i}}(t) = \frac{S_{\mathrm{i}}(t) - \bar{S}_{\mathrm{red}}(t)}{\Delta(t)}, \tag{6.10}$$

with

$$\begin{aligned} \bar{S}_{\mathrm{red}}(t) &= \sqrt{\frac{\sum_{i=1}^{N-1} S_i(t)}{N-1}}, \\ \Delta(t) &= \sqrt{\Delta_{\mathrm{i}}^2 + \sum_{i=1}^{N-1}\left(\frac{\Delta_i}{N-1}\right)^2} \end{aligned} \tag{6.11}$$

the average of the remaining PMTs and the uncertainty of the signal difference.
The relation between r and the standard deviation of the measured signals, σ_S, can be understood as follows: Let us assume a station with measured signals S_1, S_2 and S_3 for the individual PMTs, where S_2 is the highest signal. We find that

$$\begin{aligned} \frac{S_2 - \frac{S_1+S_2+S_3}{3}}{\sigma_S} &= \frac{2}{3}\frac{S_2 - \frac{S_1+S_3}{2}}{\sigma_S} \\ &= \sqrt{2}\cdot\frac{2}{3}\frac{S_2 - \frac{S_1+S_3}{2}}{\sqrt{\left(S_2 - \frac{S_1+S_3}{2}\right)^2 + \frac{3}{4}\cdot(S_2 - S_3)^2}} \\ \Rightarrow \left|\frac{S_2 - \frac{S_1+S_2+S_3}{3}}{\sigma_S}\right| &\leq \sqrt{4/3}. \end{aligned} \tag{6.12}$$

is constrained within an interval $[-\sqrt{4/3}, \sqrt{4/3}]$. Thus it follows that r and σ_S are correlated by

$$r = \frac{S_2 - \frac{S_1+S_3}{2}}{\sigma_S} \frac{\sigma_S}{\Delta} \leq \sqrt{3} \frac{\sigma_S}{\Delta}. \tag{6.13}$$

The constraints derived in Eqs. 6.12 and 6.13 have been verified in Fig. 6.5, based on a toy Monte-Carlo. Two Gaussian distributions have been generated with a sample size of 500000: One with $\bar{S} = 20$ and $\sigma_S = 1$ and another one centered around σ_S with variance of $\sigma_S^4/2$. Out of these distributions we randomly draw three values to calculate the following definitions of an uncertainty-weighted residual 50000 times: (i) With mean value and standard deviation: $(S_2 - (S_1+S_2+S_3)/3)/\sigma_S$, (ii) with reduced mean value and standard deviation: $(S_2-(S_1+S_3)/2)/\sigma_S$, (iii) with reduced mean value and an estimate of the single uncertainties: $(S_2-(S_1+S_3)/2)/\Delta$. For the definition of a statistical outlier within a sample of three measured values it is obviously neccesary to use an estimate of the single uncertainties instead of the standard deviation.
Note that the following analysis is based on zenith angles below 60°. The maximum signal $S_{\max}$ is replaced if at least one of the PMTs has a signal higher than 0.2 VEM and if it is not compatible with the other PMT(s) within the statistical fluctuations. In order to define a threshold value for r, two dependences should be accounted for: First, it has been checked that there is no strong signal dependence. The probability of observing single DLE spikes is expected to increase with zenith angle. Figure 6.6(a) shows the positive side of the distribution of r for different zenith bins. While the shape in the range $r \in [0, 3]$ does not depend significantly on θ, the tail extends to large θ. Thus, we decide to set the threshold to a value of $r = 6$, which is centered between the 95% (value $r = 4$) and 99.7% level (value $r = 8$) for almost vertical showers, as shown in Fig. 6.6(b). Note that in addition the PMTs can be hit directly by particles, which can happen in particular for vertical showers. A comparison of σ_S and r is shown in Fig. 6.7(a), for stations with 3 non-saturated PMTs. As pointed out before, a cut on either of these variables is correlated, but not equivalent.
A comparison of the number of identified bins per station for both algorithms is illustrated in Fig. 6.7(b), showing the reduction of the number of corrected bins. Our correction algorithm acts mostly as a veto to the old definition. It is interesting to check if the algorithm also works for stations with 2 PMTs or for PMTs with saturated high-gain. There, the threshold value at lowest zenith angles is slightly higher for 2 non-saturated PMTs (see Fig. 9.8(a) in the appendix) but seems applicable. For high-gain-saturated PMTs we have to modify the definition of the fluctuations to account for the missing amplification of the signal:

$$S_i(t) = \frac{(N_{\text{FADC}} - B) \cdot D/A}{p},$$

similar to Eq. 6.8, but with D/A the dynode-anode-ratio. The statistical fluctuations are then

$$\Delta_i(t) = \sqrt{\left(\frac{\sqrt{N_{\text{FADC}} \cdot D/A}}{p}\right)^2 + \left(\frac{\Delta B \cdot \sqrt{D/A}}{p}\right)^2 + \left(\frac{S_i(t)}{p} \cdot \Delta p\right)^2}. \tag{6.14}$$

The 99.7% level of r is higher than for non-saturated stations, the other levels are compatible (see Fig. 9.8(b) in the appendix). The algorithm is applied in this analysis as well. Examples of occurrences of large signals in only one PMT, for data and MC photon, can be found in the

appendix in Figs. 9.12(a)-9.12(b) and Figs. 9.13(a) to 9.13(f).
An important study is the influence of the correction on the station signal and risetime. Both algorithms reduce the signal by definition. The effect on the risetime depends on the position and size of the signal spike. The effect on signal and risetime is shown in Figs. 6.8(a) and 6.8(b). To get a further understanding of the effect on the risetime, we have performed a Mock sample study in which we inserts an artificial signal into a trace (here PMT 2) and modify its position and size. The example station we use is station 457 of event 8944584 (with a signal 8.5 VEM before adding the artificial spike). It shows that for stations with low signals the risetime, defined as $t_{1/2} = T_{50} - T_{10}$, can be significantly overestimated for large signal spikes late in the time trace (see Fig. 6.9). For spikes that appear in the first time bins a modest underestimation can be found instead. This effect is composed of the seperate effects on T_{10} and T_{50}. Note that here we only look at events in single time bins. In case of light appearing in a few time bins, as it has been found in data as well, the effect is even larger. The fraction of corrected bins in the stations analyzed is approximately 3%, amounting to a fraction of 30% of all stations with at least one corrected bin.
We have also performed this analysis on simulated photons[2] (see Fig. 9.8(c) in the appendix). As expected from the low muon fraction in photon-induced airshowers, the zenith dependence of the 99.7% level is less strong than found in observed data, while the value at almost vertical showers is compatible. Thus the correction of single time bins based on a fixed value $r \geq 6$ is not expected to introduce a bias when applied on simulated photons, other than the average direct light correction. The quality of the risetime has been improved by this work.

6.2.3 Exclusion of PMTs

The DLE identification is based on the comparison of the PMTs of a station. This requires that they are setup and working normally. In order to avoid problems of the algorithm with miscabled/rotated PMTs or very exceptional traces (for example oscillations), a very phenomenological filter has been set up. The rejection of these stations or PMTs is set as default in the xml. Note that afterpulse PMTs should also be rejected before this module.

- **Negative signal peaks:** The pathology is shown in Fig. 6.1(e). For signals with $S_i(t) < -3$ VEM in at least one time bin, the whole station is excluded from the DLE correction. This phenomenon is found in a fraction of $< 0.01\%$ of all stations in the selected dataset of 2008 for the filter described here.

- **Oscillations:** Out of the PMTs that pass the quality cuts (based on the PMT monitoring bits available since CDAS v1r0), some PMTs show oscillations around the baseline in the VEM trace, as discussed in the last section. The frequency can differ between the gains, up to 3 time bins per half period have been found in data. This algorithm searches for an oscillating pattern in the full signal trace, within a moving window of 15 time bins. The pattern starts with $S_i(t) < S_{\mathrm{thr},1}$ and the window has to contain:

  - $N_{\mathrm{neg}} \geq 3$ bins with $S_i(t) < -S_{\mathrm{thr},1}$

[2] Photon showers have been reused here and preshowered photons have been included as well as this does not strongly affect the study.

  - $N_{\text{pos}} \geq 3$ bins with $S_i(t) > S_{\text{thr},1}$
  - the sum of the signal above the upper threshold is larger than twice the total sum of the signal

  As the baseline fluctuations differ between the gains, the thresholds for high- and low-gain are

  - High-gain (HG): $S_{\text{thr},1} = 0.06$ VEM
  - Low-gain (LG): $S_{\text{thr},1} = 1.4$ VEM

  This phenomenon is found in a fraction of $\sim 0.03\%$ of all stations in the selected dataset of 2008 for the filter described above.

- **PMT miscablings and rotations:** The signal balance can also be used to detect miscabled PMTs and rotated stations by studying the asymmetry in single stations [246]. Miscabled PMTs have been found in stations 263, 831, 1134, 1318, 1667, 1721, 1724, 1782. Station 1818 seems to be rotated. These stations are excluded from the average DLE correction that is based on the asymmetry parametrization.

Setup correction

The DLE correction in this work is applied to non- and high-gain-saturated stations with signal of at least 3 VEM, with 2 or 3 good PMTs after the exclusion of oscillating, miscabled and rotated PMTs and PMTs with large negative signals. It is applied to all time bins. Low-gain-saturated stations, which are as well excluded for risetime studies, are not corrected. The average correction is not applied for the photon search for the reasons explained in the previous section. The threshold value of the individual DLE correction is a value of $r = 6$. Note that the trace is currently corrected after the reconstruction and only used for a re-calculation of the station signal and risetime. Before using it in the reconstruction the effect on the start time should be checked an possibly the first bin might have to be skipped for the correction. For the current application the effect is only small. The algorithm has been implemented in $\overline{\text{Off}}\underline{\text{line}}$ in the DLECorrectionWG module. Here we use an implementation based on the ADST files.

6.3 Station Risetime

The arrival time distribution (time trace) for a MC proton and photon shower, with a reconstructed hadronic energy of ~ 12 EeV and $\theta < 10°$, is shown in Fig. 6.10(a) ($r < 1000$ m) and Fig. 6.10(b) ($r > 1000$ m). It is clearly visible that the trace becomes broader with increasing core distance, for vertical showers (not shown) and for only a small muon component. Muons arrive early in the trace and thus the risetime for muon-rich showers is smaller than for mainly electromagnetic particles. In addition, a less deep shower maximum makes the time trace narrower for hadronic than for photon showers. The amount of signal in the early part of the trace translates to the signal **risetime**, $t_{1/2} = T_{50} - T_{10}$, which has already been discussed in 1973 by *Lapikens et al.* [247] for the Haverah Park experiment. It is defined as the time that the cumulative signal of the arrival time distribution (time trace) takes to increase from 10% to 50% (T_{50} and T_{10}). A sketch is shown in Fig. 6.10(c). The time T_x, corresponding to a certain signal quantile x, is interpolated to the center between the last bin below and the first bin above the

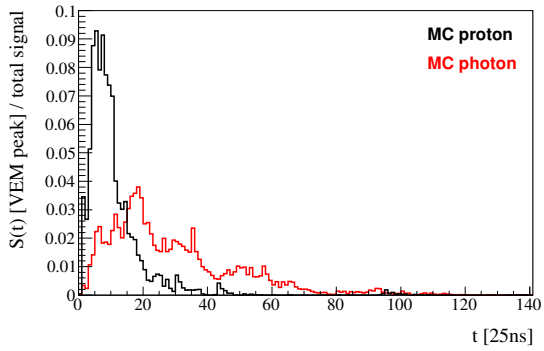

(a) Time trace, $r < 1000$ m (MC photon in red, proton in black)

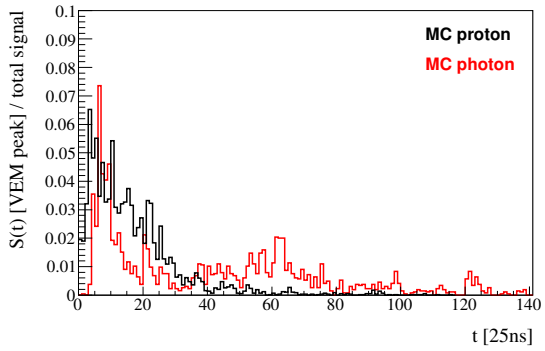

(b) Time trace, $r > 1000$ m (MC photon in red, proton in black)

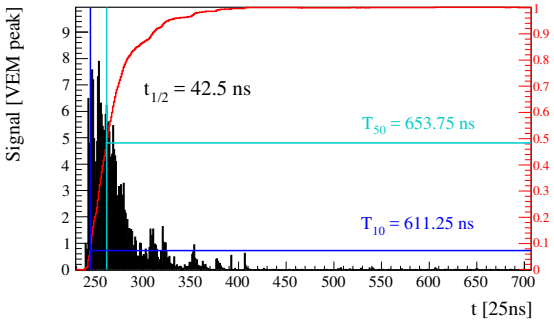

(c) The definition of the signal risetime for an arbitrary SD station.

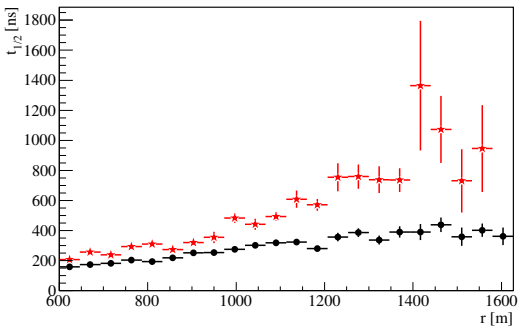

(d) Signal risetime for the data burn sample (black) and MC photon showers (red), for stations with $S_{\mathrm{obs}} > 6$ VEM, 600 m $< r <$ 2000 m and no saturation or high-gain saturation. Selected are showers with energies $19.0 < \log_{10}(E_{\gamma,\mathrm{rec}}/\ \mathrm{eV}) < 19.3$ and zenith angles $30° < \theta < 45°$.

Figure 6.10: The signal risetime $t_{1/2}$ (c,d), together with two example signal traces of a station from MC (a,b).

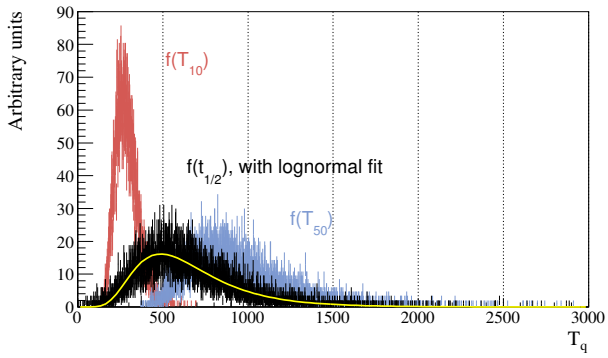

Figure 6.11: The distribution of the quantiles T_{10}, T_{50} and the risetime $t_{1/2} = T_{50} - T_{10}$. The risetime distribution has been fitted with a two-parameter lognormal function.

signal quantile. The station risetime is the average of the risetime of each single PMT. We do not work with an average time trace per station to avoid problems when mixing the high-gain (HG) and the low-gain (LG) for high-gain saturated stations with only a fraction of the PMTs saturated.
As pointed out before, photon-induced showers produce a smaller risetime of the SD signal than hadron-induced showers. This difference increases with distance to the shower core where most muons arrive (cr. Fig. 6.10(d)). The separation is expected to improve for larger inclinations where the muon content increases. Note that this plot is only for viszalization - there are differences[3] in the reconstructed MC proton showers and the risetime has not been corrected for assymetries (see Sec. 6.3).
The main focus in this study is to establish the risetime on a zenith angle range of 0° to 60°, minimizing a possible bias due to the detector sampling. The current sampling of 25 ns introduces a resolution of ~ 40 ns for the risetime [248]. Other studies reduced the maximum zenith angle to 45° to account for the sampling. Here we use the full zenith angle range and check the according possible distance and signal range that can be used for parametrizations of the average risetime and its uncertainty.

6.3.1 Shape of the signal risetime distribution

An analytical model to describe the time dependence of the signal observed in an SD station has been studied in [249]. The arrival time distribution is composed of four lognormal-distributed components. The main contribution comes from muons and the pure electromagnetic channel. In a series of approximations we will motivate that the risetime is not distributed Gaussian but asymmetrically. First we assume that the arrival-time distribution of the sum of the four components can be approximated by a three-parameter lognormal:

$$\frac{dP}{dt}(t) = \frac{1}{\sqrt{2\pi} \cdot s \cdot (t - t_1)} \cdot \exp^{-\frac{(\ln(t-t_1)-m)^2}{2s^2}} \tag{6.15}$$

[3]The version of offline differs and the modifications to the SdCalibrator have not been applied here (see Sec. 5.3).

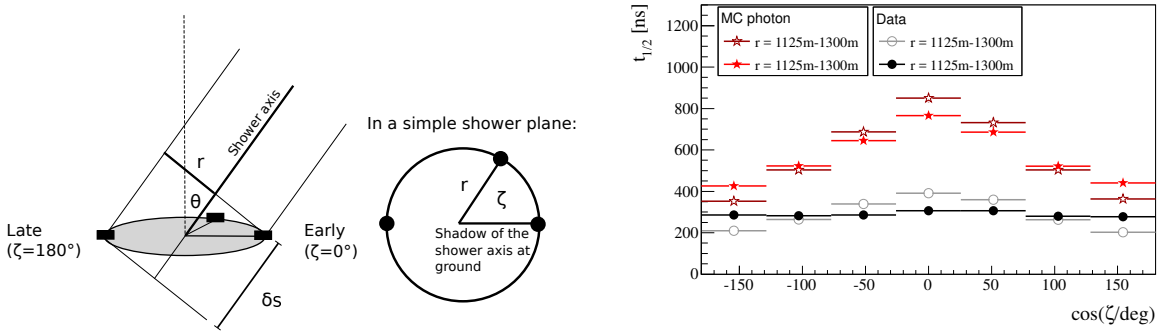

(a) Risetime asymmetry: Early and late region (δs indicates the difference in the shower age)

(b) Application of the asymmetry correction for data and MC photon. Shown is the asymmetry before (hollow markers) and after the correction (full markers). For photon showers, the asymmetry is only partly reduced.

Figure 6.12: Risetime asymmetry correction

According to [249], the quantiles are distributed as

$$\begin{aligned} f(t_q) &= A \cdot (1 - F(t_q))^{N-q\cdot(N+1)} \cdot F(t_q)^{q\cdot(N+1)} \cdot \frac{dF(t_q)}{dt}(t_q) \\ &= A \cdot (1 - F(t_q))^{N-q\cdot(N+1)} \cdot F(t_q)^{q\cdot(N+1)} \cdot \frac{dP}{dt}(t_q), \end{aligned}$$

where $F(t_q)$ denotes the c.d.f. (cumulative distribution function) of the arrival time distribution, which is a three-parameter lognormal distribution here. In a simple toy Monte-Carlo we set some fixed example values within the ranges suggested in [249]: $m = 6$, $s = 0.7$, $t_1 = 120 \cdot (800\text{ m}/1000\text{ m})^2$ and $N = 9$. The distributions for T_{10} and T_{50} are then:

$$\begin{aligned} f(T_{10}) &= A \cdot (1 - F(T_{10}))^{8} \cdot F(t_q) \cdot \frac{dP}{dt}(T_{10}) \\ f(T_{50}) &= A \cdot (1 - F(T_{50}))^{4} \cdot F(t_q)^{5} \cdot \frac{dP}{dt}(T_{50}) \end{aligned}$$

The distributions of T_{10}, T_{50} and $t_{1/2} = T_{50} - T_{10}$ is shown in Fig. 6.11. They are clearly asymmetric and the risetime (obtained from the arrival time distribution, not the signal trace of the detector,) can be described by a two-parameter lognormal fit. In order to obtain the time dependence of the SD signal trace, the arrival-time distribution has to be folded with the detector response and it was suggested in [250] that the first part of the observed signal trace can be fitted with a Moyal function. But here we only wanted to give a qualitative statement about the shape of the risetime distribution.

6.3.2 Asymmetry correction

The risetime shows a geometrical asymmetry. Stations with different azimuth angles ζ around the shower core, defined with respect to the azimuth direction of the shower, correspond to different shower ages. The difference increases with the shower inclination. The region around $\zeta = 0°$ is referred to as the *early* and $\zeta = 180°$ as the *late* region (see Fig. 6.12(a)). The

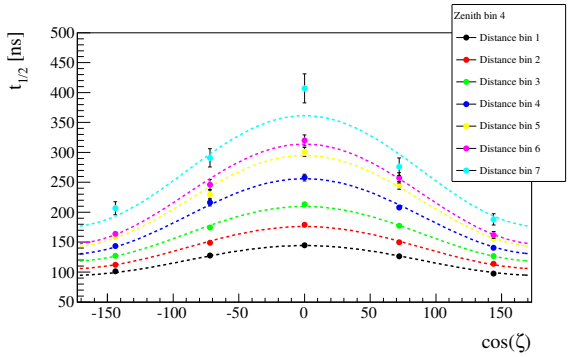

(a) Dependence of $t_{1/2}$ on the azimuth angle ζ, for $\sec(\theta) = 1.50 - 1.67$ ($S_{\text{obs}} > 15$ VEM).

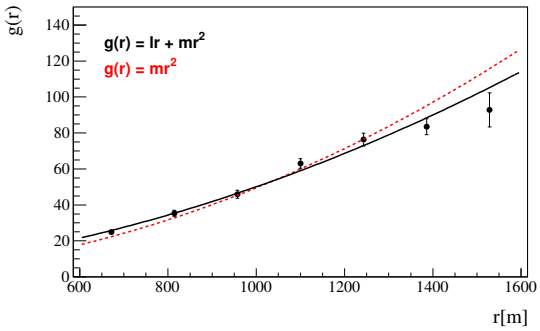

(b) Dependence of $t_{1/2}$ on the core distance r, for $\sec(\theta) = 1.50 - 1.67$ ($S_{\text{obs}} > 15$ VEM).

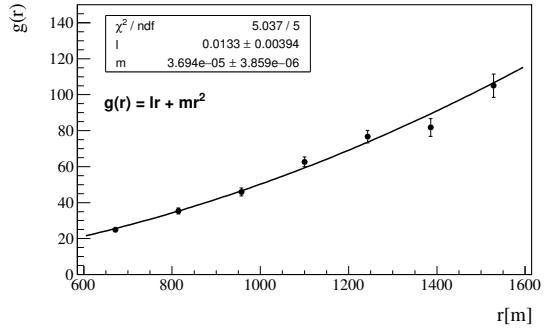

(c) Dependence of g on the core distance r, for $\sec(\theta) = 1.50 - 1.67$ ($S_{\text{exp}} > 10$ VEM).

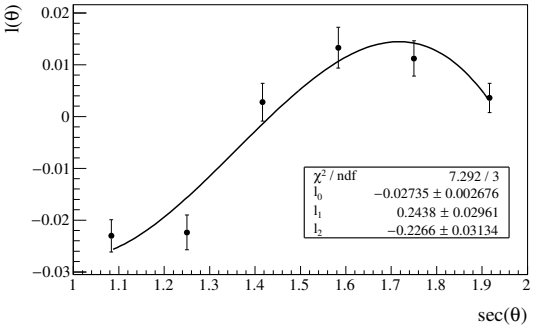

(d) Dependence of l on the zenith angle θ ($S_{\text{exp}} > 10$ VEM).

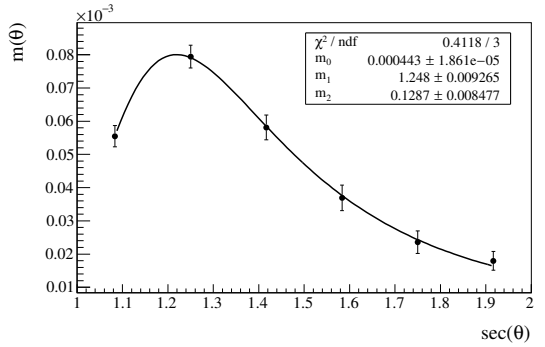

(e) Dependence of m on the zenith angle θ ($S_{\text{exp}} > 10$ VEM).

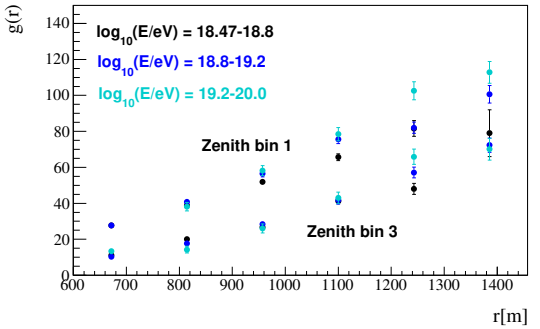

(f) Energy dependence of the risetime asymmetry ($S_{\text{exp}} > 10$ VEM)

Figure 6.13: Parametrization of the risetime asymmetry (observed data).

difference in the shower age depends on $\cos(\zeta)$ and so does the asymmetry. The magnitude of the asymmetry contains also composition information which can be used to set up a mass composition study for a sample of events [251]. For an event by event study of the risetime the **asymmetry** must be corrected for. In [248] such a correction has already been introduced, applying a deconvolution of the time traces with the single particle response. According to [252] (p.66) we do not apply a deconvolution as the effect above 600 m is moderate and the risk of instabilities in the deconvolution algorithms is high. Thus the resolution of the risetime increases from 10 ns to 40 ns [248]. Stations closer than 600 m will not be used here. We start from the risetime study in [252], introducing a few modifications and updating the parametrizations for our dataset (measured data from 2004 to 2012, reconstructed with $\overline{\text{Off}}\underline{\text{line}}$ v2r9p3 as described in Chap. 5, and with signal and risetime corrected for direct light). The event selection applied here is a rejection of bad periods, of the Comm's crisis[4] and of lightning events, requiring at least a reconstructed LDF, a reconstructed hadronic energy of 10-30 EeV, a T4 and 6T5 trigger and $\theta < 60°$. On the station level we start with non- and high-gain-saturated stations, rejecting stations with bad PMTs. Stations are required to have an observed signal $S_{\text{obs}} > 15$ VEM a risetime above 40 ns and lie within a range of 600 m and 1600 m from the shower core. The observed risetime, $t_{1/2}$, can be split in an azimuth-dependent term and an asymmetry-corrected risetime, $t_{1/2,\text{corr}}$:

$$t_{1/2} = t_{1/2,\text{corr}} + g(\theta, r) \cdot \cos(\zeta), \tag{6.16}$$

where $t_{1/2,\text{corr}}$ is the risetime corrected to the value that would be measured at $\zeta = 90°$. A fit of the risetime with this functional form is shown in Fig. 6.13(a), for 7 bins in the core distance between 600 m and 1600 m, and for $1.50 < \sec(\theta) < 1.67$. The asymmetry is reasonably well-described by the parametrization (for large θ the quality gets a bit worse but still sufficient for this analysis). The early region shows larger risetimes due to a larger number of EM particles compared to the late region, besides purely geometrical reasons. This fit has been done in 6 bins of θ covering the range $1.0 < \sec(\theta) < 2.0$. In [248, 252] it was suggested to describe the distance dependence of $g(\theta, r)$ as $g(\theta, r) = m(\theta) \cdot r^2$. The fit in the bin $\sec(\theta) = 1.50 - 1.67$ is shown in Fig. 6.13(b) (dashed line), giving a fit quality of $\chi^2/\text{NDF} = 3.2$. We suggest to add a linear term:

$$g(r) = l \cdot r + m \cdot r^2, \tag{6.17}$$

with $g(0) = 0$. A fit with the new functional form is shown in the same plot as full line. The fit quality improves to $\chi^2/\text{NDF} = 1.3$. The increase of the asymmetry with core distance is mainly due to geometrical reasons. The settings can be optimized to maximize the selection efficiency while assuring a sufficient quality. We suggest further modifications:

- Cut on the expected instead of the observed signal to avoid trigger biases, $S_{\text{exp}} > 15$ VEM and $S_{\text{obs}} > 3$ VEM.
- Set the required minimum (expected) signal from 15 VEM down to 10 VEM, which still corresponds to a trigger probability of almost 100% [187].
- Cut on a distance range of $600 - 1600$ m. Note that a distance of 1600 m in the energy range $10 - 30$ EeV corresponds to an average epected signal of 10 VEM, as shown in Fig. 9.18(b) in the appendix.

[4] Exclude the whole Comm's crisis period from 16.04.2009 to 15.11.2009 as a very restrictive solution. For the photon search a recoverable part of this period is being included.

The fits for the modified selection is shown in Figs. 6.13(c) to 6.13(e), with the zenith dependence of l and m parametrized as:

$$l(\theta) = l_0 + l_1 \cdot (\sec(\theta) - 1)^2 + l_2 \cdot (\sec(\theta) - 1)^3, \tag{6.18}$$

$$m(\theta) = m_0 \cdot \frac{1}{2\pi i} \int_{c-i\infty}^{c+i\infty} \exp\left(\frac{\sec(\theta) - m_1}{m_2} \cdot s + s \cdot \log(s)\right) \mathrm{d}s. \tag{6.19}$$

The latter is a Landau distribution with constant m_0, the most probable value m_1, the scale parameter m_2 and an arbitrary constant c. The final set of parameters is:

$$\begin{aligned} l_0 &= -0.027 \pm 0.002 \\ l_1 &= 0.24 \pm 0.02 \\ l_2 &= -0.23 \pm 0.03 \\ m_0 &= (44 \pm 1) \cdot 10^{-5} \\ m_1 &= 1.248 \pm 0.009 \\ m_2 &= 0.129 \pm 0.008. \end{aligned}$$

The fits of the azimuth and distance dependence can be found in the appendix: Figs. 9.14(a) to 9.14(f) for the azimuth dependence and Figs. 9.15(a) to 9.15(f) for the distance dependence.
For a check of the robustness of mean value and standard deviation of the sample, each bin has been fitted with a Gaussian and a lognormal distribution to avoid trigger biases (in particular at large zenith angles). The lognormal distribution describes the data well, but as the difference in the results is only small we use the sample mean and standard deviation throughout the whole risetime analysis.
The energy dependence of the asymmetry has been studied, as shown in Fig. 6.13(f). An increase of the energy reflects mostly in gaining far away stations rather than a difference in the magnitude of the asymmetry. This justifies using the energy bin of $10 - 30$ EeV to represent the full range and to establish the parametrization over a wide distance range ($600 - 1600$ m). Note that for the parametrization the signal cut must be applied on the expected signal. Otherwise large distances are dominated by trigger biases, in particular for large zenith angles. The application of the asymmetry correction on data and MC photon is shown in Fig. 6.12(b). For photon showers an asymmetry remains after an application of the correction optimized on data. The procedure is to establish a description of data first, derive an event parameter and account for its expected energy and zenith dependence in case of primary photon later.
In order to optimize the selection efficiency and quality of the risetime we have checked which distance range can be used to minimize trigger biases in the risetime distribution. First, we have applied the asymmetry correction to reduce the neccessary dimensions to be accounted for. Then we have found a p.d.f. that describes the $t_{1/2}$ distributions of data in bins of energy, zenith angle and distance. The distributions can be described with a two-parameter lognormal shape:

$$f(x) = \frac{1}{\sqrt{2\pi} \cdot x \cdot s} \cdot \exp^{-\frac{(\ln(x) - m)^2}{2s^2}}. \tag{6.20}$$

In Fig. 6.14 the distribution of $t_{1/2,\mathrm{corr}}$ has been fitted with a Gaussian and a lognormal shape in bins of energy, distance and zenith angle. Shown is the normalized χ^2 as a measure of the fit quality. The lognormal shape describes data reasonably well. Under the assumption of a lognormal shape, the possible distance range within $\theta = 0^\circ - 60^\circ$ has been checked as shown

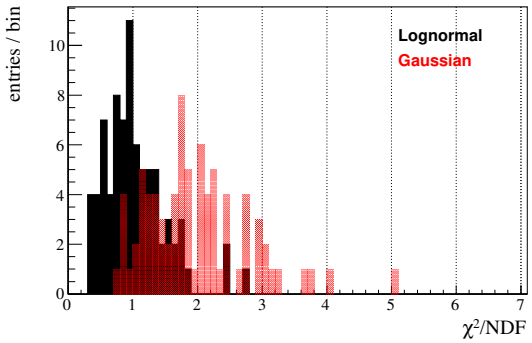

Figure 6.14: Shape of $t_{1/2,\mathrm{corr}}$ for non- and high-gain-saturated stations in data with $S > 10$ VEM. A fit with a lognormal and a Gaussian shape has been applied in each distance- and zenith angle bin. Shown is the fit quality χ^2/NDF.

in Figs. 6.15(b) and 6.15(a). The largest probability to find risetimes close to 40 ns is for large $\theta = 60°$ and at large distances. Within the given zenith range, distances between 600 m and 1600 m do not show strong biases. Previous studies were restricted to the range $0° - 45°$ [215, 252].

6.3.3 Benchmark

A key property to establish a photon-hadron separation is the dependence of the risetime on the core distance r. This can for example be done with an event-wise fit of the dependence or based on a **benchmark** that describes data. Note that from now on we work with the asymmetry-corrected risetime. Our benchmark is the average station risetime at a certain distance r, $t_{1/2}^{\mathrm{bench}}(r)$, for an event of energy E and zenith angle θ. This kind of benchmark was introduced in [248] and continued in [252]. We apply some modifications to optimize the benchmark for the SD photon search and derive an updated benchmark for our dataset. We focus on the energy bin of $10-20$ EeV, similar to [252] on $10-15$ EeV, selecting non- or high-gain-saturated stations with $S_{\mathrm{exp}} > 10$ VEM, $S_{\mathrm{obs}} > 3$ VEM and $r = 600 - 1600$ m. The dependence of the risetime on r is described as [248, 252]

$$t_{1/2,\mathrm{corr}}(r) = 40 \text{ ns} + \sqrt{A^2 + B \cdot r^2} - A, \tag{6.21}$$

with $t_{1/2,\mathrm{corr}}(0) = 40$ ns fixed to the resolution of the risetime. The functional form allows for a smooth transition from a constant behaviour at close distances to a linear dependence at large distances. The fit procedure differs from [252]: Instead of single measured values with parametrized uncertainties the fit is done with the mean value and the error of the mean (as we do not expect a large effect in the application for the photon search here), in distance bins with at least 30 entries. The fit in the bin $\sec(\theta) = 1.2-1.3$ is shown in Fig. 6.16(b), for non- and high-gain-saturated stations, along with an alternative fit of the form $t_{1/2,\mathrm{corr}}(r) = 40 \text{ ns} + Ar + Br^2$ (dashed lines). We stick with the original functional form in Eq. 6.21 as it gives a better fit quality over the full zenith range and in particular at close distances. Also, it is more robust against fluctuations at large distances. The fit has been restricted to 600 m to 1400 m, but according to the residual shown the fit describes data in the full range shown (up to 1600 m). A collection of the fits for all zenith bins can be found in Figs. 9.16(a)-9.16(e) in the appendix.

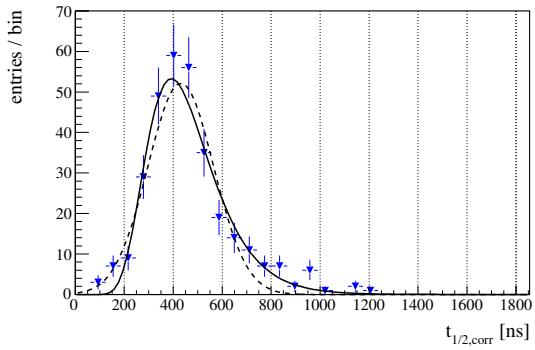

(a) Shown is the range $\log(E_{\mathrm{Hadr}}/\ \mathrm{eV}) = 18.6$ to 18.85, zenith angles $\theta = 58°$ to $60°$ and $r = 600$ m to 700 m. The distribution has been fitted with a Gaussian (dashed line, $\chi^2/\mathrm{NDF} = 64.1/13$) and with a lognormal function (full line, $\chi^2/\mathrm{NDF} = 24.8/13$). In both cases the area below 40 ns is less than 0.5%

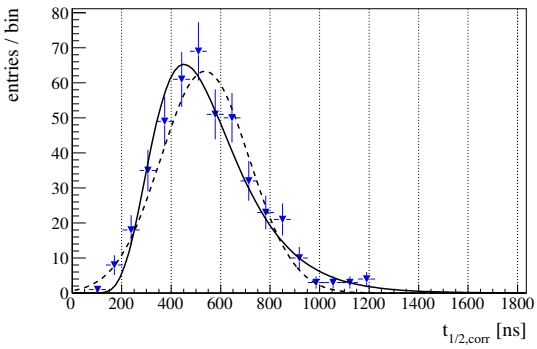

(b) Shown is the range $\log(E_{\mathrm{Hadr}}/\ \mathrm{eV}) = 18.85$ to 19.1, zenith angles $\theta = 25$ to $34°$ and $r = 1500$ m to 1600 m. The distribution has been fitted with a Gaussian (dashed line, $\chi^2/\mathrm{NDF} = 24.8/14$) and with a lognormal function (full line, $\chi^2/\mathrm{NDF} = 19.4/14$). In both cases the area below 40 ns is less than 0.5%

Figure 6.15: Maximizing the selection efficiency for the station risetime of non- and high-gain-saturated stations in data with $S > 10$ VEM.

For the parametrization of the benchmark, stations of different events are mixed and it is important to control the contribution of a change in the average X_{max}, energy or zenith angle to the shape of the benchmark. After selecting a small bin in energy and zenith angle it is sufficient to check the average X_{max} as function of r (see Fig. 6.17(c)). Above $r = 600$ m, the distribution is approximately flat, with a slight increase above 1700 m. It is difficult to separate the remaining zenith and energy dependence within the bins, as well as an X_{max} dependence and fluctuations in particular in the number of muons in order to explain the gap in the average risetime observed in the overlap region. Thus we can only make a qualitative statement. One might expect slightly lower risetimes for high-gain-saturated stations in the overlap region of no saturation and high-gain saturation as a few more early muons can saturate the high-gain and cause a risetime below the average that would be obtained for non-saturated stations. The bin in energy and zenith angle is fixed and thus we expect a slightly larger saturation probability for deeper X_{max} (corresponding to smaller risetimes in a naive geometrical assumption). A part of the gap might be of physical nature. Another part might be related to stations with problems in the baseline estimation. Figure 6.17(a) shows the range in core distance for different bins in the reconstructed energy (for $\sec(\theta) = 1.2 - 1.3$) including high-gain-saturated stations. The diagonal structure at large distances follows from the signal cut. The distance range 600 m $-$ 1600 m has a minimal bias in the energy range of $10 - 20$ EeV.
The zenith dependence of A and B for $\theta < 45°$ is described by $A(\theta) = A_0 + A_1 \cdot \exp(A_2 \cdot \sec(\theta))$ (B same functional form) in [252]. A fit of A and B is shown in Figs. 6.16(c) and 6.16(d) (blue line: exponential form, black line: alternative form). When including zenith angles up to $\theta = 60°$, this form is not sufficient anymore for parameter A (red line: exponential form, fit restricted to 45°). We suggest the following alternative, phenomenological parametrizations:

$$A(\theta) = A_0 + A_1 \cdot \cos(\theta) + A_2 \cdot \cos^2(\theta), \tag{6.22}$$

$$B(\theta) = B_0 + B_1 \cdot \cos^2(\theta) + B_2 \cdot \cos^4(\theta). \tag{6.23}$$

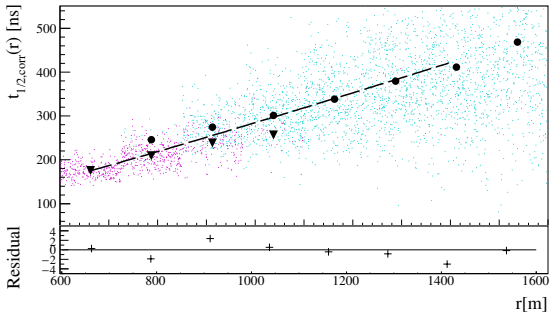

(a) Dependence on the core distance r, for $\sec(\theta) = 1.2 - 1.3$ ($S_{\mathrm{exp}} > 10$ VEM). Shown in blue are non-saturated stations, in magenta are high-gain-saturated stations. Blue and violet markers show the corresponding profiles with mean and error of the mean value. The residual is shown for the average profile of all stations shown.

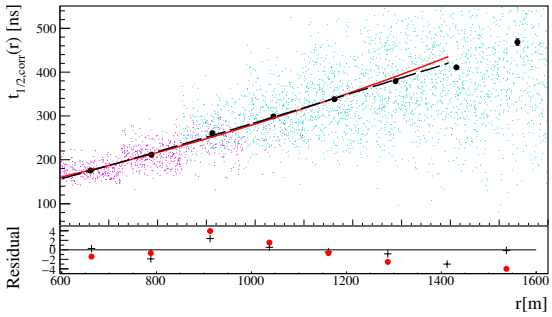

(b) Fit of the dependence on the core distance r, for $\sec(\theta) = 1.2 - 1.3$ ($S_{\mathrm{exp}} > 10$ VEM).

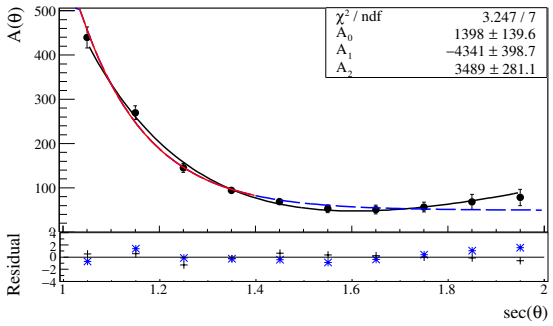

(c) Zenith dependence of A.

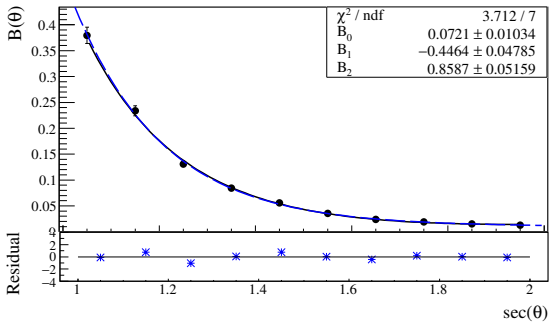

(d) Zenith dependence of B.

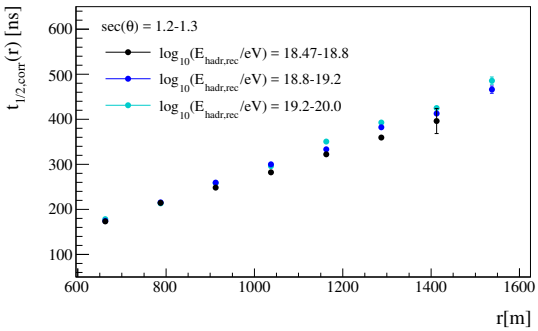

(e) Energy dependence of the benchmark ($\sec(\theta) = 1.2 - 1.3$).

Figure 6.16: Parametrization of the risetime benchmark (observed data, $E_{\mathrm{hadr,rec}} = 10 - 20$ EeV)

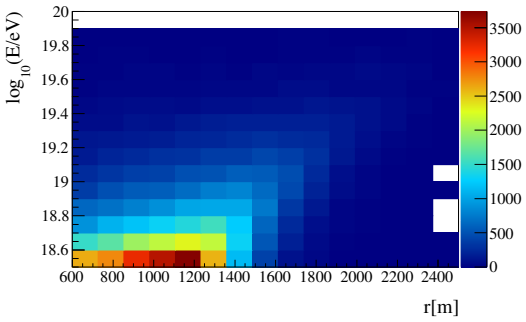

(a) Reconstructed hadronic energy (observed data).

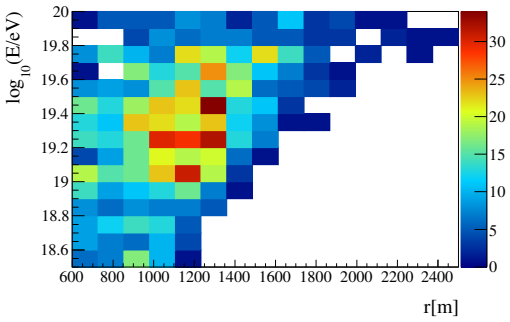

(b) True photon energy (MC photon).

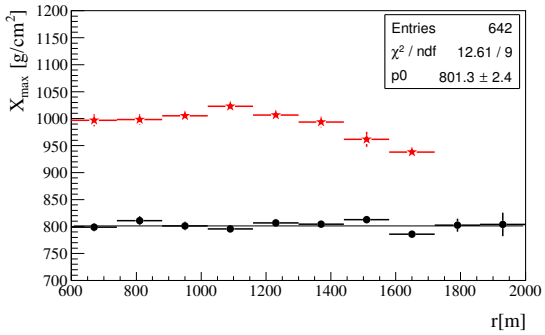

(c) Average $X_{\max}$ as function of the distance r (MC proton (black) and MC photon (red), $E_{\mathrm{MC}} = 10-20$ EeV).

Figure 6.17: Distance range for risetime stations of events with $\sec(\theta) = 1.2 - 1.4$, including high-gain-saturated stations. (Note that here the proton showers have been reconstructed with Offline version `v2r7p8`, and that we cut on the non-cleaned signal $S_{\mathrm{obs,non-cleaned}} > 6$ VEM as the DLE removal in the proton files are of an old version. This does not affect the average of all stations significantly.)

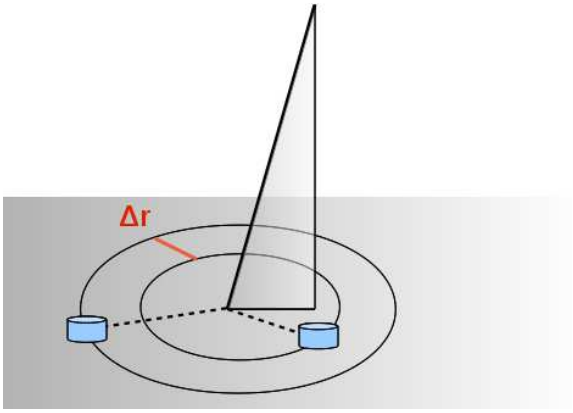

Figure 6.18: Sketch of two pair stations separated by Δr. Both stations have a compatible distance to the shower core but correspond to a different shower age.

This fit is shown as black lines along with the old functional form. For parameter B both forms are almost equivalent. The fit of A is clearly improved over the whole zenith range below 60°. The final parametrization of the benchmark is:

$$\begin{aligned} A_0 &= 1398 \pm 139 \\ A_1 &= -4342 \pm 398 \\ A_2 &= 3489 \pm 281 \\ B_0 &= 0.07 \pm 0.01 \\ B_1 &= -0.44 \pm 0.04 \\ B_2 &= 0.86 \pm 0.05 \end{aligned} \tag{6.24}$$

We have checked the energy dependence of the benchmark. There is a weak energy dependence (due to the dependence of the risetime on $X_{\max}$) which does not break the functional dependence. The main difference is the gain of far away stations (see Fig. 6.16(e)). The energy dependence is accounted for in a later step when comparing each event parameter to the photon expectation.

6.3.4 Uncertainty

Due to a still restricted amount of data from so-called *twin tanks* (two stations separated by about 11 m), we follow the idea of estimating the risetime uncertainty due to shower-to-shower fluctuations on the base of physically similar stations called *pair*. Physically similar means that a cut on the separation $\Delta r = |r_2 - r_1|$ and on the difference in the signal, $\Delta S = |S_1 - S_2| / (S_1 + S_2)$. The risetime is corrected for asymmetries. In [248] the risetime uncertainty is estimated as:

$$\sigma_{t_{1/2}} = \sqrt{\left(\sigma_{t_{1/2,\text{pair}}}\right)^2 - \left(\frac{\partial}{\partial r} t_{1/2}^{\text{bench}}(r) \cdot \Delta r\right)^2}, \tag{6.25}$$

with $\sigma_{t_{1/2,\text{pair}}} = \frac{\sqrt{\pi}}{2} \cdot \left| t_{1/2}^{(1)} - t_{1/2}^{(2)} \right|$ for the benchmark parametrization in Eq. 6.21. The second term in Eq. 6.25 corrects for the observed difference in the risetimes due the contribution from Δr. Instead, we introduce a different definition:

$$\sigma_{t_{1/2}} = \frac{\sqrt{\pi}}{2} \cdot \left| \left(t_{1/2}^{(1)} - t_{1/2}^{\text{bench}}(r_1)\right) - \left(t_{1/2}^{(2)} - t_{1/2}^{\text{bench}}(r_2)\right) \right|. \tag{6.26}$$

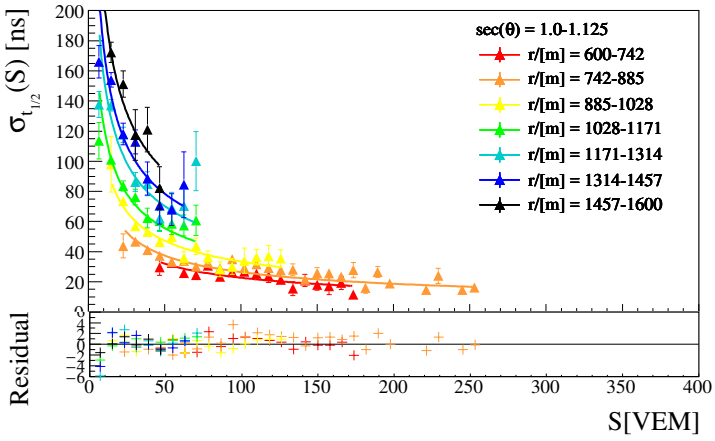

(a) Fit of the signal dependence of $\sigma_{t_{1/2}}$ ($\sec(\theta) = 1.0 - 1.125$), 1 free parameter.

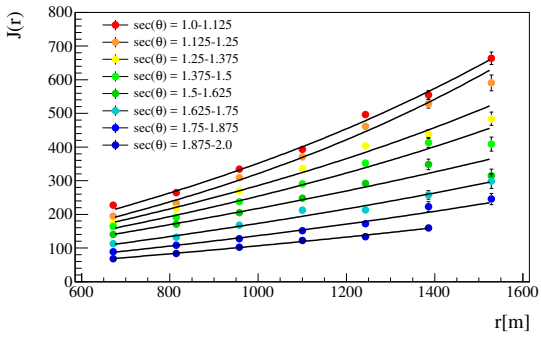

(b) Fit of the distance dependence of J.

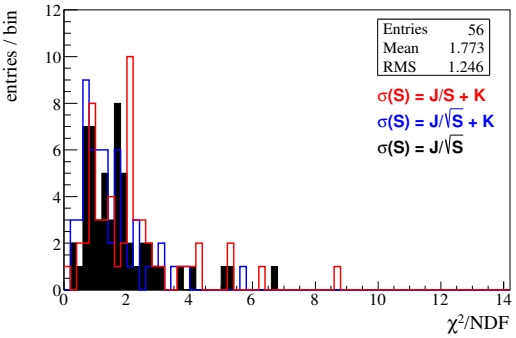

(c) Comparison of different fit functions.

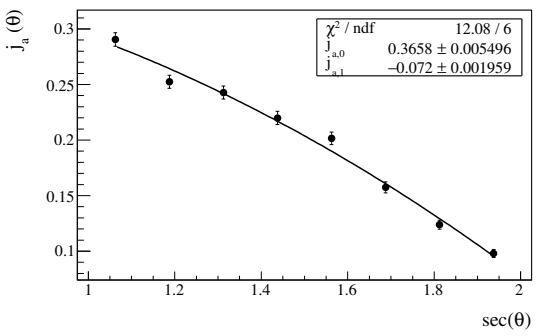

(d) Fit of the zenith angle dependence of j_a.

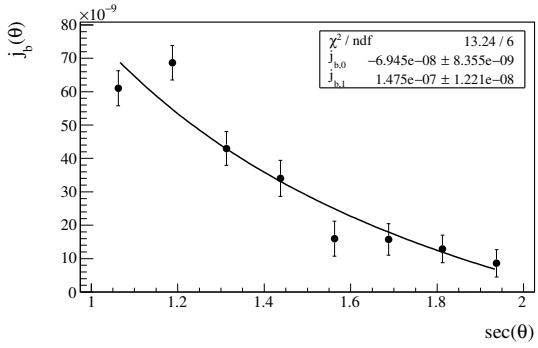

(e) Fit of the zenith angle dependence of j_b.

Figure 6.19: Parametrizations of the risetime uncertainty based on pair stations.

This can be understood when assuming that the pair stations are drawn from a distribution with the same standard deviation, separated by the difference of their expectation values. The factor $\sqrt{\pi/2}$ corrects the standard deviation for the small sample size ($N = 2$) and a further factor $1/\sqrt{2}$ scales the result to the uncertainty of a single station. Both definitions are equivalent for $r_1 \approx r_2$ and assuming that both stations are uncorrelated. When multiplying $\sqrt{\pi}/2$ to the right term in Eq. 6.25 we find that:

$$\begin{aligned}
\sigma_{t_{1/2}} &= \frac{\sqrt{\pi}}{2} \cdot \left| \left(t_{1/2}^{(1)} - t_{1/2}^{\text{bench}}(r_1)\right) - \left(t_{1/2}^{(2)} - t_{1/2}^{\text{bench}}(r_2)\right) \right| \\
&= \frac{\sqrt{\pi}}{2} \cdot \left| \left(t_{1/2}^{(1)} - t_{1/2}^{(2)}\right) - \left(\sqrt{A^2 + Br_1^2} - \sqrt{A^2 + Br_2^2}\right) \right| \qquad r_{1,2} \approx r \\
&\approx \frac{\sqrt{\pi}}{2} \cdot \left| \left(t_{1/2}^{(1)} - t_{1/2}^{(2)}\right) - \frac{Br}{\sqrt{A^2 + Br^2}} \cdot \Delta r \right| \\
&= \left| \sigma_{t_{1/2,\text{pair}}} - \frac{\sqrt{\pi}}{2} \cdot \left(\frac{\partial}{\partial r} t_{1/2}^{\text{bench}}(r) \cdot \Delta r \right) \right| . \qquad (6.27)
\end{aligned}$$

According to [252] the signals of the pair have to fulfill $\Delta S < 0.25$. Within this cut and with both stations passing the quality selection, approximately 68% of the pairs have a Δr of less than 100 m. In [248, 252] it was suggested to cut on $\Delta r < 100$ m which was applied here as well. Due to the triangular arrangement of the tanks, the smallest possible average distance (projected on the ground) is 750 m which has been confirmed in data. 57751 station pairs have been found with the station selection as for the risetime benchmark. The risetime uncertainty increases for small signals and large distances. As in [252], the signal dependence of $\sigma_{t_{1/2}}$ has been fitted with $f_1(S) = \frac{J}{\sqrt{S}} + K$ first, with S the observed signal. Based on the distribution of the reduced χ^2 of the fit, as shown in Fig. 6.19(c), this function matches the data better than $f_2(S) = \frac{J}{S} + K$ [248]. We suggest a further modification,

$$f_3(S) = \frac{J}{\sqrt{S}}, \qquad (6.28)$$

with only one free parameter (see Fig. 6.19(a)). For infinitely large signals we expect that the risetime uncertainty can have values much smaller than 25 ns due to the interpolation. Thus we assume in a simple approch that the uncertainty moves towards zero. The fit becomes more stable and the fit quality is only marginally reduced. Next the distance dependence of J is parametrized:

$$J(r) = r \cdot \left(j_a + j_b \cdot r^2\right). \qquad (6.29)$$

The zenith angle dependence of $j_{a,b}$ is described by:

$$\begin{aligned}
j_a(\theta) &= j_{a,0} + j_{a,1} \cdot \sec^2(\theta), \\
j_b(\theta) &= j_{b,0} + j_{b,1} \cdot \cos^2(\theta). \qquad (6.30)
\end{aligned}$$

These functional forms are all phenomenological. The fits are shown in Figs. 6.19(b) to 6.19(e). The final parametrization of the risetime uncertainty is:

$$\begin{aligned}
j_{a,0} &= (366 \pm 5) \cdot 10^{-3} \\
j_{a,1} &= (-72 \pm 1) \cdot 10^{-3} \\
j_{b,0} &= (-70 \pm 8) \cdot 10^{-9} \\
j_{b,1} &= (15 \pm 1) \cdot 10^{-8}. \qquad (6.31)
\end{aligned}$$

Table 6.2: Station risetime quality selection

Dataset: 01/2004 - 12/2012		
Cut	*Events passed*	*Fraction*
Data quality		
T4+6T5 trigger		
At least rec. LDF		
$0° < \theta < 60°$		
$E_{\mathrm{hadr,rec}} > 3$ EeV	82446	1
(+ Benchmark: $10 < E_{\mathrm{hadr,rec}}$/ EeV < 20	6410	0.08)
Cut	*Stations passed*	*Fraction*
No sat. or high-gain sat.	502140	1
+ $S_{\mathrm{obs}} > 6$ VEM	356302	0.71
+ $r > 600$ m	306192	0.61
+ $r < 2000$ m	301604	0.60
+ $t_{1/2,\mathrm{corr}} > 40$ ns	301142	0.60

By accounting for the signal-, distance- and zenith-dependence, the energy-dependence is under control as well.

6.3.5 Uncertainty-weighted residual δ_i

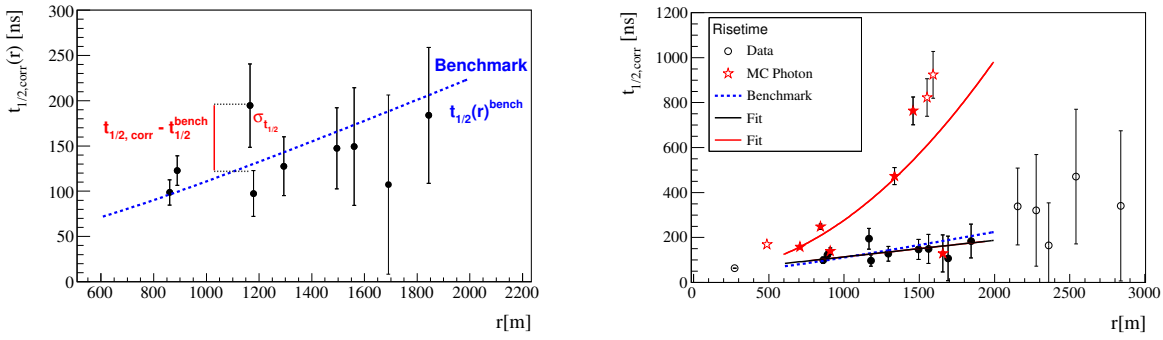

(a) Definition of δ_i

(b) Defining an event parameter

Figure 6.20: Left: Definition of an uncertainty-weighted residual δ_i of the station risetime. Right: Two different methods of defining an event parameter based on the asymmetry-corrected station risetime $t_{1/2,\mathrm{corr},i}$. (1) Event-wise fit of the distribution of $t_{1/2}(r)$ (shown as full lines). (2) Event-wise comparison of the measured risetime with the benchmark obtained from data (blue dashed line), within the uncertainty $\sigma_{t_{1/2}}$ obtained from data. Shown are example events from data (black) an MC photon (red). Hollow markers above 1000 m indicate signals below 6 VEM.

The parametrizations obtained in the previous sections have been verified on the base of the residual δ_i,

$$\delta_i = \frac{t_{1/2,\mathrm{corr},i} - t_{1/2}^{\mathrm{bench}}(r_i)}{\sigma_{t_{1/2}}(r_i)}. \tag{6.32}$$

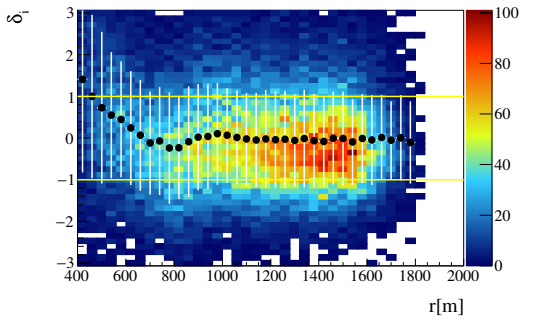

(a) Distance dependence ($S_{\mathrm{exp}} > 10$ VEM)

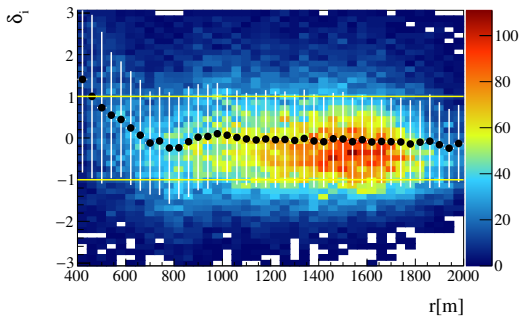

(b) Distance dependence ($S_{\mathrm{obs}} > 6$ VEM)

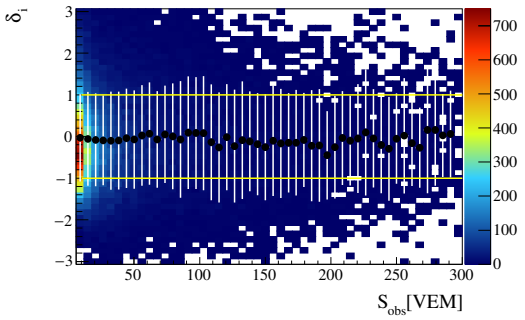

(c) Signal dependence ($S_{\mathrm{obs}} > 6$ VEM)

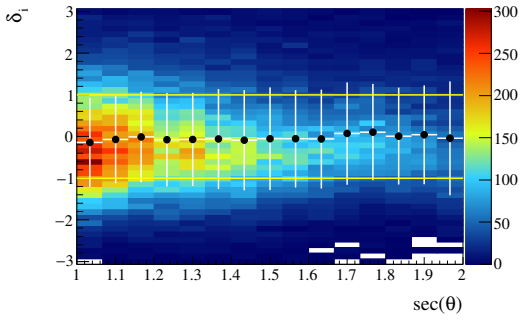

(d) Zenith dependence ($S_{\mathrm{obs}} > 6$ VEM)

Figure 6.21: Dependences of δ_i for $E_{\mathrm{hadr,rec}} = 10 - 20$ EeV. An overlayed profile shows mean value and standard deviation.

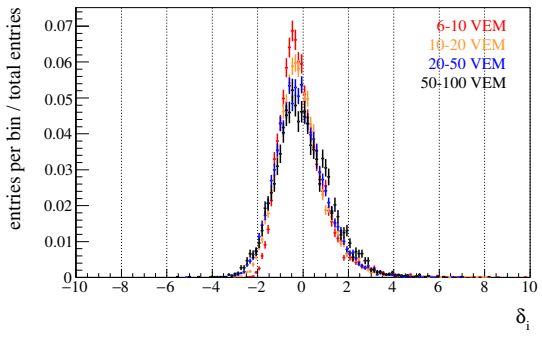

(a) Residual within signal bins

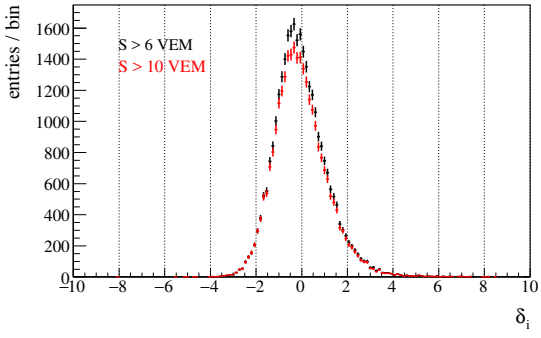

(b) Residual above a signal threshold

Figure 6.22: Study of the minimum signal for the station risetime.

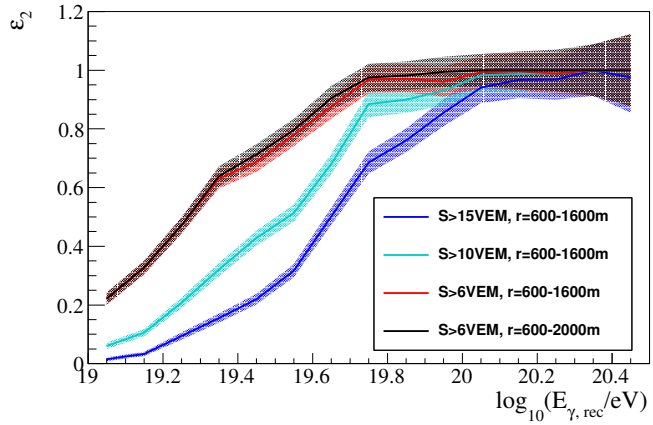

Figure 6.23: Integral parameter selection efficiency of $t_{1/2}$ for MC photon in the zenith angle range $\theta = 30° - 60°$. The selection is based on non- and high-gain-saturated stations. Preshowered photons are not excluded, each shower has been simulated five times and the spectrum has been reweighted.

The dependence of δ_i on the signal, distance and zenith angle is shown in Figs. 6.21(a) to 6.21(d). The case of $S_{\text{exp}} > 10$ VEM corresponds to the selection of the underlying parametrizations. The distributions in Fig. 6.21(a) is approximately flat and the signal- and zenith dependence as well (cf. Figs. 9.17(a) and 9.17(b) in the appendix). Thus the parametrizations have been verified. For the application of the parametrizations to photons and hadrons the expected signal is wrong in case of photons and thus the observed signal is used to reduce biases. A second, less strict selection of $S_{\text{obs}} > 6$ VEM is shown in Figs. 6.21(b) to 6.21(d) on the right. We have checked that down to an observed signal of 6 VEM the residual is stable enough to establish an event parameter, as shown in Fig. 6.22(b). For stations with signals below 10 VEM, the left tail is asymmetric but the difference is not visible in the distribution of all selected stations. Note that a distance of 2000 m corresponds on average to the an expected signal of 6 VEM for hadrons (see Fig. 9.18(a) in the appendix). The distribution of δ_i as function of the station distance to the shower core is approximately flat in the distance range of 600 m to 2000 m. It is not possible to go below 600 m as the parametrization does not describe data in this range. In [93] the risetime fit was applied on non- or HG-saturated stations with signals above 10 VEM, for events in the range of 30° and 60°. In previous and ongoing studies of the risetime, it was suggested to restrict the zenith angle range to below 45° and to select signals above 15 VEM [215, 252]. In the previous sections we have obtained a complete set of parametrizations for our dataset with a modified SDCalibrator. We have shown that the selection can be optimized to maximize the selection effiency for the SD photon search:

- The maximum zenith angle can be set back to 60°. This brings a geometrical increase of the efficiency by a factor 1/3 compared to the case of 45°.

- It turned out in [215] that the risetime calculation is biased for high-gain-saturated stations. The solution for this problem is a modification of the SdCalibrator [215, 252]. We have checked that the modification can be applied on data and MC photon for the SD photon search.

- It has been studied that, including high-gain-saturated stations and within the zenith range up to 60°, the distance range can be set to 600 − 2000 m.
- The minimum signal has been set down to 6 VEM.
- The maximum distance has been set to 2000 m, which corresponds on average to an expected signal of 6 VEM for hadrons. This is applied for all of the methods which use the parametrizations obtained in this chapter.

The effect of these modifications on the efficiency is shown in Fig. 6.23.
The final quality selection for the application of the risetime to the SD photon search is then a rejection of bad periods and bad PMTs, a T4+6T5 trigger, at least a reconstructed LDF, zenith angles $\theta < 60°$ and energies $E_{\mathrm{hadr,rec}} > 3$ EeV. Stations must be non-saturated or only high-gain-saturated, with a signal $S_{\mathrm{obs}} > 6$ VEM and located at distances within 600 m and 2000 m and with $t_{1/2,\mathrm{corr}} > 40$ ns.
There are two different methods to use the distance dependence of the asymmetry-corrected station risetime, $t_{1/2,\mathrm{corr}}$, to separate photons and hadrons (see also [93, 248, 252–256]). In both cases the station risetimes of an event are combined to one single parameter. One possible parameter is the risetime at a fixed reference distance, based on a fit of the single station risetimes as a function of the distance. A different approach avoids an event-wise fit by establishing an benchmark based on a large dataset, e.g. observed data (mainly hadrons). Here the separation parameter is based on the compatibility of the station risetimes with the benchmark (Leeds delta method).

6.3.6 Event parameter: $t_{1/2}(1000)$

This method is based on an event-wise χ^2-fit of the distribution of the station risetime $t_{1/2,\mathrm{corr}}(r)$ with a second degree polynomial:

$$f(r) = 40 \text{ ns} + a \cdot r + b \cdot r^2 \tag{6.33}$$

with r the distance to the shower core. The constant is set to the risetime resolution of 40 ns for a better stability of the fit. The fit paramters are bounded to positive values. In order to obtain an event parameter, the fit is evaluated at a reference distance of 1000 m. This parameter is called $t_{1/2}(1000)$ [257]. In [258] the untertainty of $t_{1/2}(1000)$ was revisited and corrected for a correlation term:

$$\sigma_{t_{1/2}(1000)} = \sqrt{\sigma_a^2 \cdot r^2 + \sigma_b^2 \cdot r^4 + \mathrm{Cov}(a,b) \cdot r^3} \tag{6.34}$$

Figure 6.20(b) shows an example event from data and MC photon of a compatible reconstructed energy and zenith angle. Shown event-wise fits in the distance range of 600 m to 2000 m. The quality selection in [93] is at least 4 non- or HG-saturated stations with signals above 10 VEM. Here we restrict the selection to distances of 600 − 2000 m for stations with no saturation or saturated high-gain, as the risetime paramtrizations have been verified within this range. The signal cuts compared later are $S_{\mathrm{obs}} > 10$ VEM and $S_{\mathrm{obs}} > 6$ VEM. As an alternative selection, we compare here at least 3 stations passing the station selection and at least one station closer than 1000 m to assure a sufficient lever arm for the fit.

6.3.7 Event parameter: Δ_{Leeds} (Leeds delta method)

The delta method was introduced by the Leeds Auger Group about 8 years ago and has been studied more deeply since then [248, 252, 255]. It compares the observed station risetime $t_{1/2,\text{corr},i}$ to the benchmark obtained from data, $t_{1/2}^{\text{bench}}(r_i)$, within the uncertainty $\sigma_{t_{1/2}}(r_i)$ obtained from data. The parameter is defined as

$$\begin{aligned} \Delta_{\text{Leeds}} &= \frac{1}{N}\sum_i \delta_i \\ &= \frac{1}{N}\sum_i \frac{t_{1/2,\text{corr},i} - t_{1/2}^{\text{bench}}(r_i)}{\sigma_{t_{1/2}}(r_i)} \end{aligned} \tag{6.35}$$

with $t_{1/2,\text{corr},i}$ the asymmetry-corrected station risetime of station i at distance r_i, $t_{1/2}^{\text{b}}(r_i)$ the parametrized benchmark from data, $\sigma_{t_{1/2}}(r_i)$ the parametrized uncertainty from data and N the number of selected stations. The parametrizations have been discussed earlier in this chapter. Figure 6.20(b) shows an example event from data and MC photon of a compatible reconstructed energy and zenith angle. The benchmark obtained from data is shown together with event-wise fits. Selected are non saturated and high-gain-saturated stations in the distance range of 600 m-2000 m. The signal cuts compared later are $S_{\text{obs}} > 10$ VEM and $S_{\text{obs}} > 6$ VEM. A first event selection is at least four selected stations, as for $t_{1/2}(1000)$. The event quality selection from previous studies [252] is at least two selected stations and at least five triggered stations. Another alternative selection is at least tree selected stations.

6.4 LDF Parameters

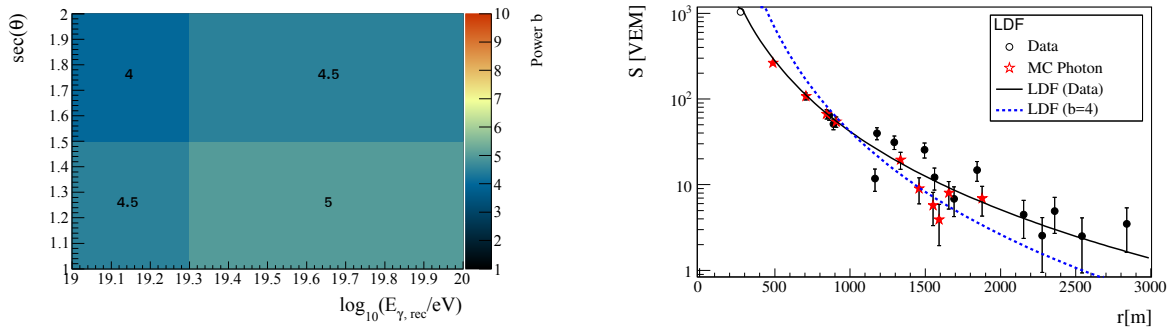

(a) b-scan

(b) Different reference LDFs

Figure 6.24: Left: Scan of the shape b of a fixed reference LDF that maximizes the photon-hadron separation, based on the merit factor η. Shown is the choice of b that maximizes η. Right: Definition of an event parameter based on different reference LDFs - a fixed LDF with $b = 4$ (blue line) and the average LDF obtained from data (black line). The error bars are $\sqrt{S}$ to visualize the definition of S_b^{n}.

The shape of the lateral density function (LDF) is different for photon and hadron primaries. This difference is correlated with X_{max} and the number of muons in the shower. For photon

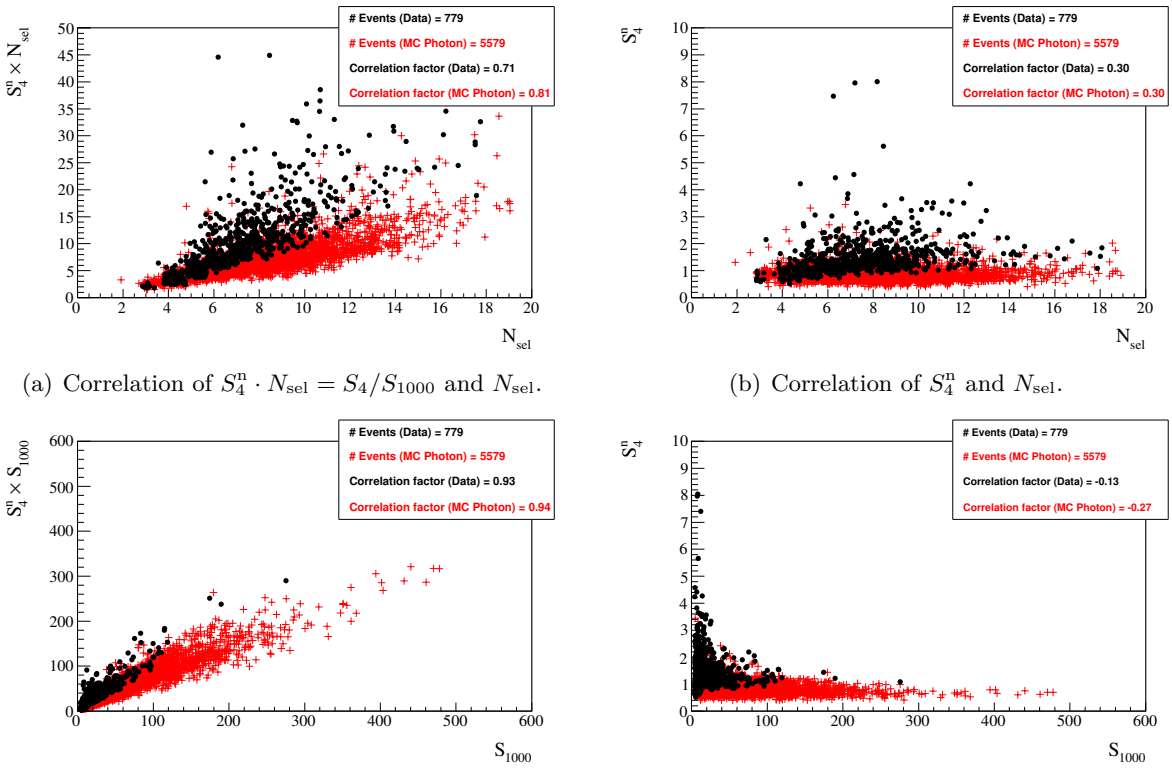

(a) Correlation of $S_4^{\mathrm{n}} \cdot N_{\mathrm{sel}} = S_4/S_{1000}$ and N_{sel}.

(b) Correlation of S_4^{n} and N_{sel}.

(c) Correlation of $S_4^{\mathrm{n}} \cdot S_{1000} = S_4/N_{\mathrm{sel}}$ and S_{1000}.

(d) Correlation of S_4^{n} and S_{1000}.

Figure 6.25: Normalization of S_4: Correlation with N_{sel} and S_{1000}. Shown are the data burn sample (black markers), excluding bad data taking periods, and non-preshowered MC photons (red markers). Events have been selected in a zenith angle range of 30° to 60° and energies $E_{\gamma,\mathrm{rec}} > 10$ EeV and with the quality selection described in this section.

primaries the LDF is steeper. As parameterizations in the reconstruction are optimized to describe the average data and the LDF fit does not fit the LDF shape parameters, β and γ cannot be used as a separation parameters. But the combatibility of the observed lateral distribution of station signals with a primary photon can be inferred from the fit quality by comparing each signal with a reference LDF. The most obvious choice would be the χ^2 of the fit. This parameter has been checked but the separation power is weak [259]. Another similar parameter, S_b, has been suggested by *Ros et al.* [260, 261],

$$S_b = \sum_{i=1}^{N_{\text{cand}}} S_i \cdot \left(\frac{r_i}{1000 \text{ m}} \right)^b , \tag{6.36}$$

where N_{cand} is the number of candidate stations, S_i is the signal observed at station i with core distance r_i and b is a fixed (positive) shape parameter. As a technical detail it should be mentioned that for the LDF parameters the signal has not been cleaned from direct light effects and PMTs discussed in this thesis have not been excluded. These effects and malfunctions affect mainly the signal rise- and falltime but not s much the total signal.
The meaning of this parameter is not obvious, but it becomes more clear when rewriting it as

$$\begin{aligned} S_b &= N_{\text{sel}} \cdot S_{1000} \times \frac{1}{N_{\text{sel}}} \sum_{i=1}^{N_{\text{sel}}} S_i \cdot \frac{1}{S_{1000} \cdot \left(\frac{r_i}{1000 \text{ m}}\right)^{-b}} && (6.37) \\ &= N_{\text{sel}} \cdot S_{1000} \times S_b^{\text{n}}. && (6.38) \end{aligned}$$

(with $N_{\text{cand}} = N_{\text{sel}}$ for events without low-gain saturation stations). It is related to the average fractional difference of the observed signal from the expected signal of a reference LDF with shape b, called S_b^{n} from now on. Two LDF shapes appear to be obvious choices: the LDF that results from the LDF fit and an optimized choice of fixed b, as shown in Fig. 6.24(b). The parameter related to the LDF fit we call R_{NKG}, with

$$R_{\text{NKG}} = \frac{1}{N_{\text{sel}}} \sum_{i=1}^{N_{,\text{sel}}} S_i \cdot \frac{1}{S_{1000} \cdot \left(\frac{r_i}{1000 \text{ m}}\right)^{\beta} \cdot \left(\frac{r_i}{1700 \text{ m}}\right)^{\beta+\gamma}}. \tag{6.39}$$

As an alternative, a fixed shape of $b = 4$ has been suggested in [262] for photon-hadron separation for the SD photon search. Using the data burn sample described in 5 up to May 15th, 2013 (excluding bad periods, the Comm's crisis period April 16th, 2009 to November 15th, 2009 and lightning events) and the simulated photon library (rejecting preshowered photons), we have performed a scan to find the optimal choice of b for the logarithm of the normalized parameter, $\log_{10}(S_b)$, which maximizes the photon-hadron separation. Simulated MC Photon showers have only been used once here. The quality event selection is described in Sec. 6.4.1. The scan is based on the merit factor η,

$$\eta = \frac{q_{50,\text{data}} - q_{50,\gamma}}{\sqrt{\sigma^2_{\text{data}} + \sigma^2_{\gamma}}}, \tag{6.40}$$

with q_{50} the 50% quantile and σ the one-sided[5] standard deviation of the distribution of a parameter q. The results are shown in Fig. 6.24(a). More details can be found in Figs. 9.20(a)-9.20(f) in the appendix. The optimal shape for the SD photon search is around $b = 4$ and

[5] For an asymmetric distribution, the standard deviation is estimated by $q_{84} - q_{50}$ (or $q_{50} - q_{26}$) for the corresponding side of the distribution.

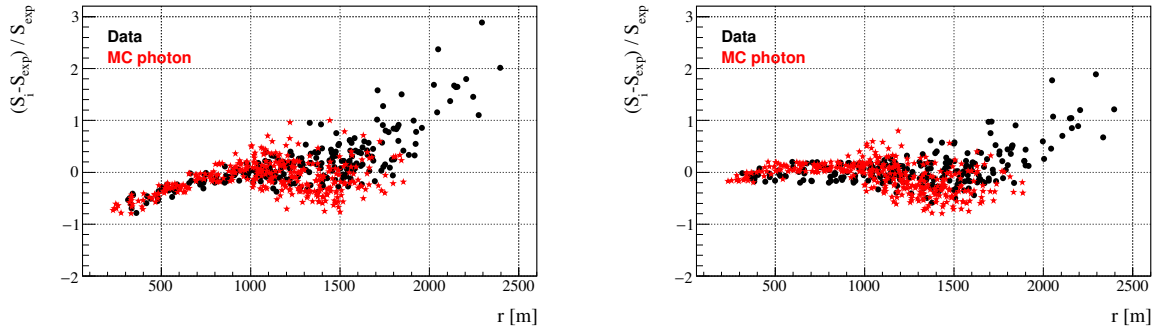

(a) $S_{4,i}$ (b) $R_{\mathrm{NKG},i}$

Figure 6.26: Contribution of single stations i to the event parameter as function of the core distance r. Shown are the data burn sample (black markers), excluding bad data taking periods, and non-preshowered MC photons (red markers). Events have been selected in a zenith angle range of 35° to 40° and energies $E_{\gamma,\mathrm{rec}}$ between 10-20 EeV and with the event and station quality selection described in this section.

reproduces the result for S_b [262].
The normalization of S_4 to N_{sel} and S_{1000} does not only give the parameter a more clear meaning but it also helps to separate to reduce the strong energy dependence. A study of the correlation of S_4^{n} with N_{sel} and S_{1000} is shown in Figs. 6.25(b)-6.25(d) (same plots for R_{NKG} in Figs. 9.19(b)-9.19(d) in the appendix). The normalization reduces the correlation of the separation parameter with N_{sel} and S_{1000}. A further advantage is a reduction of the influence of non-functioning tanks in the array. Studying the distributions of $S_{4,i}$ and $R_{\mathrm{NKG},i}$ shown in Figs. 6.26(a) and 6.26(b), both distributions have certain features that can be used to further optimize the photon-hadron separation. The distributions for data and MC photon intersect at about $r = 1000$ m, which is expected as we compare at the same reconstructed energy. For $r < 1000$ m the station contributions are negative and for $r > 1000$ m they are around zero for MC photon and significantly larger for data. The event parameter sums over the station contributions and the thus stations with $r < 1000$ m reduce the separation power. The feature for $r > 1000$ m comes from the fact that we also use stations with observed signal $S < 10$ VEM which have less than 100% trigger probability. The separation power is maximized in the following parameters:

$$S^{\mathrm{n}}_{4,1000} = S^{\mathrm{n}}_4(r > 1000\ \mathrm{m}) \quad (6.41)$$

$$R_{\mathrm{NKG},1000} = R_{\mathrm{NKG}}(r > 1000\ \mathrm{m}). \quad (6.42)$$

Note that for the application in the photon search we use the logarithm of these parameters to obtain a symmetric shape.

6.4.1 Quality selection

The advantage of these LDF parameters is a very basic quality selection which allows for almost 100% selection efficiency. They can be combined with a powerful separation parameter to improve the photon-hadron separation without loosing efficiency.
Stations with no saturation and high-gain saturation are used, rejecting stations with saturated low gain. For $S^{\mathrm{n}}_{4,1000}$ and $R_{\mathrm{NKG},1000}$ stations with $r < 1000$ m are not used. There is no further

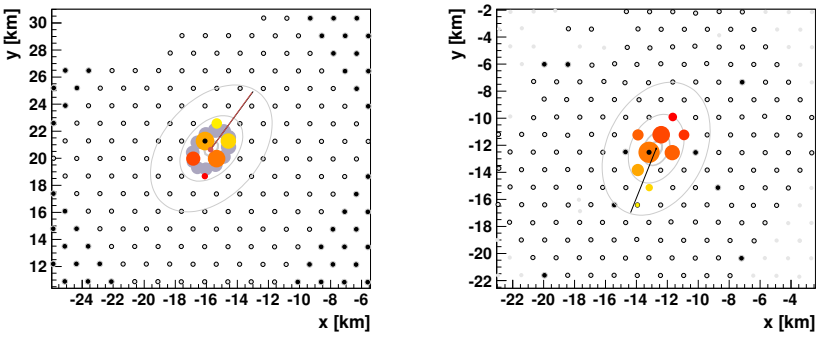

(a) Simulated MC photon ($E_{\gamma,\mathrm{rec}}$ = 19.52 eV, 6 triggered stations)

(b) Event 5120351 ($E_{\gamma,\mathrm{rec}}$ = 19.50 eV, 9 triggered stations)

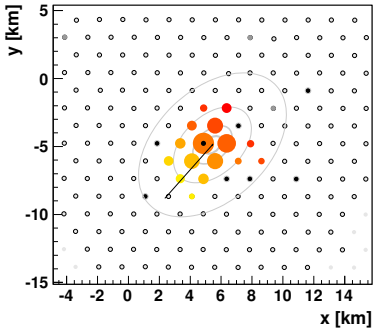

(c) Event 7264575 ($E_{\mathrm{hadr,rec}}$ = 19.50 eV, 16 triggered stations)

Figure 6.27: Number of triggered stations for a photon- and hadron shower ($\theta \approx 50°$) at the same reconstructed S_{1000} or energy.

station quality selection. The trigger probability is here used to improve the separation power. **Events** must have a reconstructed LDF (at least for R_{NKG}, but here we apply it for both parameters), T4 trigger and 6T5 trigger to avoid holes around the tank with the highest signal, zenith angles $\theta < 60°$ (higher inclinations have not been checked here) and at least one station that passes the quality selection.

6.5 Radius of Curvature

The radius of curvature has been introduced in the description of the SD reconstruction in Sec. 3.4.2. A comparison of photon and hadron showers of a similar reconstructed photon energy is shown in Fig. 7.3(e). As expected, the radius of curvature is smaller for primary photons.

6.6 Number of Candidate Stations

A very basic observable that depends on the shower maximum is the number of triggered candidate stations, N_{cand}, of a shower. Comparing showers with similar energy and zenith angle,

the number of triggered stations is expected to be larger for a primary hadron compared to a primary photon as muons increase the footprint of the shower. An example is shown in Fig. 6.27. In the SD photon search we cannot compare showers at the same energy but only at the same reconstructed S_{1000}, which corresponds to a difference of about a half decade in the energy (cf. Sec. 4.2). In this case the difference in N_{cand} is reduced. The separation as function of the zenith angle is shown in Fig. 9.23(e).

CHAPTER 7

Upper limits on the diffusive UHE photon flux and fraction

In this chapter the final parameter set is determined from all the parameters defined and studied in the previous chapter and then applied to a principal component analysis (PCA). Anyway, we start with the final analysis for a better reading.
The general approach in this work is to use a small dataset instead of hadronic simulations to find the principal component in the two-parameter-space. For a conservative limit we take the photon median (of non-preshowered photons) as the photon candidate cut. From previous limits the integral photon fraction at 95% C.L. is maximum 2%. Thus the contamination from photons in the data burn sample is expected to be small. The most powerful combination of parameters from the previous chapters, Δ_{Leeds} and $\log_{10}(R_{\mathrm{NKG,1000}})$, is studied in a PCA. The minimum energy for this analysis is set to 10 EeV to have almost 100% trigger efficiency for photon showers. The zenith range is restricted to a range from 30° to 60° to have most photon showers with a shower maximum above ground in the selected energy range. Here we reject only the non-recoverable part of the Comm's crisis. The exposure A is calculated from the number of active elementary 6T5 cells of the array. The total exposure is $A = 33805.7$ km^2 sr yr and the exposure corrected for the zenith angle range and the burned dataset of this analysis is

$$A'_{\mathrm{corr}} = \frac{2}{3} \cdot 0.98 \cdot A = 22086.4 \text{ km}^2 \text{ sr yr}. \tag{7.1}$$

The factor 2/3 comes from Eq. 3.15, evaluated for $\theta_{\mathrm{min}} = 30°$ and $\theta_{\mathrm{max}} = 60°$. For vertical showers the photon detection efficiency drops rapidly, as shown in Fig. 7.1. The basic idea for this analysis is to apply the photon energy calibration derived in Sec. 4.2 to data and simulated MC photons. In order to define a zenith- and energy-independent photon median in the principal component of MC photons, each observation of a separation parameter x is rescaled to the expectation how non-preshowered MC photons (U) would look like for the same reconstructed S_{1000} and zenith angle θ

$$x^* = \frac{x - \bar{x}_\gamma(\theta, E_{\gamma,\mathrm{rec}})}{\sigma_x(\theta, E_{\gamma,\mathrm{rec}})}, \tag{7.2}$$

with $\bar{x}$ the mean value and σ_x the standard deviation of x as expected for MC photons. The

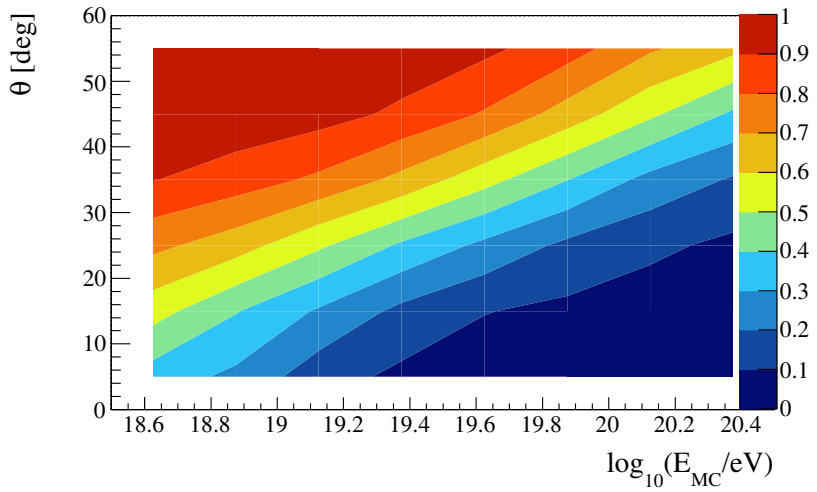

Figure 7.1: Fraction of photon showers (U) passing the selection $X_{\mathrm{gr}} - X_{\mathrm{max,MC}} > -50$ g/cm^2.

photon expectation is obtained from MC photons (U) from a binned[1] histogram, applying the quality selection of each parameter. Photon showers have been simulated in the detector up to five times to increase statistics (showers reused only for the photon expectation and for the reconstruction efficiency). The true energy is chosen here to avoid a dependence on the energy calibration. Thus we do not expect a Gaussian centered at zero for the integral spectrum of x^*. The histograms for mean, standard deviation and the statistics per bin are shown in Fig. 7.2 in the appendix. A summary of the photon expectation for the remaining parameters compared in this analysis can be found in Figs. E.21 to E.22 in the appendix.
The energy and zenith angle dependence of Δ_{Leeds} and $\log_{10}(R_{\mathrm{NKG,1000}})$ (light colors) and the successful removal of dependences expected for MC photon U (red markers) are shown in Fig. 7.3. The photon distributions of x^* are centered at zero. The data burn sample is indicated as black and grey markers to visualize the separation. The same plots for the remaining parameters can be found in Fig. E.23 in the appendix.
The PCA is based on the parameters $\Delta^*_{\mathrm{Leeds}}$ and $\log_{10}(R_{\mathrm{NKG,1000}})^*$. In order to avoid dependences on hadronic interaction models, the principal component axis is found using the data burn sample and the non-preshowered photons (U) from the MC photon sample. This gives 458 events for data and 757 events for MC photons (U) with a reconstructed photon energy of at least 10 EeV and with zenith angles of 30° to 60°. The same axis is also used for the derivation of the upper limits with $E > 20$ EeV and $E > 40$ EeV. As we use a data burn sample here, statistics do not allow to set a principal component axis in bins of energy and zenith angle. This is shown in Fig. 7.4(a). The angle of the principal component axis is $-30.4°$. The remaining 98% of the data and the MC photon sample are then used for the photon search with the axis fixed before. Figure 7.4(b) (zoom in Fig. 7.4(c)) shows the application sample together with the principal component axis and the photon candidate cut for energies above 10 EeV. The photon candidate cut is set to the median of the principal component for MC photons (U). Figures 7.5(a), 7.5(b) and 7.5(c) show the distributions of the principal component for energies above 10, 20 and 40 EeV. We find 4 photon candidate events above 10 EeV, 2 events above 20

[1] Equistatistical binning: 5 bins in $\log_{10}(E_{\gamma,\mathrm{MC}})$, 6 bins in $\sec(\theta)$.

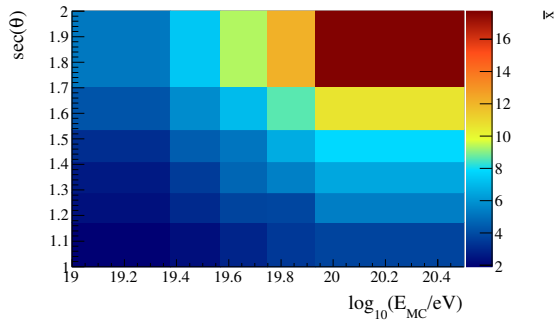

(a) $x = \Delta_{\mathrm{Leeds}}$, mean value

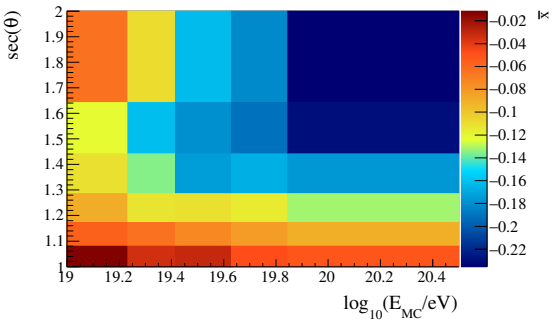

(b) $x = \log_{10}(R_{\mathrm{NKG},1000})$, mean value

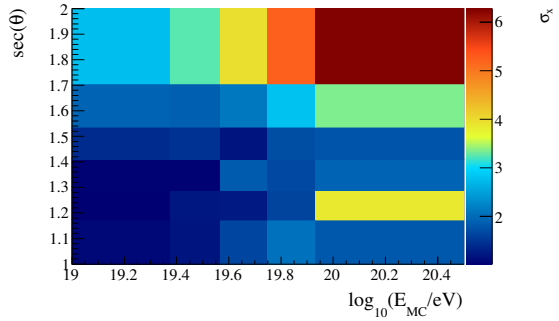

(c) $x = \Delta_{\mathrm{Leeds}}$, standard deviation

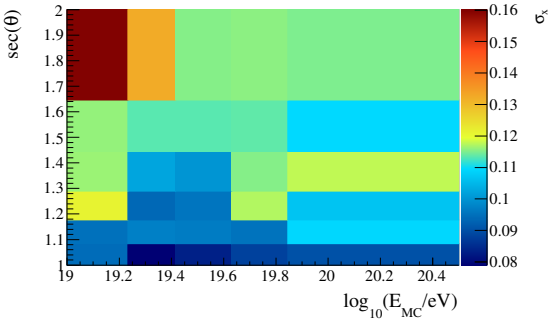

(d) $x = \log_{10}(R_{\mathrm{NKG},1000})$, standard deviation

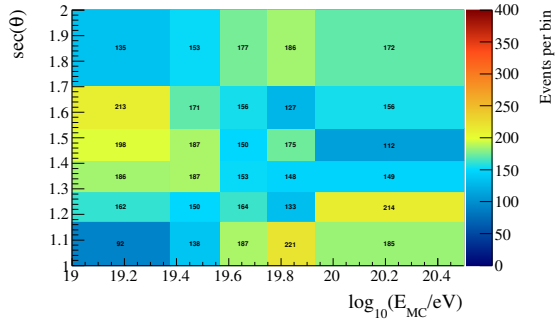

(e) $x = \Delta_{\mathrm{Leeds}}$, statistics per bin

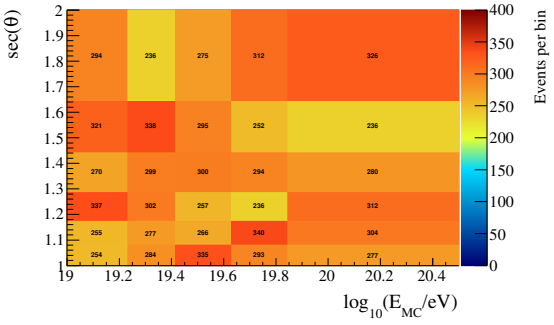

(f) $x = \log_{10}(R_{\mathrm{NKG},1000})$, statistics per bin

Figure 7.2: Mean value and standard deviation of a separation parameter x as expected from MC photon (U).

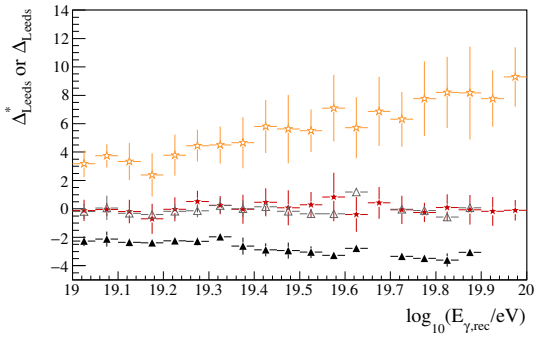

(a) $x = \Delta_{\rm Leeds}$, energy dependence

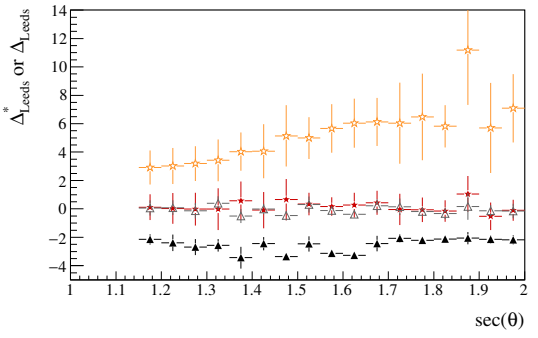

(b) $x = \Delta_{\rm Leeds}$, zenith angle dependence

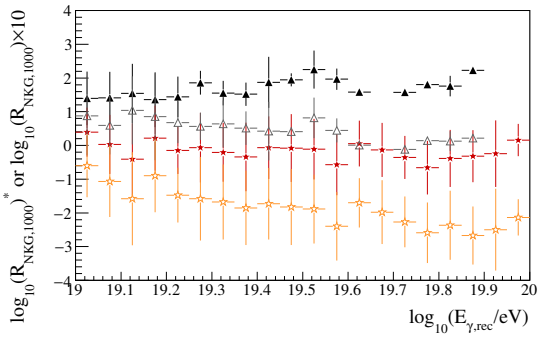

(c) $x = \log_{10}(R_{\rm NKG,1000})$, energy dependence

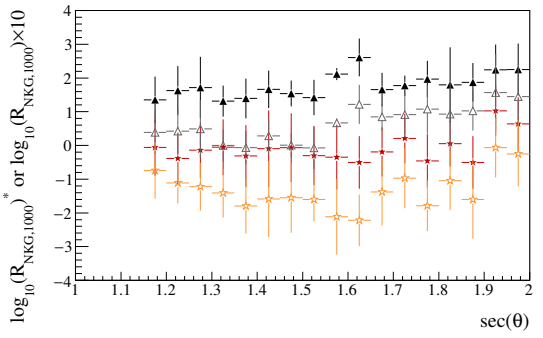

(d) $x = \log_{10}(R_{\rm NKG,1000})$, zenith angle dependence

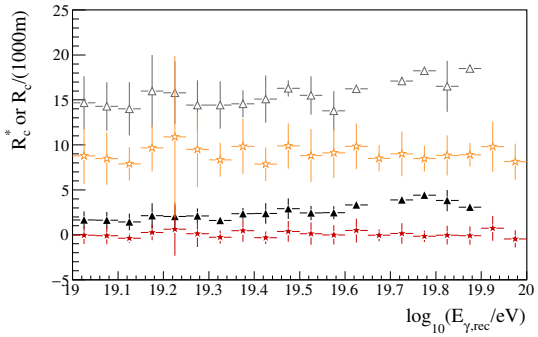

(e) $x = R_{\rm c}$, energy dependence

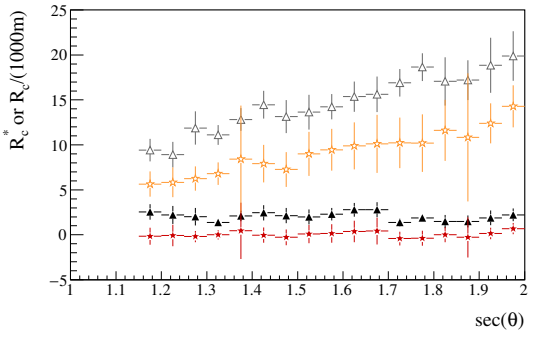

(f) $x = R_{\rm c}$, zenith angle dependence

Figure 7.3: Removal of the energy and zenith angle dependence expected for MC photons. Red and black markers show the rescaled separation parameter x^*, for data and MC photon (U). Grey and orange markers show the respective distribution of x (scaling factors are given on the y-axis).

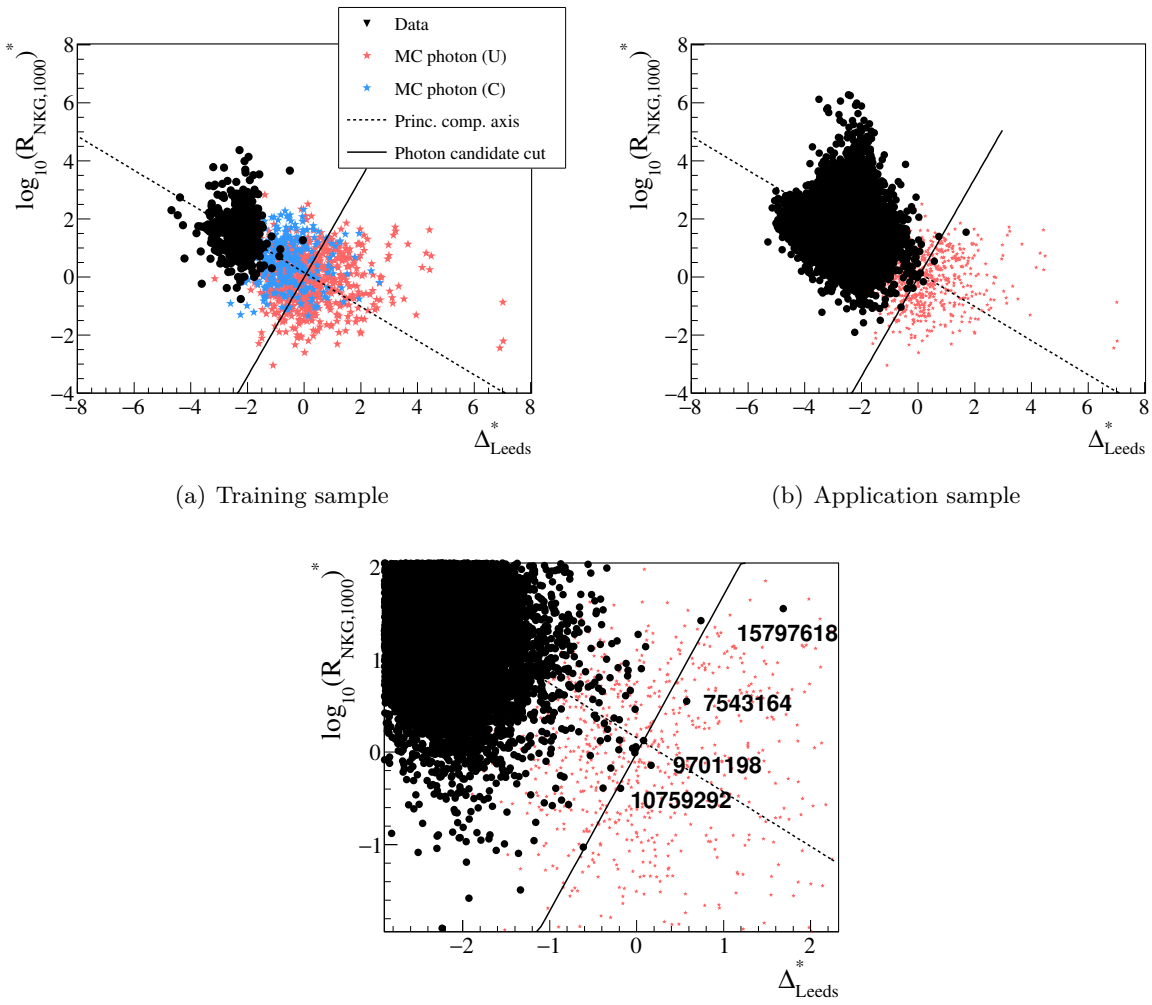

(a) Training sample

(b) Application sample

(c) Application sample, zoom

Figure 7.4: Training and application of the principal component analysis.

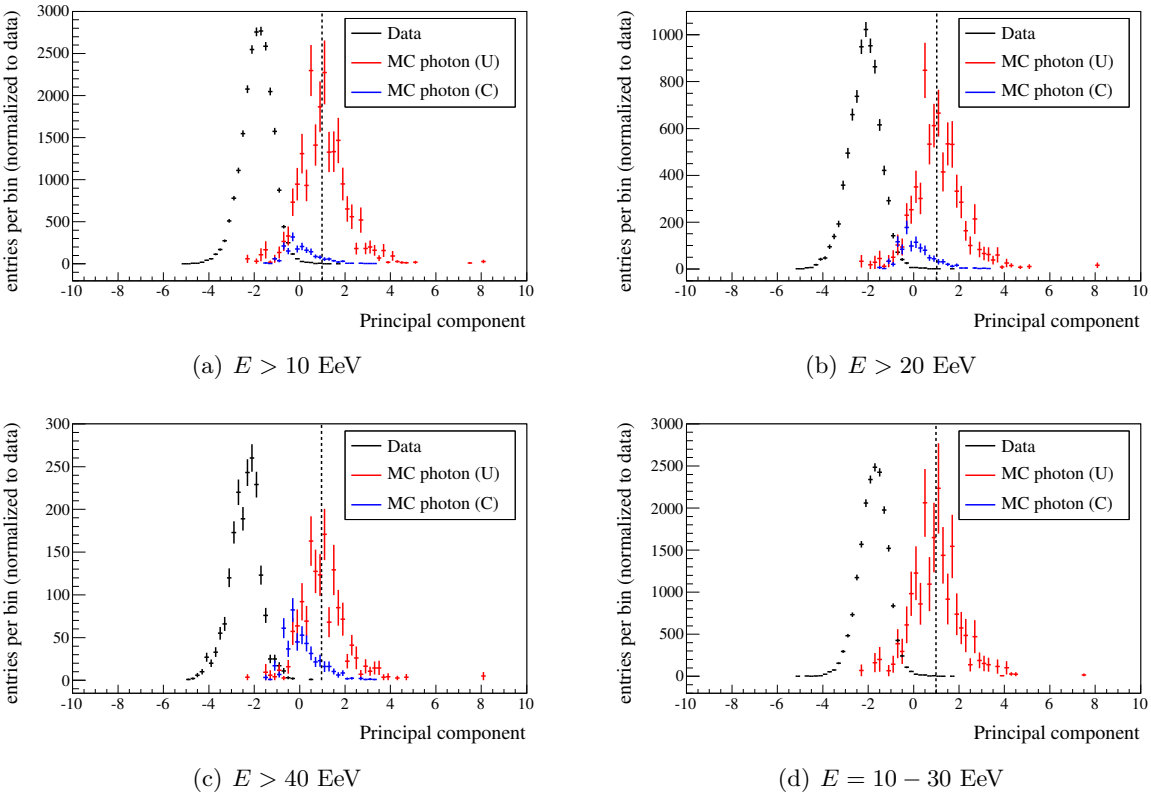

(a) $E > 10$ EeV

(b) $E > 20$ EeV

(c) $E > 40$ EeV

(d) $E = 10 - 30$ EeV

Figure 7.5: Distributions of the principal component. Histograms have been normalized to the number of events in data. The photon cut is set to the median for MC photons (U) and is indicated by the dashed lines.

EeV and no event above 40 EeV. In order to avoid dependences of the derived limits on the background, the observed number of photon candidates is entirely treated as signal as a conservative assumption. The upper limits on the integral photon flux, Φ_γ^{95}, and photon fraction, F_γ^{95}, have been defined in Eqs. 4.22 and 4.23. The photon selection and reconstruction efficiency, ε, is defined as

$$\begin{aligned} \varepsilon &= \varepsilon_{01} \cdot \varepsilon_2 \cdot \varepsilon_3 \\ &= \frac{w_{\mathrm{U+C,trigg.rec.}}(E_{\gamma,\mathrm{rec}} > E_0)}{w_{\mathrm{U+C,sim.}}(E_{\gamma,\mathrm{MC}} > E_0)} \times \frac{w_{\mathrm{U+C,par.sel.}}(E_{\gamma,\mathrm{rec}} > E_0)}{w_{\mathrm{U+C,trigg.rec.}}(E_{\gamma,\mathrm{rec}} > E_0)} \times \frac{w_{\mathrm{U+C},\gamma\mathrm{cand.}}}{w_{\mathrm{U+C,sel.}}(E_{\gamma,\mathrm{rec}} > E_0)}, \end{aligned} \tag{7.3}$$

with ε_{01} the trigger and reconstruction efficiency, ε_2 the parameter quality selection efficiency, ε_3 the photon candidate cut efficiency above the photon median obtained from non-preshowered photons (U) and with $w_{\mathrm{U+C},*}$ the total / triggered and reconstructed / quality selected / identified sum of weights of MC photon events (U+C), reweighted to a spectrum with slope α. Here we calculate ε_{01}, simulating each MC shower in the detector up to five times to increase statistics.

Applying the frequentist Feldman-Cousins approach without background subtraction, we obtain an integral flux limit of $1.9 \cdot 10^{-3}$ km^{-2} sr^{-1} yr^{-1} ($0.99 \cdot 10^{-3}$ km^{-2} sr^{-1} yr^{-1}, $0.49 \cdot 10^{-3}$ km^{-2} sr^{-1} yr^{-1}) above 10 EeV (20 EeV, 40 EeV) at 95% C.L., for zenith angles between 30° and 60°. The corresponding fraction limits are 0.72% (1.6%, 6.17%) above 10 EeV (20 EeV, 40 EeV). The photon fraction limits (cf. Eq. 4.23) have been calculated using the integrated combined Auger energy spectrum [263] above 10 EeV (20 EeV, 40 EeV), scaled to the effective exposure of this analysis (accounting for the zenith angle range, sample size and efficiency). A differential upper limit has also been placed for the first time in the range of $10 - 30$ EeV, with $\Phi_\gamma^{95} = 2.59$ km^{-2} sr^{-1} yr^{-1} and $F_\gamma^{95} \approx 2.7\%$. In this region it is most likely to observe a photon. A summary of the complete results can be found in Tab. 7.1 in the centered columns. A search for UHE photons with the surface detector using a different parameter related to the arrival time distribution has been presented in [250].

The results are shown in Fig. 7.6 (photon flux) and in Fig. 7.7 (photon fraction). A continuous line and the sensitivity of this analysis for the case of no photon candidates is also shown. In the region of $E_0 = 10$ EeV there are statistical fluctuations due to an event close to the candidate cut. The increase at highest energies comes from the photon selection and reconstruction efficiency. For the range up to ~ 40 EeV the upper limits are in the range of the GZK photon predictions from *Gelmini et al.* [75]. The upper limits on the integral photon flux were shown at the ICRC 2015 [232].

Assuming an exposure of 5042.27 km^2 sr as the average per year and 30135.90 km^2 sr yr for the integral over the years 2004-2012 (excluding the non-recoverable part of the Comm's crisis), the extrapolation of the sensitivity to the year 2025 is indicated as well by the lower line. The expected upper limits in the range of $E_0 = 10 - 30$ EeV are somewhere between the current upper limits and the sensitivity, depending on the number of photon candidates. The analysis could be improved by a background rejection, but this would also introduce a dependence on hadronic simulations. The sensivity for the year 2025 is in the range of the GZK photon predictions of *Sarkar et al.* [94] and could already challenge predictions from Lorentz invariance violation (LIV)[231].

Statistical uncertainties of the photon candidate cut are shown as well (left column for the cut shifted by $-\sigma$, right column for the cut shifted by $+\sigma$). The uncertainty σ of the photon median has been derived with the bootstrap method and influences the number of photon candidate

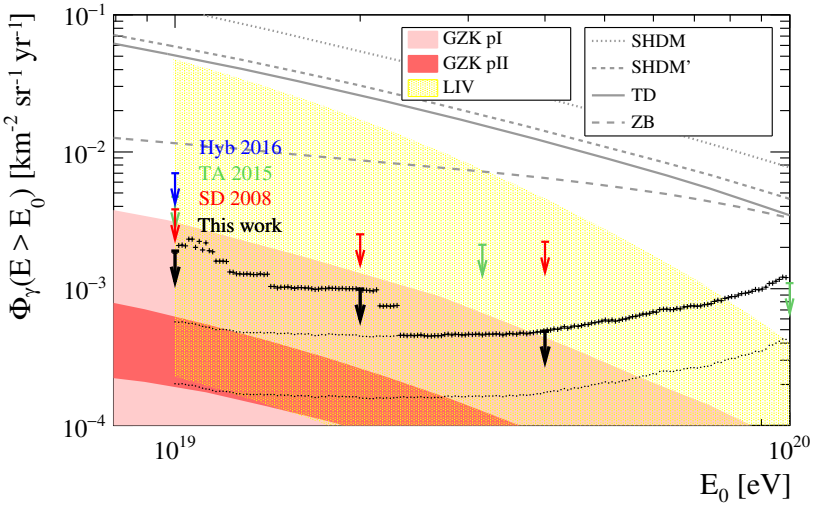

Figure 7.6: Upper limits (95% C.L.) on the integral, diffusive photon flux derived from UHECR experiments: Telescope Array (TA) [228] and the Pierre Auger Observatory (SD, Hyb) [93, 229] together with the result of this work. The sensitivity for the case of no photon candidate with the current dataset (upper line) and an extrapolation to 2025 (lower line) are indicated as lines. A continuous band of the upper limits from this work is indicated as small crosses. Assumed is an E^{-2}-spectrum for photons. In addition to top-down models (TD, Z-Burst and SHDM from [75], SHDM' from [76]) and GZK photons in astrophysical scenarios (cf. Sec. 2.6.1) [75, 94], predictions for Lorentz invariance violation (LIV) [231] are shown.

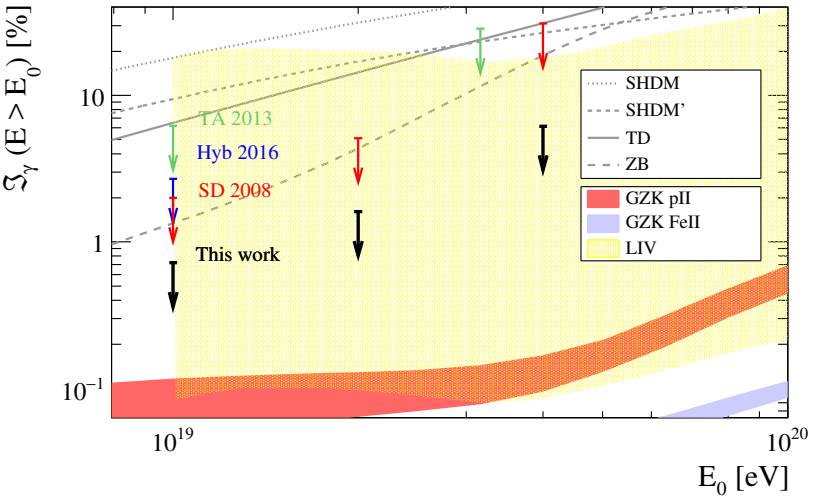

Figure 7.7: Upper limits (95% C.L.) on the integral, diffusive photon fraction derived from UHECR experiments: Telescope Array (TA) [227] and the Pierre Auger Observatory (SD, Hyb) [93, 229] together with the result of this work. Assumed is an E^{-2}-spectrum for photons. In addition to top-down models (TD, Z-Burst and SHDM from [75], SHDM' from [76]) and GZK photons in astrophysical scenarios (cf. Sec. 2.6.1) [94], predictions for Lorentz invariance violation (LIV) [231] are shown.

events, N_γ, and the photon selection and reconstruction efficiency, ε. The uncertainty of the weighted efficiencies, σ_ε is estimated as [264]:

$$\begin{aligned} \sigma_\varepsilon &= \frac{\sqrt{f_1 + f_2}}{w^2_{\text{total}}} \text{ with} \\ f_1 &= w^2_{\text{selected}} \cdot (w_{\text{total,squared}} - w_{\text{selected,squared}}) \\ f_2 &= (w_{\text{total}} - w_{\text{selected}})^2 \cdot w_{\text{selected,squared}} \end{aligned}$$

with w_* the sum of weights and $w_{*,\text{squared}}$ the sum of squared weights of the selected events (or all events). The uncertainty of the photon flux or fraction x is then

$$\sigma_x = x \cdot \frac{\sigma_\varepsilon}{\varepsilon}.$$

For $E > 10$ EeV the number of candidates varies between 8 and 3 candidates. Above 20 EeV and 40 EeV the uncertainty affects only the photon selection and reconstruction efficiency, ε. The corresponding results for different spectral indices α of the MC photons are summarized in Tab. 7.2 ($\alpha = 1.7$) and in Tab. 7.3 ($\alpha = 3.0$). For the lowest energy threshold, the statistical uncertainties dominate over the systematic effect of the spectral index and over the effect of smearing the photon energy within an uncertainty of approximately 35%. According to the real spectrum obtained with the SD, it has been checked [265] that the probability to have a triggered station removed from the second hexagon is less than 5% for an E^{-2}-spectrum and even smaller for the third hexagon. Thus the bias of using an ideal detector in simulations for this analysis is expected to be negligible in the combined quality selection of the risetime and LDF parameter with at least four selected risetime stations.

Table 7.1: UHE Photon search: The uncertainties have been obtained shifting the photon cut within statistical uncertainties of the photon candidate cut. The assumed photon spectrum is $\alpha = -2.0$ and the zenith range is $30° - 60°$. The number of photon candidates at 95% C.L. has been calculated acc. to Feldman-Cousins, without subtraction of background. The centered block for the results of an energy threshold corresponds to the photon median, the left column to the cut shifted by $-\sigma$ and the right column to the cut shifted by $+\sigma$.

Data in the training sample (2%)	458
Data in the application sample	22824
Photons (U) (training & application)	757
PCA angle	$-30.4°$
Exposure	33805.7 $\mathrm{km^2\,sr\,yr}$
Exposure (corrected for geometry and dataset)	22086.4 $\mathrm{km^2\,sr\,yr}$

	$E_0 = 10$ EeV	$E_0 = 20$ EeV	$E_0 = 40$ EeV	$E = 10 - 30$ EeV
Photon median (U)	0.99 ± 0.04	1.01 ± 0.04	0.97 ± 0.05	5
$N_\gamma(E_\gamma > E_0)$	8 / 4 / 3	2 / 2 / 2	0 / 0 / 0	5
$N_\gamma^{95}(E_\gamma > E_0)$	15.30 / 9.77 /8.26	6.73 / 6.73 / 6.73	3.10 / 3.10 / 3.10	11.26
$N_{\mathrm{non}-\gamma}(E_{\mathrm{non}-\gamma} > E_0)$	5773	1351	176	2095
ε_{01}	0.89 / 0.89 / 0.89	0.86 / 0.86 / 0.86	0.72 / 0.72 / 0.72	0.92
ε_2	0.56 / 0.56 / 0.56	0.80 / 0.80 / 0.80	0.96 / 0.96 / 0.96	0.43
ε_3	0.49 / 0.47 / 0.45	0.48 / 0.45 / 0.44	0.43 / 0.41 / 0.39	0.49
ε	0.24 ± 0.01 /	0.33 ± 0.02 /	0.30 ± 0.02 /	0.20
	0.23 ± 0.01 /	0.31 ± 0.03 /	0.29 ± 0.02 /	
	0.22 ± 0.01	0.30 ± 0.02	0.30 ± 0.02 /	
$\Phi_\gamma^{95}(E > E_0)/10^{-3}[\ \mathrm{km^{-2}\,sr^{-1}\,yr^{-1}}]$	2.8 ± 0.1 /	0.93 ± 0.06 /	0.46 ± 0.03 /	2.59
	1.9 ± 0.1 /	0.99 ± 0.09 /	0.49 ± 0.04 /	
	1.7 ± 0.1	1.01 ± 0.07	0.52 ± 0.04	
$F_\gamma^{95}(E > E_0)[\%]$	1.08 ± 0.07 /	1.5 ± 0.1 /	5.80 ± 0.4 /	2.73
	0.72 ± 0.05 /	1.6 ± 0.1 /	6.17 ± 0.5 /	
	0.64 ± 0.04	1.6 ± 0.1	6.54 ± 0.5	

Table 7.2: UHE Photon search: The uncertainties have been obtained shifting the photon cut within statistical uncertainties of the photon candidate cut. The assumed photon spectrum is $\alpha = -1.7$ and the zenith range is $30° - 60°$. The number of photon candidates at 95% C.L. has been calculated acc. to Feldman-Cousins, without subtraction of background.

Data in the training sample (2%)	458
Data in the application sample	22824
Photons (U) (training & application)	757
PCA angle	$-30.4°$
Exposure	33805.7 $\mathrm{km^2\,sr\,yr}$
Exposure (corrected for geometry and dataset)	22086.4 $\mathrm{km^2\,sr\,yr}$

	$E_0 = 10$ EeV	$E_0 = 20$ EeV	$E_0 = 40$ EeV	$E = 10 - 30$ EeV
Photon median (U)	0.99 ± 0.04	1.01 ± 0.04	0.98 ± 0.05	5
$N_\gamma(E_\gamma > E_0)$	4	2	0	5
$N_\gamma^{95}(E_\gamma > E_0)$	9.77	6.73	3.10	11.26
$N_{\mathrm{non-}\gamma}(E_{\mathrm{non-}\gamma} > E_0)$	5773	1351	176	2095
ε_{01}	0.86	0.81	0.69	0.92
ε_2	0.62	0.83	0.97	0.46
ε_3	0.45	0.43	0.39	0.49
ε	0.24 ± 0.01	0.29 ± 0.02	0.26 ± 0.02	0.21
$\Phi_\gamma^{95}(E > E_0)/10^{-3}[\ \mathrm{km^{-2}\,sr^{-1}\,yr^{-1}}]$	1.8 ± 0.1	1.04 ± 0.08	0.54 ± 0.04	2.46
$F^{95}(E > E_0)[\%]$	0.69 ± 0.04	1.7 ± 0.1	6.7 ± 0.5	2.59

Table 7.3: UHE Photon search: The uncertainties have been obtained shifting the photon cut within statistical uncertainties of the photon candidate cut. The assumed photon spectrum is $\alpha = -3.0$ and the zenith range is $30° - 60°$. The number of photon candidates at 95% C.L. has been calculated acc. to Feldman-Cousins, without subtraction of background.

Data in the training sample (2%)	458
Data in the application sample	22824
Photons (U) (training & application)	757
PCA angle	$-30.4°$
Exposure	33805.7 $\mathrm{km}^2\,\mathrm{sr\,yr}$
Exposure (corrected for geometry and dataset)	22086.4 $\mathrm{km}^2\,\mathrm{sr\,yr}$

	$E_0 = 10$ EeV	$E_0 = 20$ EeV	$E_0 = 40$ EeV	$E = 10 - 30$ EeV
Photon median (U)	0.99 ± 0.07	1.07 ± 0.07	0.98 ± 0.08	5
$N_\gamma(E_\gamma > E_0)$	4	2	0	4
$N_\gamma^{95}(E_\gamma > E_0)$	9.77	6.73	3.10	9.77
$N_{\mathrm{non}-\gamma}(E_{\mathrm{non}-\gamma} > E_0)$	5773	1351	176	2095
ε_{01}	0.98	1.02	0.90	0.98
ε_2	0.41	0.70	0.93	0.36
ε_3	0.49	0.48	0.45	0.49
ε	0.19 ± 0.02	0.34 ± 0.09	0.38 ± 0.04	0.17
$\Phi_\gamma^{95}(E > E_0)/10^{-3}[\ \mathrm{km}^{-2}\,\mathrm{sr}^{-1}\,\mathrm{yr}^{-1}]$	2.3 ± 0.2	0.9 ± 0.2	0.37 ± 0.04	2.60
$F^{95}(E > E_0)[\%]$	0.9 ± 0.1	1.4 ± 0.3	4.6 ± 0.5	2.74

7.1 Photon Candidate Events

The PCA has identified 4 photon candidate events for the integral flux above 10 EeV. The reconstructed energy and geometry and the separation parameter are summarized in Tab. 7.4. The SD traces of the non- or high-gain-saturated stations with a signal above 6 VEM and distances between 600 m and 2000 m are shown in Figs. 7.10 to 7.13 and the station risetime as a function of the distance to the shower core is shown in Fig. 7.8. We cannot give a clear interpretation without a dedicated study of hadronic simululations, but we want to briefly discuss our findings. Events 9701198 and 15797618 have been detected with the SD and FD. Thus we have a direct measurement of the energy and $X_{\max}$. The longitudinal profiles are shown in Fig. 7.15.
The reconstructed energy and $X_{\max}$ of event **9701198** and their reconstruction uncertainties should be looked at critically as the shower maximum is not in the field-of-view of the telescope. Anyway, within this restriction, the FD energy appears to be closer to the reconstructed hadronic energy than to the reconstructed photon energy of the SD. A point has been added to the elongation rate in Fig. 7.14. Within the reconstruction uncertainties, the event is not compatible with the average found for hadrons. In the SD measurement of this event, all selected stations are above the risetime benchmark from data, as shown in Fig. 7.8(a). The LDF has a structure around 1000 m and above and is below the signal expected from the LDF fit (cf. Fig. 7.9(a)). This candidate remains very interesting.
Event **15797618** has been observed by two telescopes. One telescope appears to have a hole in the longitudinal profile (cf. Fig. 7.15(a)) which might be due to a significant cloud coverage. Thus the reconstructed energy and $X_{\max}$ and their uncertainties should also be looked at critically. Still, the profile has a surprisingly good quality. The measurement of the second telescope (cf. Fig. 7.15(b)) confirms the observations of a very deep shower maximum. Within the restriction due to a possible cloud coverage, the FD energies appear to be closer to the reconstructed hadronic energy than to the reconstructed photon energy of the SD. For photon showers with LPM effect we expect outliers with a deeper shower maximum than the average found for photons and with an overestimated reconstructed photon energy. It has been checked on the simulated showers that the overestimation can be of a factor 2. Two points have been added to the elongation rate in Fig. 7.14. Within the reconstruction uncertainties, both observations of this event the event is not compatible with the average found for hadrons, but also not with the average for photons. Assuming that the reconstruction bias of the longitudinal profile is not dominant, the exceptionally deep shower maximum might be explained by a photon encountering the LPM effect. In the SD measurement of this event, station 1362 (cf. Fig. 7.11(a)) shows a particularly slow rise of the SD signal which is typical for photon-induced showers. Stations 1372 and 848 are closer to the benchmark from data but still above. Station 852 shows a structure with multiple peaks which leads to a very slow increase of the risetime. The distance dependence of the risetime is not compatible with the average expected from data (cf. Fig. 7.8(b)). The LDF does not appear to be particularly photon-like (cf. Fig. 7.9(b)). Still, this candidate remains interesting.
Event **10759292** is the only candidate event with only a moderate inclination of 30.9°. Station 1089 is only slightly above the benchmark and station 982 is below the benchmark. The remaining two stations are above the benchmark and create a slope that is larger than for the average found in data (cf. Fig. 7.8(d)). The observed signal above 1000 m is below the signal expected from the LDF fit (cf. Fig. 7.9(d)).

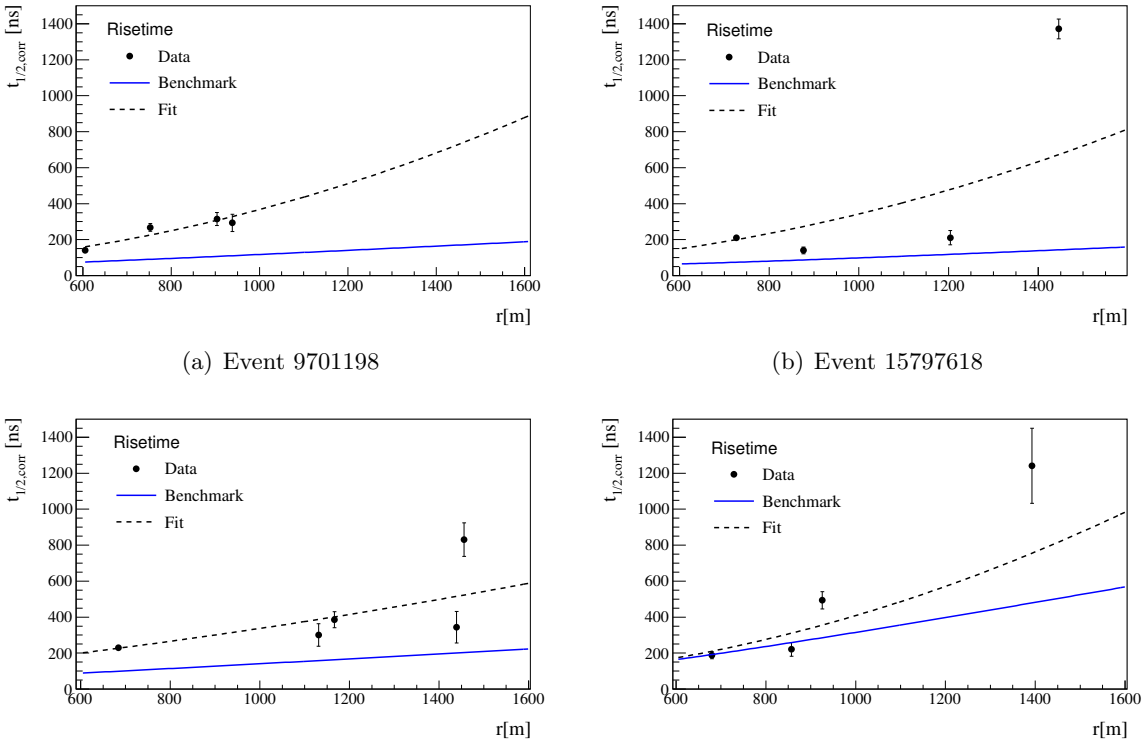

(a) Event 9701198

(b) Event 15797618

(c) Event 7543164

(d) Event 10759292

Figure 7.8: SD risetimes of the photon candidate events: Shown are stations passing the risetime quality selection applied for Δ_{Leeds}. The blue line indicates the benchmark obtained from data and the black dashed line indicates a fit as used for $t_{1/2}(1000)$. MC photon showers are expected to have larger risetimes than hadronic showers and a larger slope.

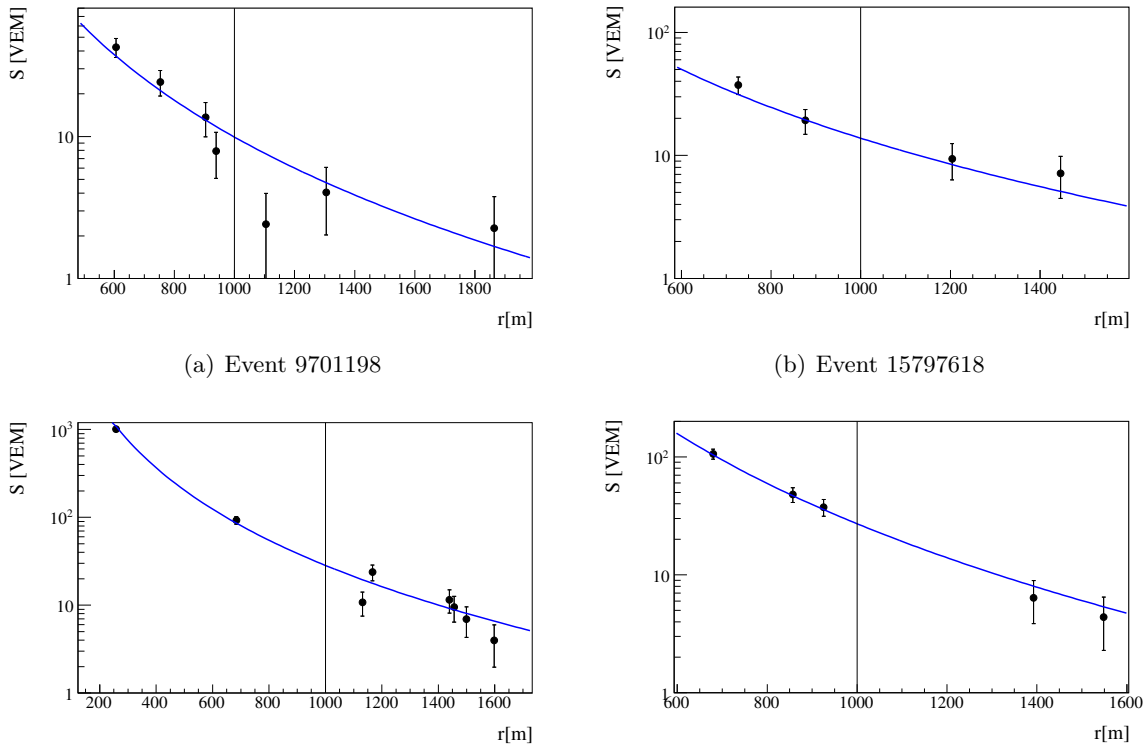

(a) Event 9701198

(b) Event 15797618

(c) Event 7543164

(d) Event 10759292

Figure 7.9: SD signals of the photon candidate events: Full markers indicate stations passing the LDF quality selection. Stations with a core distance $r > 1000$ m have been selected for $\log_{10}(R_{\mathrm{NKG},1000})$. The LDF fit result is indicated with a blue line. MC photon showers are expected to have a steeper LDF than hadronic showers. The LDF shape has been fixed to a parametrization in S_{1000} and θ obtained from data and the free parameters are S_{1000} and the shower core. Thus the stations of MC photon showers at $r \gtrsim 1000$ m are expected to have signals smaller than expected from the LDF fit.

Table 7.4: Photon candidate events - Energy, geometry, separation parameters and FD information

SD ID	θ_{SD}	ϕ_{SD}	$E_{\gamma,\mathrm{SD}}$	$E_{\mathrm{hadr,SD}}$	E_{FD}	$X_{\mathrm{max,FD}}$
9701198	56.4°	301.5°	12.9 EeV	3.59 EeV	(2.8 ± 0.5) EeV	1068 ± 74 g/cm^2
15797618	59.3°	130.5°	19.8 EeV	5.87 EeV	(3.3 ± 0.5) EeV	1309 ± 52 g/cm^2
					(4.5 ± 0.4) EeV	1284 ± 22 g/cm^2
7543164	53.9°	349.2°	22.9 EeV	9.41 EeV	no FD	no FD
10759292	30.9°	35.4°	17.1 EeV	5.11 EeV	no FD	no FD

SD ID	Δ_{Leeds}	$\log_{10}(R_{\mathrm{NKG,1000}})$	R_{c}	$t_{1/2}(1000)$	N_{cand}
9701198	5.73	-0.087	10.96 km	367.55 ns	7
15797618	9.93	0.098	11.50 km	342.89 ns	5
7543164	5.32	-0.037	11.19 km	337.06 ns	8
10759292	1.70	-0.093	6.75 km	408.58 ns	5

Event **7543164** has been a candidate to the analysis in [250]. It has the highest reconstructed photon energy of all candidates with $E_{\gamma,\mathrm{SD}} = 22.9$ EeV. Station 571 (cf. Fig. 7.12(c)) shows a particularly slow rise of the signal. All of the five selected stations are above the benchmark from data, as shown in Fig. 7.8(c). The observed signal above 1000 m is below the signal expected from the LDF fit (cf. Fig. 7.9(c)). In [250] it is one of two candidates with such behaviour. The other candidate has an energy below 10 EeV after improving the energy scale and is thus not selected for our integral limits. Event **7543164** is a very interesting candidate.
Our analysis has identified four photon candidates that cannot be ruled out due to hardware or event reconstruction issues on the SD side and also the events with FD information are - within certain restrictions - not compatible with the average for data. They remain interesting for further studies involving hadronic simulations.

7.2 Treatment of Preshowered Photons

From the SD measurement, preshowered (C) and non-preshowered (U) photons cannot be distinguished. Still they differ in observables that depend on X_{max} or on the muon content. Also, preshowered photons have a reconstructed photon energy which is on average underestimated by 20% with the calibration derived from non-preshowered photons (see Fig. 9.1(b) in the appendix). For the parameters studied here, preshowered photons lie between non-preshowered photons and hadrons. We account for the preshower effect in the following way:

- Apply the energy scale obtained from photons (U).
- Get the photon expectation from photons (U) only.
- Calculate the photon candidate cut (the median of a single rescaled parmeter (x^*) or the principal component in case of a multivariate analysis) from photons (U) only.
- Take U+C photons for both the total number of events and the selection in the calculation of the selection-, reconstruction- and photon-candidate-cut-efficiency.

Note that the preshower probability might be overestimated in this analysis as current studies of the photon flux from the GZK effect suggest a steeper spectrum than assumed here. As a

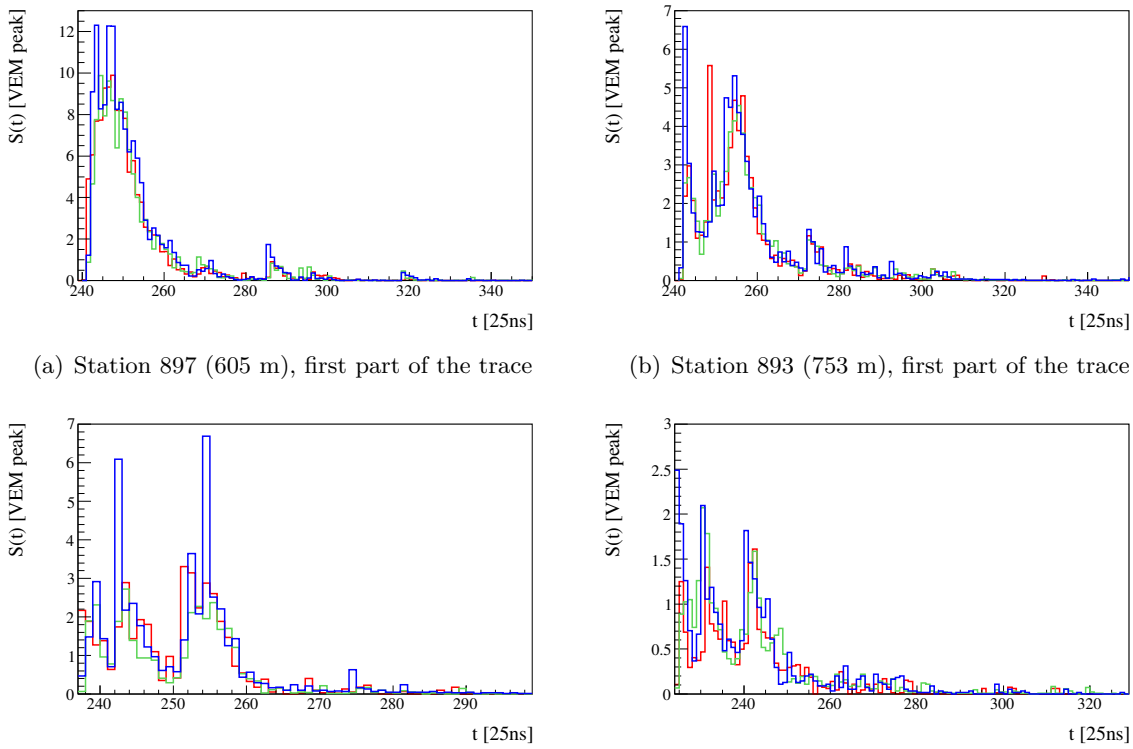

(a) Station 897 (605 m), first part of the trace

(b) Station 893 (753 m), first part of the trace

(c) Station 894 (904 m)

(d) Station 1176 (939 m)

Figure 7.10: Photon candidate event 9701198: Shown are PMT 1 (red), PMT 2 (green) and PMT 3 (blue) of the station given in the caption. Direct light has not been removed in these plots.

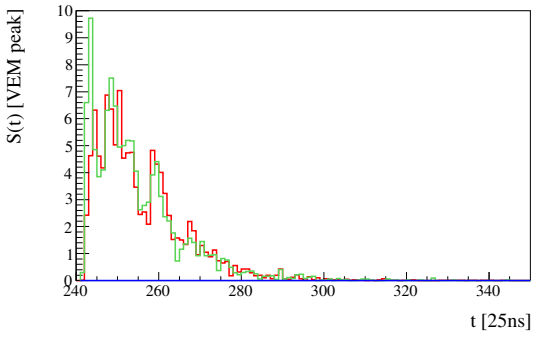

(a) Station 1362 (727 m), first part of the trace

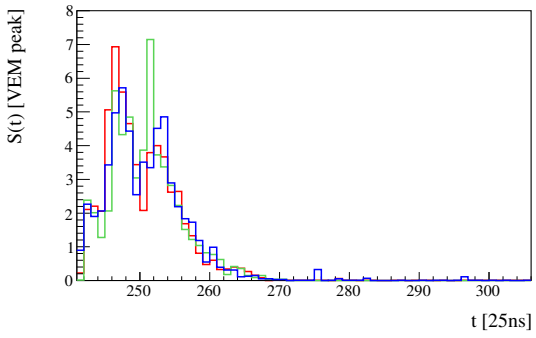

(b) Station 1372 (876 m)

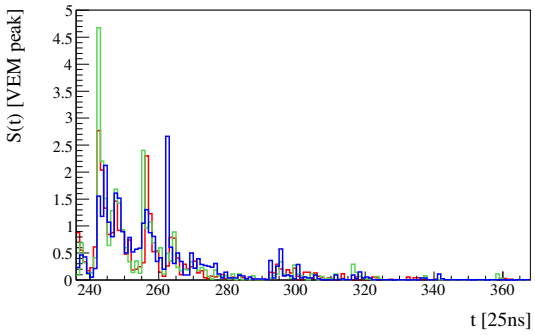

(c) Station 848 (1204 m)

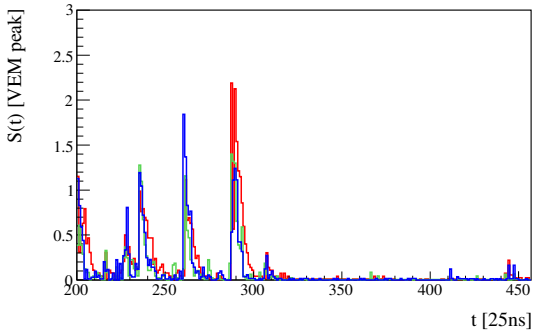

(d) Station 852 (1446 m)

Figure 7.11: Photon candidate event 15797618: Shown are PMT 1 (red), PMT 2 (green) and PMT 3 (blue) of the station given in the caption. Direct light has not been removed in these plots.

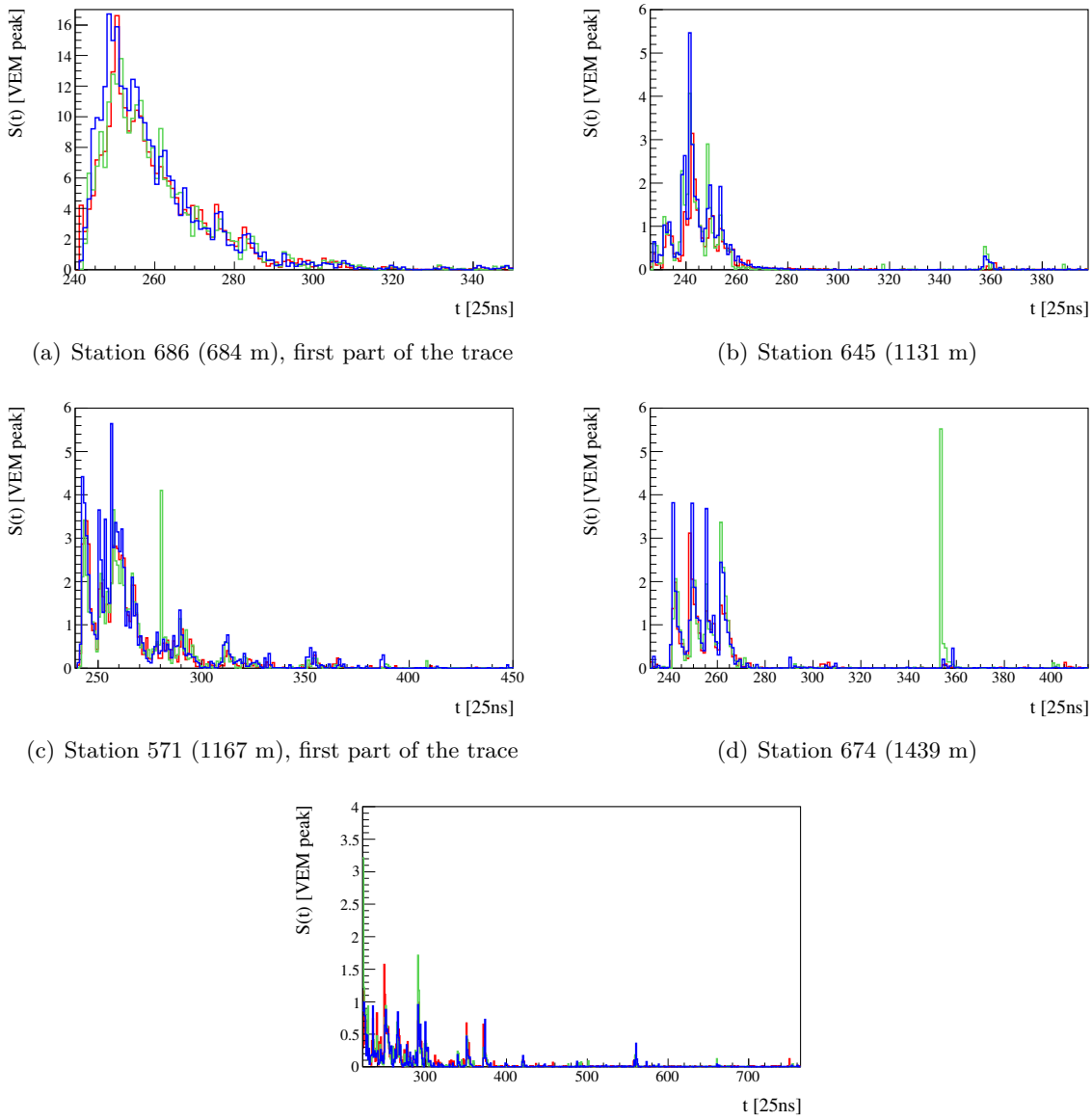

(a) Station 686 (684 m), first part of the trace

(b) Station 645 (1131 m)

(c) Station 571 (1167 m), first part of the trace

(d) Station 674 (1439 m)

(e) Station 578 (1456 m)

Figure 7.12: Photon candidate event 7543164: Shown are PMT 1 (red), PMT 2 (green) and PMT 3 (blue) of the station given in the caption. Direct light has not been removed in these plots.

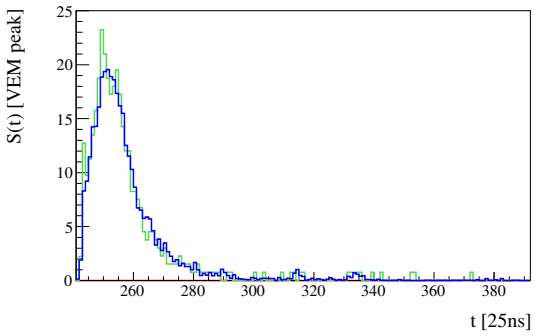

(a) Station 1089 (680 m)

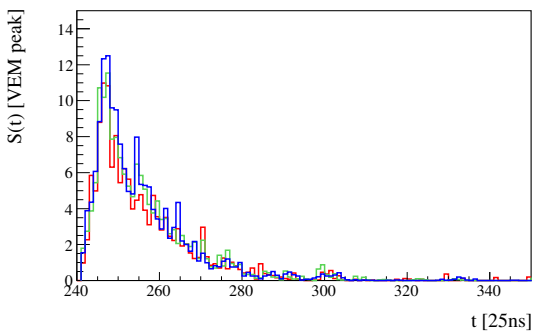

(b) Station 982 (857 m), first part of the trace

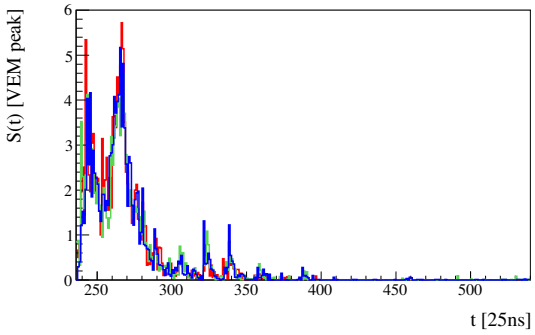

(c) Station 975 (926 m)

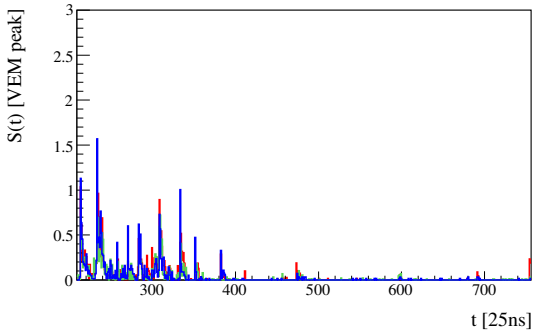

(d) Station 1486 (1393 m)

Figure 7.13: Photon candidate event 10759292: Shown are PMT 1 (red), PMT 2 (green) and PMT 3 (blue) of the station given in the caption. Direct light has not been removed in these plots.

Table 7.5: Photon candidate events - SD information

SD ID	*Station ID*	$S_{\mathrm{non-cleaned}}$	S_{cleaned}	r	$t_{1/2}$
9701198	**897**	42.47 VEM	41.14 VEM	605.20 m	137.82 ns
	893	24.15 VEM	23.23 VEM	752.76 m	276.38 ns
	894	13.65 VEM	12.29 VEM	903.53 m	297.58 ns
	1176	7.89 VEM	7.64 VEM	938.51 m	315.62 ns
15797618	**1362**	37.28 VEM	36.54 VEM	726.88 m	215.28 ns
	1372	19.25 VEM	18.85 VEM	876.42 m	131.85 ns
	848	9.38 VEM	8.71 VEM	1203.84 m	216.77 ns
	852	7.14 VEM	7.14 VEM	1445.72 m	1393.28 ns
7543164	**686**	92.95 VEM	90.83 VEM	684.28 m	250.54 ns
	645	10.81 VEM	10.52 VEM	1131.18 m	250.97 ns
	571	23.84 VEM	22.62 VEM	1166.65 m	400.41 ns
	674	11.54 VEM	10.14 VEM	1439.30 m	298.89 ns
	578	9.52 VEM	9.22 VEM	1456.11 m	896.26 ns
10759292	**1089**	105.81 VEM	105.81 VEM	679.90 m	194.79 ns
	982	47.90 VEM	47.90 VEM	857.05 m	184.72 ns
	975	37.45 VEM	37.14 VEM	925.71 m	510.37 ns
	1486	6.39 VEM	6.39 VEM	1392.82 m	1360.14 ns

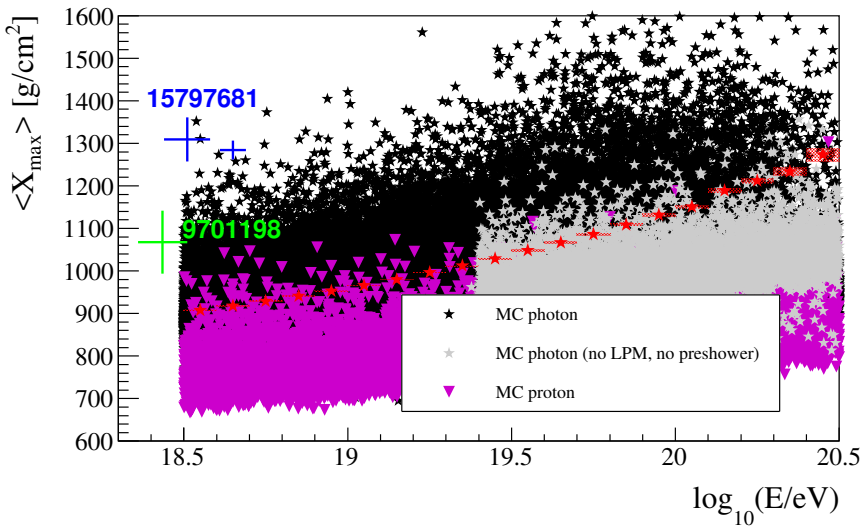

Figure 7.14: Photon candidates (which have additional FD information) are shown along with the elongation rate for non-preshowered photons (black and red), photon without preshower and LPM effect (grey) and proton (magenta) presented earlier in this thesis (Fig. 3.2). The different primaries have been simulated with CONEX, cf. App. B.

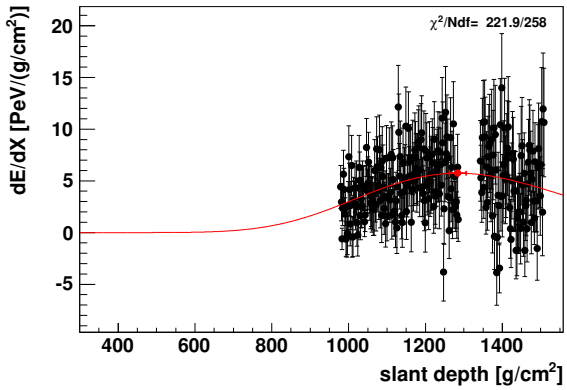

(a) Event 15797618, lonngitudinal profile (telescope 1)

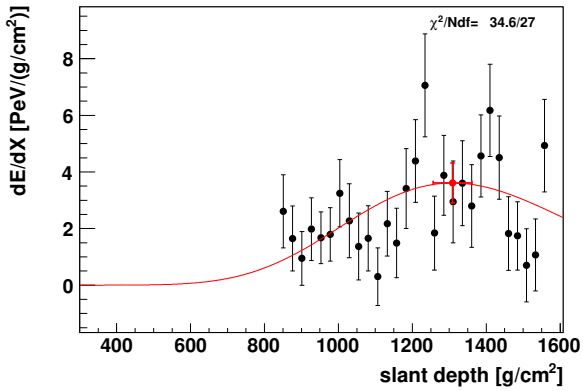

(b) Event 15797618, longitudinal profile (telescope 2)

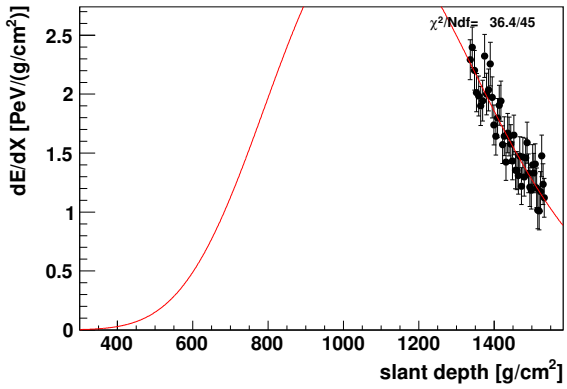

(c) Event 9701198, longitudinal profile

Figure 7.15: Two of the photon candidates have additional FD information. Shown are the longitudinal profiles of the shower.

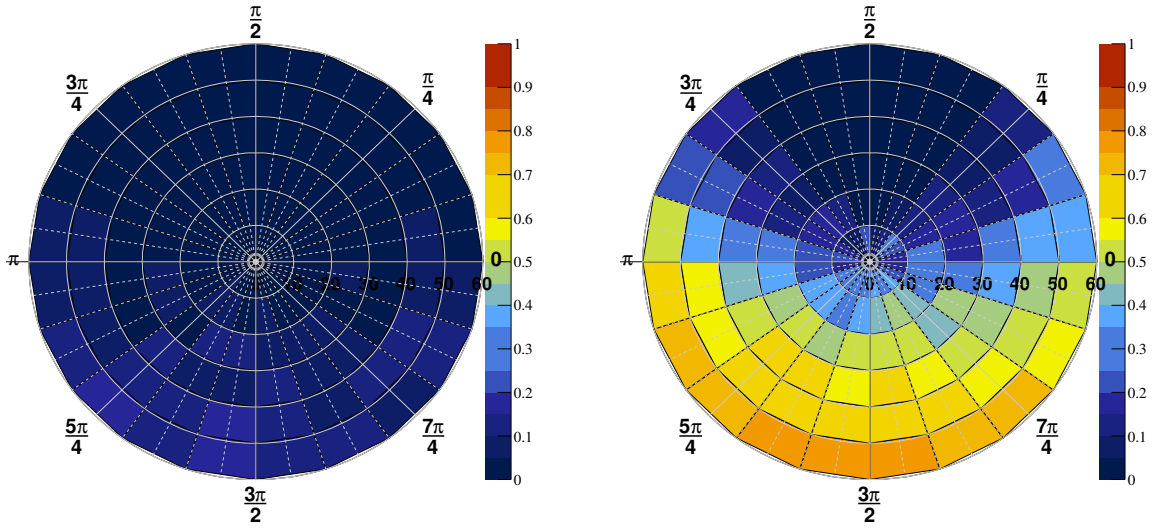

(a) For energies $10^{19.6} < E/\text{ eV} < 10^{19.85}$

(b) For energies $10^{19.85} < E/\text{ eV} < 10^{20.1}$

Figure 7.16: The preshower probability and its directional and energy dependence, based on 100000 showers simulated with CONEX (dataset is described in App. B). Directional dependence in different energy bins, with a scale from 0 (blue) to 1 (red).

simple approach we weight all photons showers (U+C) to a spectrum $\alpha = -2$ (or the spectrum assumption mentioned).
Based on a set of 100000 showers simulated with CONEX (cf. App. B), we have checked if it is possible to exclude certain regions in the space angle to obtain a significant reduction of the fraction of preshowered photons. As shown in Fig. 7.16(b), there is no small, limited region with a high preshower probability, but rather a space angle of π. Thus a geometric cut to reject preshower photons would reduce the exposure by a factor of 2. Based on this, we do not set up any directional cut.

7.3 Setting up the Parameter Set: Comparison of Parameters

The following different event-based separation parameters have been compared to find the most powerful parameter of each of the following groups:

- **Station risetime**: Δ_{Leeds} and $t_{1/2}(1000)$ (for different selections)
- **LDF shape**: $\log_{10}(R_{\text{NKG}})$, $\log_{10}(R_{\text{NKG},1000})$, $\log_{10}(S_4^{\text{n}})$ and $\log_{10}(S_{4,1000}^{\text{n}})$
- **Radius of curvature**: R_{c}
- **Number of triggered stations** belonging to an air shower: N_{cand}

The station and event quality selection(s) have been established in the previous sections. Figure 7.18 shows a comparison of the integral photon selection efficiency ε_2 for the different parameter groups. A selection efficiency of 100% is obtained for N_{cand} and (almost) for the LDF parameters. For the background we use the data burn sample and as our signal the full photon

Table 7.6: Comparison of different SD separation parameters ($E > 10$ EeV) based on the data burn sample and all MC photon showers. N_γ is the number of photon candidates and N_γ^{95} the corresponding number at 95% C.L. for the Feldman-Cousins approach). N is the number of selected stations, $n = N_{\rm cand}$ the number of triggered stations of a shower and $n_{\rm cl}$ the number of stations closer than 1000 m. S is the observed signal. Brackets indicate cases that have not been taken into account when setting up the analysis. Different selections have been specified.

Case	*Parameter*	*Selection*	N_γ (N_γ^{95})	ε_2	$N_{\rm par}$	η
1	$\Delta^*_{\rm Leeds}$	$S > 6$ VEM, $N > 3$	1 (5.145)	0.56	9.15	1.99
(2)	$\Delta^*_{\rm Leeds}$	$S > 6$ VEM, $N \geq 3$	2 (6.725)	0.82	8.17	1.67
(3)	$\Delta^*_{\rm Leeds}$	$S > 6$ VEM, $N \geq 2$, $n \geq 5$	3 (8.255)	0.82	10.06	1.54
4	$\Delta^*_{\rm Leeds}$	$S > 10$ VEM, $N > 3$	0 (3.095)	0.33	9.37	2.17
5	$\Delta^*_{\rm Leeds}$	$S > 10$ VEM, $N \geq 3$	2 (6.725)	0.62	10.89	1.96
(6)	$\Delta^*_{\rm Leeds}$	$S > 10$ VEM, $N \geq 2$, $n \geq 5$	2 (6.725)	0.77	8.78	1.40
7	$t_{1/2}(1000)^*$	$S > 6$ VEM, $N > 3$	1 (5.145)	0.56	9.15	2.04
(8)	$t_{1/2}(1000)^*$	$S > 6$ VEM, $N \geq 3$, $n_{\rm cl} > 0$	2 (6.725)	0.70	9.66	1.92
(9)	$t_{1/2}(1000)^*$	$S > 6$ VEM, $N \geq 3$	2 (6.725)	0.82	8.17	1.81
10	$t_{1/2}(1000)^*$	$S > 10$ VEM, $N > 3$	1 (5.145)	0.33	15.57	2.31
11	$t_{1/2}(1000)^*$	$S > 10$ VEM, $N \geq 3$, $n_{\rm cl} > 0$	2 (6.725)	0.54	12.48	2.17
12	$t_{1/2}(1000)^*$	$S > 10$ VEM, $N \geq 3$	2 (6.725)	0.62	10.89	1.99
13	$\log_{10}(R_{\rm NKG})^*$		18 (27.84)	1.00	27.84	1.17
14	$\log_{10}(R_{\rm NKG,1000})^*$		18 (27.84)	0.99	28.00	1.26
15	$\log_{10}(S_4^{\rm n})^*$		57 (73.345)	1.00	73.35	1.11
16	$\log_{10}(S_{4,1000}^{\rm n})^*$		22 (32.825)	0.99	33.02	1.27
17	$R_{\rm c}^*$		18 (27.84)	0.82	34.11	0.96
18	$N_{\rm cand}^*$		159 (185.345)	1.00	185.35	0.66

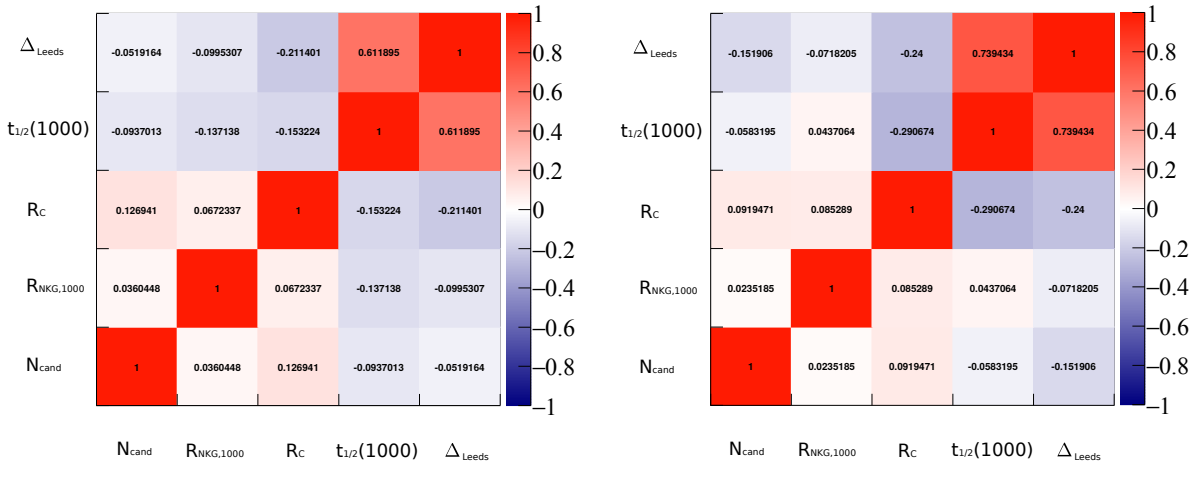

(a) Data (b) MC Photon

Figure 7.17: Correlation of the separation parameters. Note that the correlation factor has been calculated using the rescaled definition, x^*, of the respective separation parameter x. The risetime parameters have been calculated from selected stations with an observed signal $S_{\rm obs} > 6$ VEM and for events with at least four selected stations. The color scale indicates the correlation coefficient.

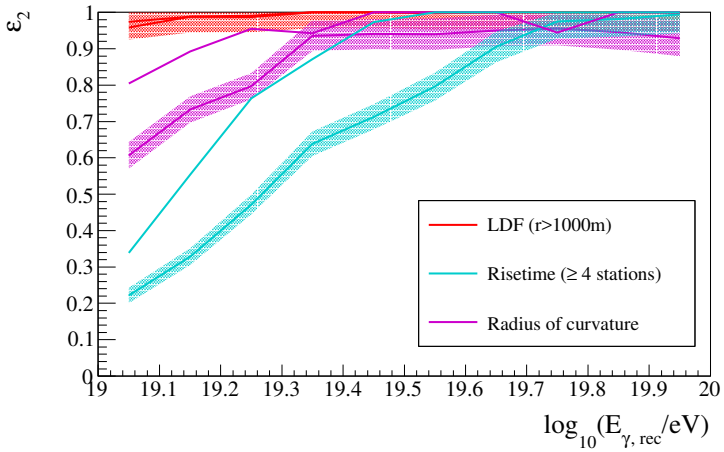

Figure 7.18: Comparison of the parameter selection efficiency for the separation parameters compared in this analysis. Shown are MC photon (lower lines) and the data burn sample (upper lines).

MC sample, assuming that the bias from the photon sample is small. The zenith and energy dependence for MC photons has been removed by using the rescaled parameter x^*, as introduced in Eq. 7.2. We have defined the following criteria to compare the single parameters:

1. Compare $N_{\mathrm{par}} = N_\gamma^{95}/\varepsilon_2$ (with N_γ^{95} the number of photon candidates that are selected with the photon median from non-preshowered photons)

2. For parameters with the same N_{par}, compare their merit factor $\eta = |\bar{x}_\gamma - \bar{x}_{\mathrm{BKG}}|/\sqrt{\sigma_\gamma^2 + \sigma_{\mathrm{BKG}}^2}$ (with $\bar{x}$ and σ_x the mean value and standard deviation of the signal and background samples)

The results for the single parameters are summarized in Tab. 7.6. The strongest parameter group is the risetime. Applying the same selection, both parameters show a compatible performance. The advantage of Δ_{Leeds} is that it does not base on an event-wise fit and is thus more stable. In previous studies [252] the following selection was applied for Δ_{Leeds}: $N_{\mathrm{St}} \geq 2$ and $N_{\mathrm{cand}} \geq 5$. We have shown that $N_{\mathrm{St}} \geq 3$ or $N_{\mathrm{St}} \geq 4$ both give a better separation in the case of $S_{\mathrm{obs}} > 6$ VEM. In any case this selection is not preferred as the cut $N_{\mathrm{cand}} \geq 5$ introduces an unneccessary energy dependence. Note that when setting up the analysis, the following cases have not been taken into account: 2, 3, 6. They have been added afterwards to complete the overview. For the LDF parameters, $\log_{10}(R_{\mathrm{NKG,1000}})$ is preferrable. We find that $\log_{10}(R_{\mathrm{NKG,1000}})$ (case 14) is more powerful than R_{c}. The radius of curvature was used e.g. for SD photon limits from 2008 [93], together with $t_{1/2}(1000)$ ($S_{\mathrm{obs}} > 10$ VEM, $N_{\mathrm{sel}} > 3$). The number of triggered stations does not add much separation. The correlation between the single parameters has been analyzed in Figs. 7.17(a) (data) and 7.17(a) (MC photon). The combination of Δ_{Leeds} (for $S_{\mathrm{obs}} > 6$ VEM, $N_{\mathrm{sel}} > 3$) and $\log_{10}(R_{\mathrm{NKG,1000}})$ has only a little correlation (absolute value of less than 0.1) and is expected to give a significant improvement compared to $t_{1/2}(1000)$ together with R_{c}.

7.4 Setting up the Parameter Set: Combination of Parameters

The most powerful parameters discussed in the previous section are: Δ_{Leeds} for the risetime parameters, $\log_{10}(R_{\mathrm{NKG,1000}})$ for the LDF parameters and in addition R_{c} and N_{cand}. As a last step of the analysis setup, we compare different combinations of these parameters on the data burn sample and all MC photon showers in a PCA. The method is the same as discussed at the beginning of this chapter. As expected, the combination **1+14**, which is Δ_{Leeds} (for $S_{\mathrm{obs}} > 6$ VEM, $N_{\mathrm{sel}} > 3$) and $\log_{10}(R_{\mathrm{NKG,1000}})$, gives the best expected performance and will be used for the final analysis. The combination **2+14**, where case **2** has the best separation for the risetime as a single parameter, is less powerful combined with the LDF parameter. Case **(10+17)** corresponds to the parameters $t_{1/2}(1000)$ ($S_{\mathrm{obs}} > 10$ VEM, $N_{\mathrm{sel}} > 3$) and R_{c}, as used in [93], without a restriction of the core distance for calculation of $t_{1/2}(1000)$. The photon hadron separation has been significantly improved.

Table 7.7: Comparison of different parameter combinations ($E > 10$ EeV) based on the data burn sample and all MC photon showers. N_γ is the number of photon candidates and N_γ^{95} the corresponding number at 95% C.L. for the Feldman-Cousins approach). The cases are the same as in Tab. 7.6.

Cases	N_γ (N_γ^{95})	ε_2	N_{par}	η
1+14	0 (3.095)	0.56	5.52	2.33
1+14+17	0 (3.095)	0.51	6.08	1.94
2+14	1 (5.145)	0.82	6.30	2.20
1+17	1 (5.145)	0.51	10.11	1.68
(10+17)	1 (5.145)	0.46	11.16	1.96

CHAPTER 8

Conclusion

In this work we have presented an update on the upper limits on the UHE photon flux and fraction with the surface detector (SD) of the Pierre Auger Observatory above 10 EeV. The dataset of 2004/01/01 to 2013/05/14 has been used to search for UHE photons. The main result of this work is a significant improvement of the last published limits, entering the region of photonoptimistic GZK-predictions. The upper limit (95% C.L.) on the diffusive, integral photon flux above 10 EeV for zenith angles between 30° and 60°, is $1.9 \cdot 10^{-3}$ km^{-2} sr^{-1} yr^{-1}, corresponding to a maximum photon fraction of 0.72%. For 20 EeV (40 EeV) it is $0.99 \cdot 10^{-3}$ km^{-2} sr^{-1} yr^{-1} ($0.49 \cdot 10^{-3}$ km^{-2} sr^{-1} yr^{-1}), corresponding to a maximum photon fraction of 1.6% (6.17%). Top-down scenarios are challenged by the results of this work. A differential upper limit has also been placed for the first time (in the range of $10-30$ EeV), with a maximum photon fraction of $\sim 2.7\%$. In this energy range it is most likely to observe a photon. Photon candidate events are being discussed briefly. Within the selection of showers that reach their shower maximum almost above the ground level of the Pierre Auger Observatory, photon-induced air-showers around 10 EeV with a delayed shower development due to the LPM effect are particularly interesting. The observation of an UHE photon would be a completely new window to look at the processes at the source or the CR propagation. But this cannot be done without dedicated simulation studies. These studies might be a topic for future analyses.

Different separation variables have been studied and compared, such as the SD signal risetime, the lateral distribution function (LDF) of the SD signal, the radius of curvature and the number of triggered stations. We have optimized the selection towards a maximum selection efficiency with a good parameter reconstruction quality. In order to define an event parameter on the base of the risetime of single SD stations, we have updated and improved the correction for an azimuthal asymmetry, the parametrization of the average risetime as a function of the distance to the shower axis (benchmark) and the risetime uncertainty. Based on these parametrizations, two different existing approaches have been compared in this analysis: Δ_{Leeds} and $t_{1/2}(1000)$. As an addition to the time domain, we have revisited work on an LDF parameter called S_4. The meaning of this parameter has been studied: Applying a normalization, the new parameter can be understood as the average fractional deviation from a reference LDF. In this context we have compared two reference LDF shapes: S_4^{n} and R_{NKG}.

The best combination out of the parameters compared in a pre-study for the final analysis is Δ_{Leeds} (signal risetime) and $\log_{10}(R_{\mathrm{NKG},1000})$ (LDF shape). These parameters allow for a

powerful compromise of high selection efficiency and good photon-hadron seperation. These parameters are combined in a multivariate analysis (principal component analysis). We have followed an approach to reduce any dependence on hadronic simulations by using a data burn sample. This limits the accuracy of the method but gives a conservative result. As a technical base for this analysis, we have improved the SD energy calibration. Different hardware issues have been studied which can create an artificial background to the UHE photon search with the SD (direct light effects, PMT afterpulses).

As a consequence of the fact that the standard SD reconstruction cannot describe photons and hadrons equally well at the same time, parameters which compare the SD information of one event with an average obtained either for data or MC photons should be favoured over event-wise fits (such as $t_{1/2}(1000)$, R_{c}). The stability of an event-wise fit within the standard SD reconstruction optimized for data cannot be assured without a loss of selection efficiency. This should be considered in future studies.
Regarding the analysis, the photon-hadron-separation can be improved by finding a principal component axis in bins of energy and zenith angle. The analysis can be improved by the usage of a larger MC photon set to reduce statistical uncertainties of the photon median. This would then require to use hadronic simulations instead of the data burn sample to have equal statistics of signal and background. We have chosen a different approach in this work: What is the best we can do to avoid a large dependence on hadronic simulations? As a further improvement, hadronic background could either be removed using hadronic simulations or the photon candidate cut could be optimized to a value more restrictive than the median for photons. The systematic effect of the photonuclear cross-section and of the thinning of photon MC showers have not been studied in this work. A challenge in the SD photon search is the treatment of the preshower effect and LPM effect without having a direct measurement of X_{max} or the energy. The current treatment has been described in detail and we have improved previous studies. Nonetheless this might be topic to future analyses. The energy calibration does not describe preshowered photons and photons with a very late X_{max} correctly. In case of the LPM effect, the energy is overestimated and thus photons with lower energies can enter the reconstructed energies studied in this analysis.

The work presented here has significantly improved previous UHE photon limits and opens several interesting topics for future analyses.

CHAPTER 9

Acknowledgements

This work would not have been possible without the support and expertise of a lot of people.
First of all I want to thank Prof. Karl-Heinz Kampert a lot for giving me the chance to work in the Astroparticle Group Wuppertal and for supervising this work on this interesting topic. I am very grateful for his continuous support also during busy days, his patience and the encouragement to be persistent in challenging parts of this analysis. He was also kindly proofreading this thesis.
Many thanks to Dr. Jose A. Bellido-Caceres for accepting to be the second reviewer of this thesis.
I'm indebted to Dr. Julian Rautenberg for innnumerable discussions about the detector electronics as well as the data analysis and for his continuous support, help and encouragement. He took the time to answer my questions, to rehearse talks, proofread this thesis and to work on the maintenance of the local computer cluster even at late hours. Thanks also for his suggestion for me to work in the Netzwerk Teilchenwelt teaching astroparticle physics to school classes, which I enjoyed a lot.
A part of this thesis was supervised by Dr. Carla Bleve. Many thanks for supporting this work with a lot of photon expertise, valuable feedback and for all preparation and work related to the ICRC presentation.
Thanks for the discussions within the photon, composition and SD reconstruction task groups. Just to name some people: Daniel Kümpel, Carla Bleve, Mariangela Settimo, Alan Watson, Jose A. Bellido-Caceres, Alexey Yuskkov, Markus Risse, Piotr Homola, Ioana Maris, Darko Veberic, Isabelle Lhenry-Yvon, Piera L. Ghia, Pierre Billoir, Lu Lu, Patricia Sanchez-Lucas, Philipp Papenbreer and Heather Cook.
Thanks to all colleagues in the Astroparticle Group Wuppertal - for the nice working atmosphere as well as the best barbecue and plenty of cool events. I'm happy that we all got to meet! A big 'thank you' to Ingrid Schaarwächter who never gets tired to help with the formalities of the institute life and who it's nice to talk with.
I'm very grateful to Daniel Kümpel for his feedback as a colleague and friend and for proofreading this thesis.
This last part is reserved for my family and friends. Thank you so much for all support, for a lot of patience and innumerable cheer-ups. And very special thanks to Tobias for always being there and going all that way with me.

Bibliography

[1] Gaisser, T. K., Stanev, T. and Tilav, S. "Cosmic Ray Energy Spectrum from Measurements of Air Showers". *Rev. Frontiers of Physics, 2013*. arXiv:1303.3565.

[2] Salamida, F. et al., Pierre Auger Collaboration. "Update on the measurement of the CR energy spectrum above 10^{18} eV made using the Pierre Auger Observatory". *32nd ICRC, Beijing, China*, 2011.

[3] Ivanov, D. et al., Telescope Array Collaboration. *32nd ICRC, Beijing, China*, 2011.

[4] Abu-Zayyad, T. et al., Telescope Array Collaboration. "The Cosmic-Ray Energy Spectrum Observed with the Surface Detector of the Telescope Array Experiment". *The Astrophysical Journal Letters*, **768**, L1, 2013. arXiv:1205.5067, doi:10.1088/2041-8205/768/1/L1.

[5] Egorova, V. P. et al. "The spectrum features of UHECRs below and surrounding GZK". *Nucl. Phys. B (Proc. Suppl.)*, **136**, 3-11, 2004. doi:10.1016/j.nuclphysbps.2004.10.060.

[6] Ivanov, A. A., Knurenko, S. P., Pravdin, M. I., Sleptsov and I. E. "Main results of the study of ultrahigh-energy cosmic rays in the Yakutsk Extensive Air Shower Array". *Moscow University Physics Bulletin*, **65**, 292-299, 2010. doi:10.3103/S0027134910040089.

[7] Abbasi, R. U. et al., HiRes Collaboration. "First Observation of the Greisen-Zatsepin-Kuzmin Suppression". *Phys. Rev. Lett.*, **100**, 101101, 2008. doi:10.1103/PhysRevLett.100.101101.

[8] Dawson, B. R. et al., working group report at UHECR2012. "The energy spectrum of cosmic rays at the highest energies". *EPJ Web of Conferences (UHECR 2012)*, **53**, 2013. arXiv:1306.6138, doi:10.1051/epjconf/20135301005.

[9] Kulikov, G. V. and Khristiansen, G. B. *Sov. Phys. JETP*, **8**, 441, 1959.

[10] Antoni, T., KASCADE Collaboration. "KASCADE measurements of energy spectra for elemental groups of cosmic rays: Results and open problems". *Astropart. Phys.*, **24**, 1-25, 2005. doi:10.1016/j.astropartphys.2005.04.001.

[11] Khristiansen, G. B. et al. "Primary cosmic ray mass composition at energies 10^{15} – 10^{17} eV as measured by the MSU EAS array". *Astropart. Phys.*, **2**, 127-136, 1994. doi:10.1016/0927-6505(94)90035-3.

[12] Apel, W. D. et al., KASCADE-Grande Collaboration. "Kneelike Structure in the Spectrum of the Heavy Component of Cosmic Rays Observed with KASCADE-Grande". *Phys. Rev. Lett.*, **107**, 171104, 2011. arXiv:1107.5885, doi:10.1103/PhysRevLett.107.171104.

[13] Peters, B. "Primary cosmic radiation and extensive air showers". *Il Nuovo Cimento*, **22**, 800-819, 1961. doi:10.1007/BF02783106.

[14] Bird, D. J. et al. "Evidence for correlated changes in the spectrum and composition of cosmic rays at extremely high energies". *Phys. Rev. Lett.*, **71**, 3401-3404, 1993. doi:10.1103/PhysRevLett.71.3401.

[15] Apel, W. D. et al., KASCADE Collaboration. "Ankle-like feature in the energy spectrum of light elements of cosmic rays observed with KASCADE-Grande". *Phys. Rev. D*, **87**, 081101, 2013. arXiv:1304.7114, doi:10.1103/PhysRevD.87.081101.

[16] Hörandel, J. R. "Models of the knee in the energy spectrum of cosmic rays". *Astropart. Phys.*, **21**, 241-265, 2004. doi:10.1016/j.astropartphys.2004.01.004.

[17] Berezinsky, V. S. and Grigorieva, S. I. *Astron. Astrophys.*, **199**, 1988.

[18] Berezinsky, V., Gazizov, A. and Kachelriess, M. "Second Dip as a Signature of Ultrahigh Energy Proton Interactions with Cosmic Microwave Background Radiation". *Phys. Rev. Lett.*, **97**, 231101, 2006. doi:10.1103/PhysRevLett.97.231101.

[19] Facal, P., Pierre Auger Collaboration. "The Pierre Auger Observatory II: Studies of Cosmic Ray Composition and Hadronic Interaction models". *32nd ICRC, Beijing, China (vol. 2)*, 105, 2011. arXiv:1107.4804.

[20] Aab, A. et al., Pierre Auger Collaboration. "Evidence for a mixed mass composition at the ankle in the cosmic-ray spectrum". *Phys. Lett. B*, **762**, 288-295, 2016. arXiv:1609.08567, doi:10.1016/j.physletb.2016.09.039.

[21] Abbasi, R. U. et al., HiRes Collaboration. "Measurement of the Flux of Ultrahigh Energy Cosmic Rays from Monocular Observations by the High Resolution Fly's Eye Experiment". *Phys. Rev. Lett.*, **92**, 151101, 2004. doi:10.1103/PhysRevLett.92.151101.

[22] Abbasi, R. U. et al., HiRes Collaboration. "First Observation of the Greisen-Zatsepin-Kuz'min Suppression". *Phys. Rev. Lett.*, **100**, 101101, 2008. doi:10.1103/PhysRevLett.100.101101.

[23] Abraham, J. et al., Pierre Auger Collaboration. "Observation of the Suppression of the Flux of Cosmic Rays above 4×10^{19} eV". *Phys. Rev. Lett.*, **101**, 061101, 2008. doi:10.1103/PhysRevLett.101.061101.

[24] Abu-Zayyad, T. et al., Telescope Array Collaboration. "The Cosmic-Ray Energy Spectrum Observed with the Surface Detector of the Telescope Array Experiment". *Astrophys. J. Lett.*, **768**, L1, 2013. doi:10.1088/2041-8205/768/1/L1.

[25] Greisen, K. "End to the Cosmic-Ray Spectrum?" *Phys. Rev. Lett.*, **16**, 748-750, 1966. doi:10.1103/PhysRevLett.16.748.

[26] Zatsepin, G. T. and Kuz'min, V. A. "Upper Limit of the Spectrum of Cosmic Rays". *JETP Lett.*, **4**, 78-80, 1966. http://www.jetpletters.ac.ru/ps/1624/article_24846.shtml.

[27] Linsley, J. "Evidence for a Primary Cosmic-Ray Particle with Energy 10^{20} eV". *Phys. Rev. Lett.*, **10**, 146-148, 1963. doi:10.1103/PhysRevLett.10.146.

[28] Harari, D. "The flux suppression at the highest energies". *Compt. Rend.*, **15**, 376–383, 2014. arXiv:1406.1117, doi:10.1016/j.crhy.2014.02.011.

[29] Harari, D., Mollerach, S. and Roulet, S. "On the ultrahigh energy cosmic ray horizon". *JCAP*, 012, 2006. doi:10.1088/1475-7516/2006/11/012.

[30] Takeda, M. et al., AGASA Collaboration. "Extension of the Cosmic-Ray Energy Spectrum beyond the Predicted Greisen-Zatsepin-Kuz'min Cutoff". *Phys. Rev. Lett.*, **81**, 1163-1166, 1998. doi:10.1103/PhysRevLett.81.1163.

[31] Takeda, M. et al., AGASA Collaboration. "Updated AGASA event list above 4×10^{19} eV". *Astron. J.*, **120**, 2190, 2000. arXiv:astro-ph/0008102.

[32] Vázquez, J. R., Rosado, J., García-Pinto, D. and Arqueros, F. "The effect of the fluorescence yield selection on the energy scales of Auger, HiRes and TA". *EPJ Web of Conferences (UHECR 2012)*, **53**, 2012. doi:10.1051/epjconf/20135310002.

[33] Kampert, K.-H. "Ultrahigh-Energy Cosmic Rays: Results and Prospects". *Braz. Journ. of Phys.*, **43**, 375-382, 2013. arXiv:1305.2363.

[34] Kotera, K. and Olinto, A. V. "The Astrophysics of Ultrahigh Energy Cosmic Rays". *Ann. Rev. Astron. Astrophys.*, **49**, 119-153, 2011. arXiv:1101.4256, doi:10.1146/annurev-astro-081710-102620.

[35] Prosin, V. V. et al., Tunka Collaboration. "The Cosmic Ray Mass Composition in the Energy Range measured with the Tunka Array: Results and Perspectives". *Nucl. Phys. B (Proc. Suppl.)*, **190**, 247-252, 2009. doi:10.1016/j.nuclphysbps.2009.03.095.

[36] Prosin, V. V. et al., Tunka Collaboration. *32nd ICRC, Beijing, China (vol.1)*, 197, 2011. doi:10.7529/ICRC2011/V01/0184.

[37] Knurenko, S. P. and Sabourov, A., Yakutsk Collaboration. *Proc. XVI ISVHECRI*, 2011. arXiv:1010.1185.

[38] Knurenko, S. P and Sabourov, A., Yakutsk Collaboration. "Study of cosmic rays at the Yakutsk EAS array: energy spectrum and mass composition". *Nucl. Phys. B (Proc. Suppl.)*, **212-213**, 241-251, 2011. doi:10.1016/j.nuclphysbps.2011.03.033.

[39] Fowler, J. W. et al., CASA-BLANCA Collaboration. "A measurement of the cosmic ray spectrum and composition at the knee". *Astropart. Phys.*, **15**, 49-64, 2001. doi:10.1016/S0927-6505(00)00139-0.

[40] Abu-Zayyad, T. et al., HiRes/MIA Collaboration. "Measurement of the Cosmic-Ray Energy Spectrum and Composition from 10^{17} to $10^{18.3}$ eV Using a Hybrid Technique". *Astrophys. J.*, **557**, 686, 2001. arXiv:astro-ph/0010652, doi:10.1086/322240.

[41] Abbasi, R. U. et al., HiRes Collaboration. "Indications of Proton-Dominated Cosmic-Ray Composition above 1.6 EeV". *Phys. Rev. Lett.*, **104**, 161101, 2010. arXiv:0910.4184, doi:10.1103/PhysRevLett.104.161101.

[42] Jui, C. C., Telescope Array Collaboration. "Cosmic Ray in the Northern Hemisphere: Results from the Telescope Array Experiment". *Proc. APS DPF Meeting*, 2011. arXiv:1110.0133.

[43] Kampert, K. H. and Unger, M. "Measurements of the cosmic ray composition with air shower experiments". *Astropart. Phys.*, **35**, 660-678, 2012. doi:10.1016/j.astropartphys.2012.02.004.

[44] Heitler, W. "Quantum Theory of Radiation". *Oxford University Press*, 1954.

[45] Alvarez-Muñiz, J., Engel, R., Gaisser, T. K., Ortiz, J. A. and Stanev, T. "Hybrid simulations of extensive air showers". *Phys. Rev. D*, **66**, 033011, 2002. arXiv:astro-ph/0205302, doi:10.1103/PhysRevD.66.033011.

[46] J. Matthews. "A Heitler model of extensive air showers". *Astropar. Phys.*, **22**, 387-397, 2005. doi:10.1016/j.astropartphys.2004.09.003.

[47] Abbasi, R. U. et al., Pierre Auger Collaboration + Telescope Array Collaboration. "Pierre Auger Observatory and Telescope Array: Joint Contributions to the 34th International Cosmic Ray Conference (ICRC 2015)". *34th ICRC, The Hague, The Netherlands*, 2015. arXiv:1511.02103.

[48] Aab, A. et al. "Searches for Anisotropies in the Arrival Directions of the Highest Energy Cosmic Rays Detected by the Pierre Auger Observatory". *Astrophys. Journ.*, **804**, 15, 2015. arXiv:1411.6111, doi:10.1088/0004-637X/804/1/15.

[49] Amenomori, M. et al. "Anisotropy and Corotation of Galactic Cosmic Rays". *Science*, **314**, 439-443, 2006. doi:10.1126/science.1131702.

[50] Abdo, A. A. et al., Milagro Collaboration. "Discovery of Localized Regions of Excess 10-TeV Cosmic Rays". *Phys. Rev. Lett.*, **101**, 221101, 2008. doi:10.1103/PhysRevLett.101.221101.

[51] Abbasi, R. et al., IceCube Collaboration. "Measurement of the Anisotropy of Cosmic-ray Arrival Directions with IceCube". *Astrophys. Journ. Lett.*, **718**, L194, 2010. doi:10.1088/2041-8205/718/2/L194.

[52] Abbasi, R. et al., IceCube Collaboration. "Observation of Anisotropy in the Galactic Cosmic-Ray Arrival Directions at 400 TeV with IceCube". *Astrophys. Journ.*, **746**, 33, 2012. doi:10.1088/0004-637X/746/1/33.

[53] Aartsen, M. G. et al., IceTop Collaboration. "Observation of Cosmic-Ray Anisotropy with the IceTop Air Shower Array". *Astrophys. Journ.*, **765**, 55, 2013. doi:10.1088/0004-637X/765/1/55.

[54] Aab, A. et al., Pierre Auger Collaboration. "Multi-resolution anisotropy studies of ultrahigh-energy cosmic rays detected at the Pierre Auger Observatory". *Submitted to: JCAP*, 2016. arXiv:1611.06812.

[55] Abreu, P. et al., Pierre Auger Collaboration. "Large-scale Distribution of Arrival Directions of Cosmic Rays Detected Above 10^{18} eV at the Pierre Auger Observatory". *Astrophys. Journ. Suppl.*, **203**, 34, 2012. arXiv:1210.3736, doi:10.1088/0067-0049/203/2/34.

[56] Abreu, P., Pierre Auger Collaboration. "Constraints on the Origin of Cosmic Rays above 10^{18} eV from Large-scale Anisotropy Searches in Data of the Pierre Auger Observatory". *The Astrophysical Journal Letters*, **762**, L13, 2013. arXiv:1212.3083, doi:10.1088/2041-8205/762/1/L13.

[57] Abraham, J. et al. "Correlation of the highest-energy cosmic rays with the positions of nearby active galactic nuclei". *Astropart. Phys.*, **29**, 188-204, 2008. Erratum-ibid. 30:45,2008. arXiv:0712.2843, doi:10.1016/j.astropartphys.2008.01.002.

[58] Abreu, P. et al. "Search for signatures of magnetically-induced alignment in the arrival directions measured by the Pierre Auger Observatory". *Astropart. Phys.*, **35**, 354–361, 2012. doi:10.1016/j.astropartphys.2011.10.004.

[59] Abreu, P. et al., Pierre Auger Collaboration. "Bounds on the density of sources of ultra-high energy cosmic rays from the Pierre Auger Observatory". *JCAP*, 009, 2013. doi:10.1088/1475-7516/2013/05/009.

[60] Blümer, H. and Kampert, K. H. *Phys. Blätter*, **56**, 39-45, 2000. doi:10.1002/phbl.20000560311.

[61] Fermi, E. "On the Origin of the Cosmic Radiation". *Phys. Rev.*, **75**, 1169-1174, 1949. doi:10.1103/PhysRev.75.1169.

[62] Blandford, R. D. and Ostriker, J. P. "Particle acceleration by astrophysical shocks". *Astrophys. Journ. Lett.*, **221**, L29-L32, 1978. doi:10.1086/182658.

[63] Bell, A. R. "The acceleration of cosmic rays in shock fronts. I". *Monthly Notices of the Royal Astron. Soc.*, **182**, 147-156, 1978.

[64] Bell, A. R. "Particle acceleration by shocks in supernova remnants". *Invited talk at 33rd ICRC, Rio de Janeiro, Brazil*, 2013. arXiv:1311.5779.

[65] Hillas, A. M. "The Origin of Ultra-High-Energy Cosmic Rays". *Annual Rev. Astron. Astrophys.*, **22**, 425-444, 1984. doi:10.1146/annurev.aa.22.090184.002233.

[66] Bhattacharjee, P. and Sigl, G. "Origin and propagation of extremely high-energy cosmic rays". *Phys. Rep.*, **327**, 109-247, 2000. doi:10.1016/S0370-1573(99)00101-5.

[67] Baade, W. and Zwicky, F. "On Super-Novae". *Proc. of the National Academy of Sciences*, **20**, 254-259, 1934. doi:10.1073/pnas.20.5.254.

[68] Hewitt, J. W. et al., Fermi LAT Collaboration. "The 1st Fermi LAT SNR Catalog: Probing the Gamma-ray Population". *33rd ICRC, Rio de Janeiro, Brazil*, 2013. arXiv:1307.6570.

[69] Hjorth, J. "The supernova / gamma-ray burst / jet connection". *Phil. Trans. R. Soc. A*, **371**, 2013. arXiv:1304.7736, doi:10.1098/rsta.2012.0275.

[70] MacFadyen A. I. and Woosley, S. E. "Collapsars: Gamma-Ray Bursts and Explosions in "Failed Supernovae"". *Astrophys. Journ.*, **524**, 262, 1999. doi:10.1086/307790.

[71] Rieger, F. M., Bosch-Ramon, V. and Duffy, P. "Fermi acceleration in astrophysical jets". *Astrophys. and Space Science*, **309**, 119-125, 2007. doi:10.1007/s10509-007-9466-z.

[72] Blasi, P., Epstein, R. I. and Olinto, A. V. "Ultra-High-Energy Cosmic Rays from Young Neutron Star Winds". *Astrophys. Journ. Lett.*, **533**, L123, 2000. doi:10.1086/312626.

[73] Kang, H., Ryu, D. and Jones, T. W. "Cluster Accretion Shocks as Possible Acceleration Sites for Ultra–High-Energy Protons below the Greisen Cutoff". *Astrophys. Journ.*, **456**, 422, 1996. arXiv:astro-ph/9507113, doi:10.1086/176666.

[74] Rachen, J. P. and Biermann, P. L. "Extragalactic Ultra-High Energy Cosmic-Rays - Part One - Contribution from Hot Spots in Fr-II Radio Galaxies". *Astron. Astrophys.*, **272**, 161, 1993. arXiv:astro-ph/9301010.

[75] Gelmini, G. B., Kalashev, O. E. and Semikoz, D. V. "GZK Photons as Ultra-High-Energy Cosmic Rays". *J. Exp. Theor. Phys.*, **106**, 1061-1082, 2008. doi:10.1134/S106377610806006X.

[76] Ellis, J., Mayes, V. E. and Nanopoulos, D. V. "Ultrahigh-energy cosmic rays particle spectra from crypton decays". *Phys. Rev. D*, **74**, 115003, 2006. doi:10.1103/PhysRevD.74.115003.

[77] Weiler, T. J. "Resonant Absorption of Cosmic-Ray Neutrinos by the Relic-Neutrino Background". *Phys. Rev. Lett.*, **49**, 234-237, 1982. doi:10.1103/PhysRevLett.49.234.

[78] Kalashev, O. E., Kuz'min, V. A. and Semikoz, D. V. "Ultrahigh-energy cosmic rays. Propagation in the galaxy and anisotropy". *Mod. Phys. Lett.*, **A16**, 2505-2515, 2001. arXiv:astro-ph/0006349, doi:10.1142/S0217732301005990.

[79] Berezinsky, V., Kachelriess, M. and Vilenkin, A. "Ultrahigh Energy Cosmic Rays without Greisen-Zatsepin-Kuzmin Cutoff". *Phys. Rev. Lett.*, **79**, 4302-4305, 1997. arXiv:astro-ph/9708217, doi:10.1103/PhysRevLett.79.4302.

[80] Kuzmin, V. A. and Rubakov, V. A. "Ultra-High Energy Cosmic Rays: a Window to Post-Inflationary Reheating Epoch of the Universe?" *Phys. Atom. Nucl.*, **61**, 1028-1030, 1998. arXiv:astro-ph/9709187.

[81] Blasi, P., Dick, R. and Kolb, E. W. "Ultra-high energy cosmic rays from annihilation of superheavy dark matter". *Astropart. Phys.*, **18**, 57-66, 2002. arXiv:astro-ph/0105232, doi:10.1016/S0927-6505(02)00113-5.

[82] Birkel, M. and Sarkar, S. "Extremely high energy cosmic rays from relic particle decays". *Astropart. Phys.*, **9**, 297-309, 1998. arXiv:hep-ph/9804285, doi:10.1016/S0927-6505(98)00028-0.

[83] Kachelriess, M. and Semikoz, D. V. "Superheavy dark matter as UHECR source versus the SUGAR data". *Phys. Lett. B*, **577**, 1-9, 2003. arXiv:astro-ph/0306282, doi:10.1016/j.physletb.2003.10.017.

[84] Kim, H. B. and Tinyakov, P. "Constraining superheavy dark matter model of UHECR with SUGAR data". *Astropart. Phys.*, **21**, 535-542, 2004. arXiv:astro-ph/0306413, doi:10.1016/j.astropartphys.2004.03.004.

[85] Siffert, B., Lazarotto, B., de Mello Neto, J. R. T. and Olinto, A. "Dark matter halos and the anisotropy of ultra-high energy cosmic rays in the Pierre Auger Observatory". *Braz. J. Phys.*, **37**, 48-51, 2007. doi:10.1590/S0103-97332007000100016.

[86] Swordy, S. P., L'Heureux, J., Meyer, P. and Muller, D. "Elemental abundances in the local cosmic rays at high energies". *Astrophys. Journ.*, **403**, 658-662, 1993. doi:10.1086/172235.

[87] Haverkorn, M. et al. "The Outer Scale of Turbulence in the Magnetoionized Galactic Interstellar Medium". *Astrophys. Journ.*, **680**, 362-370, 2008. arXiv:0802.2740, doi:10.1086/587165.

[88] Jansson, R. and Farrar, G. R. "A New Model of the Galactic Magnetic Field". *Astrophys. Journ.*, **757**, 14, 2012. arXiv:1204.3662, doi:10.1088/0004-637X/757/1/14.

[89] Arlen, T. et al. "Constraints on Cosmic Rays, Magnetic Fields, and Dark Matter from Gamma-Ray Observations of the Coma Cluster of Galaxies with VERITAS and Fermi". *Astrophys. Journ.*, **757**, 123, 2012. arXiv:1208.0676, doi:10.1088/0004-637X/757/2/123.

[90] Dolag, K., Grasso, D., Springel, V. and Tkachev, I. "Constrained simulations of the magnetic field in the local Universe and the propagation of ultrahigh energy cosmic rays". *JCAP*, **2005**, 009, 2005. doi:10.1088/1475-7516/2005/01/009.

[91] Sigl, G., Miniati, F. and Ensslin, T. A. "Ultrahigh energy cosmic rays in a structured and magnetized universe". *Phys. Rev. D*, **68**, 043002, 2003. doi:10.1103/PhysRevD.68.043002.

[92] Risse, M. and Homola, P. "Search for Ultra-High Energy Photons Using Air Showers". *Mod. Phys. Lett. A*, **22**, 749, 2007. arXiv:astro-ph/0702632, doi:10.1142/S0217732307022864.

[93] Abraham, J. et al., Pierre Auger Collaboration. "Upper limit on the cosmic-ray photon flux above 10^{19} eV using the surface detector of the Pierre Auger Observatory". *Astropart. Phys.*, **29**, 243-256, 2008. doi:10.1016/j.astropartphys.2008.01.003.

[94] Sarkar, B., Kampert, K.-H., Kulbartz, J., Maccione, L., Nierstenhoefer, N. and Sigl, G. "Ultra-High Energy Photon and Neutrino Fluxes in Realistic Astrophysical Scenarios". *32nd ICRC, Beijing, China*, 2011. doi:10.7529/ICRC2011/V02/1087.

[95] Stecker, F. W. "Effect of Photomeson Production by the Universal Radiation Field on High-Energy Cosmic Rays". *Phys. Rev. Lett.*, **21**, 1016-1018, 1968. doi:10.1103/PhysRevLett.21.1016.

[96] Puget, J. L., Stecker, F. W. and Bredekamp, J. H. "Photonuclear interactions of ultrahigh energy cosmic rays and their astrophysical consequences". *Astrophys. J.*, **205**, 638-654, 1976. doi:10.1086/154321.

[97] Stecker F. W. and Salamon, M. H. "Photodisintegration of Ultra-High-Energy Cosmic Rays: A New Determination". *Astrophys. J.*, **512**, 521, 1999. doi:10.1086/306816.

[98] Khan, E. et al. "Photodisintegration of ultra-high-energy cosmic rays revisited". *Astropart. Phys.*, **23**, 191-201, 2005. doi:10.1016/j.astropartphys.2004.12.007.

[99] Alvarez-Muñiz, J., Risse, M. (Pierre Auger Collaboration) and G. I. Rubtsov, B. T. Stokes (Telescope Array Collaboration). "Review of the Multimessenger Working Group at UHECR-2012". *EPJ Web of Conferences (UHECR 2012)*, **53**, 2013. arXiv:1306.4199, doi:10.1051/epjconf/20135301009.

[100] Settimo, M. et al., Pierre Auger Collaboration. "An update on a search for ultra-high energy photons using the Pierre Auger Observatory". *32nd ICRC, Beijing, China*, 2011. arXiv:1107.4805.

[101] Salamida, F. et al., Pierre Auger Collaboration. "Measurement of the energy spectrum of cosmic rays above 10^{18} eV using the Pierre Auger Observatory". *32nd ICRC, Beijing, China*, 2011. arXiv:1107.4809.

[102] Armengaud, E., Sigl, G., Beau, T. and Miniati, F. "CRPropa: A numerical tool for the propagation of UHE cosmic rays, γ-rays and neutrinos". *Astropart. Phys.*, **28**, 463-471, 2007. doi:10.1016/j.astropartphys.2007.09.004.

[103] Sigl, G., Kampert, K.-H., Kulbartz, J., Maccione, L. and Nierstenhoefer, N. "Simulating Ultra-High Energy Nuclei Propagation with CRPropa". *32nd ICRC, Beijing, China*, 2011. doi:10.7529/ICRC2011/V06/0760.

[104] Hooper, D., Taylor, A. M. and Sarkar, S. "Cosmogenic photons as a test of ultra-high energy cosmic ray composition". *Astropart. Phys.*, **34**, 340-343, 2011. doi:10.1016/j.astropartphys.2010.09.002.

[105] Adriani, O. et al., PAMELA Collaboration. "A statistical procedure for the identification of positrons in the PAMELA experiment". *Astropart. Phys.*, **34**, 1-11, 2010. arXiv:1001.3522, doi:10.1016/j.astropartphys.2010.04.007.

[106] Ackermann, M. et al., Fermi LAT Collaboration. "Measurement of Separate Cosmic-Ray Electron and Positron Spectra with the Fermi Large Area Telescope". *Phys. Rev. Lett.*, **108**, 011103, 2012. arXiv:1109.0521, doi:10.1103/PhysRevLett.108.011103.

[107] Aguilar, M. et al., AMS Collaboration. "First Result from the Alpha Magnetic Spectrometer on the International Space Station: Precision Measurement of the Positron Fraction in Primary Cosmic Rays of $0.5 - 350$ GeV". *Phys. Rev. Lett.*, **110**, 141102, 2013. doi:10.1103/PhysRevLett.110.141102.

[108] Blum, K., Katz, B. and Waxman, E. "AMS-02 Results Support the Secondary Origin of Cosmic Ray Positrons". *Phys. Rev. Lett.*, **111**, 211101, 2013. doi:10.1103/PhysRevLett.111.211101.

[109] Abreu, P. et al., Pierre Auger Collaboration. "A Search for Point Sources of EeV Neutrons". *Astrophys. Journ.*, **760**, 148, 2012. arXiv:1211.4901, doi:10.1088/0004-637X/760/2/148.

[110] Aab, A. et al., Pierre Auger Collaboration. "A Targeted Search for Point Sources of EeV Neutrons". *Astrophys. Journ. Lett.*, **789**, L34, 2014. doi:10.1088/0004-637X/760/2/148.

[111] Vandenbroucke, J., Fermi LAT Collaboration. "Physics and astrophysics with gamma-ray telescopes". *Nucl. Phys. B (Proc. Suppl.)*, **229-232**, 258-264, 2012. doi:10.1016/j.nuclphysbps.2012.09.041.

[112] Ackermann, M. et al. "The First Fermi-LAT Catalog of Sources above 10 GeV". *Astrophys. Journ. Suppl.*, **209**, 34, 2013. arXiv:1306.6772, doi:10.1088/0067-0049/209/2/34.

[113] Ackermann, M. et al., Fermi LAT Collaboration. "Detection of the Characteristic Pion-decay Signature in Supernova Remnants". *Science*, **339**, 807-811, 2013. arXiv:1302.3307, doi:10.1126/science.1231160.

[114] Halzen, F. "The highest energy neutrinos: first evidence for cosmic origin". 2013. arXiv::1311.6350.

[115] Waxman, E. "High Energy Cosmic Ray and Neutrino Astronomy". *Astronomy at the Frontiers of Science*, **1**, 43-68, 2011. arXiv:1101.1155, doi:10.1007/978-94-007-1658-2_3.

[116] Aartsen. M. G. et al., IceCube Collaboration. "Evidence for High-Energy Extraterrestrial Neutrinos at the IceCube Detector". *Science*, **342**, 2013. arXiv:1311.5238, doi:10.1126/science.1242856.

[117] Aartsen. M. G. et al., IceCube Collaboration. "Observation of High-Energy Astrophysical Neutrinos in Three Years of IceCube Data". *Phys. Rev. Lett.*, **113**, 101101, 2014. arXiv:1405.5303, doi:10.1103/PhysRevLett.113.101101.

[118] Aartsen. M. G. et al., IceCube Collaboration. "Evidence for Astrophysical Muon Neutrinos from the Northern Sky with IceCube". *Phys. Rev. Lett.*, **115**, 081102, 2015. arXiv:1507.04005, doi:10.1103/PhysRevLett.115.081102.

[119] Aartsen. M. G. et al., IceCube Collaboration. "All-sky Search for Time-integrated Neutrino Emission from Astrophysical Sources with 7 yr of IceCube Data". *Astrophys. J.*, 151, 2017. arXiv:1609.04981, doi:10.3847/1538-4357/835/2/151.

[120] Aartsen, M. G. et al., IceCube Collaboration. "First Observation of PeV-Energy Neutrinos with IceCube". *Phys. Rev. Lett.*, **111**, 021103, 2013. arXiv:1304.5356, doi:10.1103/PhysRevLett.111.021103.

[121] Abreu, P. et al. "Search for ultrahigh energy neutrinos in highly inclined events at the Pierre Auger Observatory". *Phys. Rev. D*, **84**, 122005, 2011. arXiv:1202.1493, doi:10.1103/PhysRevD.84.122005.

[122] Rubtsov, G. I. et al., Telescope Array Collaboration. "Search for ultra-high energy photons and neutrinos using Telescope Array surface detector". *32nd ICRC, Beijing, China*, 2011. doi:10.1088/1742-6596/409/1/012087.

[123] Abreu, P. et al., Pierre Auger Collaboration. "Search for Point-like Sources of Ultra-high Energy Neutrinos at the Pierre Auger Observatory and Improved Limit on the Diffuse Flux of Tau Neutrinos". *Astrophys. Journ.*, **755**, L4, 2012. arXiv:1210.3143, doi:10.1088/2041-8205/755/1/L4.

[124] Aab, A. et al. "Improved limit to the diffuse flux of ultrahigh energy neutrinos from the Pierre Auger Observatory". *Phys. Rev. D*, **91**, 092008, 2015. arXiv:1504.05397, doi:10.1103/PhysRevD.91.092008.

[125] Aab, A. et al. "A Search for Point Sources of EeV Photons". *Astrophys. Journ.*, **789**, 160, 2014. arXiv:1406.2912, doi:10.1088/0004-637X/789/2/160.

[126] A. Aab et al. "A Targeted Search for Point Sources of EeV Photons with the Pierre Auger Observatory". *Astrophys. Journ. Lett.*, **837**, L25, 2017. arXiv:1612.04155.

[127] Bothe, W. "Zur Vereinfachung von Koinzidenzzählungen". *Z. Phys.*, **59**, 1, 1929.

[128] Rossi, B. "Method of Registering Multiple Simultaneous Impulses of Several Geiger's Counters". *Nature*, **125**, 636, 1930. doi:10.1038/125636a0.

[129] Rossi, B. "Ueber die Eigenschaften der durchdringenden Korpuskularstrahlung im Meeresniveau". *Z. Phys.*, **82**, 151-178, 1933. doi:10.1007/BF01341486.

[130] Schmeiser K. and Bothe, W. "Die harten Ultrastrahlschauer". *Ann. Phys.*, **424**, 161-177, 1938. doi:10.1002/andp.19384240119.

[131] Kohlhörster, W., Matthes, I. and Weber, E. "Gekoppelte Höhenstrahlen". *Naturwiss.*, **26**, 576, 1938. doi:10.1007/BF01773491.

[132] Auger, P. et al. "Extensive Cosmic-Ray Showers". *Rev. Mod. Phys.*, **11**, 288-291, 1939. doi:10.1103/RevModPhys.11.288.

[133] Schmidt, F. "CORSIKA Shower Images" [online]. http://www.ast.leeds.ac.uk/~fs/showerimages.html.

[134] Hörandel, J. R. "On total inelastic cross sections and the average depth of the maximum of extensive air showers". *J. Phys. G: Nuclear and Particle Physics*, **29**, 2439, 2003. arXiv:astro-ph/0309010, doi:10.1088/0954-3899/29/11/001.

[135] Hörandel, J. R. "Cosmic Rays from the knee to the second knee: 10^{14} to 10^{18} eV". *Mod. Phys. Lett. A*, **22**, 1533-1551, 2007. arXiv:astro-ph/0611387, doi:10.1142/S0217732307024139.

[136] Ulrich, R, Engel, R. and Unger, M. "Hadronic multiparticle production at ultrahigh energies and extensive air showers". *Phys. Rev. D*, **83**, 054026, 2011. arXiv:1010.1185, doi:10.1103/PhysRevD.83.054026.

[137] Abreu, P. et al., Pierre Auger Collaboration. "Measurement of the Proton-Air Cross Section at $\sqrt{s} = 57$ TeV with the Pierre Auger Observatory". *Phys. Rev. Lett.*, **109**, 062002, 2012. arXiv:1208.1520, doi:10.1103/PhysRevLett.109.062002.

[138] Gaisser, T. K. and Hillas, A. M. "Reliability of the Method of Constant Intensity Cuts for Reconstructing the Average Development of Vertical Showers". *15th ICRC, Plovdiv, Bulgaria*, 383, 1977.

[139] Bethe, H. and Heitler, W. "The passage of last electrons and the theory of cosmic showers". *Proc. Roy. Soc.*, **A146**, 83, 1937.

[140] Carlson, J. F. and Oppenheimer, J. R. "On Multiplicative Showers". *Phys. Rev.*, **51**, 220-231, 1937. doi:10.1103/PhysRev.51.220.

[141] Rossi, B. and Greisen, K. "Cosmic-Ray Theory". *Rev. Mod. Phys.*, **13**, 240-309, 1941. doi:10.1103/RevModPhys.13.240.

[142] Hillas, A. M. "The sensitivity of Cerenkov radiation pulses to the longitudinal development of cosmic-ray showers". *J. Phys. G*, **8**, 1475, 1982. doi:10.1088/0305-4616/8/10/017.

[143] Giller, M. et al. "Energy spectra of electrons in the extensive air showers of ultra-high energy". *J. Phys. G*, **30**, 97, 2004. doi:10.1088/0954-3899/30/2/009.

[144] Nerling, F., Blümer, J., Engel, R. and Risse, M. "Universality of electron distributions in high-energy air showers - Description of Cherenkov light production". *Astropart. Phys.*, **24**, 421-437, 2006. doi:10.1016/j.astropartphys.2005.09.002.

[145] D. Góra et al. "Universal lateral distribution of energy deposit in air showers and its application to shower reconstruction". *Astropart. Phys.*, **24**, 484-494, 2006. doi:10.1016/j.astropartphys.2005.09.007.

[146] Schmidt, F., Ave, M., Cazon, L. and Chou, A. "Applying EAS universality to ground detector data". *30th ICRC, Merida, Mexico*, 2007. arXiv:0706.1990.

[147] Lafebre, S. et al. "Universality of electron-positron distributions in extensive air showers". *Astropart. Phys.*, **31**, 243-254, 2009. doi:10.1016/j.astropartphys.2009.02.002.

[148] Lipari, P. "Concepts of "age" and "universality" in cosmic ray showers". *Phys. Rev. D*, **79**, 063001, 2009. doi:10.1103/PhysRevD.79.063001.

[149] Mueller. "(unknown title)". *Diploma thesis, Karlsruhe*, 2008.

[150] Kamata, K. and Nishimura, J. "The Lateral and the Angular Structure Functions of Electron Showers". *Progr. Theor. Phys. (Suppl.)*, **6**, 93-155, 1958. doi:10.1143/PTPS.6.93.

[151] Greisen, K. "Cosmic Ray Showers". *Ann. Rev. of Nucl. Sci.*, **10**, 63-108, 1960. doi:10.1146/annurev.ns.10.120160.000431.

[152] Maurel, D., Ave, M., Roth, M. and Gonzalez, J. "Universality of the time structure of ground particle distributions and its application to the reconstruction of extensive air showers". *33rd ICRC, Rio de Janeiro, Brazil*, 2013.

[153] McBreen, B. and Lambert, C. J. "Interactions of high-energy ($E > 5 \times 10^{19}$ eV) photons in the Earth's magnetic field". *Phys. Rev. D*, **24**, 2536-2538, 1981. doi:10.1103/PhysRevD.24.2536.

[154] Erber, T. "High-Energy Electromagnetic Conversion Processes in Intense Magnetic Fields". *Rev. Mod. Phys.*, **38**, 626-659, 1966. doi:10.1103/RevModPhys.38.626.

[155] Bertou, X., Billoir, P. and Dagoret-Campagne, S., Pierre Auger Collaboration. "LPM effect and pair production in the geomagnetic field: a signature of ultra-high energy photons in the Pierre Auger Observatory". *Astropart. Phys.*, **14**, 121-130, 2000. doi:10.1016/S0927-6505(00)00112-2.

[156] Finlay, C. C. et al. "International Geomagnetic Reference Field: the eleventh generation". *Geophys. J. Int.*, **183**, 1216-1230, 2010. doi:10.1111/j.1365-246X.2010.04804.x.

[157] Homola, P. et al. "Simulation of ultra-high energy photon showers with PRESHOWER". *Nucl. Phys. B (Proc. Suppl.)*, **151**, 119–120, 2006. doi:10.1016/j.nuclphysbps.2005.07.022.

[158] Heck, D., Knapp, J., Capdevielle, J. N., Schatz G. and Thouw, T. "A Monte Carlo Code to Simulate Extensive Air Showers". *FZKA*, 1998.

[159] Bergmann, T., et al. "One-dimensional hybrid approach to extensive air shower simulation". *Astropart. Phys.*, **26**, 420-432, 2007. doi:10.1016/j.astropartphys.2006.08.005.

[160] Landau, L. D. and Pomeranchuk, I. J. *Dokl. Akad. Nauk. SSSR*, **92**, 1953.

[161] Migdal, A. B. "Bremsstrahlung and Pair Production in Condensed Media at High Energies". *Phys. Rev.*, **103**, 1811-1820, 1956. doi:10.1103/PhysRev.103.1811.

[162] Bethe, H. and Heitler, W. "On the Stopping of Fast Particles and on the Creation of Positive Electrons". *Proc. R. Soc. Lond. A*, **146**, 83-112, 1934. doi:10.1098/rspa.1934.0140.

[163] Klein, S. "Suppression of bremsstrahlung and pair production due to environmental factors". *Rev. Mod. Phys.*, **71**, 1501-1538, 1999. doi:10.1103/RevModPhys.71.1501.

[164] Cillis, A. N., Fanchiotti, H., Garcia Canal, C. A. and Sciutto, S. J. "Influence of the LPM effect and dielectric suppression on particle air showers". *Phys. Rev. D*, **59**, 113012, 1999. doi:10.1103/PhysRevD.59.113012.

[165] Nelson, W. R., Hirayama, H. and Rogers, D. W. O. "The Egs4 Code System". *SLAC-0265 etc.*, 1985.

[166] Fletcher, R. S. et al. "SIBYLL: An Event generator for simulation of high-energy cosmic ray cascades". *Phys. Rev. D*, **50**, 5710–5731, 1994. doi:10.1103/PhysRevD.50.5710.

[167] Ahn, E.-J. et al. "Cosmic ray interaction event generator SIBYLL 2.1". *Phys. Rev. D*, **80**, 094003, 2009. arXiv:0906.4113, doi:10.1103/PhysRevD.80.094003.

[168] Kalmykov, N. N., Ostapchenko, S. S. and Pavlov, A. I. "Quark-gluon string model and EAS simulation problems at ultra-high energies". *Nucl. Phys. B (Proc. Suppl.)*, **52**, 17–28, 1997. doi:10.1016/S0920-5632(96)00846-8.

[169] Ostapchenko, S. "On the re-summation of enhanced Pomeron diagrams". *Phys. Lett. B*, **636**, 40–45, 2006. arXiv:hep-ph/0602139, doi:10.1016/j.physletb.2006.03.026.

[170] Ostapchenko, S. "Nonlinear screening effects in high energy hadronic interactions". *Phys. Rev. D*, **74**, 014026, 2006. doi:10.1103/PhysRevD.74.014026.

[171] Ostapchenko, S. "Monte Carlo treatment of hadronic interactions in enhanced Pomeron scheme: QGSJET-II model". *Phys. Rev. D*, **83**, 014018, 2011. doi:10.1103/PhysRevD.83.014018.

[172] Werner, K., Liu, F.-M. and Pierog, T. "Parton ladder splitting and the rapidity dependence of transverse momentum spectra in deuteron-gold collisions at the BNL Relativistic Heavy Ion Collider". *Phys. Rev. C*, **74**, 044902, 2006. doi:10.1103/PhysRevC.74.044902.

[173] Pierog, T. et al. *FZKA*, 2009.

[174] Cazon, L. "Constraints and measurements of hadronic interactions in extensive air showers with the Pierre Auger Observatory". *Proc. TAUP 2013*. arXiv:1405.5095.

[175] Nellen, L., Pierre Auger Collaboration. "The observation of a muon deficit in simulations from data of the Pierre Auger Observatory". *J. Phys.: Conference Series*, **409**, 012107, 2013.

[176] dâĂŹEnterria, D. et al. "Constraints from the first {LHC} data on hadronic event generators for ultra-high energy cosmic-ray physics". *Astropart. Phys.*, **35**, 98–113, 2011. arXiv:1101.5596, doi:10.1016/j.astropartphys.2011.05.002.

[177] Parsons, R. D. et al. "Systematic uncertainties in air shower measurements from high-energy hadronic interaction models". *Astropart. Phys.*, **34**, 832–839, 2011. doi:10.1016/j.astropartphys.2011.02.007.

[178] Risse, M. et al. "Photon air showers at ultra-high energy and the photonuclear cross-section". *Czechoslovak Journal of Physics*, **56**, A327-A336, 2006. doi:10.1007/s10582-006-0166-7.

[179] Eidelmann, S. et al., Particle Data Group. "The Review of Particle Physics". *Phys. Lett. B*, **592**, 2004. doi:10.1016/j.physletb.2004.06.001.

[180] Cudell, J. R. et al., COMPETE Collaboration. "Hadronic scattering amplitudes: Medium-energy constraints on asymptotic behavior". *Phys. Rev. D*, **65**, 074024, 2002. doi:10.1103/PhysRevD.65.074024.

[181] A. Donnachie and P. V. Landshoff. "New data and the hard pomeron". *Phys. Lett. B*, **518**, 63–71, 2001. doi:10.1016/S0370-2693(01)01048-6.

[182] Glauber, R. J. "Cross Sections in Deuterium at High Energies". *Phys. Rev.*, **100**, 242-248, 1955. doi:10.1103/PhysRev.100.242.

[183] Hillas, A. M. "Shower simulation: lessons from {MOCCA}". *Nucl. Phys. B (Proc. Suppl.)*, **52**, 29–42, 1997. doi:10.1016/S0920-5632(96)00847-X.

[184] Heck, D. and Knapp, J. "Upgrade of the Monte Carlo Code CORSIKA to Simulate Extensive Air Showers with Energies $> 10^{20}$ eV". *FZKA*, 1998.

[185] Bruijn, R., Knapp, J. and Valiño, I., Pierre Auger Collaboration. "Testing the surface detector simulation for the Pierre Auger Observatory". *32nd ICRC, Beijing, China*, 2011. doi:10.7529/ICRC2011/V02/0228.

[186] Oehlschläger, J. "Map of the Pierre Auger Observatory" [online].

[187] Abraham, J. et al., Pierre Auger Collaboration. "Trigger and aperture of the surface detector array of the Pierre Auger Observatory". *Nucl. Instr. Meth. A*, **613**, 29-39, 2010. doi:10.1016/j.nima.2009.11.018.

[188] Abreu, P. et al. "The Lateral Trigger Probability function for the Ultra-High Energy Cosmic Ray showers detected by the Pierre Auger Observatory". *Astropart. Phys.*, **35**, 266–276, 2011. arXiv:0712.2832, doi:http://dx.doi.org/10.1016/j.astropartphys.2011.08.001.

[189] Abraham, J. et al., Pierre Auger Collaboration. "Properties and performance of the prototype instrument for the Pierre Auger Observatory". *Nucl. Instr. Meth. A*, **523**, 50-95, 2004. doi:10.1016/j.nima.2003.12.012.

[190] Allekotte, I. et al., Pierre Auger Collaboration. "The surface detector system of the Pierre Auger Observatory". *Nucl. Instr. Meth. A*, **586**, 409-420, 2008. arXiv:0907.4282, doi:10.1016/j.nima.2007.12.016.

[191] Abraham, J. et al., Pierre Auger Collaboration. "The fluorescence detector of the Pierre Auger Observatory". *Nucl. Instr. Meth. A*, **620**, 227-251, 2010. arXiv:0712.2832, doi:10.1016/j.nima.2010.04.023.

[192] Aab, A. et al., Pierre Auger Collaboration. "The Pierre Auger Observatory: Contributions to the 33rd International Cosmic Ray Conference". *33rd ICRC, Rio de Janeiro, Brazil*, 2013. arXiv:1307.5059.

[193] Abraham, J. et al., Pierre Auger Collaboration. "Operations of and Future Plans for the Pierre Auger Observatory". *31st ICRC, Lodz, Poland*, 2009. arXiv:0906.2354.

[194] Bertou, X. et al., Pierre Auger Collaboration. "Calibration of the surface array of the Pierre Auger Observatory". *Nucl. Instr. Meth. A*, **568**, 839-846, 2006. doi:10.1016/j.nima.2006.07.066.

[195] Aglietta, M. et al., Pierre Auger Collaboration. "Calibration of the surface array of the Pierre Auger Observatory". *29th ICRC, Pune, India*, 279-282, 2005.

[196] Lhenry-Yvon, I. "CDAS production v1r0: overview of new data available". *GAP 2012-077 (internal technical note)*, 2012.

[197] Parizot, E., Lhenry-Yvon, I., Allard, D., Ghia, P. and Navarra, G. "First steps towards the definition of a "quality trigger" (T5) for the SD acceptance calculation". *GAP 2004-023 (internal technical note)*, 2004.

[198] Lachaud, C. and Bertou, X. "Local Stations Trigger Monitoring Files". *GAP 2003-046 (internal technical note)*, 2003.

[199] Rivera Bretel, H. M. "Measurement of the energy spectrum of cosmic rays above 3×10^{17} eV using the infill array of the Pierre Auger Observatory". *PhD thesis*, 2013.

[200] Ghia, P. L., Lhenry-Yvon, I. and Rivera, H. "Study of the consistency of T2 files with SD and infill event rate". *GAP 2012-026 (internal technical note)*, 2012.

[201] Argirò S. et al. "The offline software framework of the Pierre Auger Observatory". *Nucl. Instrum. Meth. A*, **580**, 1485–1496, 2007. doi:10.1016/j.nima.2007.07.010.

[202] Veberič, D. and Roth, M. (for the offline team). "Offline Reference Manual: SD Reconstruction". *GAP 2005-035 (internal technical note)*, 2005.

[203] Bonifazi, C., Ghia, P. L. and Lhenry-Yvon, I. "On the unstable period of data-taking in 2009". *GAP 2010-002 (internal technical note)*, 2010.

[204] Bruijn, R. "Presentation ("Some comments on the FADC traces")". *Auger Collaboration Meeting, March 2011*, 2011.

[205] Bruijn, R. "Presentation ("Modifications to the treatment of FADC traces")". *Auger Analysis Meeting, June 2011*, 2011.

[206] Roth, M. et al., Pierre Auger Collaboration. "The Lateral Distribution Function of Shower Signals in the Surface Detector of the Pierre Auger Observatory". *28th ICRC Tsukuba, Japan*, 2003. arXiv:0308392v1.

[207] Newton, D., Knapp, J. and Watson, A. A. "The optimum distance at which to determine the size of a giant air shower". *Astropart. Phys.*, **26**, 414–419, 2007. doi:10.1016/j.astropartphys.2006.08.003.

[208] Ave, M. et al. "The accuracy of signal measurement with the water Cherenkov detectors of the Pierre Auger Observatory". *Nucl. Instr. Meth. A*, **578**, 180–184, 2007. doi:10.1016/j.nima.2007.05.150.

[209] Hiller, R. and Roth, M. "An update on the signal accuracy using the infill array". *GAP 2012-012 (internal technical note)*, 2012.

[210] Hillas, A. M. et al. *12th ICRC, Hobart, Australia*, 1001, 1971.

[211] Pesce, R. et al., Pierre Auger Collaboration. "Energy calibration of data recorded with the surface detectors of the Pierre Auger Observatory: an update". *32nd ICRC, Beijing, China*, 2011.

[212] Billoir, P. et al. "A sampling procedure to regenerate particles in a ground detector from a "thinned" air shower simulation output". *Astropart. Phys.*, **30**, 270–285, 2008. doi:10.1016/j.astropartphys.2008.10.002.

[213] S. Agostinelli et al., Pierre Auger Collaboration. "Geant4 - a simulation toolkit". *Nucl. Instrum. Meth. A*, **506**, 250-303, 2003. doi:10.1016/S0168-9002(03)01368-8.

[214] Ghia, P. L., Pierre Auger Collaboration. "Testing the surface detector simulation for the Pierre Auger Observatory". *30th ICRC, Merida, Mexico*, 2007.

[215] Bueno, A, Sanchez-Lucas, P. and Watson, A. A. "The Δ-method revisited". *GAP 2013-078 (internal technical note)*.

[216] Billoir, P., Roucelle, C. and Hamilton, J. C. "Evaluation of the Primary Energy of UHE Photon-induced Atmospheric Showers from Ground Array Measurements". 2007. arXiv:astro-ph/0701583.

[217] Ros, G., Medina-Tanco, G. A., Supanitsky, D., de Peral, L. and Rodrigues-Frías, M. D. "Internal technical note: Reconstruction of the primary energy of UHE photon-induced showers from Auger SD". 2010.

[218] Schmidt, F., Ave, M., Cazon, L. and Chou A. "A model-independent method of determining energy scale and muon number in cosmic ray surface detectors". *Astropart. Phys.*, **29**, 355–365, 2008. doi:10.1016/j.astropartphys.2008.03.004.

[219] Ave, M., Engel, R., Gonzalez, J., Heck, D., Maurel, D., Pierog, T. and Roth, M. "Prediction of the tank response S(r,DX,E | theta, phi) from shower universality". *GAP 2011-087 (internal technical note)*, 2011.

[220] Neyman, J. "Outline of a Theory of Statistical Estimation Based on the Classical Theory of Probability". *Royal Society of London Philosophical Transactions Series A*, **236**, 333-380, 1937. doi:10.1098/rsta.1937.0005.

[221] Feldman, G. J. and Cousins, R. D. "Unified approach to the classical statistical analysis of small signals". *Phys. Rev. D*, **57**, 3873-3889, 1998. arXiv:physics/9711021, doi:10.1103/PhysRevD.57.3873.

[222] Shinozaki, K. et al., AGASA Collaboration. "Upper Limit on Gamma-Ray Flux above 10^{19} eV Estimated by the Akeno Giant Air Shower Array Experiment". *Astrophys. J.*, **571**, L117, 2002. doi:10.1086/341288.

[223] Ave, M., Hinton, J. A., Vázquez, R. A., Watson, A. A. and Zas, E. "New Constraints from Haverah Park Data on the Photon and Iron Fluxes of Ultrahigh-Energy Cosmic Rays". *Phys. Rev. Lett.*, **85**, 2244–2247, 2000. arXiv:astro-ph/0007386, doi:10.1103/PhysRevLett.85.2244.

[224] Rubtsov, G. I. et al. "Upper limit on the ultrahigh-energy photon flux from AGASA and Yakutsk data". *Phys. Rev. D*, **73**, 063009, 2006. doi:10.1103/PhysRevD.73.063009.

[225] Glushkov, A. V. et al., Yakutsk EAS Array. "Constraining the fraction of primary gamma rays at ultra-high energies from the muon data of the Yakutsk extensive-air-shower array". *JETP Lett.*, **85**, 131-135, 2007. doi:10.1134/S0021364007030010.

[226] Glushkov, A. V. et al., Yakutsk EAS Array. "Constraints on the flux of primary cosmic-ray photons at energies $E > 10^{18}$ eV from Yakutsk muon data". *Phys. Rev. D*, **82**, 041101, 2010. doi:10.1103/PhysRevD.82.041101.

[227] Abu-Zayyad, T. et al., Telescope Array Collaboration. "Upper limit on the flux of photons with energies above 10^{19} eV using Telescope Array surface detector". *Phys. Rev. D*, **88**, 112005, 2013. arXiv:1304.5614, doi:10.1103/PhysRevD.88.112005.

[228] Rubtsov, G. I. et al., Telescope Array Collaboration. "Telescope Array search for photons and neutrinos with the surface detector data". *Proc. 34th ICRC, The Hague, The Netherlands*, **PoS**, 331, 2016.

[229] Aab, A. et al., Pierre Auger Collaboration. "Search for photons with energies above 10^{18} eV using the hybrid detector of the Pierre Auger Observatory". *to be submitted to JCAP*, 2016. arXiv:1612.01517.

[230] Supanitsky, A. D. and Medina-Tanco, G., JEM-Euso Collaboration. "Identification of extreme energy photons with JEM-EUSO". *33rd ICRC, Rio de Janeiro, Brazil*, 2013.

[231] Galaverni, M. and Sigl, G. "Lorentz Violation for Photons and Ultrahigh-Energy Cosmic Rays". *Phys. Rev. Lett.*, **100**, 021102, 2008. arXiv:0708.1737, doi:10.1103/PhysRevLett.100.021102.

[232] Bleve, C. for the Pierre Auger Collaboration, Pierre Auger Collaboration. "Update of the neutrino and photon limits from the Pierre Auger Observatory". *34th ICRC, The Hague, The Netherlands*, 61-68, 2015. arXiv:1509.03732.

[233] Risse, M. et al., AGASA Collaboration. "Upper Limit on the Photon Fraction in Highest-Energy Cosmic Rays from AGASA Data". *Phys. Rev. Lett.*, **95**, 171102, 2005. doi:10.1103/PhysRevLett.95.171102.

[234] Bass, S. A. et al. "Microscopic models for ultrarelativistic heavy ion collisions". *Prog. Part. Nucl. Phys.*, **41**, 255–369, 1998. arXiv:nucl-th/9803035, doi:10.1016/S0146-6410(98)00058-1.

[235] Bleicher, M. et al. "Relativistic hadron-hadron collisions in the ultra-relativistic quantum molecular dynamics model". *J. Phys. G*, **25**, 1859, 1999. arXiv:hep-ph/9909407, doi:10.1088/0954-3899/25/9/308.

[236] Cudell, J. R. et al. "High-energy forward scattering and the Pomeron: Simple pole versus unitarized models". *Phys. Rev. D*, **61**, 034019, 2000. Erratum DOI:10.1103/PhysRevD.63.059901. doi:10.1103/PhysRevD.61.034019.

[237] International Association of Geomagnetism and Working Group V-MOD Aeronomy. "International Geomagnetic Reference Field: the eleventh generation". *Geophys. Journ. Int.*, **183**, 1216–1230, 2010. doi:10.1111/j.1365-246X.2010.04804.x.

[238] Bleve, C. "Update of Corsika for the IGRF-11 model". *Private communication.*

[239] Middendorf, L. "Search for Ultra-High Energy Photons from Centaurus A with the Pierre Auger Observatory". *Master thesis*, 2012.

[240] Abraham, J. et al., Pierre Auger Collaboration. "Measurement of the energy spectrum of cosmic rays above 10^{18} eV using the Pierre Auger Observatory". *Phys. Lett. B*, **685**, 239-246, 2010. arXiv:1002.1975, doi:10.1016/j.physletb.2010.02.013.

[241] Lhenry-Yvon, I. "List of malfunction PMTs". *Private communication.*

[242] Lopez-Aguera, A., Olmos-Gilbaja, V. M., Rodriguez Fernandez, G. "Direct light in inclined showers". *GAP 2003-112 (internal technical note)*, 2003.

[243] Gomez Albarracin, F. A., Dova, M. T. and Wahlberg, H. "Width of the rise time distributions: a novel approach to primary mass discrimination (... and iron again)". *GAP 2006-063 (internal technical note)*, 2006.

[244] Fitzner, A., Grebe, S., Schoorlemmer, H. and Timmermans, C. "Angular reconstruction with less than three SD stations using relative PMT signals". *GAP 2010-053 (internal technical note)*, 2010.

[245] Smith, B., Wileman, C. and Watson, A. A. "Can the risetime be used to infer the position of shower maximum?" *GAP 2007-092 (internal technical note)*, 2007.

[246] Meyer, H. and Mariş, I. "Detection of miss-cabled PMTs and rotated stations using the signal asymmetries". *GAP 2013-066 (internal technical note)*, 2013.

[247] Lapikens, J., Watson, A. A., Wild, P. and Wilson, J. G. "The relation of longitudinal development to shower front structure". *Proc. 13th ICRC, Denver, Colorado*, **Volume 4**, 1973.

[248] Wileman, C. "The Spread in the Arrival Times of Particles in Air-Showers for Photon and Anisotropy Searched Searches". *PhD thesis*, 2008.

[249] Ave, M., Bertou, X, Engel, R. and Roth, M. "A model for the time-dependent signal in water Cherenkov detectors". *GAP 2013-072 (internal technical note).*

[250] L. Lu. "A Search for Photons of Energy above 6×10^{18} eV Using Data from the Water-Cherenkov Detectors of the Pierre Auger Observatory". *PhD thesis*, 2015.

[251] Aab, A. et al., Pierre Auger Collaboration. "Azimuthal asymmetry in the risetime of the surface detector of the Pierre Auger Observatory". *Phys. Rev. D*, **93**, 072006, 2016. arXiv:1604.00978, doi:10.1103/PhysRevD.93.072006.

[252] Cook, H. L. "Limit to the Ultra-High Energy Gamma-Ray Flux Using Data from the Surface Detectors of the Pierre Auger Observatory". *Master thesis*, 2012.

[253] The Pierre Auger Collaboration. "Photon activities wihtin Auger: A collection of current results and ideas". *GAP 2005-096 (internal technical note)*, 2006.

[254] Healy, M., Barnhill, D., Arisaka, K., Lee, J. and Boghrat, P. "A study of composition trends using rise time and curvature data". *GAP 2006-092 (internal technical note)*, 2006.

[255] Smith, B. E. "The Mass Composition of Cosmic Rays Above 1 EeV Inferred Using the Spread in Arrival Times of Air Shower Particles". *PhD thesis*, 2008.

[256] Mora, K. "Composition studies of Ultra High Energy Cosmic Rays using Data of the Pierre Auger Observator". *PhD thesis*, 2010.

[257] Barnhill, D. "Composition Analysis of Ultrahigh Energy Cosmic Rays Using the Pierre Auger Observatory Surface Detector". *PhD Thesis / GAP 2005-092 (internal technical note)*, 2005.

[258] Jarne, C., Wahlberg, H. and Dova, M. T. "Risetime at 1000 m revisited". *GAP 2013-079 (internal technical note)*, 2013.

[259] Krohm, N., Bleve, C., Kampert, K-H. and Rautenberg, J. "Looking for an LDF Parameter for the SD Photon Search". *GAP 2012-059 (internal technical note)*, 2012.

[260] Ros, G., Supanitsky, D., Medina-Tanco, G. A., del Peral, L., D'Olivo, J. C. and Rodríguez Frías, M. D. "A new parameter for composition discrimination of Ultra-High Energy Cosmic Rays". *GAP 2009-103 (internal technical note)*.

[261] Ros, G. et al. "A new composition-sensitive parameter for ultra-high energy cosmic rays". *Astropart. Phys.*, **35**, 140-151, 2011. doi:10.1016/j.astropartphys.2011.06.011.

[262] Ros, G., Medina-Tanco, G. A., Supanitsky, D., del Peral, L. and Rodríguez Frías, M. D. "S_b for photon-hadron discrimination". *GAP 2010-052 (internal technical note)*.

[263] Schulz, A. et al., Pierre Auger Collaboration. "The measurement of the energy spectrum of cosmic rays above 3×10^{17} eV with the Pierre Auger Observatory". *33rd ICRC, Rio de Janeiro, Brazil*, 2013.

[264] Casadei, D. "Estimating the selection efficiency". *2012_JINST_7_P08021*, **7**, P08021, 2012. arXiv:0908.0130, doi:10.1088/1748-0221/7/08/P08021.

[265] Bleve, C. *Private communication in preparation for [232]*, 2015.

[266] Abramowitz, M. and Stegun, I. "Handbook of Mathematical Functions with Formulas, Graphs, and Mathematical Tables". Dover Publications, tenth edition, 1964. ISBN 978-0-486-61272-0.

[267] Veberič, D., Pierre Auger Collaboration. "Estimation of Signal in Saturated Stations of Pierre Auger Surface Detector". *33rd ICRC, Rio de Janeiro, Brazil*, 2013.

Appendix

A Upper Limits

The cumulative χ^2-distribution $F_{\chi^2}(\nu, c)$ is related [266] to Gamma-functions by

$$\begin{aligned} F_{\chi^2}\ (c,\ \nu) &= \frac{\int_0^c t^{\nu/2-1} e^{-t/2} dt}{2^{\nu/2}\Gamma(\nu/2)} \\ &= \frac{\int_0^{c/2} 2 \cdot a^{\nu/2-1} e^{-a} da}{2\Gamma(\nu/2)} \\ &= \frac{\gamma(\nu/2, c/2)}{\Gamma(\nu/2)} \end{aligned} \tag{A.1}$$

Assume the following equation for an upper limit b (as it is found in several places for the derivation of confidence intervals)

$$\begin{aligned} \alpha/2 &= e^{-b} \cdot \sum_{k=0}^{n-1} \frac{b^k}{k!} \\ &= 1 - \frac{\gamma(n-1, b)}{\Gamma(n-1)}. \end{aligned} \tag{A.2}$$

Comparing Eq. A.1 and A.2 we find that

$$F_{\chi^2}\ (2\nu_{\mathrm{s}}^{\mathrm{up}},\ 2(n+1)) = 1 - \alpha/2. \tag{A.3}$$

B Conex Showers

For some studies, different primaries (γ, p, Fe) have been simulated with CONEX [159]. This program allows for a relatively fast simulation of extensive air showers, even compared to thinned simulations with CORSIKA. Is is based on a "one-dimensional hybrid approach combining an explicit Monte-Carlo simulation of the high energy part of hadronic and EM cascades in the atmosphere [...] with a numeric soution of cascade equations for smaller energy sub-showers" [159]. We use the following models: High-energy interactions are treated with the QGSJETII.04 model. Photonuclear interactions are accounted for with the EGS4 model. The magnetic field is set to the IGRF-11 model, as for year 2013, for the location of the Auger site. Showers have been thinned at a level 10^{-6}. The following showers have been simulated with zenith angles below 60°, assuming a flat detector ($\cos(\theta) \cdot \sin(\theta)$):

- **Photon:** 100000 photon showers from an E^{-1} spectrum have been simulated with energies $10^{18.5}$ eV to $10^{20.5}$ eV. The LPM and geomagnetic preshower effect have been accounted for. Additionally, a set of 10000 photons has been simulated in the energy range $10^{19.4}$ eV to $10^{20.5}$ eV without preshower effect or LPM effect.
- **Proton:** 50000 proton showers from an E^{-1} spectrum have been simulated with energies $10^{18.5}$ eV to $10^{20.5}$ eV.
- **Iron:** 50000 iron showers from an E^{-1} spectrum have been simulated with energies $10^{18.5}$ eV to $10^{20.5}$ eV.

C SD Simulation

Module sequence used for SD simulation and reconstruction of CORSIKA simulations:

```
<sequenceFile
     xmlns:xsi="http://www.w3.org/2001/XMLSchema-instance"
     xsi:noNamespaceSchemaLocation='/opt/Offline/v2r9p3-icrc13-final/share/auger-offline/config/ModuleSequence.xsd'>

      <enableTiming/>

      <moduleControl>

           <loop numTimes="1" pushEventToStack="yes">
                <module> EventFileReaderOG </module>
                <loop numTimes="5" pushEventToStack="yes">
                     <module> EventGeneratorOG </module>
                     <loop numTimes="unbounded" pushEventToStack="no">
                       <module> CachedShowerRegeneratorOG </module>
                       <module> G4TankSimulatorOG </module>
                     </loop>
                     <module> SdSimulationCalibrationFillerOG </module>
                     <module> SdPMTSimulatorOG </module>
                     <module> SdFilterFADCSimulatorMTU </module>
                     <module> SdBaselineSimulatorOG </module>
                     <module> TankTriggerSimulatorOG </module>
                     <module> TankGPSSimulatorOG </module>
                     <module> EventFileExporterOG </module>
                     <module> CentralTriggerSimulatorXb </module>
                     <module> CentralTriggerEventBuilderOG </module>
                     <module> EventBuilderOG </module>
                     <module> EventCheckerOG </module>
                     <module> SdCalibratorOG </module>
                     <module> SdSignalRecoveryKLT[1] </module>
                     <module> SdMonteCarloEventSelectorOG </module>
                     <module> SdEventSelectorOG </module>
                     <module> SdPlaneFitOG </module>
                     <module> LDFFinderKG </module>
                     <module> SdEventPosteriorSelectorOG </module>
                     <module> Risetime1000LLL </module>
                     <module> RecDataWriterNG </module>
                </loop>
           </loop>

      </moduleControl>

</sequenceFile>
```

D SD Reconstruction

Module sequence used for SD data reconstruction:

```
<sequenceFile>
```

[1]The PMTs are operated in a way to assure a large dynamic range (10 bit). The range has to cover most of the signals, starting at about 1000-2000 VEM close to the core, within a few hundred ns, dropping rapidly to a few VEM from single particles arriving at 1000m or more. Therefore the signal is measured with two different gains. If a gain is saturated, it creates an undershoot in the FADC trace, which is problematic for any trace-based calculations. In case of high-gain saturation the signal can be easily recovered using non-saturated low-gain. If the low-gain is also saturated, the signal can be recovered [267].

```
    <moduleControl>
        <loop numTimes="unbounded">
            <module> EventFileReaderOG </module>
            <module> SdQualityCutTaggerOG </module>
            <module> SdPMTQualityCheckerKG </module>
            <module> TriggerTimeCorrection </module>
            <module> SdCalibratorOG </module>
            <module> SdStationPositionCorrection </module>
            <module> SdBadStationRejectorKG </module>
            <module> SdSignalRecoveryKLT </module>
            <module> SdEventSelectorOG </module>
            <module> SdPlaneFitOG </module>
            <module> LDFFinderKG </module>
            <module> Risetime1000LLL </module>
            <module> SdEventPosteriorSelectorOG </module>
            <module> RecDataWriterNG </module>
        </loop>
    </moduleControl>

</sequenceFile>
```

The LDF is parametrized by a modified NKG-type function with shape parameters β and γ (cf. Eq. 3.18)

$$S(r) = S_{1000} \cdot \left(\frac{r}{1000\ \text{m}}\right)^{\beta} \cdot \left(\frac{r + 700\ \text{m}}{1000\ \text{m} + 700\ \text{m}}\right)^{\beta+\gamma}, \tag{D.4}$$

$$\begin{aligned} \beta \quad = \quad & a_0 + a_1 \cdot \log_{10}(S_{1000}) \\ & +(b_0 + b_1 \cdot \log_{10}(S_{1000})) \cdot \sec(\theta) \\ & +(c_0 + c_1 \cdot \log_{10}(S_{1000})) \cdot \sec^2(\theta), \end{aligned} \tag{D.5}$$

$$\begin{aligned} \text{with} \quad & a_0 = -3.72 \\ & a_1 = 0.0967 \\ & b_0 = 1.74 \\ & b_1 = -0.242 \\ & c_0 = -0.274 \\ & c_1 = 0.0349, \end{aligned}$$

$$\begin{aligned} \gamma \quad = \quad & fo_0 + fo_1 \cdot \log_{10}(S_{1000}) \\ & + \frac{fa_0 + fa_1 \cdot \log_{10}(S_{1000})}{\mathrm{e}^{(fs_0 + fs_1 \cdot \log_{10}(S_{1000})) \cdot (\cos^2(\theta) - fp_0 - fp_1 \cdot \log_{10}(S_{1000}))} + 1} \\ & + fb \cdot \frac{\cos(\theta)^{2 \cdot fet}}{\mathrm{e}^{(\log_{10}(S_{1000}) - fps) \cdot fss} + 1} \ - \ \beta, \end{aligned} \tag{D.6}$$

$$\begin{aligned} \text{with} \quad & fo_0 = -1.87 \\ & fo_1 = -0.183 \\ & fa_0 = 0.490 \\ & fa_1 = -0.065 \\ & fp_0 = 0.483 \\ & fp_1 = 0.005 \\ & fs_0 = 19.6 \\ & fs_1 = -2.10 \\ & fb = -0.272 \\ & fet = 2.32 \\ & fps = 1.95 \\ & fss = 18.01 \end{aligned}$$

E Figures and Tables

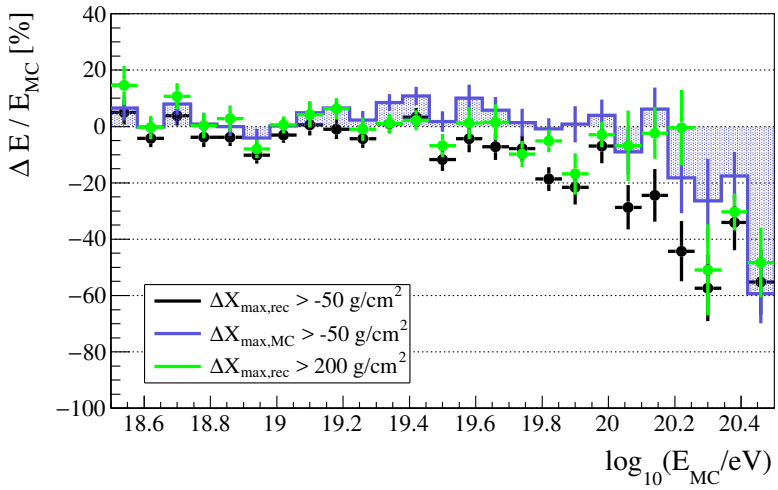

(a) Photon energy scale, comparing different $X_{\max}$ cuts. Showing mean and error of the mean.

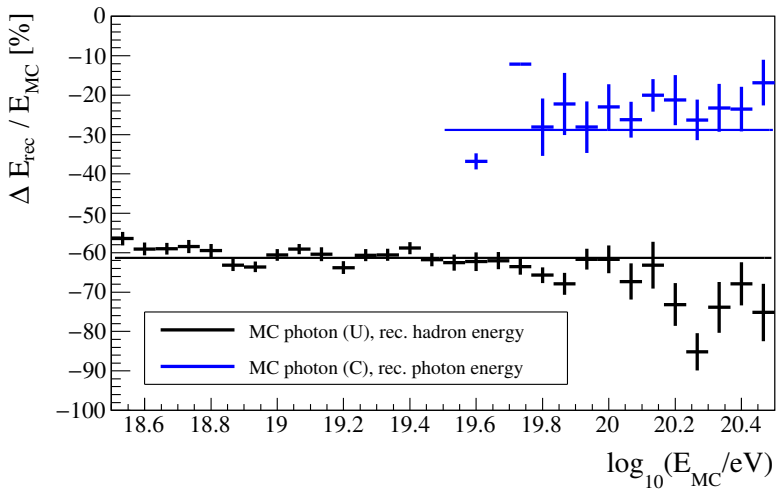

(b) Case 1: Photon energy scale (U) for preshowered photons (C). Case 2: Hadronic energy scale for non-preshowered photons.

Figure E.1: Relative errors of the different energy scales with respect to the MC truth. Showers have been simulated in the detector five times.

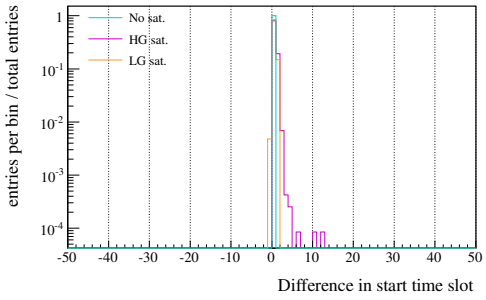

(a) Starttime bin (difference in multiples of 25 ns), for selected stations

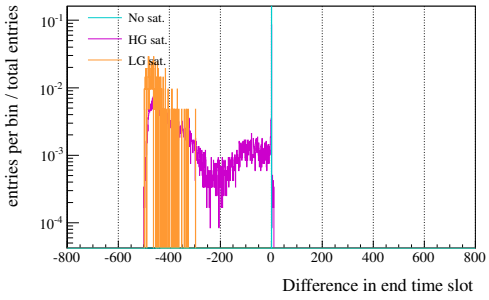

(b) Stoptime bin (difference in multiples of 25 ns), for selected stations

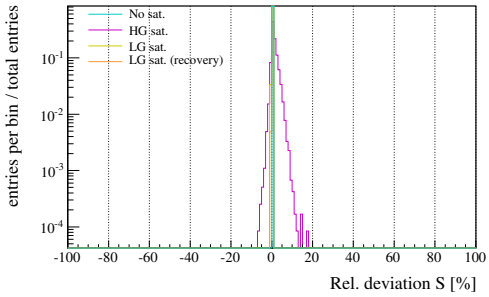

(c) Signal S, for selected stations

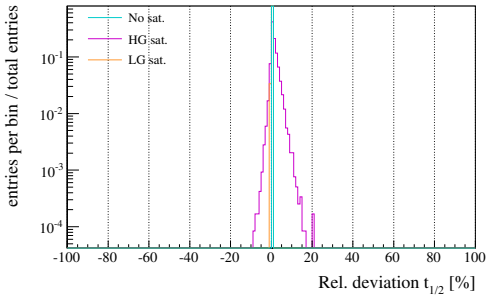

(d) Risetime $t_{1/2}$, for selected stations

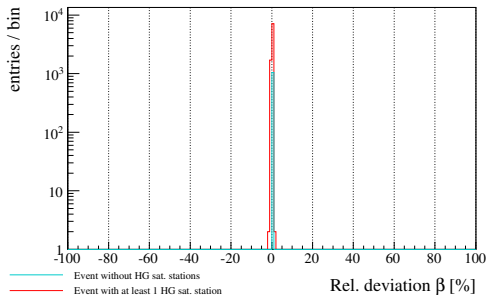

(e) LDF shape parameter β, for selected events

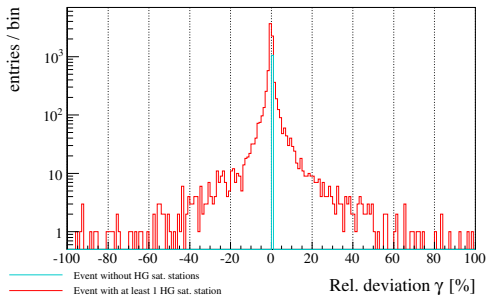

(f) LDF shape parameter γ, for selected events

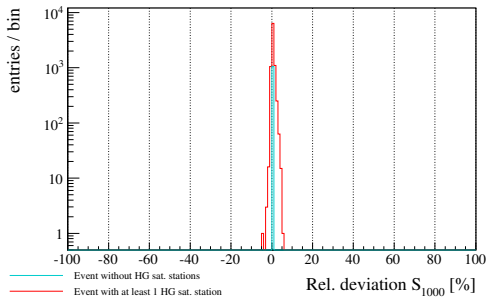

(g) S_{1000}, for selected events

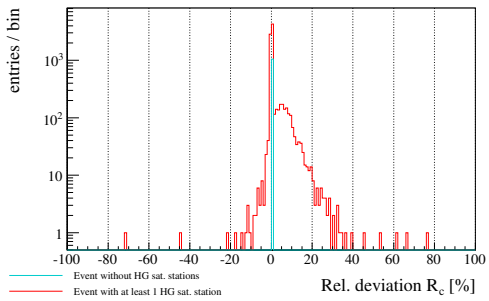

(h) Radius of curvature R_c, for selected events

Figure E.2: Relative difference of reconstructed quantities with and without applying **Mod. 1** to the SdCalibrator, applied on **observed data**. Mean and standard deviation can be found in Tab. E.2. Cyan: Selected non-saturated stations of events with no saturated station, magenta: selected HG.saturated stations of events with at least one HG-saturated station, orange: LG-saturated stations of events with at least one HG-saturated station.

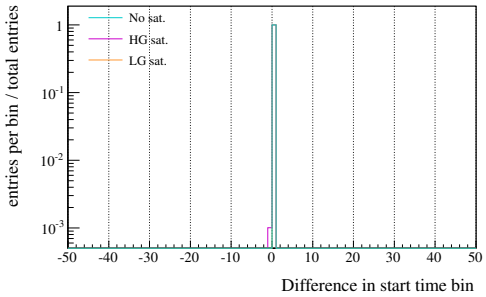

(a) Starttime bin (difference in multiples of 25 ns), for selected stations

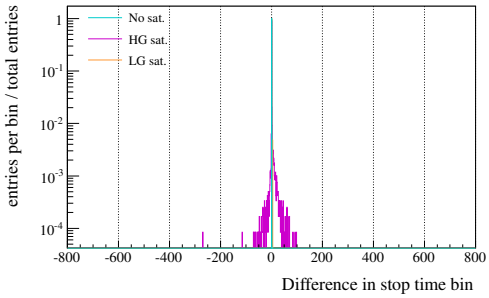

(b) Stoptime bin (difference in multiples of 25 ns), for selected stations

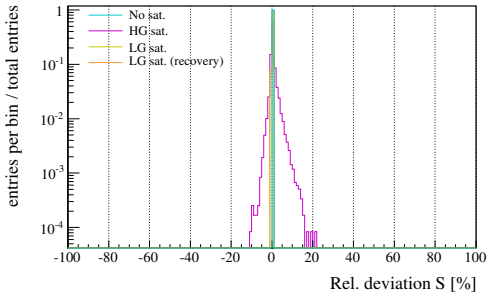

(c) Signal S, for selected stations

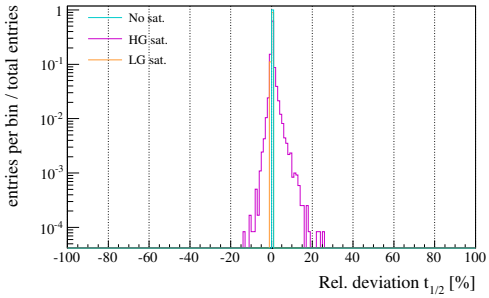

(d) Risetime $t_{1/2}$, for selected stations

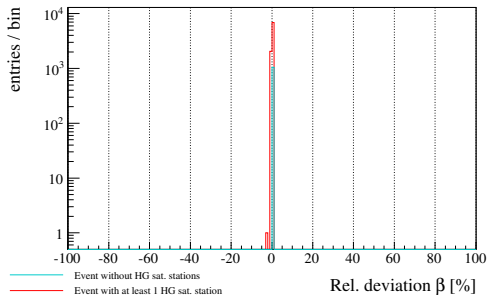

(e) LDF shape parameter β, for selected events

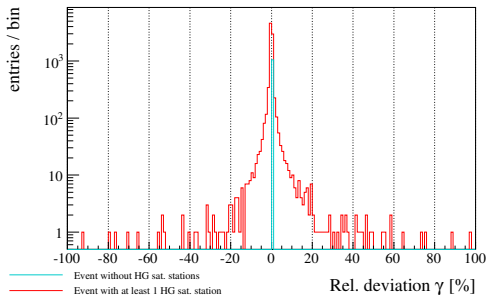

(f) LDF shape parameter γ, for selected events

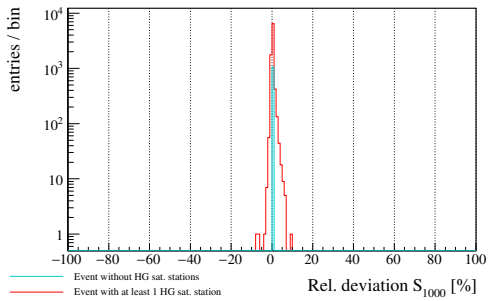

(g) S_{1000}, for selected events

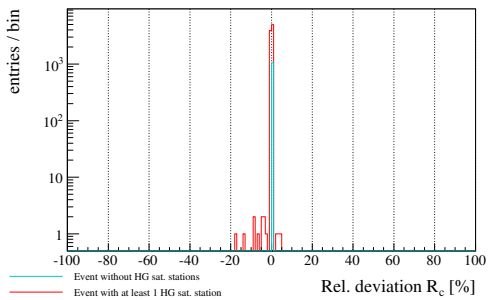

(h) Radius of curvature R_c, for selected events

Figure E.3: Relative difference of reconstructed quantities with and without applying **Mod. 3** to the SdCalibrator, applied on **observed data**. Mean and standard deviation can be found in Tab. E.2. Cyan: Selected non-saturated stations of events with no saturated station, magenta: selected HG-saturated stations of events with at least one HG-saturated station, orange: LG-saturated stations of events with at least one HG-saturated station.

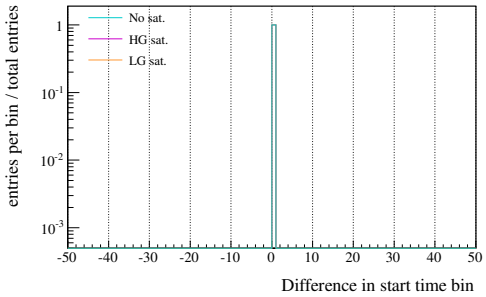

(a) Starttime bin (difference in multiples of 25 ns), for selected stations

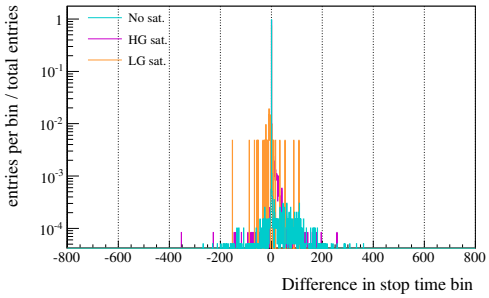

(b) Stoptime bin (difference in multiples of 25 ns), for selected stations

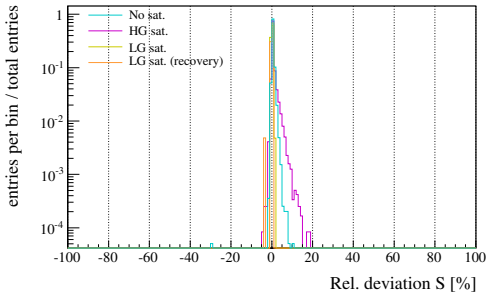

(c) Signal S, for selected stations

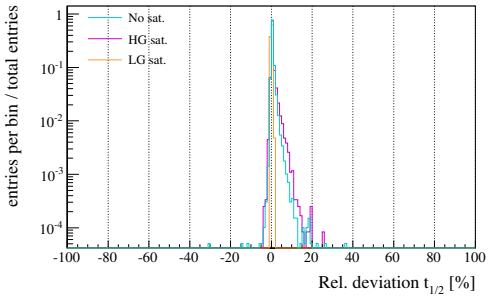

(d) Risetime $t_{1/2}$, for selected stations

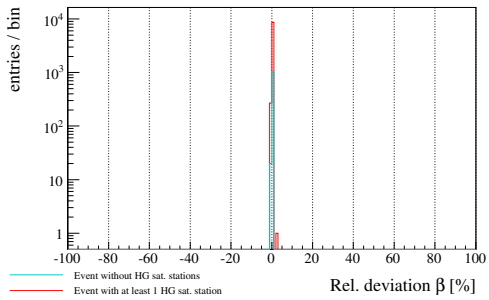

(e) LDF shape parameter β, for selected events

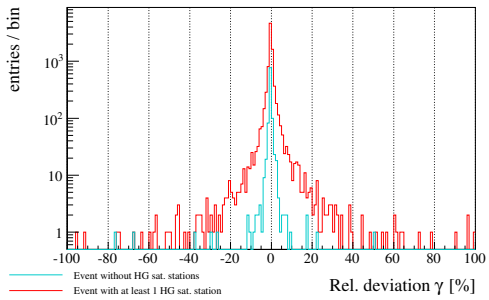

(f) LDF shape parameter γ, for selected events

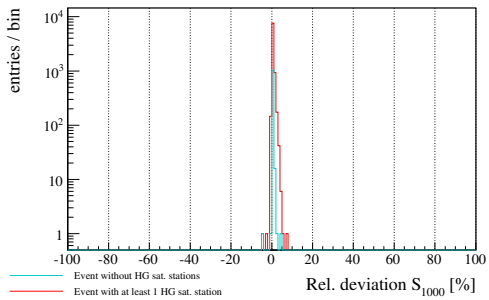

(g) S_{1000}, for selected events

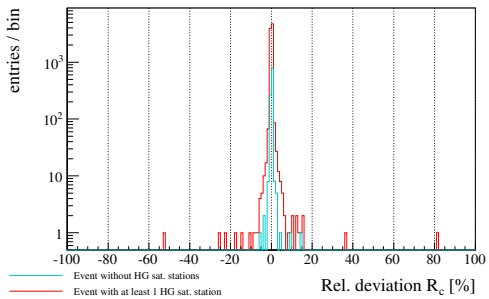

(h) Radius of curvature R_c, for selected events

Figure E.4: Relative difference of reconstructed quantities with and without applying **Mod. 2** to the SdCalibrator, applied on **observed data**. Mean and standard deviation can be found in Tab. E.2. Cyan: Selected non-saturated stations of events with no saturated station, magenta: selected HG-saturated stations of events with at least one HG-saturated station, orange: LG-saturated stations of events with at least one HG-saturated station.

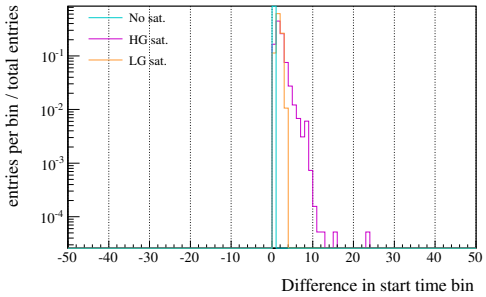

(a) Starttime bin (difference in multiples of 25 ns), for selected stations

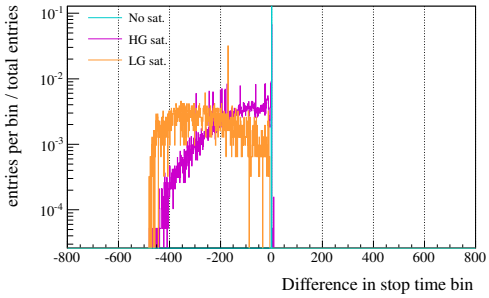

(b) Stoptime bin (difference in multiples of 25 ns), for selected stations

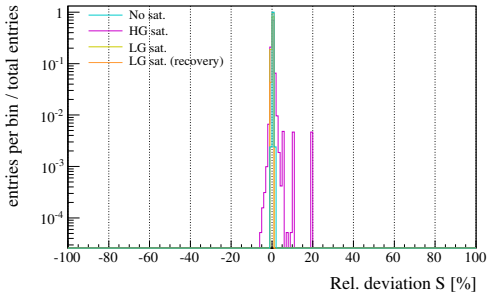

(c) Signal S, for selected stations

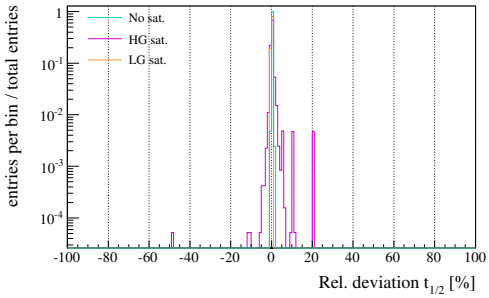

(d) Risetime $t_{1/2}$, for selected stations

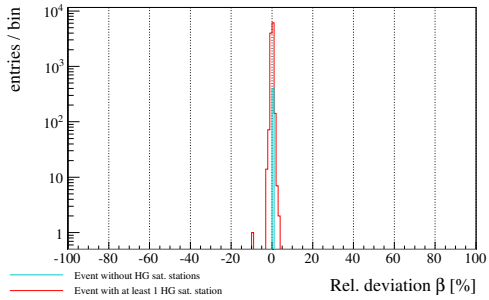

(e) LDF shape parameter β, for selected events

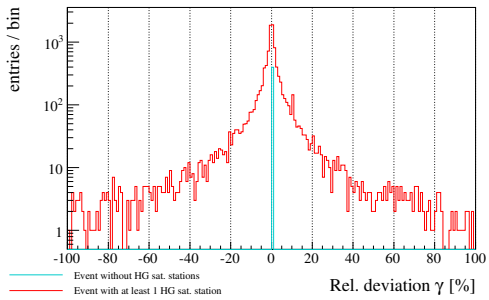

(f) LDF shape parameter γ, for selected events

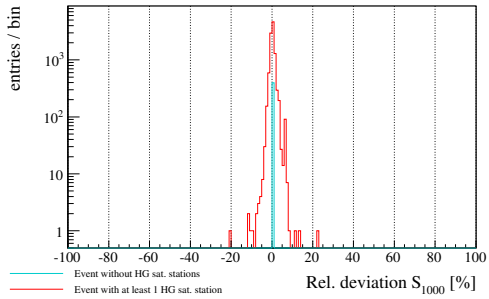

(g) S_{1000}, for selected events

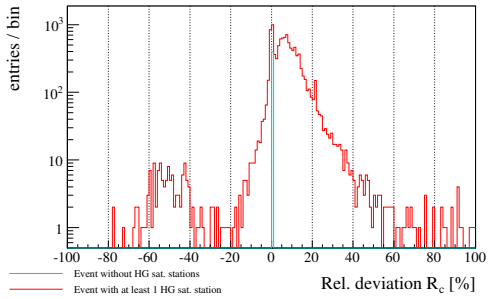

(h) Radius of curvature R_c, for selected events

Figure E.5: Relative difference of reconstructed quantities with and without applying **Mod. 1** to the SdCalibrator, applied on **MC photon**s. Mean and standard deviation can be found in Tab. E.2. Cyan: Selected non-saturated stations of events with no saturated station, magenta: selected HG-saturated stations of events with at least one HG-saturated station, orange: LG-saturated stations of events with at least one HG-saturated station.

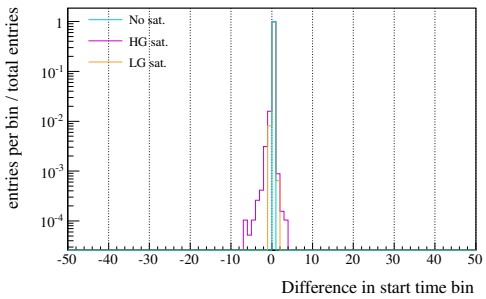

(a) Starttime bin (difference in multiples of 25 ns), for selected stations

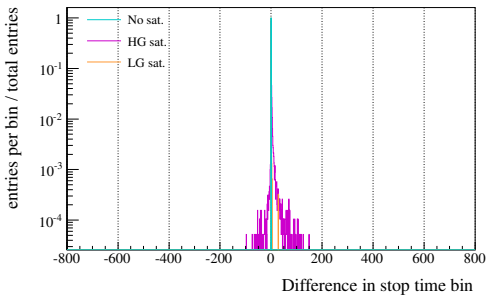

(b) Stoptime bin (difference in multiples of 25 ns), for selected stations

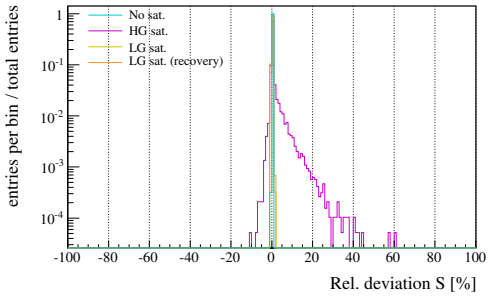

(c) Signal S, for selected stations

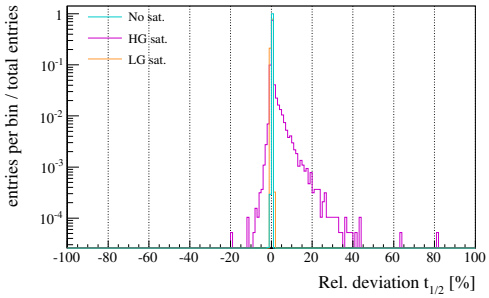

(d) Risetime $t_{1/2}$, for selected stations

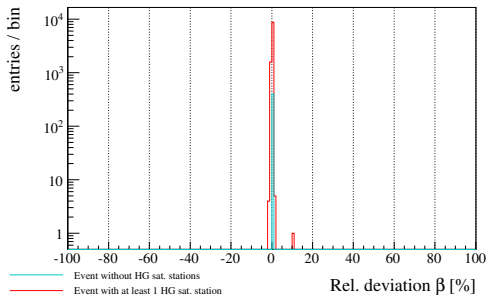

(e) LDF shape parameter β, for selected events

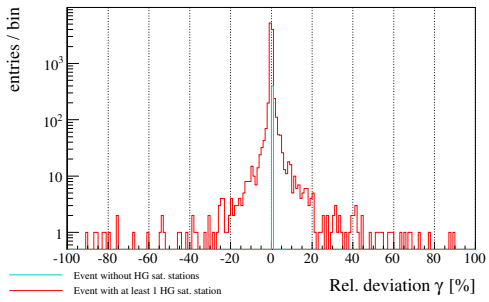

(f) LDF shape parameter γ, for selected events

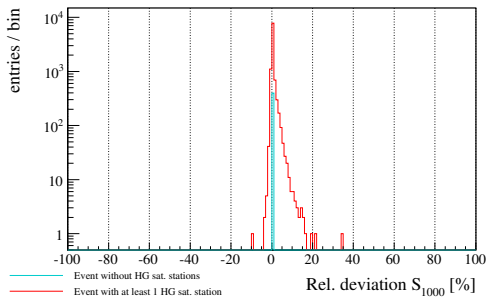

(g) S_{1000}, for selected events

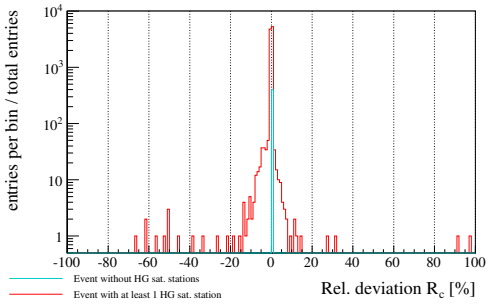

(h) Radius of curvature R_c, for selected events

Figure E.6: Relative difference of reconstructed quantities with and without applying **Mod. 3** to the SdCalibrator, applied on **MC photons**. Mean and standard deviation can be found in Tab. E.2. Cyan: Selected non-saturated stations of events with no saturated station, magenta: selected HG-saturated stations of events with at least one HG-saturated station, orange: LG-saturated stations of events with at least one HG-saturated station.

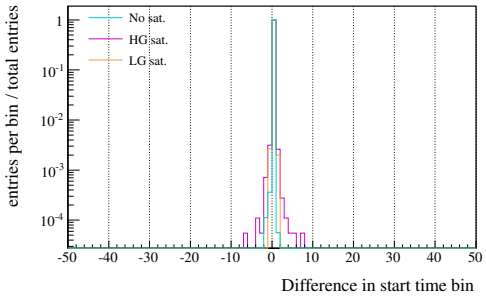

(a) Starttime bin (difference in multiples of 25 ns), for selected stations

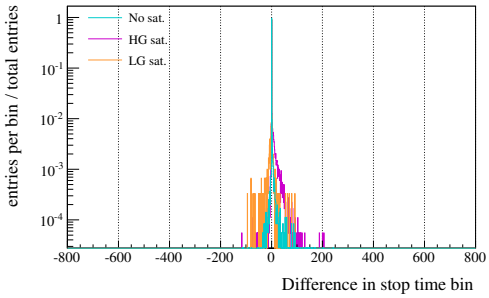

(b) Stoptime bin (difference in multiples of 25 ns), for selected stations

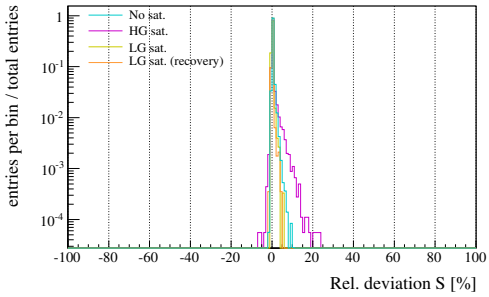

(c) Signal S, for selected stations

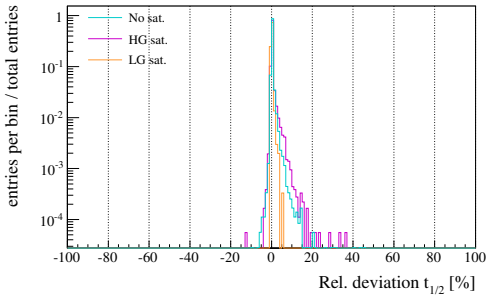

(d) Risetime $t_{1/2}$, for selected stations

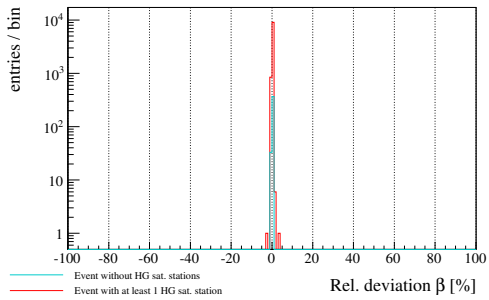

(e) LDF shape parameter β, for selected events

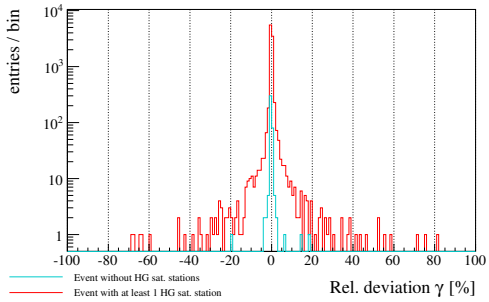

(f) LDF shape parameter γ, for selected events

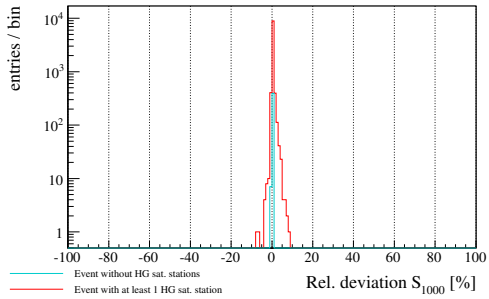

(g) S_{1000}, for selected events

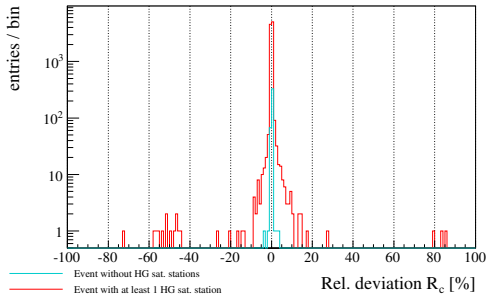

(h) Radius of curvature R_c, for selected events

Figure E.7: Relative difference of reconstructed quantities with and without applying **Mod. 2** to the SdCalibrator, applied on **MC photon**s. Mean and standard deviation can be found in Tab. E.2. Cyan: Selected non-saturated stations of events with no saturated station, magenta: selected HG-saturated stations of events with at least one HG-saturated station, orange: LG-saturated stations of events with at least one HG-saturated station.

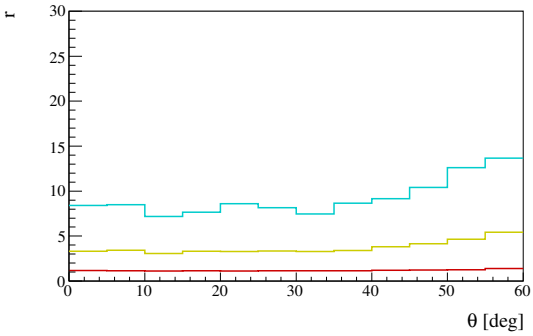

(a) Non-saturated stations with 2 good PMTS

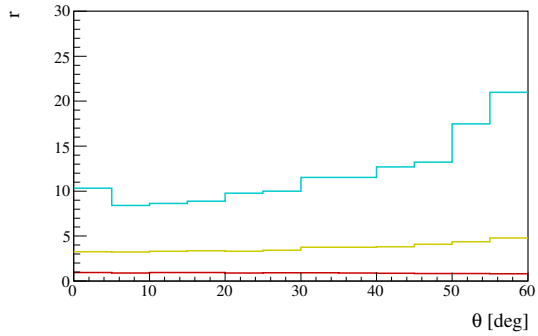

(b) High-gain-saturated stations with 3 good PMTs

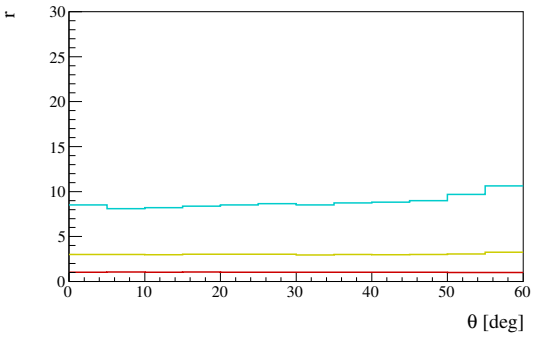

(c) Simulated photon, non-saturated stations with 3 good PMTS

Figure E.8: Fixing the threshold value of r to identify signal outliers in one PMT: Zenith angle dependence of the confidence levels according to 68% (red), 95% (yellow) and 99.7% (cyan) probability.

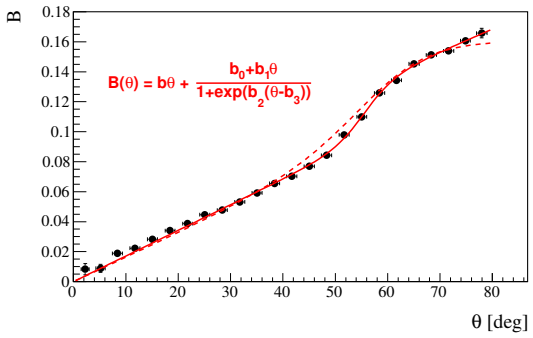

(a) Linear term

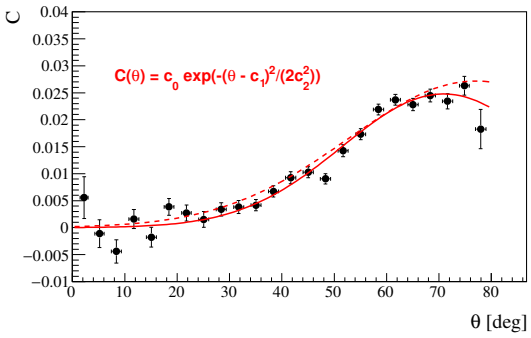

(b) Quadratic term

Figure E.9: Parametrization of the zenith angle dependence of the asymmetry parameters B, C of the signal balance $S_i/\bar{S}$ (high-gain-saturated stations). The linear term (B) is fit first and kept fixed in a second fit for the quadratic term (C). The dashed line shows the fit obtained with non-saturated stations.

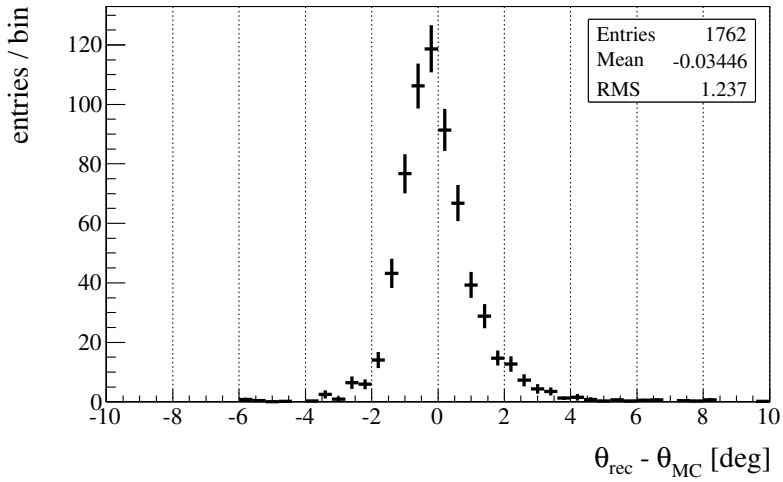

Figure E.10: Reconstruction bias of the zenith angle θ for simulated photons, compared to the true zenith angle (from MC).

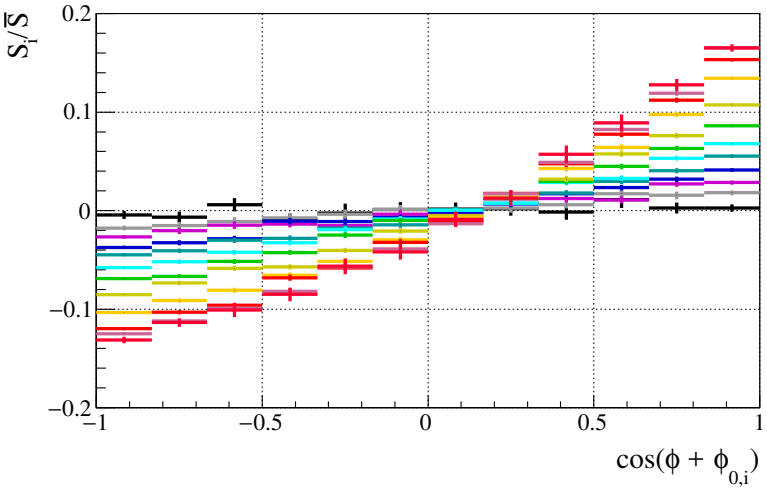

Figure E.11: Azimuthal asymmetry of the signal S_i of PMT i at an azimuthal position $\phi_{0,i}$. The color scale from black to red indicates increasing zenith angles from 0° to 80°.

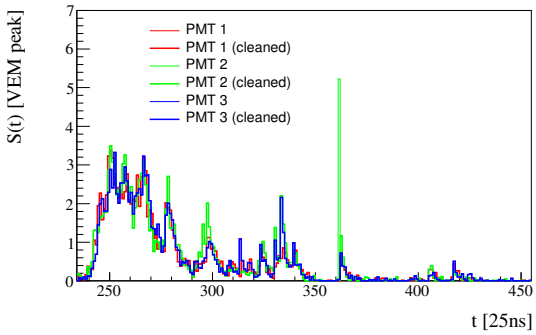

(a) MC photon, showing the full trace.

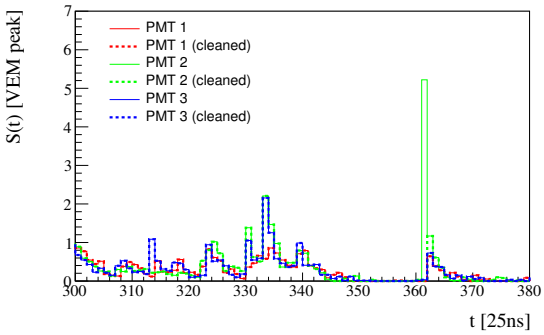

(b) MC photon, focussing the relevant bin 361. These bins are identified with the DLECorrectionGG module but not with the new correction algorithm.

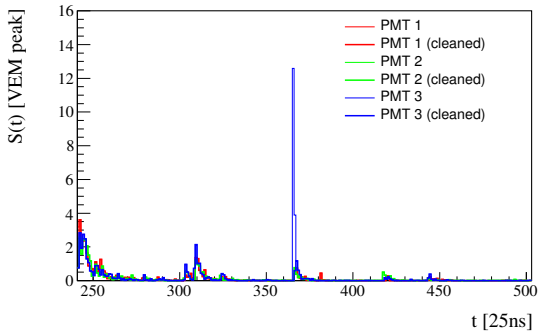

(c) Data, event 4557361, station 987, showing the full trace.

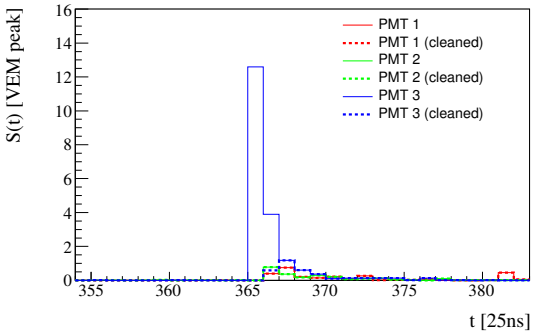

(d) Data, event 4557361, station 987, focussing the relevant bins 365 and 366. This bin is also identified with the new correction algorithm.

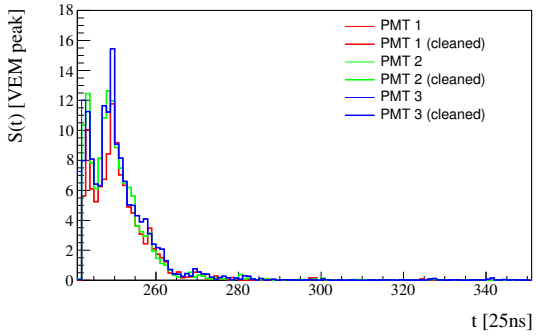

(e) Data, event 4614066, station 1482, showing the full trace.

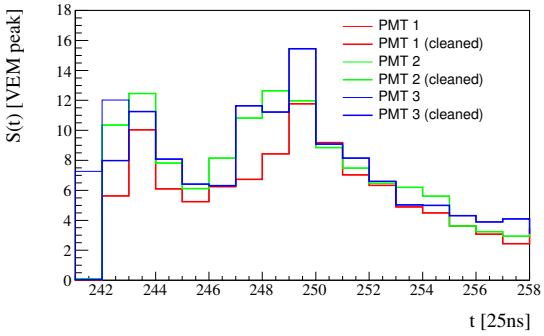

(f) Data, event 4614066, station 1482, focussing the relevant bin 247. This bin is identified with the DLECorrectionGG module but not with the new correction algorithm.

Figure E.12: Examples of signal spikes in only 1 PMT and their correction. Thin lines indicate the trace before, bold lines the trace after correction.

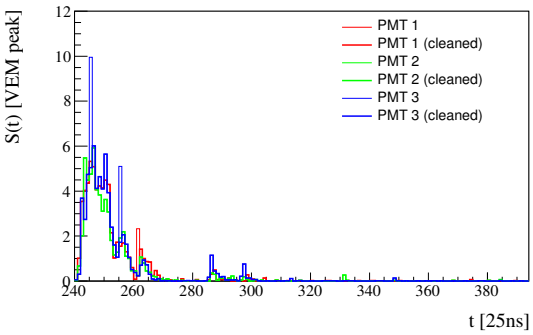

(a) Data, event 6418230, station 824, showing the full trace.

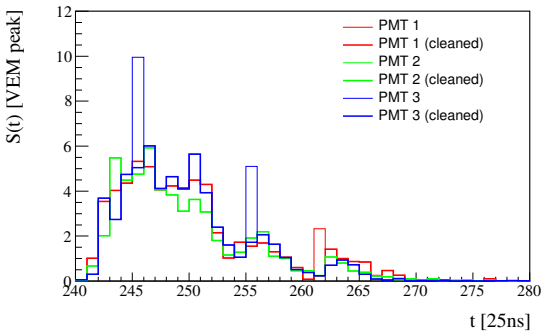

(b) Data, event 6418230, station 824, focussing the relevant bin 261. This bin is not identified with the DLECorrectionGG module but with the new correction algorithm.

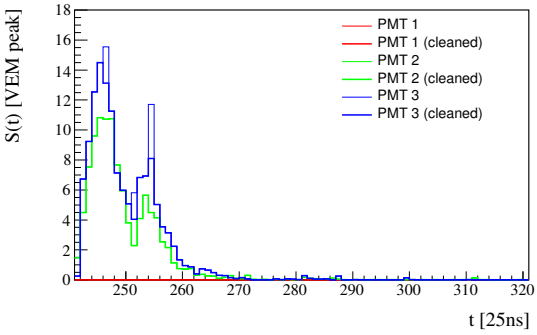

(c) Data, event 6277689, station 126, showing the full trace.

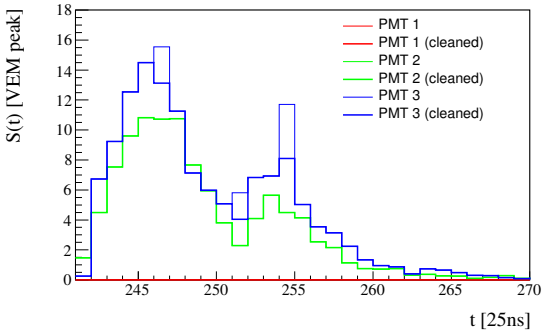

(d) Data, event 6277689, station 126, focussing the relevant bins 246, 251 and 254. These bins are identified with the DLECorrectionGG module but not with the new correction algorithm. This station has only two good PMTs.

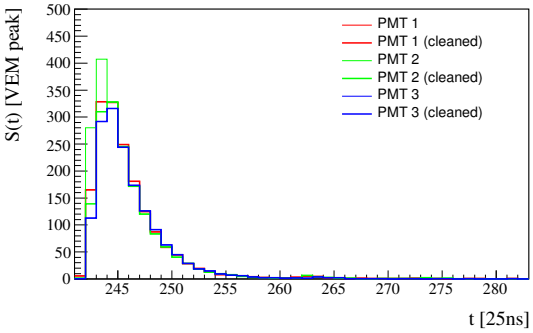

(e) Data, event 5211349, station 839, showing the full trace.

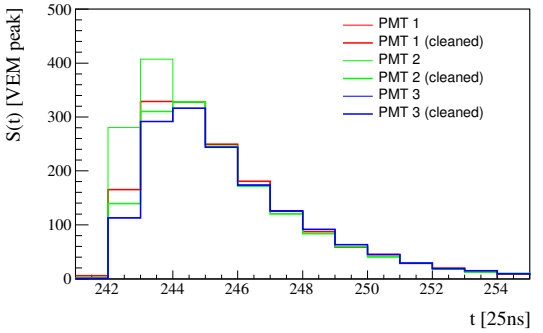

(f) Data, event 5211349, station 839, focussing the relevant bins 242 and 243. These bins are identified with the DLECorrectionGG module but not with the new correction algorithm. This station is high-gain-saturated.

Figure E.13: Examples of signal spikes in only 1 PMT and their correction. Thin lines indicate the trace before, bold lines the trace after correction.

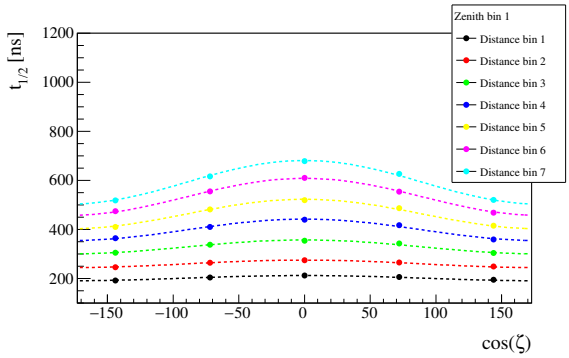

(a) $\sec(\theta) = 1.0 - 1.16$

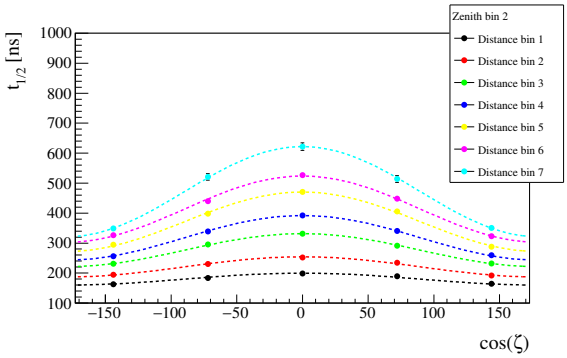

(b) $\sec(\theta) = 1.16 - 1.32$

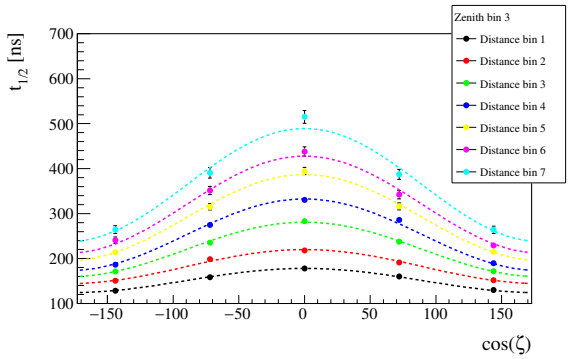

(c) $\sec(\theta) = 1.32 - 1.48$

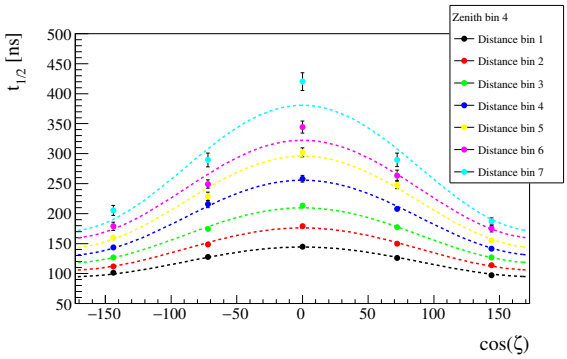

(d) $\sec(\theta) = 1.48 - 1.64$

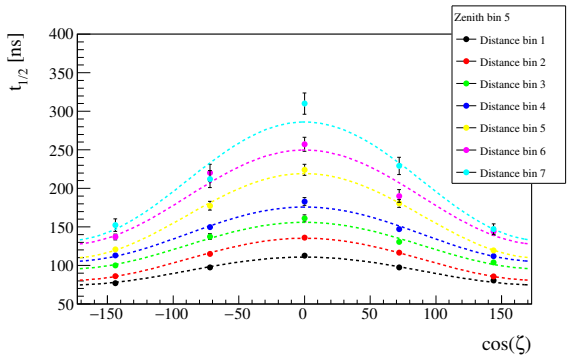

(e) $\sec(\theta) = 1.64 - 1.8$

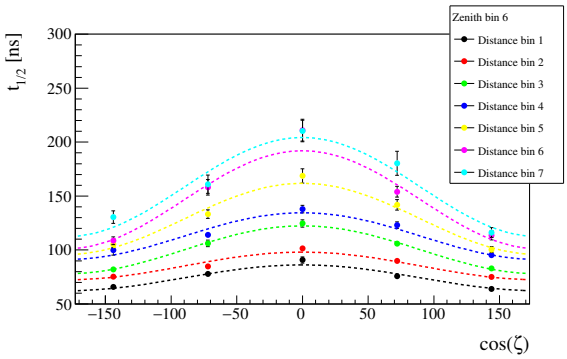

(f) $\sec(\theta) = 1.8 - 2.0$

Figure E.14: Parametrization of the risetime asymmetry (azimuth dependence)

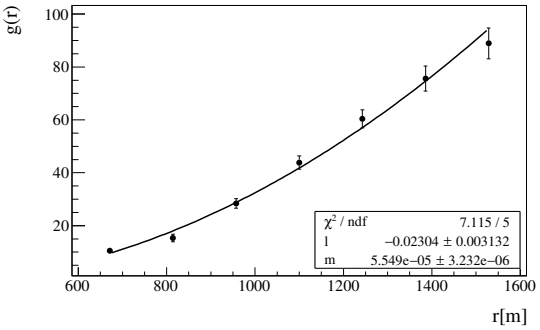

(a) $\sec(\theta) = 1.0 - 1.16$

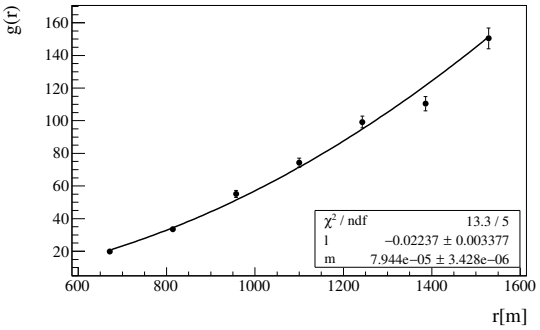

(b) $\sec(\theta) = 1.16 - 1.32$

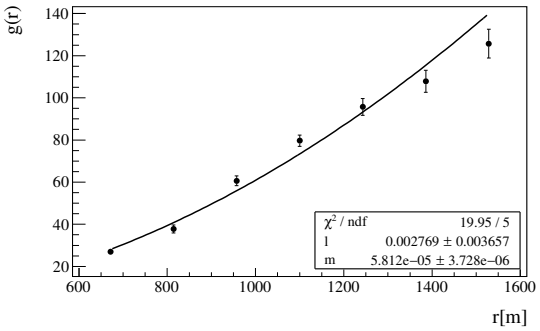

(c) $\sec(\theta) = 1.32 - 1.48$

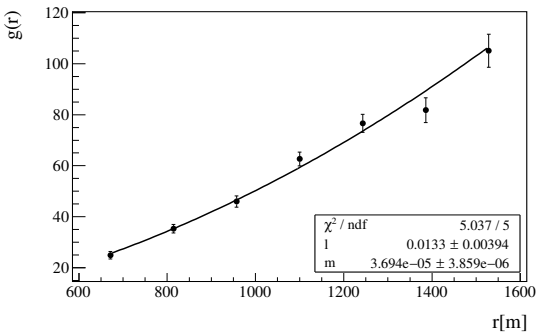

(d) $\sec(\theta) = 1.48 - 1.64$

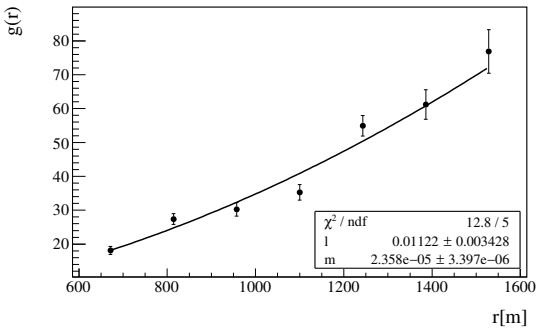

(e) $\sec(\theta) = 1.64 - 1.8$

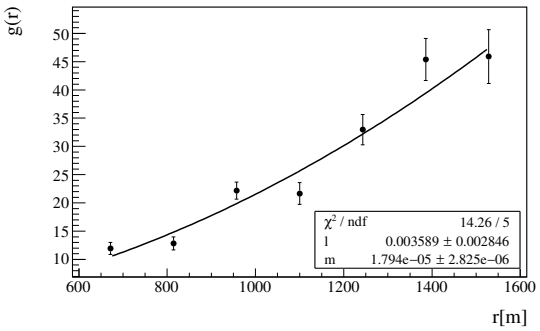

(f) $\sec(\theta) = 1.8 - 2.0$

Figure E.15: Parametrization of the risetime asymmetry (distance dependence)

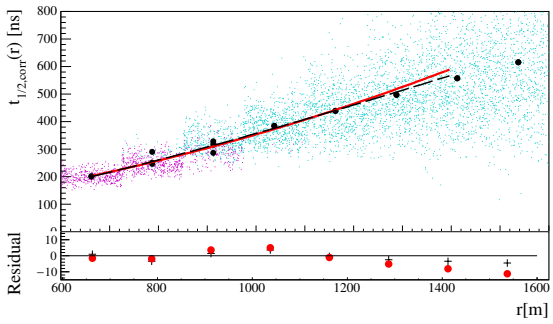

(a) $\sec(\theta) = 1.0 - 1.1$

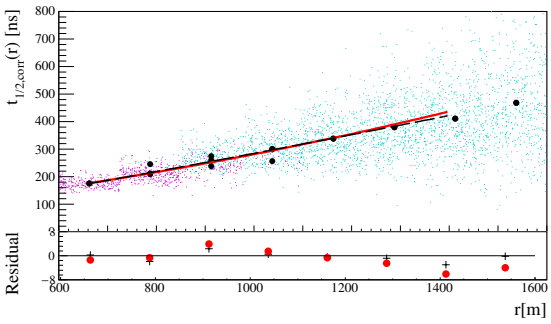

(b) $\sec(\theta) = 1.2 - 1.3$

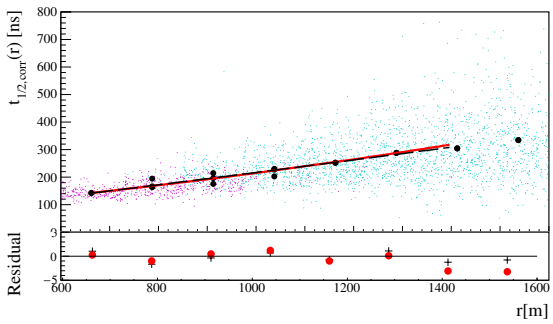

(c) $\sec(\theta) = 1.4 - 1.5$

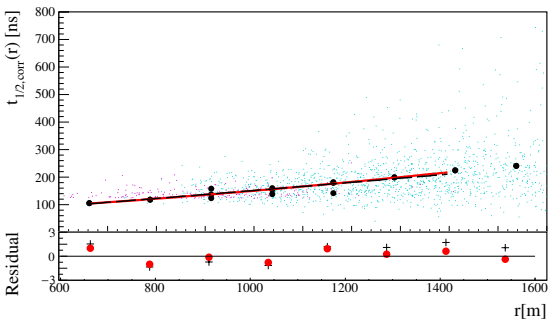

(d) $\sec(\theta) = 1.6 - 1.7$

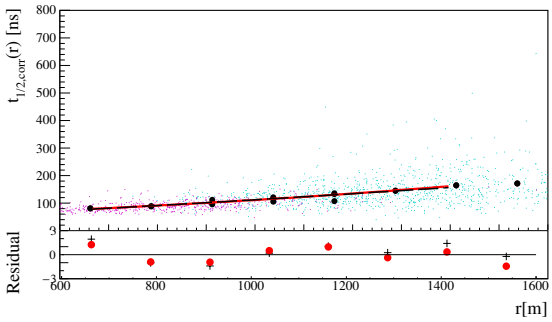

(e) $\sec(\theta) = 1.8 - 1.9$

Figure E.16: Parametrization of the risetime benchmark (distance dependence)

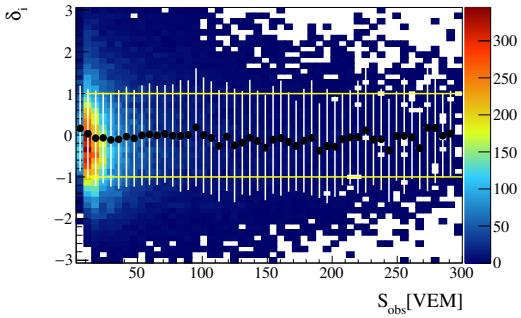

(a) Signal dependence ($S_{\rm exp} > 10$ VEM). The increase of the mean value below 10 VEM is due to the cut on the expected signal.

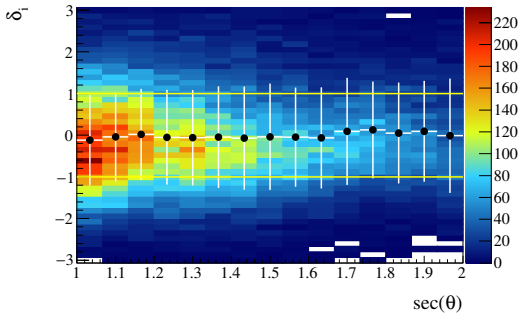

(b) Zenith dependence ($S_{\rm exp} > 10$ VEM)

Figure E.17: Uncertainty-weighted residual, δ_i, of the station risetime, with $E_{\rm hadr,rec} = 10 - 20$ EeV. An overlayed profile shows mean value and standard deviation.

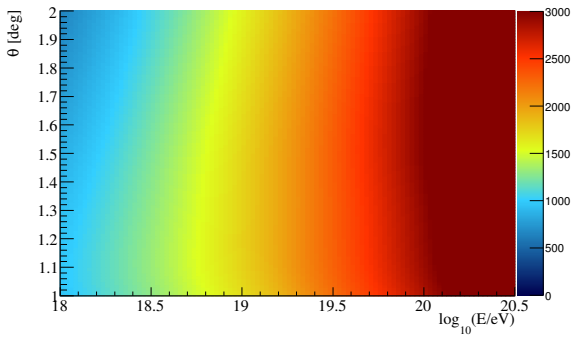

(a) $S_{\rm exp} = 6$ VEM

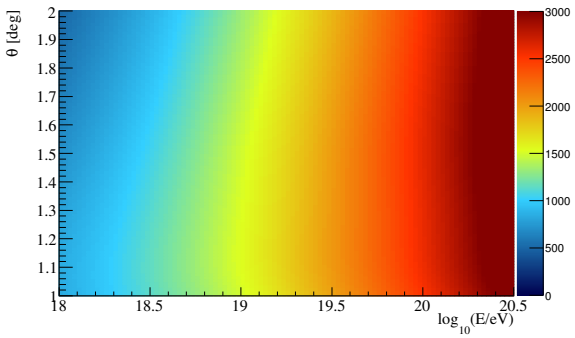

(b) $S_{\rm exp} = 10$ VEM

Figure E.18: Distance corresponding to an expected signal $S_{\rm exp}$.

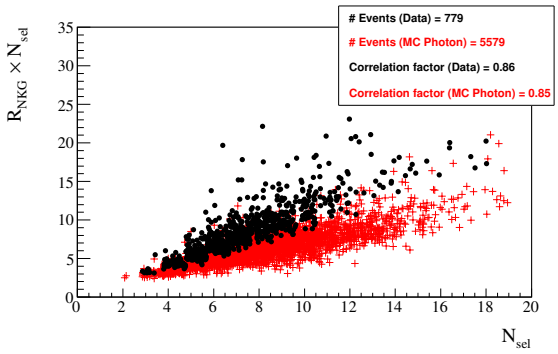

(a) Correlation of $R_{\mathrm{NKG}} \cdot N_{\mathrm{sel}}$ and N_{sel}.

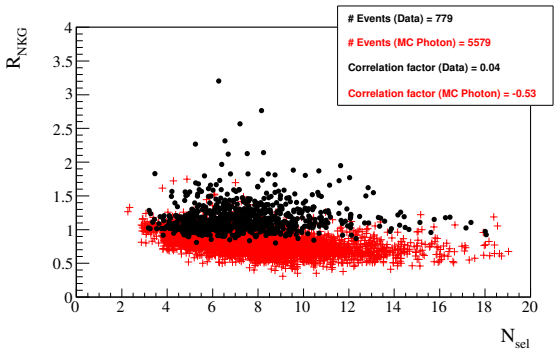

(b) Correlation of R_{NKG} and N_{sel}.

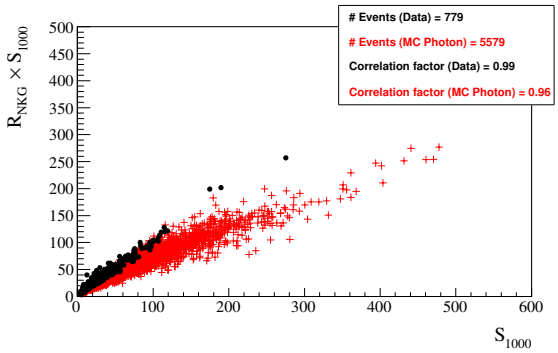

(c) Correlation of $R_{\mathrm{NKG}} \cdot S_{1000}$ and S_{1000}.

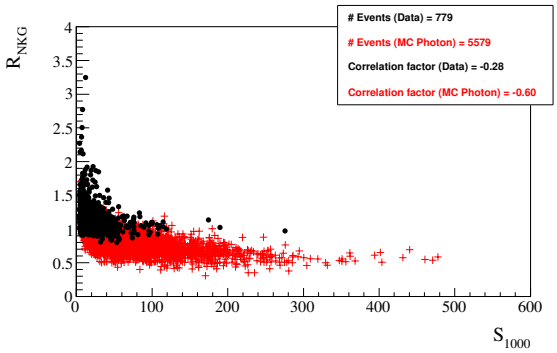

(d) Correlation of R_{NKG} and S_{1000}.

Figure E.19: Normalization of R_{NKG}: Correlation with N_{sel} and S_{1000}.

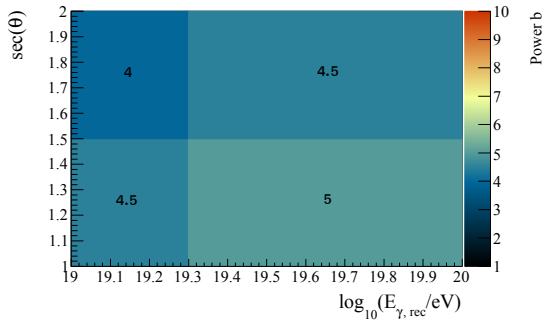

(a) The choice of b that maximizes the merit factor η.

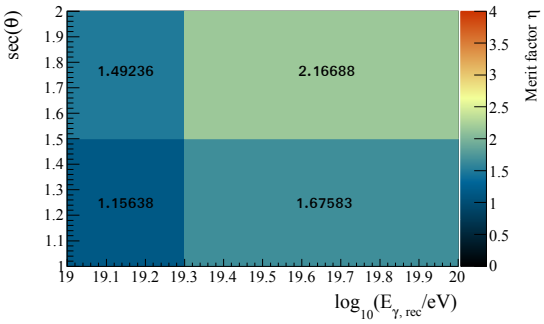

(b) The maximum merit factor η from the scan of b.

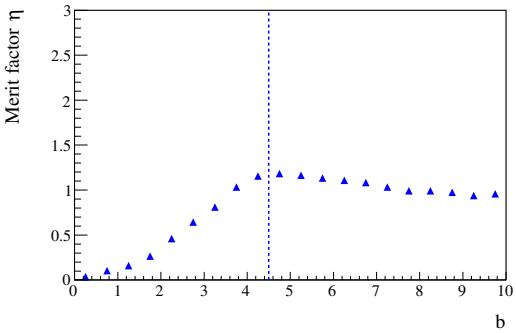

(c) Scan: Energy bin 0, θ bin 0

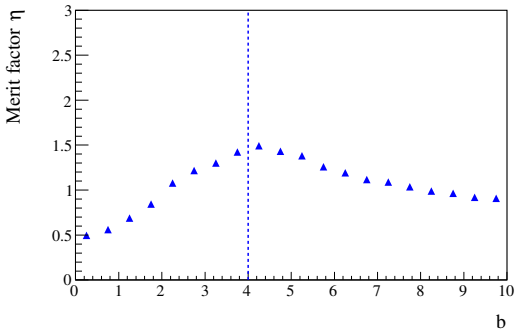

(d) Scan: Energy bin 0, θ bin 1

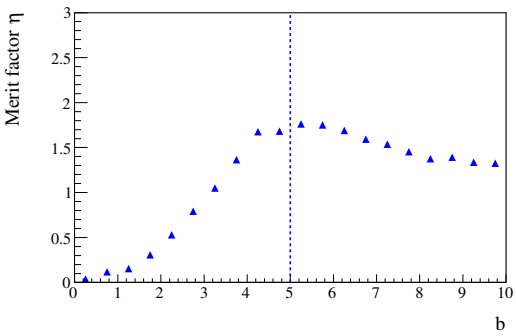

(e) Scan: Energy bin 1, θ bin 0

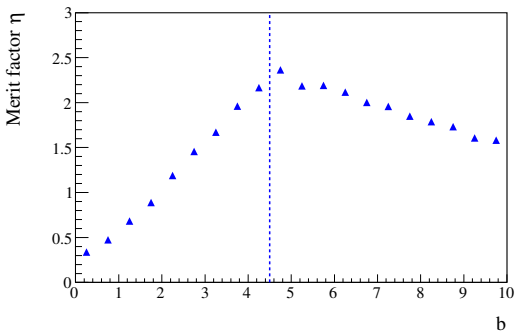

(f) Scan: Energy bin 1, θ bin 1

Figure E.20: Scan of the shape b of a fixed reference LDF that maximizes the photon-hadron separation, based on the merit factor η.

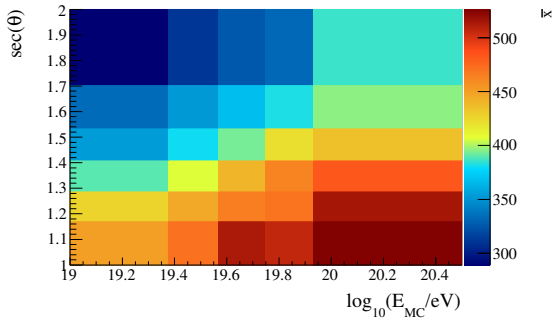

(a) $x = t_{1/2}(1000)$, mean value

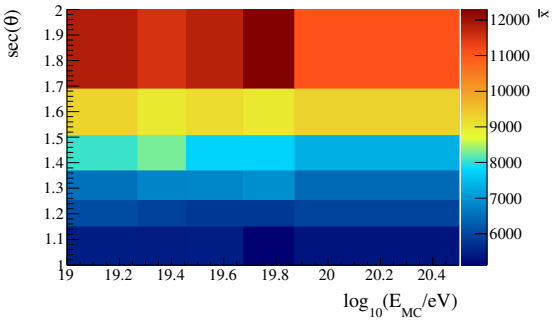

(b) $x = R_c$, mean value

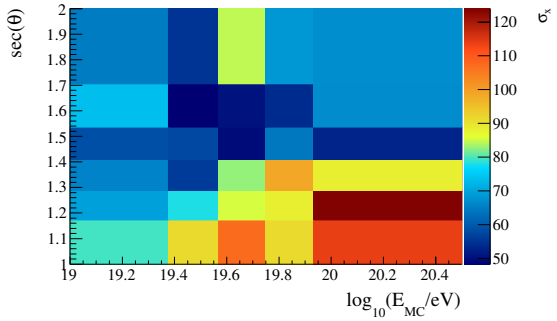

(c) $x = t_{1/2}(1000)$, standard deviation

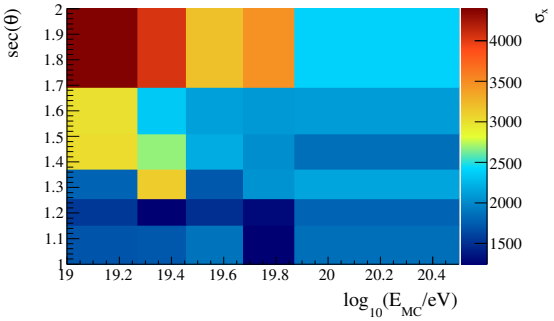

(d) $x = R_c$, standard deviation

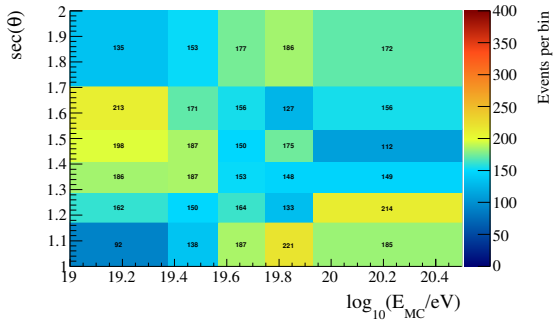

(e) $x = t_{1/2}(1000)$, number of events

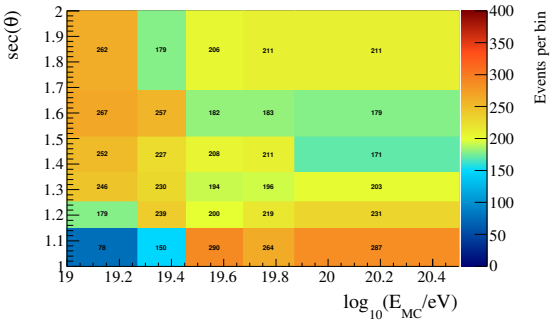

(f) $x = R_c$, number of events

Figure E.21: Mean value and standard deviation of a separation parameter x as expected from MC photon (U).

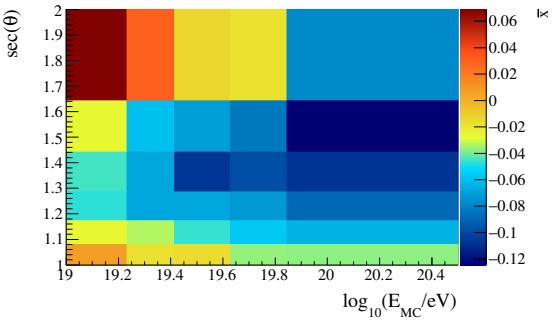

(a) $x = \log_{10}(S^{\mathrm{n}}_{4,1000})$, mean value

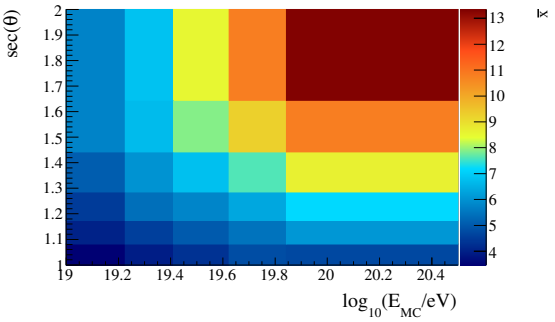

(b) $x = N_{\mathrm{cand}}$, mean value

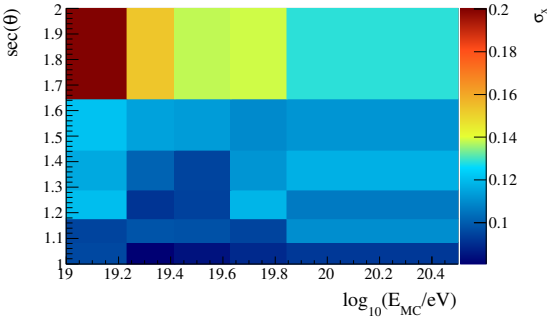

(c) $x = \log_{10}(S^{\mathrm{n}}_{4,1000})$, standard deviation

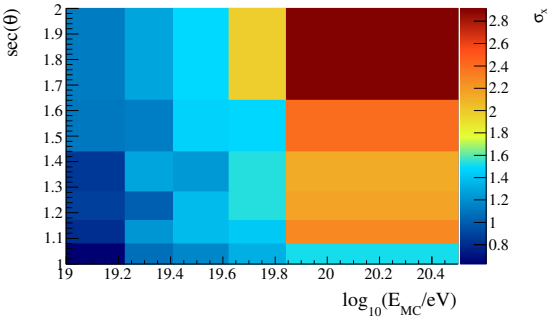

(d) $x = N_{\mathrm{cand}}$, standard deviation

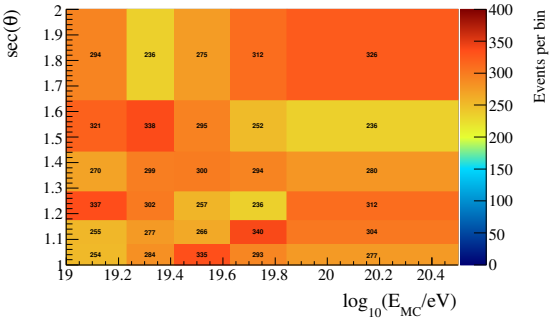

(e) $x = \log_{10}(S^{\mathrm{n}}_{4,1000})$, number of events

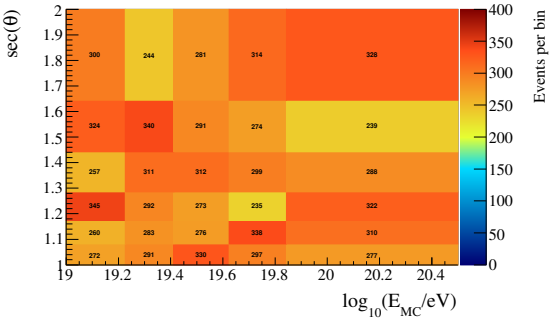

(f) $x = N_{\mathrm{cand}}$, number of events

Figure E.22: Mean value and standard deviation of a separation parameter x as expected from MC photon (U).

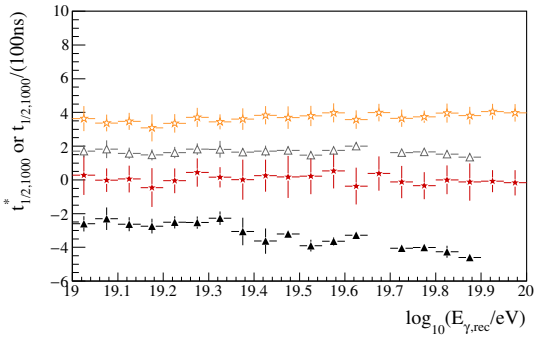

(a) $x = t_{1/2}(1000)$, energy dependence

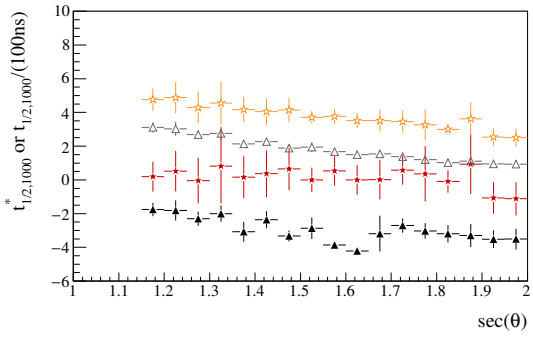

(b) $x = t_{1/2}(1000)$, zenith angle dependence

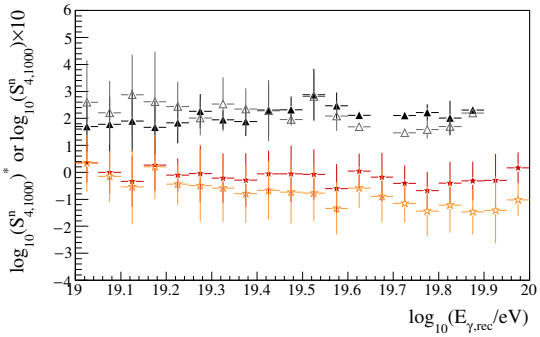

(c) $x = \log_{10}(S^n_{4,1000})$, energy dependence

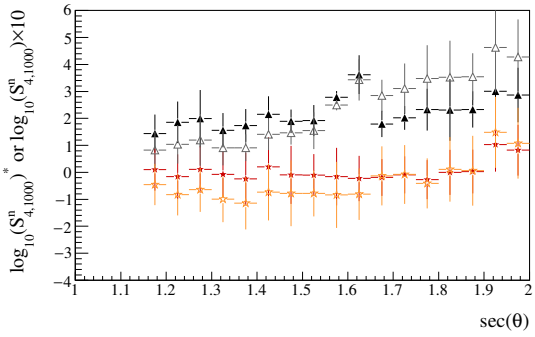

(d) $x = \log_{10}(S^n_{4,1000})$, zenith angle dependence

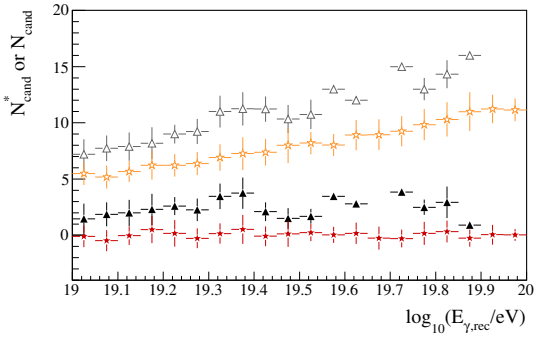

(e) $x = N_{\mathrm{cand}}$, energy dependence

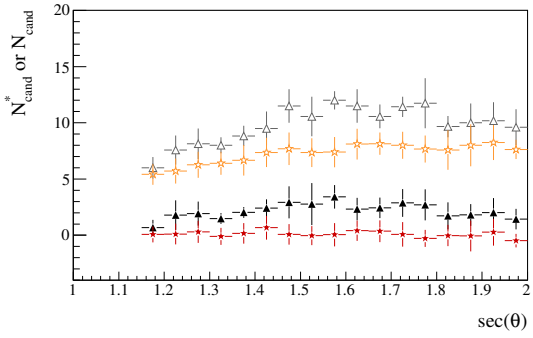

(f) $x = N_{\mathrm{cand}}$, zenith angle dependence

Figure E.23: Removal of the energy and zenith angle dependence expected for MC photons. Red and black markers show the rescaled separation parameter x^*, for data and MC photon (U). Grey and orange markers show the respective distribution of x (scaling factors are given on the y-axis).

Table E.1: SdCalibrator modifications: Consecutive application of the modifications on **observed data**. Discussed are the relative effect on the quantities on the left, for different saturation levels. For events the saturation level *HGSat* means that at least one station has one or more high-gain-saturated PMTs. In case of very small or no effect we write "small" or "none".

	Sat.	*Mod. 1*	*Mod. 2*	*Mod. 3*	*All*
start-time	No	none	none	small	small
	HG	increase max. 10 bins (250ns)	none	small, max. shift by -25ns	increase max. 12 bins (300ns)
stop-time	No	none	$\bar{x} = 0.8$bins, $\sigma = 14.2$bins	none	$\bar{x} = 0.8$bins, $\sigma = 14.2$bins
	HG	$\bar{x} = -301$bins	$\bar{x} = 1.3$bins, $\sigma = 9.0$bins	$\bar{x} = 0.3$bins, $\sigma = 5.4$bins	$\bar{x} = -300$bins
signal	No	none	$\bar{x} = 0.5\%$, $\sigma = 0.6\%$	none	$\bar{x} = 0.5\%$, $\sigma = 0.6\%$
	HG	$\bar{x} = 1.3\%$, $\sigma = 1.6\%$	$\bar{x} = 0.6\%$, $\sigma = 1.3\%$	$\bar{x} = 0.6\%$, $\sigma = 1.6\%$	$\bar{x} = 2.5\%$, $\sigma = 2.9\%$
risetime	No	none	$\bar{x} = 0.6\%$, $\sigma = 1.1\%$	none	$\bar{x} = 0.6\%$, $\sigma = 1.1\%$
	HG	$\bar{x} = 1.4\%$, $\sigma = 1.9\%$	$\bar{x} = 0.7\%$, $\sigma = 1.4\%$	$\bar{x} = 0.6\%$, $\sigma = 1.7\%$	$\bar{x} = 2.7\%$, $\sigma = 3.3\%$
S_{1000}	No	none	$\bar{x} = 0.4\%$, $\sigma = 0.3\%$	none	$\bar{x} = 0.4\%$, $\sigma = 0.3\%$
	HG	$\bar{x} = 0.5\%$, $\sigma = 0.7\%$	$\bar{x} = 0.5\%$, $\sigma = 0.5\%$	$\bar{x} = 0.2\%$, $\sigma = 0.6\%$	$\bar{x} = 1.2\%$, $\sigma = 1.2\%$
β	No	none	small	none	small
	HG	small	small	small	small
γ	No	none	$\bar{x} = -0.5\%$, $\sigma = 4.2\%$	none	$\bar{x} = -0.5\%$, $\sigma = 4.2\%$
	HG	$\bar{x} = -0.2\%$, $\sigma = 8.5\%$	$\bar{x} = -0.2\%$, $\sigma = 5.6\%$	$\bar{x} = 0.0\%$, $\sigma = 4.4\%$	$\bar{x} = -0.3\%$, $\sigma = 10.9\%$
θ	No	none	small	none	small
	HG	$\bar{x} = 0.0\%$, $\sigma = 0.9\%$	small	small	$\bar{x} = 0.0\%$, $\sigma = 1.0\%$
R_c	No	none	$\bar{x} = 0.0\%$, $\sigma = 0.7\%$	none	$\bar{x} = 0.0\%$, $\sigma = 0.7\%$
	HG	52% events, $\sim 5\%$ increase	$\bar{x} = 0.0\%$, $\sigma = 1.3\%$	$\bar{x} = 0.0\%$, $\sigma = 0.3\%$	$\sim 56\%$ events, $\sim 5\%$ increase

Table E.2: SdCalibrator modifications: Consecutive application of the modifications on reconstructed **MC photons**. Dicussed are the relative effect on the quantities on the left, for different saturation levels. For events the saturation level *HGSat* means that at least one station has one or more high-gain-saturated PMTs. In case of very small or no effect we write "small" or "none".

	Sat.	*Mod. 1*	*Mod. 2*	*Mod. 3*	*All*
start-time	No	none	none	small	small
	HG	increase max. 20 bins (500ns)	small, max. shift by ±175ns	small, max. shift by -25ns	increase max. 24 bins (600ns)
stop-time	No	none	$\bar{x} = 0.3$bins, $\sigma = 4.9$bins	none	$\bar{x} = 0.3$bins, $\sigma = 4.9$bins
	HG	$\bar{x} = -127$bins	$\bar{x} = 1.9$bins, $\sigma = 7.8$bins	$\bar{x} = 0.7$bins, $\sigma = 5.8$bins	$\bar{x} = -123$bins
signal	No	none	$\bar{x} = 0.2\%$, $\sigma = 0.5\%$	none	$\bar{x} = 0.2\%$, $\sigma = 0.5\%$
	HG	$\bar{x} = 0.4\%$, $\sigma = 1.6\%$	$\bar{x} = 0.4\%$, $\sigma = 1.3\%$	$\bar{x} = 0.8\%$, $\sigma = 2.9\%$	$\bar{x} = 1.5\%$, $\sigma = 3.6\%$
risetime	No	small	$\bar{x} = 0.2\%$, $\sigma = 0.9\%$	none	$\bar{x} = 0.2\%$, $\sigma = 0.9\%$
	HG	$\bar{x} = 0.4\%$, $\sigma = 1.7\%$	$\bar{x} = 0.3\%$, $\sigma = 1.2\%$	$\bar{x} = 0.8\%$, $\sigma = 2.7\%$	$\bar{x} = 1.4\%$, $\sigma = 3.4\%$
S_{1000}	No	none	$\bar{x} = 0.1\%$, $\sigma = 0.1\%$	none	$\bar{x} = 0.6\%$, $\sigma = 0.6\%$
	HG	$\bar{x} = 0.3\%$, $\sigma = 1.2\%$	$\bar{x} = 0.2\%$, $\sigma = 0.6\%$	$\bar{x} = 0.4\%$, $\sigma = 1.2\%$	$\bar{x} = 1.0\%$, $\sigma = 2.0\%$
β	No	none	small	none	small
	HG	$\bar{x} = 0.1\%$, $\sigma = 0.4\%$	small	small	$\bar{x} = 0.1\%$, $\sigma = 0.4\%$
γ	No	none	$\bar{x} = 0.0\%$, $\sigma = 1.6\%$	none	$\bar{x} = 0.0\%$, $\sigma = 1.6\%$
	HG	$\bar{x} = 0.4\%$, $\sigma = 15.0\%$	$\bar{x} = 0.0\%$, $\sigma = 3.5\%$	$\bar{x} = 0.0\%$, $\sigma = 4.8\%$	$\bar{x} = -0.3\%$, $\sigma = 15.7\%$
θ	No	none	small	none	small
	HG	$\bar{x} = 0.0\%$, $\sigma = 0.7\%$	$\bar{x} = 0.0\%$, $\sigma = 0.3\%$	$\bar{x} = 0.0\%$, $\sigma = 0.7\%$	$\bar{x} = 0.1\%$, $\sigma = 2.2\%$
R_c	No	none	$\bar{x} = 0.0\%$, $\sigma = 0.3\%$	none	$\bar{x} = 0.0\%$, $\sigma = 0.3\%$
	HG	90% events, $\sim 5\%$ increase	$\bar{x} = 0.0\%$, $\sigma = 2.5\%$	$\bar{x} = -0.1\%$, $\sigma = 2.7\%$	$\sim 89\%$ events, $\sim 5\%$ increase

Table E.3: Photon predictions: Photons from astrophysical scenarios (GZK) and Lorentz invariance violation (LIV). *Low* and *high* refers to a pessimistical or optimistical scenario for the photon search. The primary particle is proton (p) or iron (Fe).

Scenario	*BG: Radio*	*IR*	*IGMF*	*Spectrum: Source*	*Observer*	*Ref.*
pI						[75]
Low	High (Clark)		10^{-9} G	$\alpha = -1$, $E_{\max} = 10^{21}$ eV	HiRes	
High	Low (Protheroe)		10^{-11} G	$\alpha = -1$, $E_{\max} = 10^{21}$ eV	HiRes	
pII						[94]
Low	High (Clark)	High	10^{-9} G	$\alpha = -2$, $E_{\max} = 10^{21}$ eV	Auger 2011	
High	Low (Protheroe)	Low	10^{-11} G	$\alpha = -2$, $E_{\max} = 10^{21}$ eV	Auger 2011	
FeII						[94]
Low	High (Clark)	High	10^{-9} G	$\alpha = -2$, $E^{Z}_{\max} = Z \cdot 10^{21}$ eV	Auger 2011	
High	Low (Protheroe)	Low	10^{-11} G	$\alpha = -2$, $E^{Z}_{\max} = Z \cdot 10^{21}$ eV	Auger 2011	
pIII						[104]
Low	High (Clark)		$3 \cdot 10^{-12}$ G	$\alpha = -2$, $E_{\max} = 1/26 \cdot 10^{22}$ eV	Auger 2011	
High	Low		$3 \cdot 10^{-12}$ G	$\alpha = -2$, $E_{\max} = 1/26 \cdot 10^{22}$ eV	Auger 2011	
FeIII						[104]
Low	High (Clark)		$3 \cdot 10^{-12}$ G	$\alpha = -2$, $E^{Z}_{\max} = Z/26 \cdot 10^{22}$ eV	Auger 2011	
High	Low		$3 \cdot 10^{-12}$ G	$\alpha = -2$, $E^{Z}_{\max} = Z/26 \cdot 10^{22}$ eV	Auger 2011	